

Begrijpen van de fotokatalytische activiteit van MOFs:
een gecombineerd experimenteel en theoretisch onderzoek

Understanding photocatalytic activity of MOFs:
a combined experimental and theoretical study

Kevin Hendrickx

Promotor: prof. dr. P. Van Der Voort

Promotor: prof. dr. ir. V. Van Speybroeck

Proefschrift ingediend tot het behalen van de graad van

Doctor in de Wetenschappen: Chemie

Vakgroep Chemie

Voorzitter: prof. dr. I. Van Driessche

Faculteit Wetenschappen

Academiejaar 2017-2018

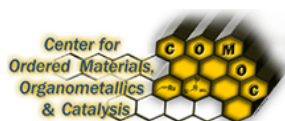
Vakgroep Toegepaste Fysica

Voorzitter: prof. dr. ir. C. Leys

Faculteit Ingenieurswetenschappen en Architectuur

Academiejaar 2017-2018





This research was conducted at the Center for Ordered Materials, Organometallics and Catalysis and at the Center for Molecular Modeling

Leden van de examencommissie

Voorzitter

prof. dr. Klaartje De Buysser (Universiteit Gent)

Examencommissie

prof. dr. Frank De Proft (Vrije Universiteit Brussel)

prof. dr. Dirk De Vos (Katholieke Universiteit Leuven)

dr. Karen Hemelsoet (Universiteit Gent)

dr. Kurt Lejaeghere (Universiteit Gent)

prof. dr. Dirk Poelman (Universiteit Gent, *Secretaris*)

dr. Monique van der Veen (TU Delft)

prof. dr. Pascal Van Der Voort (Universiteit Gent, *promotor*)

prof. dr. ir. Veronique Van Speybroeck (Universiteit Gent, *promotor*)

Langsam und schmerzhaft.

2 Flöten. $\frac{3}{8}$

2 Oboen. $\frac{3}{8}$

1 Englisches Horn $\frac{3}{8}$

1. u. 2. Fagott $\frac{3}{8}$

2. Horn. $\frac{3}{8}$

Violoncelle. $\frac{3}{8}$

R. Wagner

Voorwoord

Kevin Hendrickx
2017, Gent

Contents

Voorwoord	ix
Contents	xi
List of Abbreviations	xv
Samenvatting	xix
Summary	xxiii
I Setting the scene	1
1 Introduction	3
1.1 Challenges for the 21th century	3
1.2 Materials design	4
1.3 Goal and outline	6
2 Metal-Organic Frameworks	11
2.1 Towards coordination polymers	11
2.1.1 Coordination chemistry	11
2.1.2 Porous materials	12
2.1.3 The dream of materials scientists	13
2.1.4 Birth of MOFs	15
2.1.5 Natural MOFs	16
2.1.6 What's next?	18
2.2 Applications	19
2.2.1 From gas sorption to catalysis	21
2.2.2 Industrial perspectives	24
2.3 A systematic stability study	25
2.3.1 Introduction	25
2.3.2 Materials and Methods	27
2.3.3 Results and Discussion	29
2.3.4 Conclusions	35

2.4	UiO-66: A stable MOF	36
2.4.1	Structure	36
2.4.2	Synthesis	38
2.4.3	Electronic structure of UiO-66	40
3	Photocatalysis	43
3.1	Materials for light-harvesting	43
3.2	Photocatalysis	44
3.3	MOFs and photocatalysis	48
3.3.1	UiO-66	49
4	Experimental and computational methods	53
4.1	Experimental methods	53
4.1.1	Characterization	53
4.1.2	Optical spectroscopy	55
4.1.3	Gas phase photocatalysis setup	60
4.2	Computational modelling	62
4.2.1	Quantum description of matter	63
4.2.2	Density Functional Theory	64
4.2.3	Time-Dependent DFT	65
4.2.4	Dynamic methodology	67
II	Understanding intrinsic light absorption	71
5	Intrinsic light-absorption in MOFs	73
5.1	Introduction	74
5.2	Materials and methods	75
5.2.1	Experimental Details	76
5.2.2	Computational methodology	78
5.3	Results and Discussion	81
5.3.1	Experimental Results	81
5.3.2	Theoretical Absorption Spectra and Charge Analysis	82
5.3.3	Electronic absorption spectra of inorganic-organic cluster models	86
5.3.4	Band gap alterations	88
5.3.5	Geometry of linkers in Gas phase vs framework	90
5.3.6	Density of state and band structure analysis	90
5.4	Conclusion	96

6	Vibrational fingerprint	99
6.1	Introduction	99
6.2	Methodology	102
6.2.1	Ab initio molecular dynamics	102
6.2.2	Calculation of VPS and ϵ PS	103
6.3	Results	103
6.3.1	Dynamic vs Static excitation energies	103
6.3.2	Vibrational analysis	110
6.3.3	VPS vs. ϵ PS	114
6.4	Conclusions	120
III	Improving photocatalytic properties	123
7	Improving charge transfer via metal doping	125
7.1	Introduction	126
7.2	Materials and methods	129
7.2.1	Synthesis	129
7.2.2	Characterization	130
7.2.3	Empirical model for charge-state transition levels	131
7.2.4	Computational details	131
7.3	Results and discussion	133
7.3.1	Synthesis and Characterization	133
7.3.2	Spectroscopy	139
7.3.3	Charge-state transition levels	143
7.3.4	Computational assessment	149
7.4	Catalysis	155
7.5	Conclusion	157
8	Improving charge transfer via defect engineering	159
8.1	Introduction	159
8.2	Results and discussion	160
8.2.1	Defect structures	160
8.2.2	Electronic properties	163
8.3	Conclusions	172
9	Conclusions and perspectives	173
9.1	Conclusions	173
9.2	Perspectives	175
J	Supplementary Information	177
	Supplementary Information of chapter 2	179
	Supplementary Information of chapter 8	193

K List of Publications	197
Bibliography	203
Acknowledgments	233

List of Abbreviations

AI	Ab Initio
AS	As-Synthesizes
B3	Becke threeparameter (Exchange)
BDC	benzene-1,4-dicarboxylate
BFSTEM	Bright-Field Scanning Transmission Electron Microscopy
BLB	Bouguer-Lambert-Beer
BO	Born-Oppenheimer
BOMD	Born-Oppenheimer Molecular Dynamics
BPDC	4,4'biphenyldicarboxylicacid
BTC	benzenetricarboxylate
CN	Coordination Number
COF	Covalent Organic Framework
COMOC	Center for Ordered Materials, Organometallics and Catalysis
CSVr	Canonical Sampling through Velocity Rescaling
CT	Charge Transfer
DFT	Density Functional Theory
DMA	Dimethylacetamide
DMF	Dimethylformamide
EDX	Energy-Dispersive X-rays
EN	Electronegativity
ϵ PS	ϵ -Power Spectrum
ES	Excited State
ET	Energy Transfer
eV	electron volt
FEG	Field Emission Gun
fum	fumaric acid
GGA	Generalized Gradient Approximation
GPW	Gaussian Plane Waves
GS	Ground State
hcb	honeycomb (topology)
HE	Hirshfeld Extended
HF	Hartree-Fock
HI	Hirshfeld Iterative

HKUST	Hong Kong University of Science and Technology
HOCO	Highest Occupied Crystalline Orbital
HOMO	Highest Occupied Molecular Orbital
HPC	High Performance Computing
HRBE	Host Referred Binding Energy
ILD	Inter-Linker Distance
ISC	Inter-System Crossing
IRMOF	Isorecticular Metal-Organic Framework
IUPAC	International Union of Pure and Applied Chemistry
KET	Key Enabling Technologies
KS	Kohn-Sham
LDA	Local Density Approximation
LMCT	Ligand-to-metal charge transfer
Ln	Lanthanide
LUCO	Lowest Unoccupied Crystalline Orbital
LUMO	Lowest Unoccupied Molecular Orbital
LYP	Lee-Yang-Parr (correlation)
MCD	Multiple Concentration Detection
MGI	Materials Genome Initiative
MID	Multiple Ion Detection
MIL	Matériaux de l'Institut Lavoisier
MD	Molecular Dynamics
MOF	Metal-Organic Framework
PBE	Perdew-Burke-Ernzerhof
PCP	Porous Coordination Polymer
PDOS	Projected Density-of-States
PES	Potential Energy Surface
PL	Photo-Luminescence
PMO	Periodic Mesoporous Organosilica
PSM	Post-Synthetic Modification
PXRD	Powder X-Ray Diffraction
QM	Quantum Mechanics
RT	Room Temperature
SBU	Secondary Building Unit
SOMOS	Singly Occupied Molecular Orbital
TEM	Transmission Electron Microscopy
TDDFT	Time-Dependent Density Functional Theory
TGA	Thermogravimetric Analysis
THF	Tetrahydrofuran
TPA	Terephthalic Acid (see BDC)
UiO	Universitetet i Oslo (University of Oslo)
UV/Vis	Ultraviolet/Visible

vdW	van der Waals
VPS	Velocity Power Spectrum
VRBE	Vacuum Referred Binding Energy
SAPO	Silico Alumino Phosphate
SEM	Scanning Electron Microscopy
SI	Système Internationale
STY	Space-Time Yield
XPRD	X-ray Powder Diffraction
XRD	X-Ray Diffraction
ZIF	Zeolite Imidazolate Framework
ZSM	Zeolite Socony Mobil

Samenvatting

Metaal-Organische Roosters (MOFs) vertegenwoordigen een interessante klasse van materialen dankzij het nagenoeg ongelimiteerd aantal van structuren welke kunnen gevormd worden gecombineerd met hun uitzonderlijke eigenschappen. Origineel exploiteerden onderzoekers overwegend hun ongeëvenaarde porositeit en intern oppervlak in toepassingen als gas sorptie en scheiding. Hiernaast buit men ook de goed gedefinieerde kristallijne structuur en de transitietaalnodes uit in heterogene katalyse. Recentelijk zijn onderzoekers gestart om hun specifieke elektronische structuur in meer hoogwaardige toepassingen zoals bv luminescentie en fotokatalyse beginnen te onderzoeken en te exploiteren. Dit werk valt onder het laatst aangehaalde onderzoeksgebied.

Het werk in dit proefschrift legt de focus op de UiO-66 MOF, een Zr-gebaseerde MOF dat twaalfvoudig gecoördineerde Zr-nodes omvat, gelinkt door bidentaat tereftaalzuur liganden. Dit resulteert in een uitzonderlijk stabiele structuur met vele mogelijkheden voor diverse toepassingen. De robuuste synthese, welke toelaat om gemakkelijk verschillende isostructurele materialen te bouwen, heeft geresulteerd in een ruime belangstelling van zowel de wetenschappelijke gemeenschap als recentelijk ook de industrie. In dit proefschrift wordt een **gecombineerde experimentele en computationele benadering** naar voor geschoven om in detail **de elektronische structuur van dit materiaal te bestuderen en aan te passen voor een verbeterde activiteit in fotokatalyseprocessen**.

Ten einde de geëxciteerde toestand van moleculen te bestuderen, heeft TDDFT de weg geplaveid om grotere systemen te bestuderen met een redelijke precisie tegen een haalbare computationele kostprijs. Een eerste hoofdstuk van dit werk handelt over een **uitgebreide studie omtrent de functionalizatie van de organische linkers en het effect op de elektronische structuur en lichtabsorptie eigenschappen** van een set van gefunctionaliseerde UiO materialen. Een grote basis-set test en een studie van verscheidene DFT functionalen heeft een combinatie van de B3LYP functionaal met een Pople triple- ζ basis set met diffuse en polariserende functies (6-311+G(d,p))

naar voor geschoven als meest kost-efficiënte methode. In dit hoofdstuk gebruiken we een *bottom-up* benadering om de MOF te deconstrueren tot zijn kleinste eenheden, de linkers en anorganische clusters, om deze onderdelen afzonderlijk te onderzoeken. Vervolgens bouwen we eerst cluster modellen met deze bouwstenen en tot slot maken we berekeningen op het gehele periodieke materiaal. Deze modulaire benadering liet toe om de verschillende aspecten van de elektronische structuren te bestuderen. Eerst, de toevoeging van een elektron-donerende groep voegt een nieuwe absorberende band bij in het UV/Vis spectrum vergeleken met de originele BDC linker. Via TDDFT laten we zien dat deze band zuiver linkerbaseerd is en we tonen aan dat de overgang overeenstemt met de HOMO-LUMO excitatie van de linker. Zorgvuldige observatie van de orbitalen welke een rol spelen in deze overgang laat zien dat de bijdrage van de elektron gevende groep verdwijnt in de geëxciteerde toestand, hetgeen wij verder kunnen verklaren door de Hirschfeld-I lading te bestuderen. Via TDDFT berekeningen op een eenvoudig clustermodel, welke 1 anorganische cluster omvat beëindigd met mierenzuur en twee TPA linkers, werd de Ligand-naar-Metaal-Ladingstransfer (LMCT) onderzocht en bleek inefficiënt te zijn, maar niettemin afhankelijk van de functionele groep. Uiteindelijk lieten de periodieke resultaten toe om de invloed van de functionele groep te begrijpen in termen van een gevulde band ingevoegd in de oorspronkelijke band gap. Deze reductie in band gap werd experimenteel waargenomen en een goede overeenstemming met de DFT resultaten werd gevonden.

De TDDFT berekeningen in dit hoofdstuk werden allemaal statisch uitgevoerd, bij 0K in gasfase, en soms werd er geen perfecte overeenstemming gevonden tussen de berekende en experimentele spectra. Om het belang van de **flexibiliteit in het rooster op een meer fundamenteel niveau te begrijpen**, hebben we een **complexe studie uitgevoerd om de vibrationele vingerafdruk van de serie UiO-66 en UiO-67 type materialen** te bepalen. De invloed van nucleaire bewegingen op de geëxciteerde eigenschappen worden duidelijk verhelderd door steekproefsgewijs het potentieel energie oppervlak van de grondtoestand te bekijken via ab initio moleculaire dynamische (AIMD) simulaties. Vervolgens werden gemiddelde dynamische absorptie eigenschappen berekend en vergeleken met absorptie gegevens van een geoptimaliseerde geometrie. De steekproef werd uitgevoerd voor zowel de gasfase organische linker als het volledige periodische UiO rooster. Rekening houdende met de afzonderlijke simulaties welke verschillende sets van gegenereerde geometrieën behelzen, laat de analyse toe de invloed van het rooster, temperatuur en harmonische en anharmonische nucleaire bewegingen te bepalen.

Het tweede deel van dit proefschrift bespreekt mogelijkheden om de elektronische structuur van het materiaal verder te verbeteren. De meest gebruikelijke manier is de **dopering van het materiaal met verschillende metaal ionen**. In het eerste stadium presenteren we een strategie gebaseerd op microgolven om de tijd- en energierovende methode gebruikt in de huidige MOF chemie te verbeteren. Een vermindering van de synthesetijd van 5 dagen naar enkele uren werd bereikt en daarenboven behielden de MOFs een betere kristallijne structuur. Aan de hand van deze methode synthetiseerden we diverse gedopeerde UiO-structuren (Ti, Hf, Ce, Nd, Yb, Eu) en onderzochten we via experimentele en computationele methoden de invloed op de elektronische structuur. Omtrent de isovalente (Ti, Hf) structuren is reeds veel data beschikbaar in literatuur. Het combineren van de inspanningen van verschillende onderzoeksgroepen met onze nieuwe computerresultaten geven een volledig en diep **begrip van het ladingsoverdracht-mechanisme** in deze materialen. Dopering met lanthaniden levert een reeks materialen op met diverse eigenschappen. Aangezien de energieniveaus van deze overgangsmetalen zich gedragen op een unieke en voorspelbare manier, kunnen ze uitgelijnd worden met de UiO energieniveaus via spectroscopische metingen en een simpel empirisch model. Dit model laat dan toe experimentele metingen te verklaren en ook voorspellingen te doen over het gedrag van deze materialen.

Een tweede manier om de elektronische eigenschappen van de materialen die we vooropstelden te verbeteren was de **inclusie van defecten in het materiaal**. Verschillende onderzoekers hebben synthetische methodes ontwikkeld om het aantal en het type van defecten in de UiO-66 te controleren. Via DFT berekeningen op zowel het periodieke materiaal als de cluster modellen hebben we de **invloed ontrafeld van linkerdefecten op de elektronische eigenschappen**, die aantonen dat de aanwezigheid van Zr atomen met 2 of 3 ongecoördineerde plaatsen een zelfde effect hebben als de inclusie van bijvoorbeeld een Ti atoom in de node.

Bij het ontwikkelen van UiO-66 roosters voor fotokatalyse zijn er **verschillende wegen mogelijk om hun lichtabsorptie en ladingsoverdrachtseigenschappen te sturen**. Het grotendeels onafhankelijke gedrag van linkers en anorganische nodes maakt het mogelijk de elektronische structuur met de verschillende bestanddelen te modelleren. Dit werd gebruikt om via een gecombineerde theoretische en experimentele aanpak de elektronische structuur op een fundamenteel niveau te ontrafelen via een modulaire aanpak. Bovendien hebben de inzichten die we bereikten met onze studie gecombineerd met de nieuwe lanthanide gedopeerde materialen in een duidelijk en consistent beeld van de ontwikkelde UiO materialen, en zullen hopelijk

verder onderzoek bevorderen in het domein van lichtgebaseerde toepassingen met MOFs.

Summary

Metal-Organic Frameworks represent a very interesting class of compounds thanks to the almost unlimited amount of structures that can be generated, combined with their exceptional properties. ‘Traditionally’ researchers exploited their unequalled porosity and internal surfaces for gas sorption and separation applications and the advantages of their well-defined structures and transition metal nodes in heterogenous catalysis. More recently, researchers started to investigate and exploit their specific electronic structure in more high-end applications as e.g. luminescence and photocatalysis. This work is situated in this last area of research.

The work in this thesis centers around the UiO-66 material, a Zr-based MOF containing 12-fold coordinated Zr-nodes linked by terephthalic acid linkers, yielding an exceptionally stable structure with many possibilities in a plethora of applications. The robust synthesis, allowing to built easily several isostructural materials resulted in a large interest both by the scientific community as well as the industry. In this thesis a **combined experimental and computational approach is followed to study in detail the electronic structure of this material and its evaluation for photocatalytic processes.**

In a first stage of this thesis, we investigate the **intrinsic light-absorption properties of a set of functionalized UiO-materials.** To study excited states in molecules, TDDFT has paved the way to study larger systems with a reasonable accuracy at a feasible computational cost. A large basis-set test and a study of different DFT functionals brought forward that a combination of the B3LYP functional with a Pople triple- ζ basis set with diffuse and polarization functions 6-311+G(d,p) yields very accurate results at a limited computational cost. In a first instance, we use bottom-up approach by breaking down the MOF to its smallest constituents, the linkers and the inorganic nodes, and investigate these parts separately. Then, we build first cluster models with these bricks and finally perform calculations on the full periodic material. This modular approach allowed to observe different aspects of the electronic structure. First, the addition of an electron donating group

adds an extra absorption band in the Ultraviolet/Visible (UV/Vis) spectrum compared to the original TPA linker. Via TDDFT we show that this band is purely linker-based and we show that the transition corresponds to the HOMO-LUMO excitation of the linker. Careful observation of the orbitals playing a role in this transition showed that the contribution of the electron donating group vanishes in the excited state, which we could explain by studying the Hirshfeld-I charges. Via TDDFT calculations on a simple cluster model, containing 1 inorganic node terminated by formic acid anions and two TPA linkers, the Ligand-To-Metal-Charge Transfer (LMCT) was investigated and shown to be inefficient, but nevertheless functionalization dependent. Finally the periodic results allowed to understand the influence of the functional group in terms of a filled gap state, introduced in the band gap of the material. This reduction in band gap was measured experimentally and a good correspondence with the DFT results was found.

The TDDFT calculations in this previous chapter were all performed statically, at 0K in gas phase, and sometimes a not perfect match between the the computational and experimental spectra was found. In order to **understand the importance of the flexibility of the framework on a more fundamental level**, we performed a complex study to determine the vibrational fingerprint of a series of UiO-66 and UiO-67 type materials. The impact of nuclear motions on the excitation properties are accounted for by sampling the potential ground-state surface using ab initio molecular dynamics (AIMD) simulations. Subsequently, averaged dynamic absorption properties are calculated and compared with absorption data from an optimized geometry. The sampling is performed for both the gas phase organic linker and the fully periodic UiO framework. Given the distinct simulations involving various sets of generated geometries, the analysis allows addressing the influence of the periodic framework, temperature and harmonic and anharmonic nuclear motions.

The second part of this thesis discusses ways to tune the electronic structure of the material. The most familiar way is the **doping of the material with different metal ions**. In a first stage, we present a microwave-based strategy in order to improve on the time- and energy-consuming methodology used in current MOF chemistry. A reduction of synthesis times from 5 days to a few hours was achieved and moreover the materials showed a much better preserved crystallinity. With this method, a series of doped UiO frameworks (Ti, Hf, Ce, Nd, Yb, Eu) was synthesised. First, a computational and experimental study of the doping of UiO-66 with isovalent metal ions (Ti, Hf) was performed. Our computational calculations shed light on the **charge transfer mechanisms**. Combining the effort of several research groups with

our new computational results yields a complete and profound understanding on the charge transfer mechanism in this materials. Since the energy levels of these dopants behave in a peculiar and predictable way, they could be aligned with the UiO energy levels via photoluminescence measurements.

In order to bring the above procedure to new application areas and obtain a more fundamental understanding, we inserted several Lanthanide (Ln) ions in the UiO framework via our aforementioned microwave method. Since the energy levels of these transition metals behave in a peculiar and predictable way, they could be aligned with the UiO energy levels via photoluminescence measurements.

A second way to improve the electronic properties of the materials we proposed was the **inclusion of defects** in the material. Several researchers developed synthetic methods to tune the number and type of defects in the UiO-66. Via DFT calculations on both the periodic material as well as cluster models we **unravalled the influence of linker defects on the electronic properties**, showing that the presence of Zr atoms with 2 or 3 uncoordinated sites have a similar effect as the inclusion of e.g. a Ti atom in the node.

When designing UiO-66 frameworks for photocatalysis, **different pathways are available to engineer their absorption and charge transfer capabilities**. The largely independent behaviour of linkers and inorganic nodes enables to engineer the electronic structure by modulating the different constituents. This work uses a combined experimental and theoretical approach to unravel the electronic structure at a fundamental level, via a modular approach. Furthermore, the insights obtained by our study combined with the current available literature resulted in a clear and consistent picture of the engineered UiO materials and hopefully will incite further research in the domain of light-based applications with MOFs.

Part I

Setting the scene

1

Introduction

1.1 Challenges for the 21th century

Despite the depleted fossil fuel reserves and the ever more pressing consequences of anthropogenic climate changes, global energy consumption shows a continuous rise. [1] The need for more green and sustainable processes has inspired researchers for decades to investigate alternative energy sources to cope for the human needs. The contiguousness of irreversible consequences that will affect the larger sheer of the human population has led to tremendous advancements in science, giving us at least the hope that chemistry researchers in the 21st century hold the key to solve many of these problems of sustainability.

Although the sun is an unlimited source of energy, current needs for energy and materials are mostly based on fossil fuel feedstock. Many progress has been made in the design of materials and processes based on these, but unfortunately these are not renewable. The natural oil reserves are the result of millions of years of chemical transformations of dead plants and other organisms. The exploitation of green plants to obtain energy from e.g. agricultural waste could offer a renewable source although still highly restricted. One has to make sure the interference on the cultivation for food stays limited, which is not always the case with current technologies. The direct use of sunlight both for energy and chemical synthesis is nowadays regarded as a promising route to head towards more sustainable processes. All of the above are connected via different pathways as shown in figure 1.1. Central

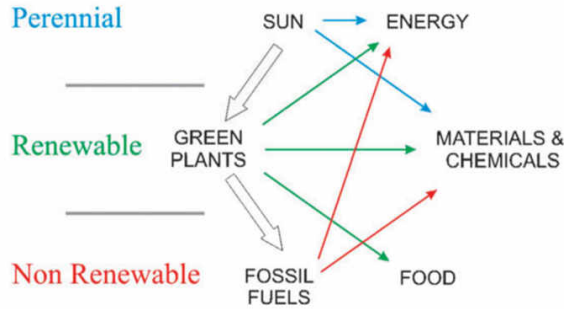


Figure 1.1: Schematic representation of the solar energy flow. Green plants convert solar radiation into chemical compounds that after time become fossil fuels. (open arrows) Plants have supplied mankind with a renewable source for food, energy and materials. (green arrows) Evolution and growing needs turned people towards non-renewable fossil fuels for its needs (red arrows). Direct use of sunlight for energy and materials is the key towards more sustainable processes. (blue arrows) Taken from [2]

are green plants, which is the main renewable source used by the human race to account for its food, energy and materials needs. With the industrial revolutions, man turned towards non-renewable fossil fuels to cope with the ever increasing energy demand. The high energy density of this feedstock has advanced technology and general welfare enormously, though the negative side effects are becoming too pressing to neglect. Finally, the blue arrows point to the direct use of sunlight, not only for energy supply, but also to create materials and chemicals, in many ways similar to photosynthesis in plants. Although much progress has been made in the fields of photochemistry and photophysics that resulted in many interesting technologies and materials, efficiencies are still rather low, impeding their routine use for now. However, to see the advancements in the field of modern materials sciences comforts us that we are heading in the good direction.

1.2 Materials design

At the core of finding new solutions for the aforementioned problems is the design of new materials. From communication technology to construction works, high-end materials are ever more needed to follow the growing complexity of our creations. This becomes clear from the listing by the European Commission of advanced materials development as one of the Key Enabling

Technologies (KETs), underpinning the importance of innovation across a range of sectors to tackle several 21st century problems, to drive economic growth and create jobs.

It has generally been acknowledged that computational modelling plays a vital role in designing new materials and to obtain fundamental understanding of already developed materials. Thanks to the ever increasing computer resources and evolving theoretical models, the field of computational modelling has become an important player in chemistry. Whereas before theoretical models were mainly used to understand the outcome of an experiment, current computational research is evolving towards a tool that helps experimentalist in choosing and developing the right experiments and even in predicting the outcome. With the aid of high throughput methods, scientist can screen uncountable amounts of materials, which would take an infeasible amount of time for experimentalists to synthesise and characterize every material. Moreover, the deep fundamental understanding that can be gained from theoretical calculations can help for the design of similar materials, or grasp where improvements can be made.

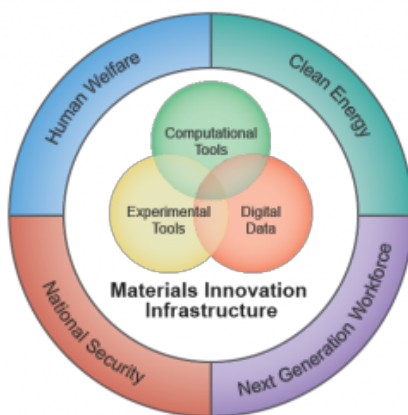


Figure 1.2: Schematic representation of input needed for materials design. Taken from mgi.gov

Figure 1.2 is a general scheme showing the synergy between the scientific methodologies and problems we are addressing. It is a central figure published by scientists of the Materials Genome Project (MGI). This project, funded by the US government aims at closing the gap between computational and experimental materials research towards computationally guided design. To achieve this, a combination of experimental measurements, com-

putational models and statistical analysis of big data are used in close collaboration to move toward a computationally guided design.

Essential is the close collaboration between experimentalists and computational scientists. This thesis was performed as a synergistic research project between an experimental group specialised in porous materials (COMOC - Center for Ordered Materials, Organometalics and Catalysis) and a computational group with many years of experience in modelling porous materials and spectroscopic properties (CMM - Center for Molecular Modeling).

1.3 Goal and outline

Metal-organic frameworks (MOFs) represent a highly interesting class of materials applied in a plethora of fields, ranging from gas storage and separation to catalysis. More recently, researchers started to unravel their interesting electronic properties and exploit these for amongst others photocatalysis. This thesis will use a **combined experimental and theoretical approach** to extend our knowledge of the materials at the nanoscale, in order to **tune their electronic structure**. The need for a complete understanding of this phenomenon is high, since only when the electronic structure of the frameworks at hand is well-understood, necessary changes can be made for the improvement of the materials in a diverse set of applications exploiting their particular electronic features. We believe this synergistic approach will advance our general knowledge on MOFs for photocatalytic and electronic applications and help within the future design of novel materials for light-based applications.

The main objectives of this thesis are:

- Study systematically the stability of UiO materials to understand how these materials relate to other often used MOFs
- Understand the electronic structure of pristine UiO-66
- Understand the influence of functionalized linkers to the light-absorption properties
- Study the influence of dynamic effects to the light-absorption properties
- Improve the photocatalytic activity via controlled doping of the metal nodes and understand the influence on the electronic structure

- Investigate the viability of defect engineering as a new pathway in electronic structure engineering for MOFs

This thesis is divided in three parts. **Part I** contains a set of introductory chapters discussing the state-of-the-art experimental and computational methodology used, as well as a general introduction to the materials studied in this work. Herein we learn that to create an efficient photocatalyst, the material should exhibit a strong absorption in a wide wavelength range (preferably including the visible part of the spectrum) and should allow separation of the photo-generated exciton in order to create redox-active charge carriers. **Part II** of this thesis then sheds light on the first item mentioned above: the light-responsiveness. Since the light-absorption of the MOF materials in this study is linker-based, an extended study of the linkers and MOFs via absorption spectroscopy and advanced molecular modelling approaches allows to understand all the processes on a fundamental level. Since the MOFs are constructed modularly, a bottom-up approach is followed and hence the different building blocks are studied separately before reconstructing the full periodic structure. **Part III** on the other hand will take a closer look to the second requirement, the efficient charge carrier separation. Since electron-hole recombination is the main quenching mechanism impeding the photocatalytic activity, the electron (or hole) should be able to migrate from the linker toward the inorganic node. From here, the life time should be sufficient to initiate a redoxreaction of an adsorbed reactant. The third part offers several pathways to tune this migration, first by metal doping, then by addition of defects in the structure.

The three parts are subdivided in several chapters. More in detail, the chapters are ordered in the following way:

- Chapter 2 starts with an introduction to MOF materials and a short history note. A detailed review on their construction as well as a broad and non-exhaustive overview of the applications is provided. Next, we present a systematic stability study of some of the most common MOF materials available in literature. Knowledge of the stability of the materials in different chemical environments is of indisputable importance to compare materials and find the right material for a given application. The chapter concludes with a more detailed introduction of UiO-66, the material studied intensively in this work.
- Chapter 3 will introduce the basic concepts and needs in modern photocatalysis and give insight in the current problems and drawbacks of

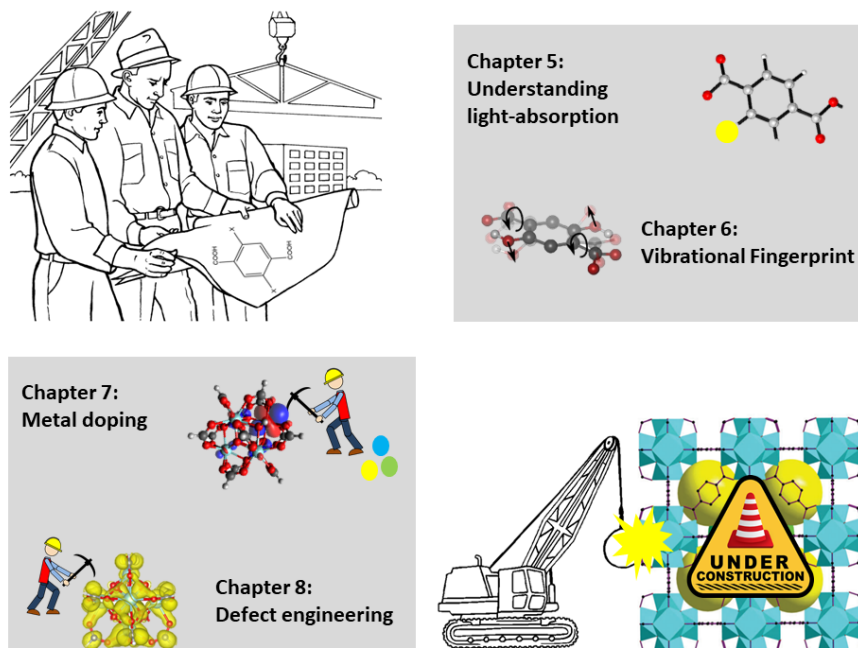


Figure 1.3: Overview of the general set-up of this thesis. Chapter 5 and 6 concern themselves with the understanding of light-absorption on a fundamental level. Chapter 7 and 8 discuss two pathways to improve photocatalytic properties of UiO-66, via metal doping and via defect engineering

state-of-the art materials. Again, a more specific framing of photocatalysis in the field of MOF and specifically UiO research is provided.

- Chapter 4 starts with a short overview of the main characterization techniques used, before providing a more detailed discussion on spectroscopy. The photocatalysis set-ups are discussed in detail hereafter. The second section focusses on the computational background needed for this thesis and specifically DFT and its Time-dependent variant are introduced. Also a short introduction to the dynamic methodology using advanced Molecular Dynamics techniques is provided.
- Chapter 5 will study the absorption of light in UiO-66 and how this is influenced by linker functionalization. A series of UiO-66-X materials is constructed and their UV/Vis absorption spectra are provided. Next, via a bottom-up approach, the contributions of the different constituents are discussed, starting from the isolated linkers, simple clus-

ter models and ending with the full period material. All the different levels yield complementary information and are all needed to gain a complete understanding of the material.

- In chapter 6 we will try to understand some of the features found in the previous chapter. A detailed study of the influence of vibrational modes on the electronic spectra is provided by means of advanced molecular dynamics simulations coupled to TDDFT.
- The goal of chapter 7 is to provide a detailed discussion on the influence of metal doping on the electronic structure of UiO-66. First, a microwave-based methodology for fast incorporation of metal impurities is introduced and evaluated for isovalent ions as well as lanthanides. Then, a detailed discussion on isovalently doped UiO-66 is provided, corroborating by means of spectroscopy and computational calculations the literature available on Ti doped UiO and its improved photocatalytic activity. The materials are then tested in gas phase photocatalysis. Finally, a series of lanthanide doped materials is studied. Via photoluminescence measurements and absorption spectroscopy the charge-state transition levels could be aligned with the UiO-66 band structure and show which lanthanides could offer interesting electronic changes.
- A second pathway is provided in chapter 8, where we discuss in detail how missing linker defects influence the electronic properties of the UiO-66 material. Again a multi-levelled study was performed to understand the electronic effects occurring upon defect inclusion.
- Finally, Chapter 9 summarizes the main findings and conclusions of this work. Furthermore, an outlook is provided for future directions in this field.

2

Metal-Organic Frameworks

2.1 Towards coordination polymers

Before introducing Metal-Organic Frameworks (MOFs), the materials studied in this work, a small hint will be given on the scientific advancements that led to their origin. The concepts of coordination chemistry will be introduced followed by a short introduction to porous materials. Both key concepts in 20th century inorganic materials chemistry are necessary to understand the formation and specific chemistry of (porous) coordination polymers (PCPs). Via the general philosophy of reticular chemistry we then can take a look to MOF chemistry, which are a subclass of the PCPs.

2.1.1 Coordination chemistry

The Nobel prize in chemistry from 1913 was awarded to Alfred Werner ‘*in recognition of his work on the linkage of atoms in molecules by which he has thrown new light on earlier investigations and opened up new fields of research especially in inorganic chemistry*’. With his investigation, Werner paved the way for modern coordination chemistry. Before his research, the origin of bonds between metal ions and neutral ligands were not fully understood. Werner postulated the existence of a *primary* and *secondary valency*, which are nowadays known as *oxidation state* and *coordination number*. [3]

According to the IUPAC, ‘*each coordination compound either is, or contains, a coordination entity (or complex) that consists of a central atom to which other*

groups are bonded. A coordination compound is any compound that contains a coordination entity. A coordination entity is an ion or neutral molecule that is composed of a central atom, usually that of a metal, to which is attached a surrounding array of other atoms or groups of atoms, each of which is called a ligand.' [4] The bonding interactions originate from interaction of the empty orbitals of the central metal cation (Lewis acid) with lone pair orbitals of the ligand. (Lewis base). The geometry and electronic characteristics of the complexes are determined by the orbital interactions.

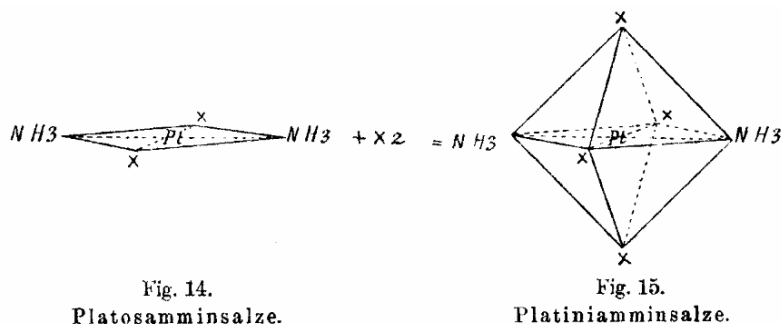


Figure 2.1: Figures from Werners original publication in 1893, describing the geometries of two Pt complexes [3]

Nowadays, coordination compounds are omnipresent in chemistry and are used in e.g. homogeneous catalysis and supramolecular chemistry. Although traditionally it was regarded as a field within inorganic chemistry, the use of ever more complex organic ligands built a bridge towards organic chemistry. The result of this synergy is perfectly demonstrated by the development of the field of Porous Coordination Polymers (PCP) or Metal-Organic Frameworks (MOFs), which will be introduced in the next sections.

2.1.2 Porous materials

Before introducing the actual materials that are the subject of this work, a last concept has to be introduced: porosity. Once more, according to the IUPAC [5], porosity *is a concept related to texture and refers to the pore space in a material*. They divide porous materials in three subgroups, depending of the size of the voids present in the material: microporous materials (pores <2 nm), mesoporous materials (pores of 2-50 nm) and macroporous materials (>50 nanometer). It was with the discovery of natural zeolites by the Swedish mineralogist Axel Frederik Cronstedt in the 18th century [6] and their first lab synthesis in 1862 [7] that researchers in all fields of science started to un-

ravel the complex structures and see the possibilities of these materials for several applications. Zeolites are a class of 3D interconnected aluminosilicates, and up-to-date still the most studied and applied nanoporous material. They form a crystalline framework, built out of tetrahedral $M-O_4$ building blocks ($M=Al, Si$). The tetrahedra are sharing one oxygen atom, resulting in different pore or channel topologies. Around 200 known zeolites are known up to date. [8] Zeolites are vital for the petrochemical industry. Thanks to their open metal sites that can act as Lewis acids, they are able to crack large hydrocarbons in crude oil feeds into a whole series of useful products. [9] Less far from our daily life, they are also found in detergents, where their exceptional ion-exchange capabilities are exploited.

Their exceptional stability and easy production are the reason that Zeolites are still the main workhorses in the petrochemical industry. However, as a limited set of building blocks, or Secondary Building Units (SBUs) are available, the set of materials is rather limited and their use in fine chemistry and high-end applications is limited. With the development of PCPs, a whole new range of materials became available, meeting these requirements.

2.1.3 The dream of materials scientists

Engineering materials like Lego®, is one of the dreams of most materials scientists and has been a long-standing challenge in the design of novel crystalline solid-state materials. Via the clicking together of simple, cheap and carefully engineered bricks, one can build up complex and well-defined structures. Unfortunately, to achieve this in real life is a very big challenge.

Most of the synthetic methods in materials chemistry are referred to as ‘shake and bake’ methods, since traditionally mixing reagents and heating them to high temperatures easily yields new solid-state materials. However, since these starting materials undergo structural changes at these temperatures, a poor relation between reactant and product is found and hence poor reproducibility and control is the result.

The concept of *Reticular Design* has become reachable with the discovery of porous coordination polymers. [12, 13] The basic idea of reticular design is that by choosing appropriate SBUs, crystals with specific, highly predictable properties can be formed. The SBUs retain their original rigid structure and hence a much better control of the final product can be achieved.

However, the complexity of all factors governing the construction process still makes the design of these materials far from trivial. The idea is very

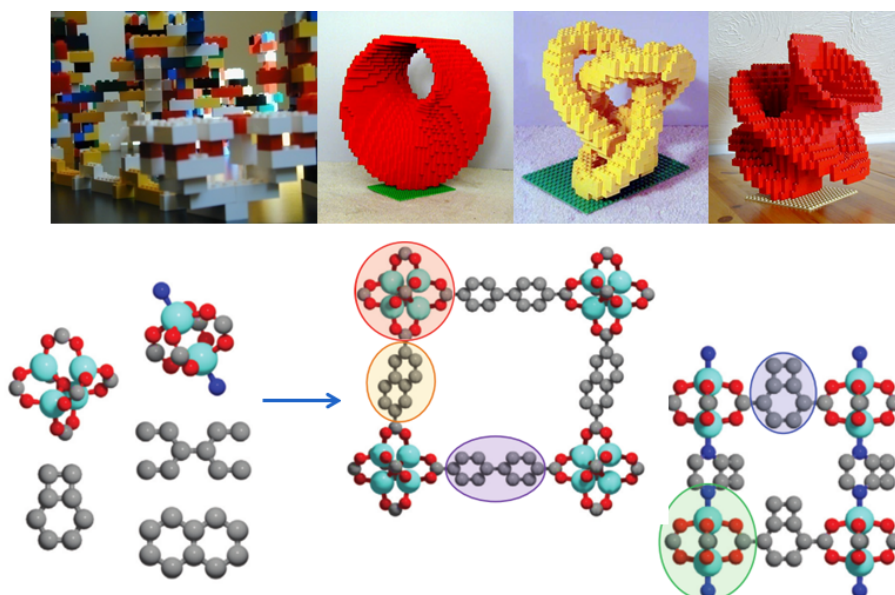


Figure 2.2: The dream of materials scientists made possible by MOF chemistry: clicking building blocks together as Lego®. Based on [10] and Lego ®artwork by [11]



Figure 2.3: Growth of coordination polymers taken from [14]

nicely represented in figure 2.3, representing Metamorphosis II by Escher. Simple, well-defined tectons (or SBUs) interact coordinatively to form new topologies that can lead to architectures of an unexpected complexity. Full understanding of their coordination chemistry and crystal growth is crucial for the further development of MOFs. And even then, understanding how they form their highly complex final architecture, let aside predict, remains a big challenge in materials design.

2.1.4 Birth of MOFs

It is difficult to identify a definitive ‘first’ MOF paper, since several early papers already dwell with concepts of hybrid solid materials whilst still being far away from the MOFs as we know them nowadays. [15–18] Hoskins and Robson proposed in 1989 a new class of materials formed by linking together metal centres with a tetrahedral or an octahedral array of rod-like connecting structures, showing that MOFs can be engineered by carefully choosing the molecular building blocks. [19] Nonetheless, we had to wait until 1999 before Yaghi showed the full possibilities of this class of materials by introducing the MOF-5 with its exceptionally high stability and internal surface area. [20] It was also in this paper that Yaghi introduced the term MOF. In the early 2000s, MOF chemistry (in particular based on carboxylate linkers) was further developed predominantly by the groups of Yaghi, Férey and Kitagawa. According to IUPAC, a MOF is defined as a *Coordination Polymer (or alternatively Coordination Network) with an open framework containing potential voids* [21]. MOFs are in a way nothing more than coordination compounds, as already defined by Werner in 1893 (see section 2.1.1), with an ‘infinite’ number of central atoms.

Figure 2.4 shows how a MOF is constructed. The two main SBUs are a metal or metal-oxide cluster, defined hereafter as the (inorganic) node on the one hand, and on the other hand organic polytopic ligands, hereafter referred to as linkers. Several examples of often used SBUs are shown in figure 2.4. In order to show the coordination number of the inorganic nodes more clearly, the organic carboxylic groups are included in the representation. The carboxyl group is the most often encountered as connection part between the organic part and the inorganic part, however, other functional groups are also possible, notably phosphonate, pyridyl and imidazolate groups. Furthermore, the topology of the ligands can be varied too, and one can find regularly bi- to tetrapolytopic ligands in MOF literature.

One can see that the hybrid modular nature of MOFs gives, in theory, unlimited possibilities to create new materials. The great advances of computational algorithms nowadays make it possible to identify promising MOF structures in a high-throughput way and understanding their structure-property relationships. [10,23] Computationally guided design represents a very powerful tool in materials chemistry by narrowing down the set of MOFs to be synthesized in the lab to a reachable subset.

Although in comparison to e.g. Zeolites, MOFs still lack the high stability that is necessary to compete with these materials in industrial and everyday

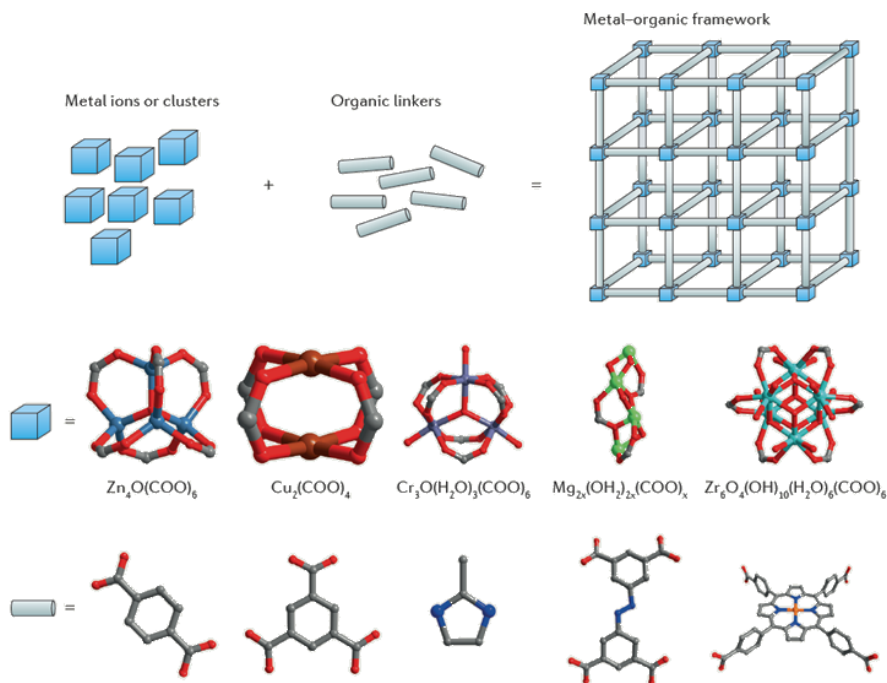


Figure 2.4: Schematic representation of MOF formation. Metal clusters, represented by cubes, are linked together via organic linkers, rod-like shapes, and form a 3D crystalline network. Several prototypical examples of metal clusters and linkers are provided, all leading to different topologies. Based on [22]

applications, it is the combination of their high tuneability, structural uniformity and high porosity (typical zeolite pore sizes range from 3.5–8 Å whilst pores in MOFs can be as large as 10 nm [24]) that makes MOFs stand out within the group of other functional porous materials. This versatility has resulted in a plethora of MOF structures and different fields of applications, which will be briefly introduced further in this thesis. The interested reader can also find a number of excellent reviews, notably the seminal 2004 review of Kitagawa [25], by Férey [26] and several thematic issues in *Chemical Reviews*. [27, 28]

2.1.5 Natural MOFs

Although the hydrothermal synthesis of MOFs would make one think that these metal-organic nano-architectures should be found in nature, it was only recently that Huskić et al. [29] discovered the first naturally occurring

MOF-like structures. They found that in two rare organic minerals, stepanovite and zhemchuzhnikovite, structures similar to synthetically obtained metal-oxalate MOFs can be found, exhibiting almost nanometer-wide (0.9nm for zhemchuzhnikovite) pore apertures and channels respectively.

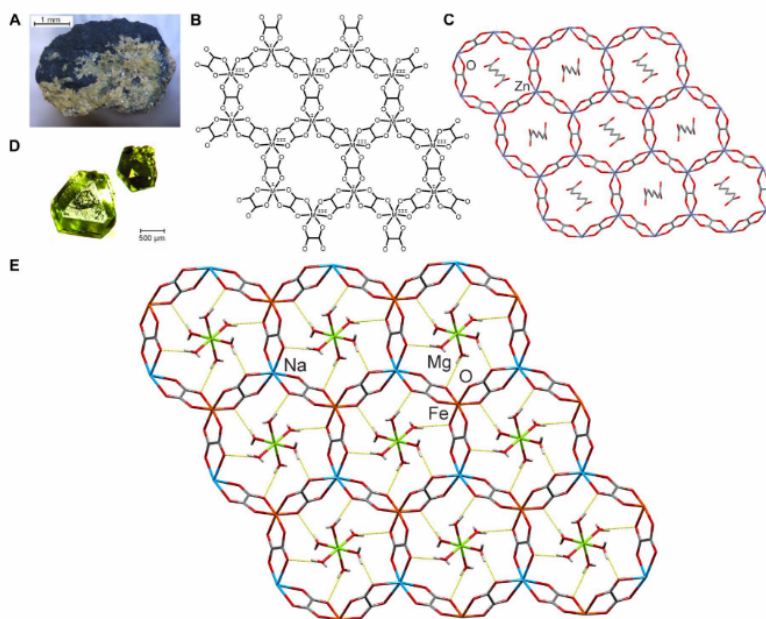


Figure 2.5: Stepanovite is a mineral with a MOF structure. (A) Stepanovite sample, Chai-Tumus coal deposit (Sakha-Yakutia, Siberia, Russia; sample from E. I. Nefedov's collection). (B) Schematic of an open anionic **hcb** framework composed of M^I and M^{III} nodes bridged by oxalates. (C) A single layer of an analogous zinc-based proton-conducting MOF material, including guests [30]. (D) Crystals of synthetic stepanovite. (E) A single metal-organic layer in stepanovite, viewed along the crystallographic c axis, displaying the anionic **hcb** $[\text{NaFe}(\text{ox})_3]^{2-}$ framework, with apertures occupied by $\text{Mg}(\text{H}_2\text{O})_6^{2+}$. Hydrogen bonds between $\text{Mg}(\text{H}_2\text{O})_6^{2+}$ guests and $[\text{NaFe}(\text{ox})_3]^{2-}$ framework are highlighted as yellow dotted lines.

Zhemchuzhnikovite and stepanovite are thus far the only known organic minerals exhibiting open structures. This discovery shows that the coordination-driven self-assembly processes, well-known in MOF synthesis on the lab-scale, can also play a role in natural geological processes. Although neither

of the two materials exhibit permanent porosity due to the presence of hydrated magnesium guests in the pores, they exhibit similarities to previously reported synthetic MOFs. [30] Not only structural similarities are found, also the reversible loss and absorption of water molecules was observed, demonstrating the stability of individual **hcb** (honeycomb topology) layers upon desolvation. Moreover, the extended hydrogen-bonded architectures suggest the potential of these materials for proton conduction [31]. These natural porous metal-organic architectures challenge our view of MOFs as strictly ‘lab-made’ materials. Moreover, since some organic minerals involve multi-dentate organic molecules already used in MOF synthesis, such as mellitic acid or different purines [32–34], we can expect to find other MOF minerals in the future.

2.1.6 What’s next?

A careful reader may have spotted a missing link in the previous parts. We discussed the formation of zeolites from purely inorganic SBUs and the chemistry of MOFs being a hybrid between purely inorganic building bricks and organic linkers. So, is it possible to construct 3D topologies from purely organic parts? The answer is yes, and this is subject of the growing field of Covalent Organic Frameworks (COFs). These materials show a remarkable stability, high tuneability and interesting electronic properties and this development is in full expansion. The interested reader is referred to several excellent reviews available in literature. [35–39]

Thanks to COFs, we can now complete a scheme showing the diverse set of chemical architectures that can be formed by assembling inorganic and organic SBUs from 0D to 3D. This collection is shown in figure 2.6 Herein, we have ‘simple’ organic molecules as 0D purely organic materials. The set of 0D materials is completed by the classic coordination clusters and inorganic nanoparticles. These materials are already around in chemistry research for many centuries. One level up, we can find polymers as the most famous subset, together with 1D coordination polymers and nanowires. If we then go to the 2D and 3D materials, we arrive at the layered and framework materials. For clarity, many related systems, such as active carbons, (periodic) mesoporous (organo)silicas [40,41], mesoporous carbons [42] and supramolecular coordination compounds [43] are not included herein. One should also be careful with the labelling of the dimensions which can often be ambiguous. For example, within MOF science, frameworks can also be labelled 0D to 3D depending on the connectivity of the metal nodes. This is reviewed in [26].

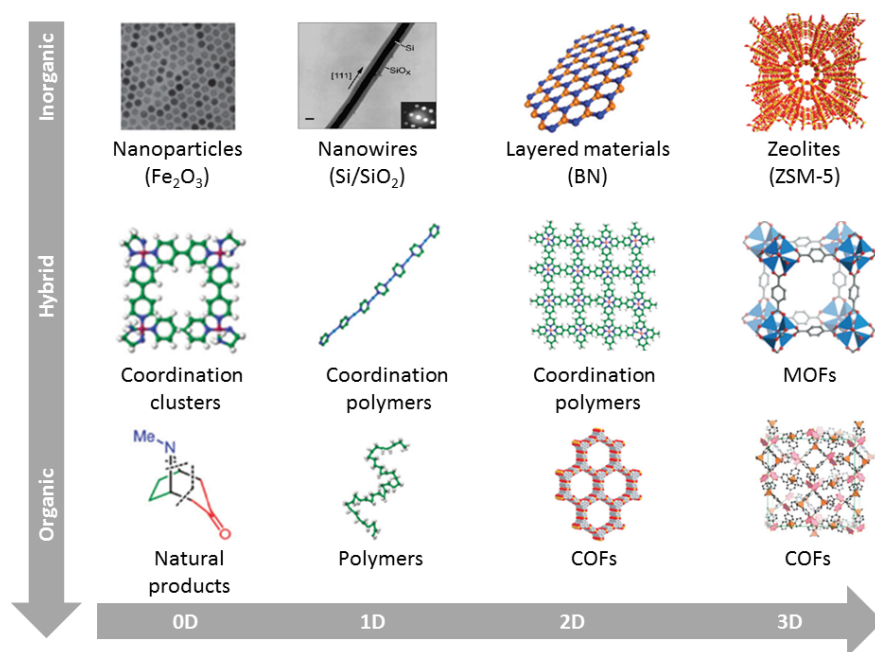


Figure 2.6: Selected examples for diverse assembly of building units to construct inorganic/hybrid/organic chemical architectures, ranging from the discrete 0D/non-porous/amorphous structures to the extended 3D/porous/crystalline structures. Based on the review by Ding et al. and references cited herein. [35]

2.2 Applications

As already mentioned, the reason why MOFs represent such an interesting class of materials is their high tuneability, allowing to make materials designed for a specific application with perfectly tuned characteristics. [44,45] It is by no means the goal to provide a complete overview in this thesis. The interested reader is referred to e.g. the 2012, 2014 and 2017 thematic issues about MOFs in Chemical Reviews [27,28,45] where recent developments are extensively treated.

Taken from the classic review of Kitagawa [25], figure 2.7 shows in a general way the fields of applications of MOFs. Herein it can be seen that this can range across very different fields of research. The enormous internal surface area (surpassing $14000 \text{ m}^2/\text{g}$ [46], in comparison to zeolites typically ranging from $200\text{-}600 \text{ m}^2/\text{g}$) is an ideal starting point for gas sorption and

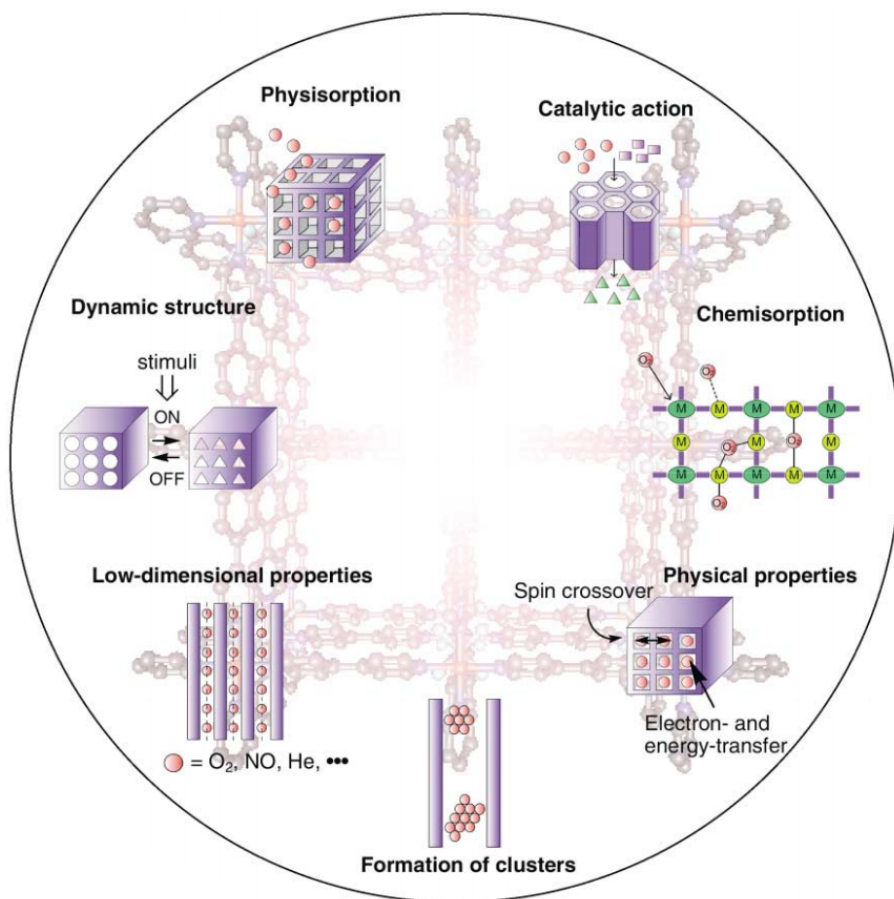


Figure 2.7: Overview of MOF applications, taken from [25]

separation, CO₂ sequestration, hydrogen storage etc. On the other hand, the broad chemical versatility offers an interesting playground for e.g. tailored (photo)catalysis whilst MOFs with dynamical structures (e.g. breathing frameworks) then again offer compelling possibilities as responsive materials or drug delivery systems. Figure 2.8 summarizes the mean differences of MOFs compared to other porous materials.

In what follows, a short general overview of the main fields of application of MOFs will be provided.

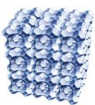
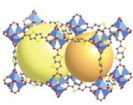

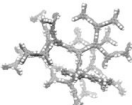
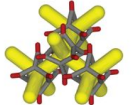
	Zeolites	Metal-organic frameworks ⁱ	Covalent-organic frameworks	Porous organic polymers	Porous molecular solids
					
Porosity	Microporous or mesoporous ⁱⁱ ; narrow pore size distributions	Can be ultraporous ⁱⁱⁱ /mesoporous; narrow pore size distributions	Can be ultraporous/mesoporous; narrow pore size distributions	Can be ultraporous/mostly microporous; broader pore sizes	Can be ultraporous/mesoporous, but this is rare so far
Crystallinity	Typically high; can also be amorphous	Typically high	Modest to high	Amorphous	High, but amorphous examples, too
Stability	Thermal stability generally excellent; can be acid/base sensitive	Poor to good; growing number of water-stable MOFs	Boronates ^{iv} generally poor; imines ^v generally good	Good to excellent, especially hydrothermal	Generally poor, though isolated examples of hydrothermal stability
Modularity/diversity	High; new structures can be based on known zeotypes ^{vi}	Very high even for single-linker MOFs; also multivariate MOFs ^{vi}	In principle high; less developed than MOFs	Very high; multiple linkers and linker functions possible ^{viii}	Cocrystals possible ^{ix} ; not widely exemplified yet
Processing	Insoluble, but technologies for films, composites and pellets are well developed	Insoluble, though many recent examples of composite and films	Insoluble, but examples of surface growth	Modest processability, with exception of soluble PIMs ^x	Soluble, as for PIMs could be advantage or disadvantage, depending on function
Designability	Excellent, though design of organic templates can still be challenging ^{xi}	Excellent; isorecticular principles of node/strut metal-organic bonding are well developed ^{xii}	In principle good, as for MOFs; isorecticular approach possible	Composition control good; 3-D structure control more challenging	Isolated cage can encode functions, ^{xiii} but no general isorecticular strategy
Unique selling points	Stability; low cost, commercially proven technology	Structural and chemical control for diverse range of materials	Electronic properties	Extended conjugation for CMPs ^{xiv} ; solution-processing for PIMs	Solution processing; physical properties intrinsic to cages
Summary	Developed but still actively growing area; zeolites have major commercial importance	Established and highly active field; as yet, no large-scale applications	Much less developed than MOFs, but early promise for organic electronics	Rapidly growing in number; diverse chemistry; commercial application for PIMs ^{xv}	New area with fewer examples, but early promise for specific molecular separations

Figure 2.8: Overview of MOF properties compared to other porous materials. taken from [47]

2.2.1 From gas sorption to catalysis

MOFs were originally exploited for their use in gas sorption applications. [48] The internal surface of the materials can mount up to more than 10000 m^2/g [46]. The use of MOFs as molecular sponges is hence a straightforward choice. For example the storage of energy-relevant gases, such as hydrogen [49–51] or methane. [52]. The safe storage of these gasses is important for their use as e.g. fuels. Furthermore, sequestration of CO_2 has proven to be one of the crucial needs with rising environmental concerns. [53] Also the absorption and degradation of toxic gasses [54,55] and general air purification systems have been evaluated. [56] Differences in the size and shape of gas molecules or in interactions with the framework can also result in an efficient separation of gas mixtures. The high tuneability of MOFs allows to design materials that can perform difficult but economically important separations, e.g. O_2/N_2 , light hydrocarbons, isomers, CO_2/CH_4 and many more. [57,58]

The porous structure of MOFs also allows to absorb biomolecules. By carefully tuning the interaction strength of the molecules and the framework, a

targeted and slow release can be achieved. In spite of the fact that still a lot of research is needed before these systems can be implemented in real life, several promising materials have been developed. [59,60] Not only therapeutic molecules can be encapsulated, also bioactive linkers can be used to construct the framework. Here, slow degradation of the MOF framework releases the molecules e.g. at specifically targeted cancer cells. [32,61]

MOFs offer exciting possibilities in the field of heterogeneous catalysis thanks to their high degree of crystallinity and porosity. [27, 62, 63] The pore/cage structure of the MOFs allows to transport reagents to and from active sites and moreover control their diffusion or even their transition state geometry. It is hence important that MOFs can retain their open structure during catalysis, showing again the importance of stability issues that need to be addressed when using MOFs. The overall problems with chemical, thermal and mechanical stability of the materials has resulted in a slow rising of catalysis related papers compared to other fields. However, with the continuously increasing number of stable MOFs, the development of MOF-based catalysts has boomed the last 20 years.

Figure 2.9 shows an overview of the general strategies that can be adopted to use MOFs in catalysis. The MOF as such contains transition metals, each with their distinctive catalytic activity. The metal atoms need to be reachable for reactants at a coordinatively unsaturated site or defect site to be active. [18] Also the ligands can contain functional sites that are inherent to the linker, or are post-synthetically added (PSM). Not only organic functional groups can be added, also e.g. metal complexes can be supported on specific organic bridges, or on the inorganic node. [64] A final strategy can be the inclusion of active guest species that are heterogenized in the MOF cage [65] or inclusion of nanoparticles. [66,67]

Although gas sorption and catalysis are the two most extensively researched applications for MOFs, several groups also exploit other properties in advanced applications.

An interesting subfield in MOF research are stimuli responsive materials. [68,69] This set of materials can undergo structural changes in response to a certain physical (pressure, temperature, photo-excitation...) or chemical (pH, solvent,...) changes. This can be exploited thanks to the flexible topology inherent to certain materials, but also by e.g. introducing molecular photo-switches as ligands. This offers attracting pathways to design sensors and dynamic materials.

The inherent structural characteristics of MOFs has made researchers realise

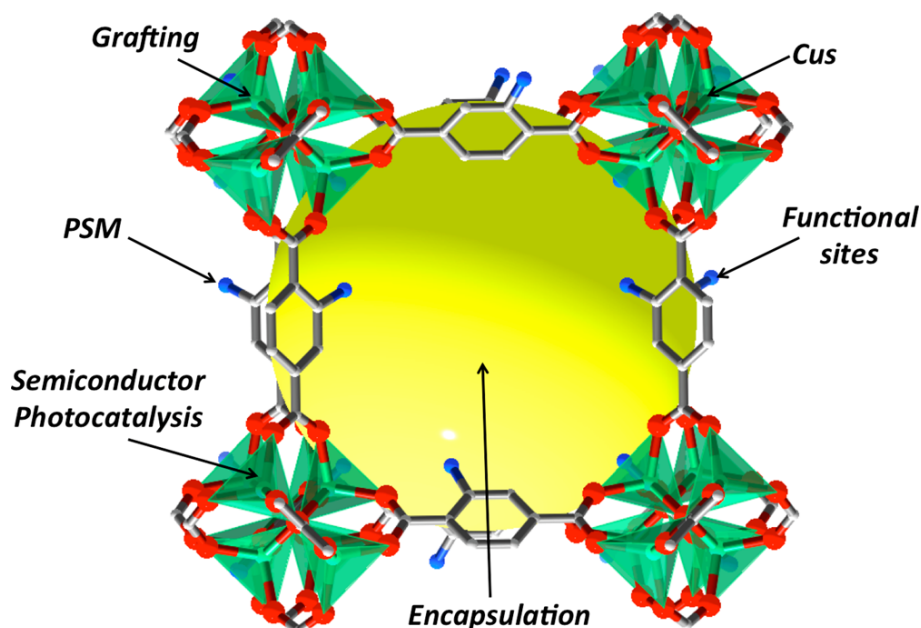


Figure 2.9: Overview of different strategies to incorporate catalytic active sites in MOFs. Taken from [63]

their great possibilities in light-based applications. Since MOFs combine different constituents known in luminescence and photocatalysis research in one crystalline material, several research groups devoted themselves to the fundamental study of the electronic properties of these materials. Inclusion of lanthanides or chromophoric guests in the pores allows for a diverse set of applications in the fields of luminescence [70, 71] and photocatalysis. Since the latter one is one of the main topics of this work, we will introduce photocatalysis and the use of MOFs herein in a separate chapter.

Introduction of paramagnetic metals into the framework can introduce magnetic properties. MOFs offer the possibility to study magnetic moment exchange interactions between nearest-neighbours in a diverse set of topologies, and allow for a careful tuning of these properties. Many researchers have performed research on magnetism in MOFs combined to a second property (e.g. electrical conductivity). Recent studies show the great opportunities to be explored in the fields of molecular spintronics. Also responsive dynamic frameworks are still only an emerging but promising field within MOF research. [72, 73]

Combination of stimuli-responsive, luminescent and magnetic properties has

led to a large number of studies in the field of MOF-based sensing devices. [71,74] MOFs have shown great potential in several crucial domains of sensing applications, being explosives, highly toxic species, biomolecules etc. This has led to their prototype implementation in several real-life application as will be introduced further on.

A less straightforward but nonetheless promising application is the use of MOFs in explosive research. Not only can MOFs stabilize highly explosive molecules in order to increase the safety upon using them, they also can be constructed from labile nitrogen-containing linkers and be used as explosive as such. [75,76]

In the field of electrochemistry, and more specifically the design of new batteries, MOFs have emerged as a new electrode material given their tunability making it possible to design reversible Li absorbing or sieving materials. [77, 78] Also as proton conducting materials in electrolytic fuel cells, several researchers demonstrated that MOFs can outperform many of the existing materials. [79]

2.2.2 Industrial prospectives

Researchers already predicted the enormous potential of MOFs for several applications in the early 2000s. It was Yaghi's 2003 paper on hydrogen storage in MOF-5, where researchers started to realise the possibilities of the new set of materials. [49] Shortly after, BASF started to produce three MOF structures under the tradename Basolite[®], which made available MIL-53, HKUST-1 en MOF-5 on a large scale. Notwithstanding their 'easy' synthesis procedures on lab scale, the upscaling of the synthesis procedure is not straightforward and is one of the main limiting steps to be overcome.

Recently, several companies originating from academia started to produce tailor-made products (MOFapps [80], MOFtechnologies [81],...) Their goal is to guide and inform industries where MOF-based technologies can bring an improvement to their current processes. The company NuMAT [82] was the first company to bring a fully commercially available apparatus on the market in 2016, based on MOFs, for diverse gas separation applications (IonX[®]).

Basolite A520 is now used as a sorbent to store and deliver natural gas in automotive industries. Several prototype cars already drove fuelled via natural gas or hydrogen gas stored in tanks filled with the Basolite material. It was with the EcoFuel Asia Tour that took place in 2007 where for the first

time a Volkswagen Caddy EcoFuel using natural gas was driven from Berlin to Bangkok, emitting much less CO₂ than a comparable gasoline based car. Although no heavy drop in capacity was found in the MOFs after the harsh conditions, it was found that the mechanical stress led to the formation of a significant amount of fine particles in the tank.

A complete overview of all the industry related applications and perspectives is outside the scope of this work, but the interested reader is referred to some recent reviews in the field. [83–85]

One of the major problems still hampering the use of MOFs in industrial applications is the limited chemical, thermal and mechanical stability of most known MOFs at short and long terms. Even though great advancements have been made, not many materials are known that are stable in a wide range of chemical environments. Although knowledge about this is of fundamental importance and most authors perform some stability tests when constructing a new material, no systematic study of the common MOF materials was performed up to date, impeding the comparison of different frameworks for a certain application. In the next section we show the results of our systematic study of several of the known ‘stable’ MOFs via a series of standardized tests, allowing to compare materials from different research groups on the same scale.

2.3 A systematic stability study

2.3.1 Introduction

Studying the stability of a (new) material is of key importance within materials research. If a new compound, e.g. a catalyst, cannot withstand the conditions in which it will be used (e.g. solvent, temperature, mechanical pressure,...) further optimization is needed. Within the field of MOFs, stability issues have been a major drawback of this class of materials. Most MOFs have a low thermal stability (range 573–673 K) and are unstable in water. The latter is due to the hydrophilic properties of the metal nodes which results in a strong interaction with water molecules and therefore leads to the cleavage of coordination bonds, hence destroying the framework [86].

Since the pioneering study of Low et al. many other studies have been carried out on the water sensitivity of MOFs [87–89]. Very few MOFs showed no structural integrity loss in the presence of water. However, there are several types of MOFs that demonstrate promising results. For instance, the pyrazolate based frameworks show remarkable stability after exposure to boiling

water and other solvents, which is attributed to the high pK_a value of the imidazole ligands [90]. Besides the pyrazolate based frameworks, the hydrothermally synthesized MIL series constructed from octahedrally coordinated aluminium or chromium metal clusters (respectively MIL-53 and MIL-101) and zeolitic imidazolate frameworks (ZIFs) have been reported to be stable in water [91,92]. In particular the ZIF-8 material, in which the zinc atoms are coordinated to methylimidazolate ligands via Zn-N bonds, possesses a very high stability, not only under mechanical pressure but also in aqueous solutions [93,94]. The higher basicity of the imidazolate linker, in comparison to the carboxylate linkers, results in stronger metal-ligands bonds with the zinc and therefore in an enhanced stability towards water [90].

Interesting work on the water-stability of MIL-101(Cr) was performed in a study on dehumidification over hierarchically porous MOFs and the use as advanced water adsorbents, by Férey et al. [95]. Furthermore, MOFs constructed from Zr₆-based nodes also show a remarkably high stability (mechanical, hydrolytical, and chemical). The stability of these Zr-based MOFs, of which UiO-66 is a prototypical example, is due to the strong Coulombic interaction of the highly oxophilic Zr^{IV} metal sites with the negatively charged termini of the carboxylate linkers [96].

In order to make MOFs able to compete with current standard industrial set-ups, a critical and standardized evaluation of the long-term chemical, thermal, and hydrothermal stability is of paramount importance. Many of these industrial processes are performed in the presence of acids or bases (liquid phase reactions) or at elevated temperature (gas phase reactions) for an extended period of time. Furthermore, the stability of MOFs towards commonly used oxidants is also very crucial in e.g. oxidative processes. Although there have already been studies on the chemical, thermal, and hydrothermal stability of MOFs, to the best of our knowledge no systematic or long-term stability investigations have been carried out, making it hard to objectively compare different materials. [97] This is why we made a series of standardized tests to compare different popular MOF materials in the same circumstances.

The results and text of this section are based on:

A systematic study of the chemical and hydrothermal stability of some 'stable' Metal-Organic Frameworks

K. Leus, T. Bogaerts, J. De Decker, H. Depauw, K. Hendrickx, H. Vrielinck, V. Van Speybroeck and P. Van Der Voort *Micropor. Mesopor. Mater.*, **2016**, 226, 110-116

Contribution to this work: Synthesis, systematic stability tests and characterization of UiO type materials.

2.3.2 Materials and Methods

All chemicals were purchased from Sigma Aldrich or TCI Europe and used without further purification. Nitrogen adsorption experiments were carried out at -196°C using a Belsorp mini II gas analyzer. Prior to analysis, the samples were dried under vacuum at 120°C to remove adsorbed water. X-Ray powder diffraction (XRPD) patterns were collected on an ARL X'TRA X-ray diffractometer with Cu $K\alpha$ radiation of 0.15418 nm wavelength and a solid state detector. Thermogravimetric Analysis (TGA) was performed on an SDT 2960 from TA Instruments.

Synthesis MOF materials

UiO-66-X ($X=\text{H}, \text{NH}_2$) materials were synthesized according to a slightly modified procedure of Van Der Voort et al. [98] given in section 2.4 of this chapter. The synthetic procedure of **UiO-67** was based on the recipe of Farha et al. [99]. 0.27 mmol ZrCl_4 and 0.38 mmol 4,4'-diphenyldicarboxylic acid (BPDC) were dissolved in 15 mL DMF and 0.5 mL concentrated HCl. The resulting solution was sonicated for 20 minutes and subsequently transferred to a thermoblock at 80°C for 12 hours. After filtration and washing with DMF and ethanol, the samples were dried under dynamic vacuum at 90°C , and activated at 150°C (3 hours).

The other MOFs were synthesised according to literature recipes. **MIL-101(Cr)** was synthesized according to a slightly adapted recipe from Edler et al. [100]. **NH₂-MIL-101(Al)** was prepared in a few smaller batches as proposed by Fischer et al. [101]. For the synthesis of **Cu-BTC** a procedure based on Tranchemontagne et al. was followed. [102] **MIL-53 (Al)** was synthesized according to a slightly modified procedure of Férey et al. [103]. For the synthesis of **ZIF-8**, an aqueous procedure by Gross and co-workers was followed. [104] For more details on the synthesis procedure, we refer to the publication of this work, or the separate publications mentioned in this paragraph.

Chemical stability

The chemical stability tests were performed by exposing the MOFs for 3 or 60 days to acidic conditions (HCl, pH=0 and pH=4), basic conditions (NaOH, pH=12) or under oxidizing conditions (5 wt. % H_2O_2). Additionally, the stability of the MOFs was examined by exposing them to air and water for respectively 3 or 60 days. All the tests were carried out at room temperature (RT) without stirring. It was important to only assess the pH effect. Therefore, a simple acid (HCl) and base (NaOH) were selected for the tests, rather than, for instance, an oxidizing acid such as HNO_3 .

Hydrothermal stability

The hydrothermal stability study was conducted by exposing the MOF samples to saturated steam for 5 hours at 200°C . Herefore we used a setup as shown in figure 2.10. The MOF was placed in a porcelain crucible on top of a Teflon cylinder. Milli-Q[®] water was used for the experiment.

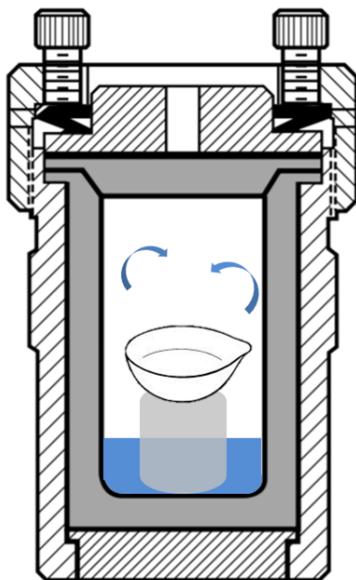


Figure 2.10: Schematic representation of the setup used for hydrothermal stability tests.

2.3.3 Results and Discussion

For clarity, only the results (XRD, BET) relevant for this work are given in this chapter. The reader interested in the data of the other samples is referred to the supporting information in chapter J of this manuscript.

Hydrothermal stability

In table 2.1, a general overview is presented of the stability of all the pristine MOF materials and after exposing them to water, air, acidic-, basic-, oxidative-, and a hydrothermal environment. The table is based on an evaluation of both the resulting Langmuir surface and the analysis of the XPRD measurements.

The UiO-66 and NH_2 -UiO-66 frameworks are stable after 5 hours at 200°C under autogenous pressure, while the UiO-67 material is completely destroyed as can be seen in fig. 2.11. The lack of stability of the UiO-67 material to H_2O exposure was recently assigned to the linker hydrolysis caused by clustering of H_2O molecules near the Zr_6 nodes and to rotational effects of the extended organic linker [105].

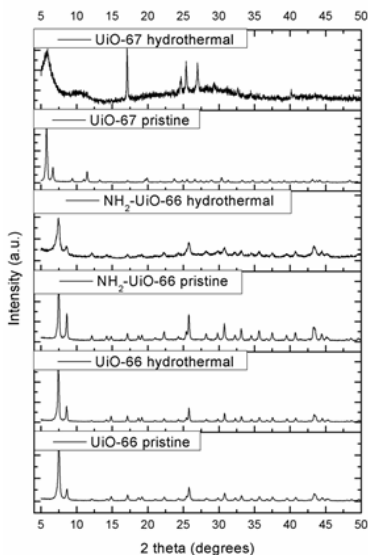


Figure 2.11: XPRD data for the pristine UiO-type structures or after hydrothermal treatment

As can be seen from the same table, MIL-101(Cr) preserved its crystalline structure after the steaming test. This observation is in agreement with

other reports in which the high moisture-stability of MIL-101 (Cr) was already stated [106–108]. In contrast to the high hydrothermal stability of the MIL-101 (Cr), it is known that the MIL-101 analogues of Fe^{3+} and Al^{3+} show a much lower resistance to hydrolysis. This last conclusion was also confirmed by our study, demonstrating that the NH_2 -MIL-101(Al) is highly sensitive to water, which leads to transformation into the thermodynamically more stable NH_2 -MIL-53(Al) material. The latter observation is in agreement with the recent report of Senker et al., demonstrating that the NH_2 -MIL-101(Al) already transforms into NH_2 -MIL-53(Al) after only 5 minutes exposure to water. [109] Besides the MIL-101(Cr), the NH_2 -MIL-53 is also stable under the examined steaming conditions as no changes are observed in the XRPD pattern in comparison to the pristine NH_2 -MIL-53. In contrast to the NH_2 -MIL-53, the MIL-53 (Al) exhibits a partial hydrolysis of the framework as studied by Bellat et al. and Jhung et al. [97, 110]

The copper paddle-wheeled framework, Cu-BTC, is known to be unstable under steaming conditions [111, 112] which was also confirmed by our study. On the other hand, the ZIF-8 framework can withstand the hydrothermal treatment, as no changes are observed in the crystal structure and only a minor decrease in the Langmuir surface area was noted. This observation is in agreement with previous studies showing that ZIF-8 is resistant to steam for hours and to boiling water for at least a week. [88, 94]

Chemical stability

Stability towards acids According to our study, both UiO-66 and NH_2 -UiO-66 exhibit a good stability in acidic conditions, even after exposure for 2 months in $\text{pH} = 0$ solutions. The short-term stability of both materials was already observed by the group of Lillerud, who reported that no loss in crystallinity was observed after 2 h in HCl ($\text{pH} = 1$) [113]. In the recent report of Zhong et al., it was shown that UiO-66 can be kept intact in solutions of $\text{pH} = 2$ to $\text{pH} = 6$ for at least 24 h, in the absence of fluorine [114]. However, although both materials show no loss in crystallinity, we observed that the Langmuir surface area decreased significantly for both MOFs after exposure for 3 days at $\text{pH} = 0$. The Langmuir surface areas of the pristine UiO-66 and NH_2 -UiO-66 are respectively $1008 \text{ m}^2/\text{g}$, and $885 \text{ m}^2/\text{g}$, whereas afterwards they dropped to $549 \text{ m}^2/\text{g}$ and $712 \text{ m}^2/\text{g}$, respectively. In contrast to UiO-66, UiO-67 shows a much lower stability towards acids. In a $\text{pH} = 4$ solution, the framework is still well preserved as can be seen from the XRPD pattern in figure 2.12. Also, no significant loss in the Langmuir surface area is observed. However, after immersing the material for 2 months in this solution, the framework shows a significant decrease in crystallinity

	3 days												2 months												Steam test		
	pH=0				pH=4				pH=12				H ₂ O ₂				H ₂ O				air						
	XRD		N ₂		XRD		N ₂		XRD		N ₂		XRD		N ₂		XRD		N ₂		XRD		N ₂				
MIL-101 (Cr)																											
NH ₂ -MIL-101 (Al)																											
MIL-53 (Al)																											
NH ₂ -MIL-53																											
UiO-66																											
NH ₂ -UiO-66																											
UiO-67																											
CuBTC																											
ZIF-8																											

Table 2.1: Concluding overview on the stability (N₂ and XRD) of the examined MOFs in the various media. The XRPD pattern and surface area can be largely preserved (green), completely destroyed (red) or partially destroyed, degraded or transformed (yellow with lines)

and in surface area. Moreover, the MOF is completely destroyed after 3 days at $\text{pH} = 0$, as only the diffraction peaks from the free organic linker, (4,4'-diphenyldicarboxylic acid), can be observed in the XRPD pattern.

In our study, we corroborated the extremely high stability under acidic conditions of MIL-101(Cr) as no changes were observed in the XRPD patterns even after exposing the material for 2 months in a $\text{pH} = 0$ solution. As a matter of fact, the Langmuir surface area even increased drastically after treating the MOF with acidic solutions (from $2001 \text{ m}^2/\text{g}$, to $3180 \text{ m}^2/\text{g}$ or higher), due to the removal of left-over starting reagents (e.g., terephthalic acid) which we further proved via TGA experiments.

In contrast to MIL-101(Cr), NH_2 -MIL-101(Al) shows a very low stability in acid medium. The NH_2 -MIL-101(Al) structure is completely converted into the thermodynamically more stable NH_2 -MIL-53 after 3 days in a $\text{pH} = 4$ solution, whereas in a $\text{pH} = 0$ solution, the MOF was completely dissolved after a few minutes. Next to NH_2 -MIL-101(Al), the ZIF-8 and Cu-BTC structures were also immediately dissolved after exposure to a solution of $\text{pH} = 0$. However, ZIF-8 still possesses a good crystallinity after 3 days in a $\text{pH} = 4$ solution, whereas Cu-BTC already starts to form a new crystalline phase, which was also observed after exposing it to water. After 2 months in $\text{pH} = 4$, the ZIF-8 shows a significant degradation. Although part of the MOF's diffraction peaks are still present in XRPD, new diffraction peaks can be observed as well, which were also noted after storage for 2 months in water and can be assigned to carbonates [115].

MIL-53(Al) material exhibits a rather good stability at $\text{pH} = 4$ for 3 days. No changes in the crystallinity are observed, which is corroborating the report of Huang et al. [107] However, although no changes are observed in the XRPD pattern, a significant decrease is noted in the Langmuir surface area in comparison to the pristine material which shows that the MIL-53(Al) gradually decomposes. As expected, after immersing the material for a period of 3 days in a solution of $\text{pH} = 0$, the structure is completely destroyed and only the diffraction peaks of the terephthalic acid linkers can be observed in the XRPD pattern. In comparison to MIL-53(Al), the functionalized NH_2 -MIL-53 exhibits an enhanced stability under acidic conditions, as even exposure for 2 months at $\text{pH} = 4$ shows no difference in the crystallinity of this MOF. However, in stronger acidic conditions ($\text{pH} = 0$), the material experiences a gradual decomposition. After suspending the material for 2 months at $\text{pH} = 0$ the structure of NH_2 -MIL-53 is almost completely destroyed and only the diffraction peaks of the free 2-aminoterephthalic acid were observed.

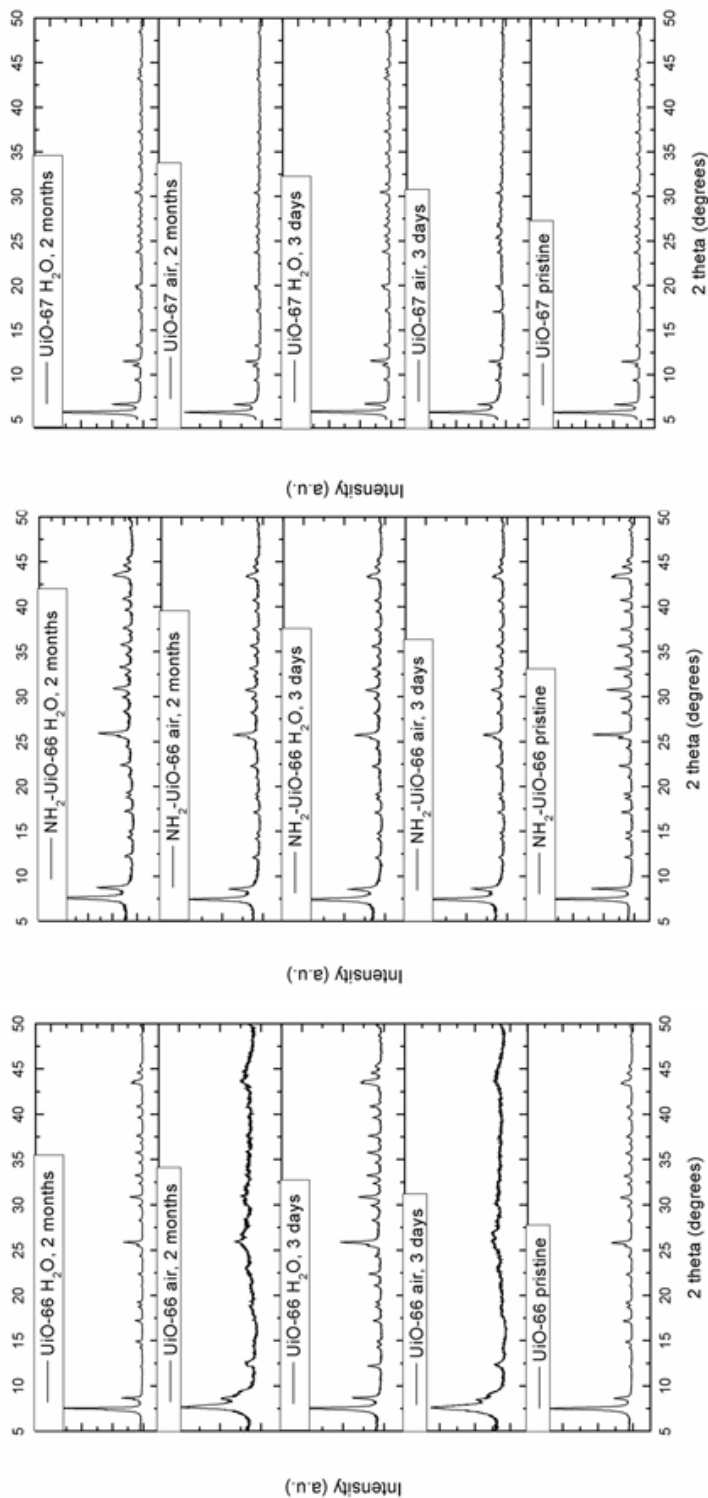


Figure 2.12: XPRD data for the pristine UiO-type structures or after chemical treatment

Stability towards bases The UiO-66, NH₂-UiO-66 and UiO-67 reveal a high resistance towards bases. No changes are observed in their XRPD patterns and only a slight decrease is observed in the Langmuir surface areas. However at higher pHs, Lillerud et al. have noticed that the UiO-66 framework starts to transform in a less crystalline material within 2 hours, whereas the treatment of NH₂-UiO-66 with NaOH led to a total decomposition of the MOF into an amorphous phase. [113]

In addition to the very high stability of MIL-101(Cr) in acidic media, we also observed a high stability towards alkaline environment. No changes in the crystallinity are observed after 2 months in a pH = 12 solution. Additionally, the Langmuir surface area increases significantly, an effect which was also observed after the treatment with acid.

In contrast to the very high stability of the MIL-101 (Cr), the NH₂-MIL-101(Al) and Cu-BTC framework show an exceptionally low stability towards bases. After contact for only 3 days at pH = 12, a complete structure transformation of NH₂-MIL-101(Al) into NH₂-MIL-53 is observed, whereas the Cu-BTC framework is converted into other crystalline phases, which were also observed after contact in water and acidic media.

MIL-53(Al) and NH₂-MIL-53 exhibit a good stability in alkaline media. No loss of crystallinity was observed from the XRPD patterns. However, there is a significant decrease in the Langmuir surface area of the MIL-53(Al), in comparison to the pristine MOF, in agreement with the reports of Jhung et al. and Huang et al. [97, 107]

ZIF-8 shows proper stability in alkaline solutions. After 3 days in a pH = 12 solution, no changes are observed in the XRPD pattern and only a minor decrease in Langmuir surface area is noted, in agreement with the report of Yaghi et al. [94]. However, after contact for 2 months in a pH = 12 solution, extra diffraction peaks are observed, which can be assigned to the formation of carbonates. [115]

Stability towards peroxides UiO-66 and NH₂-UiO-66 show a remarkable stability in the peroxide solution, which is in contrast with the UiO-67. Even after 2 months exposure, no changes are observed in the XRPD pattern of the NH₂-UiO-66 (see Fig. 2.12). However, where the Langmuir surface area of UiO-66 stayed unaltered, with the NH₂-UiO-66 a significant decrease was observed (from 885 m²/g to 486 m²/g after 2 months).

In contrast to the previous examined media, in which the MIL-101(Cr) showed an exceptionally high stability, after 2 months of exposure to the H_2O_2 solution, the MIL-101(Cr) is completely converted into another crystalline phase, i.e., the MIL-53(a.s.) structure. The ZIF-8 material is almost fully amorphized after 2 months in said solution, whereas the Cu-BTC material is transformed into a crystalline phase which we could not directly identify. These MOFs did, however, preserve their crystallinity after 3 days contact time with the peroxide solution (even though their Langmuir surface area did decrease). In contrast, the UiO-67 and NH_2 -MIL-101(Al) showed a complete degradation after only 3 days in the oxidative environment. The NH_2 -MIL-101(Al) is converted into the thermodynamically more stable NH_2 -MIL-53 structure, whereas with the UiO-67, only the diffraction peaks of free linker 4,4'-diphenyldicarboxylic acid can be observed.

Also for the MIL-53(Al), a gradual decrease in the Langmuir surface area is noted in time (from $1531 \text{ m}^2/\text{g}$, to $607 \text{ m}^2/\text{g}$, and $241 \text{ m}^2/\text{g}$, after respectively 3 days and 2 months), in addition to progressive structural transformation into a new crystalline phase. This phase was also observed after the hydrothermal treatment and exposure to acidic media, and could be assigned to free organic linker and γ -AlO(OH). A gradual degradation of the framework was also noted for the NH_2 -MIL-53. After 2 months in the H_2O_2 solution, new diffraction peaks appear showing that the NH_2 -MIL-53 structure is modified.

2.3.4 Conclusions

In this work, we presented for the first time a systematic comparison of the stability of several metal-organic frameworks. In order to investigate these materials, not only the crystallinity before and after the tests was compared, but also the porosity. In the reports of many new MOF materials, some kinds of stability tests are proposed, yet in this work, all the materials were treated under the same conditions to allow a fair comparison. A complete overview of the results is provided in table 2.1 For most of the MOFs under examination, i.e., MIL-101(Cr), NH_2 -MIL-101(Al), MIL-53(Al), NH_2 -MIL-53, UiO-66, NH_2 -UiO-66, UiO-67, ZIF-8, and Cu-BTC, the hydrothermal stability was confirmed. The chemical stability towards acids and bases was overall disappointing, especially after a 2 months exposure time, with a few notable exceptions. One example worth noting was MIL-101(Cr), that reached a higher internal surface area after an acid or alkaline washing step, proving to be an adequate purification method. The NH_2 -MIL-101(Al) structure, however, shows a very low stability, as it can be easily converted to the more thermodynamically stable NH_2 -MIL-53 framework. Very few of the examined MOFs showed a good stability in 5 wt. % H_2O_2 solution. Only the UiO-66

and NH_2 -UiO-66 material showed no loss in crystallinity after exposure for 2 months. Furthermore, it was shown that it is important to not only consider the crystallinity to assess the stability of a material, but also the porosity features. Many materials which appeared to retain their crystallinity based on the XRPD analysis exhibit a significant decrease in internal surface area. Both analyses should be consistently applied to verify the stability of a material.

2.4 UiO-66: A stable MOF

Zr-based MOFs, and more specifically the series developed at Oslo University (UiO) by Lillerud and co-workers, [116] are an interesting class of frameworks with great possibilities for different applications. They are very stable materials as shown in the previous section and have a fairly robust synthesis (see 2.4.2), allowing the inclusion of genuinely different linkers and metals. This resulted in a plethora of functionalized materials with the UiO crystal structure (see 2.4.1). [98, 117–119] Moreover, the straightforward synthesis procedure allows for efficient upscaling from the lab scale to a pilot scale plant, as was demonstrated by Ahn et al. [120] The number of scientific papers concerning the UiO-66 material has been subjected to a dramatic rise since the first publication of the material.

Given all the notable properties of the UiO-66 material, we chose this material as the central material for this work, providing an excellent platform for further modifications and catalytic trials.

2.4.1 Structure

In section 2.1, the surprising beauty and complexity of coordination polymers was introduced. The simple building units form a microstructure via coordinative interactions and herefrom crystals can grow. This complexity is also true in the case of Zr-based MOFs. Figure 2.13 shows for the same Zr node type that different ligands lead to completely different final MOF structures. The UiO-66 is shown on the far right side of this figure. The building units of UiO-66 are an inorganic unit, consisting of 6 zirconium atoms and covalently bonded oxygens with the general stoichiometry $\text{Zr}_6\text{O}_4(\text{OH})_4$ and the organic linker. In the case of UiO-66 this is terephthalic acid (TPA) or 1,4- benzenedicarboxylic acid (BDC), both names are used throughout literature.

The UiO-66 structure in figure 2.13 shows to be 12-fold connected. This high coordination number is at the basis of the remarkable stability of the mate-

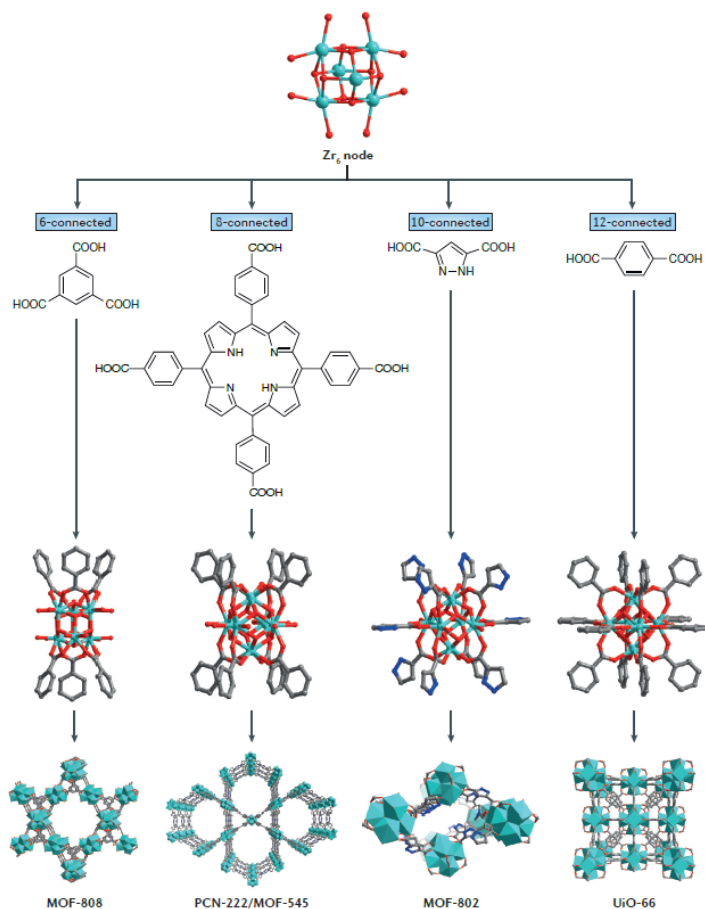


Figure 2.13: Different connectivities of the Zr_6 node leading to different topologies. [22]

rial. This connectivity lead to the formation of two pore types as displayed in figure 2.14, namely a smaller tetrahedral cage and a larger octahedral cage. The complex structure of the UiO-66 was originally refined out of powder diffraction data. Fortunately, thanks to modulated synthesis procedures (see further) single crystal measurements could be performed to confirm these measurements. Moreover, Valenzano et al. corroborated this via extensive EXAFS and other spectroscopic techniques [121]. They also discuss in detail the reversible OH removal/addition to the Zr node.

Isorecticular expansion of the UiO frameworks with e.g. biphenyl and triphenyl linkers led to the UiO-67 and UiO-68 materials. These materials show a tremendous increase in pore size and specific surface area. Unfortunately, the

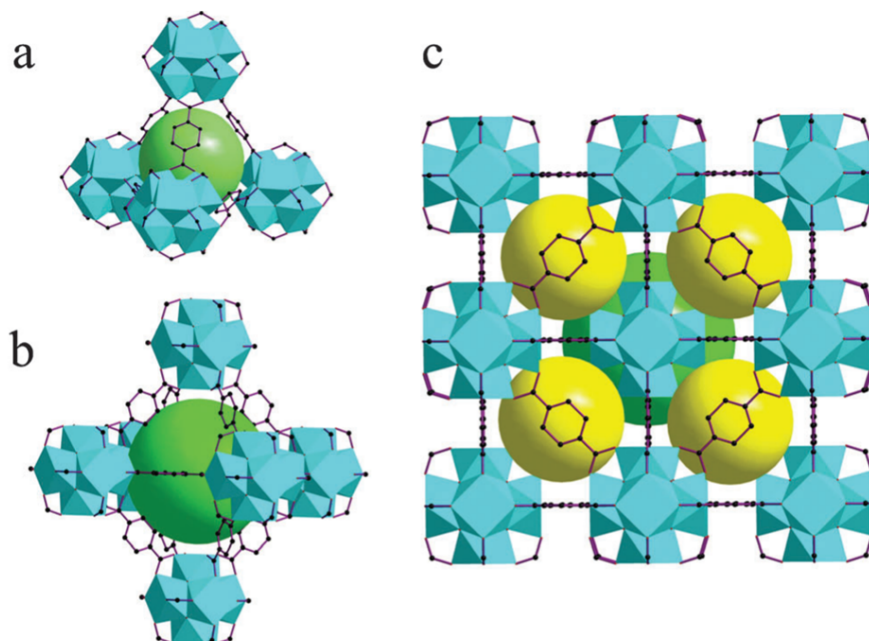


Figure 2.14: Structure of UiO-66 MOF (c): Combination of one octahedral cage (b) and two adjacent tetrahedral cages (a) forming a cubic unit consisting of eight inorganic $\text{Zr}_6\text{O}_4(\text{OH})_4$ bricks. Zirconium, oxygen, carbon, and hydrogen atoms are represented in red, blue, gray, and white, respectively. [122]

increase in surface area is inversely correlated with their stability as shown for UiO-67 in the previous section. The general architecture of the materials in this series and shows a $Fm\bar{3}m$ space group.

2.4.2 Synthesis

One of the great advantages of the UiO-66 and related materials is their very robust and straightforward synthesis. A plethora of starting materials, solvents as well as synthesis conditions can be used and still provide a UiO-type structure. However, the quality of the materials is highly variable. Crystal size and morphology, overall crystallinity and surface area, amount of defects and many more characteristics are changed to a certain extent depending on the synthesis strategy followed.

The general procedure used in this thesis is based on the work of Shyam et al. [98]. They developed a procedure starting from the easy-to-handle

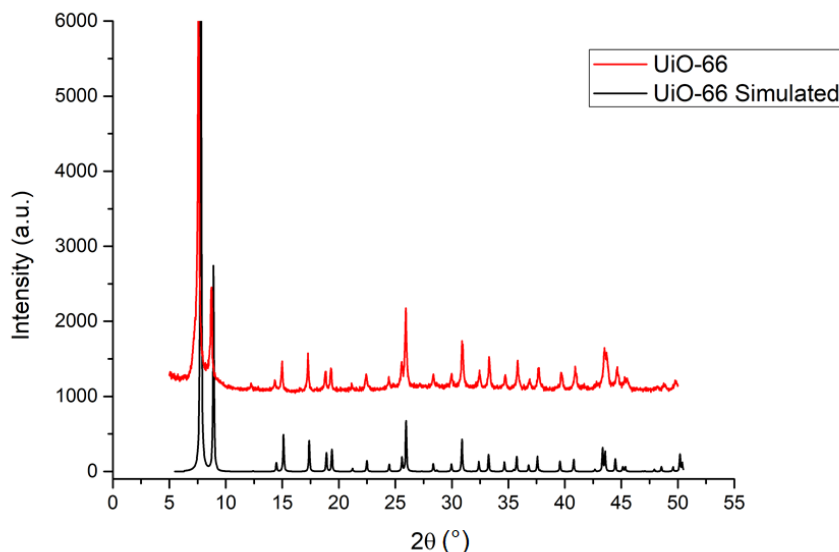


Figure 2.15: XRD diffractogram for the pristine UiO-66 compared to the calculated values for the $Fm\bar{3}m$ space group.

$\text{ZrO}_2\text{Cl}_2 \cdot 8\text{H}_2\text{O}$ precursor in contrast to the usually used ZrCl_4 . The great advantage is that this salt is stable in air and hence can be handled outside an inert atmosphere. Moreover, this synthesis could be easily scaled up using Teflon-lined autoclaves in stead of pyrex tubes as the original recipe. Routinely, we could achieve about 0.3-0.5g of product depending on the linker of choice. The procedure consists out of a hydrothermal synthesis step and a consecutive activation step to remove unreacted species out of the framework material:

Synthesis method 1 A mixture of $\text{ZrO}_2\text{Cl}_2 \cdot 8\text{H}_2\text{O}$ (0.93 mmol), $\text{H}_2\text{BDC-X}$ (0.93 mmol) and formic acid (9.54 mmol) in dimethylacetamide (DMA) (9 mL) was placed in a Teflon line autoclave. The autoclave was sealed and heated in a muffle furnace to 150 °C, kept at this temperature for 24h, then cooled spontaneously to room temperature. The precipitate was collected by filtration, washed with DMA and acetone (2x3 mL) and dried in air. These samples are labelled ‘As-Synthesised’ (AS)

Activation A suspension of the AS-form of each compound (0.3-0.5 g) was stirred in DMF (20 mL) under ambient conditions for 12h. The filtered solid was further stirred in methanol (30 mL) under ambient conditions for 24h.

The methanol-exchanged forms of the compounds were subsequently heated at 65 °C under dynamic vacuum for 24h to obtain the activated forms of the compounds. For the UiO-66-X compounds where X = NO₂, NH₂, (NH₂)₂, (SH)₂, OH and (OH)₂ further heating at higher temperatures (110 °C for 12h) was needed to obtain increased porosity.

A different procedure used in this thesis is based on the more reactive ZrCl₄ salt and acetic acid as modulator. In this thesis, a typical procedure implied the following steps:

Synthesis method 2 ZrCl₄ (0.087 mmol) and 2-aminoterephthalic acid (0.065 mmol) were dissolved in DMF (15 mL) in a glass vial using sonification for 15 minutes. The resulting solution was transferred into a Teflon-lined autoclave and heated to 120 °C for 24 h. The final sample was cooled to room temperature spontaneously and filtered of using a .25μm membrane filter. Activation was performed as described above.

The procedure based on ZrCl₄ is still the most used procedure in literature and various recipes can be found. [99, 107, 122, 123] Behrens and co-workers showed that the choice and amount of modulator determine to a great extent the crystal growth of the UiO-66 crystals. [123]

It can be seen from figure 2.16 that both methods give crystals of different sizes.

2.4.3 Electronic structure of UiO-66

Regarding their electronic structure, MOFs are still mostly described with traditional solid state terminology. Nevertheless, in recent literature, this classical view of MOFs has been challenged and has attributed to these materials significantly different properties than typical insulators [124, 125] This difference in behaviour is because MOFs retain many of their discrete, molecular characteristics. Instead of showing a delocalized valence and conduction band, a more localized highest occupied and lowest unoccupied crystal orbital (HOCO and LUCO) can be observed.

The electronic Density of States (DOS) of the pristine UiO-66 material is shown in figure 2.17. On the left of the figure the periodic structure of 1 supercell is plotted with the two main building units indicated: the organic linker and the zirconium node. Both parts feature distinct electronic bands in the DOS that is plotted on the right-hand side. If we take a closer look, we see that the states below the Fermi level are linker-based states, except for the

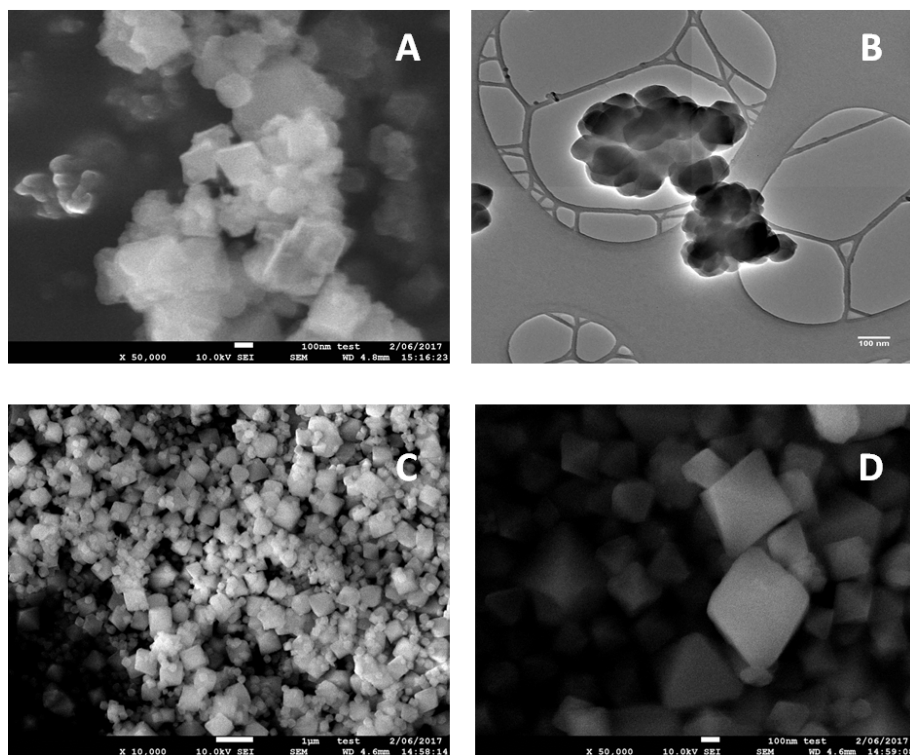


Figure 2.16: SEM (A,C,D) and TEM (B) images of the UiO-66 synthesised following two different recipes. Method 1 (A,B) yields clustered small crystallites whilst method 2 results in larger crystallites (up to $1\mu\text{m}$)

HOCO, which consists of $\mu\text{-O-OH}$ states. This is however an artificial phenomenon caused by the level of theory (PBE). If we perform calculations at the HSE level of theory, this band lowers and the HOCO is formed by purely linker states. Next, if we look at the LUCO, this also consists of a pure linker state. Hence, the lowest excitation of the material will be a pure linker-based excitation, requiring an energy as labelled ΔE_{abs} . After the LUCO linker states, a set of Zr-based bands can be found in the DOS. These bands consist of the Zr d-orbitals. Since the gap between the linker states and these Zr d orbitals is an important quantity in the remainder of this thesis, it is labelled ΔE_{LMCT} referring to the energy needed for the Ligand-To-Metal-Charge Transfer.

Figure 2.17 represents one of the central figures of this thesis, showing the two ‘work-in-progress’ regions. Engineering of the ΔE_{abs} will be done by adding functional groups to the organic linker as presented in chapters 5 and

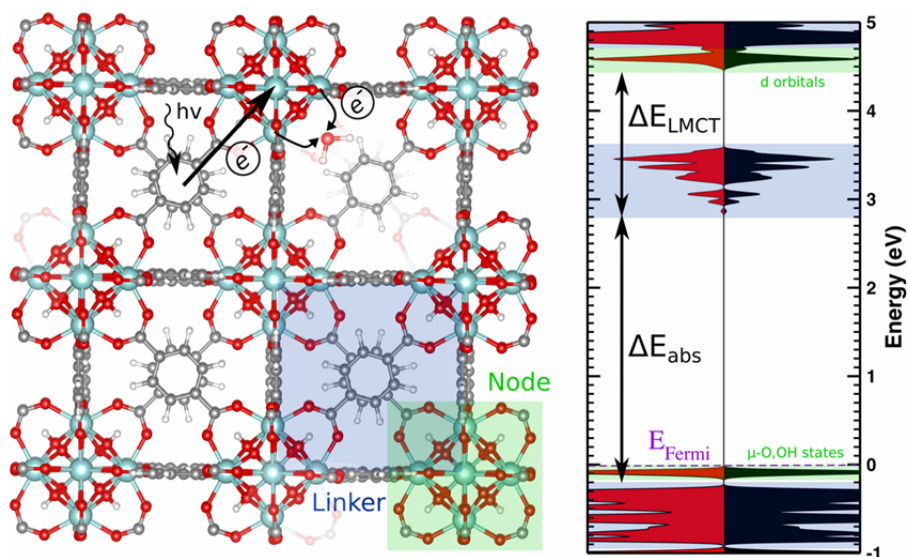


Figure 2.17: Scheme showing relating the different constituent parts of the UiO-66 framework to their respective quasi-localized bands in the DOS. Adapted from [126]

6. On the other hand, lowering the metal stated to overlap with the linker LUCO will be the subject of the last two chapters dealing with metal doping and defect engineering.

Owing to their high stability in various environments, their easy and scalable synthesis, interesting electronic and acid-base properties, zirconium based MOFs have lead to a plethora of applications. [120, 127–132]

A recent review of the group of Hong-Chai Zhou gives an overview of the most recent advances of the synthesis and applications of zirconium MOFs. [122] The use of UiO materials in photocatalysis will be discussed more elaborately in the next chapter.

3

Photocatalysis

3.1 Materials for light-harvesting

One of the major scientific challenges of the 21st century is the change from energy intensive and polluting processes to green and sustainable alternatives. A promising approach is the conversion of solar energy, an abundant and incessant energy source, into chemical energy via photocatalytic processes. [133, 134] Natural photosynthesis is the prototype example of an efficient process based on solar energy, using a highly complex set of hierarchically assembled units to convert the energy into chemical bonds. [133, 135] The roots of the implementation of solar-driven chemical conversions in our daily technology lie in the seminal work of Honda and Fujishima, who studied photocatalytic water splitting on TiO_2 . [136] Since then, novel materials have been developed for these processes, enabling many environmentally friendly applications and yielding a deep understanding of the fundamental physics of semiconductor-based photocatalysis. [137–141] It remains however **challenging to design a system that is highly active, uses a broad range of the electromagnetic spectrum, is stable, and has a reasonable cost.**

3.2 Photocatalysis

When cataloguing materials in terms of their electronic structure, they are traditionally divided in metals, semiconductors and insulators. This division is determined by the band gap, which represents the forbidden energy gap that is present at the Fermi level. In other words, the band gap is the energy that is required to excite an electron from the valence band, i.e. the HOMO (Highest Occupied Molecular Orbital) in molecular terms, to the conduction band, the LUMO (Lowest Unoccupied Molecular Orbital). Figure 3.1 shows a schematic representation of the different cases that are possible.

A metal is classically described as a material where the valence and conduction band overlap completely. Hence, no forbidden region is present and electrons can move ‘freely’ around in that band. Insulators on the other hand have a large forbidden zone between the valence and conduction band, impeding electrons to move around in the material and hence are not conductive. For semiconductors, a band gap is present of an energy in between metals and insulators, thus implying that if a certain energy is added to the system (be it thermally, light excitation,...) an electron from the valence band can be excited to the conduction band.

Upon excitation of a semiconductor, an exciton is created. This represents the semi-bound state of an electron (e^-) excited from the valence to the conduction band and the corresponding positive hole (h^+) that is left behind in the valence band. The formation of this exciton is the primary processes when looking at photocatalysis. The excited electron and hole both contain a certain potential energy which can initiate different processes.

A first process which can occur very fast is the direct recombination of the electron-hole with emission of a photon or via non-radiative relaxation. In this way the charge carriers loose their potential energy and the material is back in its ground state. If the exciton does not recombine, the electron and the hole can migrate through the material. At the surface, the charge carriers can interact with absorbed species on the substrate. The electron can for example effectively interact with electron acceptors and for example reduce O_2 to the superoxide radical anion $O_2^{\cdot-}$ or an absorbed organic species. It should be noted that direct recombination is detrimental to the photocatalytic activity, since the typical time constant is in the ns regime, whilst a chemical interaction with absorbed species takes much longer.

The general idea of photocatalysis is shown in figure 3.2. Herein we see the excitation of the material with light of a certain energy $h\nu$. The recombina-

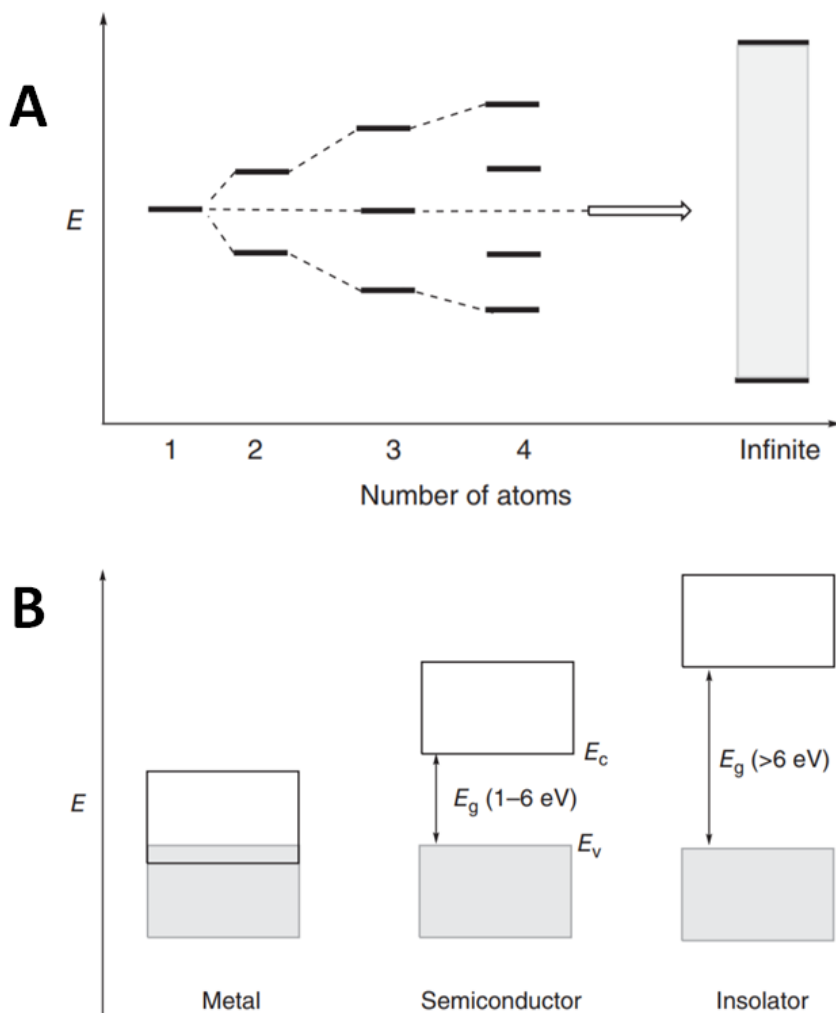


Figure 3.1: Schematic representation of the band structure of a material. (A) shows the evolution of the energy levels of a linear chain with respect to the number of atoms. (B) represents a simple example of the three main classes in solid state materials. Taken from [142]

tion process is indicated with the dotted line. If the charge carriers can be separated efficiently and migrate to the surface, a reduction of an electron acceptor, or the oxidation of an electron donor can take place.

In order to generate an exciton, the material needs to be excited with e.g. light. For e.g. TiO_2 , the most classical example of a photocatalyst, the band

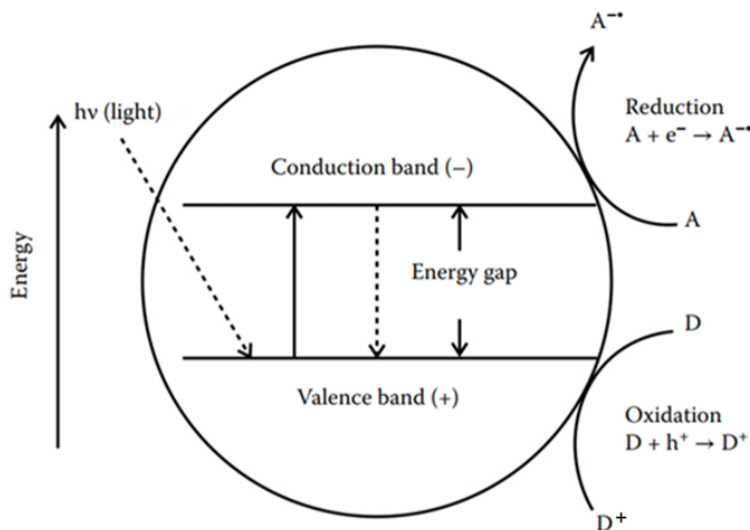


Figure 3.2: Schematic representation of the basic principle of photocatalysis. Taken from [143]

gap is 3.2 eV for the active anatase crystal phase. This energy corresponds to a wavelength of 388nm, which is in the UV region of the electromagnetic spectrum. So in order to effectively use undoped TiO_2 as a photocatalyst, light with a wavelength $< 388\text{nm}$ is needed, which implies a big problem when looking at the solar spectrum.

Figure 3.3 show a coarse representation of the solar spectrum. Starting from 250nm we can find about 3% of the emission in the UV region. The main part of the solar spectrum can be found in the visible region and the near infrared. It is immediately clear that if one wants to harvest solar energy, the most efficient materials should absorb in the visible range since the normalized emission is much stronger here.

If we take a new look to the example of TiO_2 , we see that in order to excite this semiconductor, only a very small fraction (about 4%) of the solar spectrum can be used. It is needless to say that this is far from an efficient process. Luckily, several methods can be employed to improve this. By doping with electron rich or poor dopants (n-type, or p-type doping respectively) the Fermi level can be shifted by introducing inter-band gap states. Furthermore, sensitizing by means of e.g. large conjugated organic chromophores

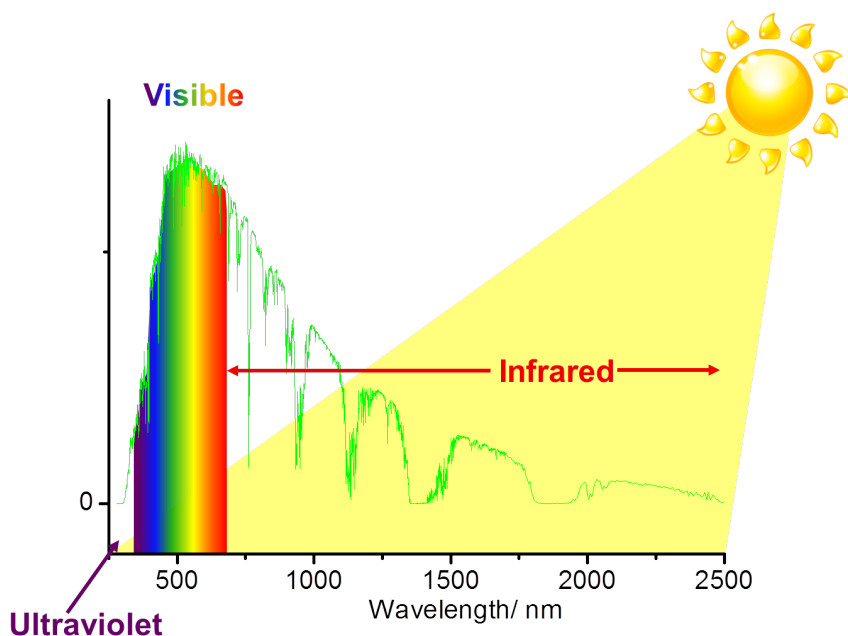


Figure 3.3: Spectrum of the sun. Taken from [144]

has proven to be an efficient strategy.

Considering the above mentioned, we can understand now that three fundamental processes are indispensable to successfully convert the solar energy to chemical energy. All three steps have their own efficiencies, sidepathways etc., foreclosing the overall efficiency of the material. A first step is the actual **harvesting of solar light**. In this process, the absorbed energy creates an excited state, embodied in two charge carriers. In nature, large conjugated organic molecules are used in this process, and these types of molecules are also used when mimicking the natural pathways (e.g. larger molecular dyes are classical photosensitizers). A second step consists of a **separation and migration** of the charge carriers. This process is crucial to prevent immediate recombination and hence loss of the redox potential. Classically this energy transfer is described by diffusion of localized (Frenkel) or delocalized (Wannier) excitons in semiconductor physics. On the other hand in supramolecular assemblies, the transfer mechanisms are described in terms of Förster (dipole-dipole coupling) or Dexter (electron exchange) pathways. Finally, the charge carriers **initiate two half reactions** (oxidation and reduction for the hole and electron respectively) at the catalytic centres.

In order to combine the three steps, complex assemblies and multi-component systems are necessary. For this, the natural process is still by far the most efficient and artificial systems still are greatly limited by the challenges that assembling these parts contain. Moreover, it needs to be mentioned that to complete the catalytic cycle, the catalyst needs to return to its original ground state. In nature, this process is completely closed and very efficient. However, in artificial photosynthesis, 1 of the half-cycles is mostly ignored and sacrificial donors are added to complete the process since the optimization of one of the half-cycles usually represents already sufficient challenges to cope with and only few materials exists that cope with both half-cycles. [145] The current need for sacrificial donors limits the sustainability of a photocatalytic process [146] and the integration of all steps into a single material, able to operate without sacrificial donor is in my view one of the most important challenges to be addressed in future research.

3.3 MOFs and photocatalysis

As discussed in the previous section, it is very challenging to design a photocatalytic system that is highly active, uses a broad range of the electromagnetic spectrum, is stable, and has a reasonable cost. In this view, MOFs represent an emerging class of photoactive materials, because they combine molecular functionality and control in a solid state material, yet the stability of most MOFs remains a point of attention. In principle this means that by carefully choosing the linker and inorganic nodes, both the sensitizer and catalytically active centres can be included in the same material and hence provide the structural organization to allow an integration of the three necessary steps in photosynthesis described above, and which represent the major scientific challenges when designing new photoactive materials. In section 2.4.3, it was introduced that the electronic structure of MOFs is not easily described in traditional solid state terminology. This difficulty arises due to the fact that MOFs retain many of their discrete, molecular characteristics, notwithstanding their description of crystalline solid-state materials. MOFs are hence better described as periodic arrays of self-assembled molecules with discrete molecular absorption modes. [125, 147] Instead of showing a delocalized valence and conduction band, a more localized highest occupied and lowest unoccupied crystal orbital (HOCO and LUCO) can be observed.

The discrete nature of MOFs can be exploited for photocatalysis. [148] The activity of a material is highly determined by the lifetime of the created charge carriers. To increase the lifetime, the created exciton has to be separated to prevent fast recombination of its composing electron-hole pair. The

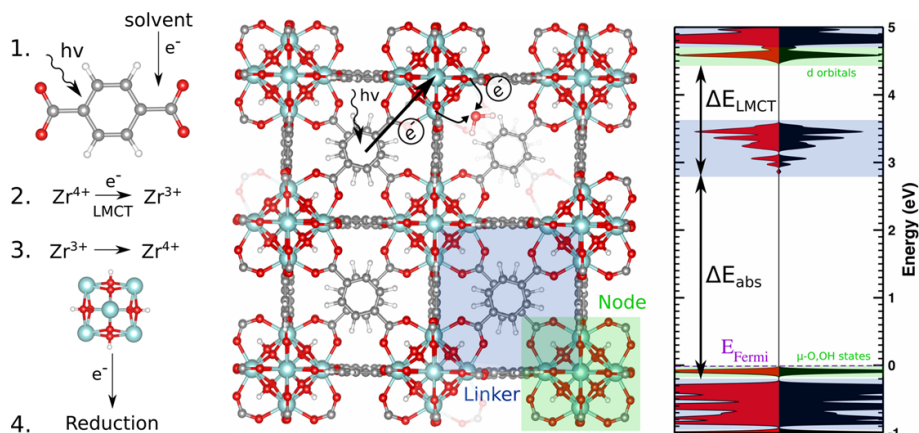


Figure 3.4: Basic steps occurring in a UiO-66 photocatalytic process

modular nature of MOFs allows for the optimization of their different constituents in order to achieve e.g. a fast migration of an electron excited at the linker to the inorganic node. Generally, this will occur as a ligand-to-metal charge transfer (LMCT) since the organic linkers usually contain an aromatic system, which can be excited using UV/Vis light. This LMCT process has been discussed in different materials as one of the main mechanisms underlying the photocatalytic activity of MOFs. [147]

3.3.1 UiO-66

The UiO-66 is a remarkable material, not only thanks to its extraordinary stability or high catalytic activity in acid-base catalysis, but also when regarding its electronic structure. As explained before, one of the main properties a good photocatalyst should have is the efficient charge carrier separation upon the generation of an electron-hole pair. This is needed to increase the lifetime and catalytic ability of the generated charges.

Figure 7.1 represents the basic idea of the LMCT process described above, lying at the basis of the photocatalytic activity of the material. In an ideal process, the aromatic BDC linker is excited using light with an energy of about 4 eV. The created electron should be able to move towards the inorganic node, reducing the zirconium from Zr^{4+} to Zr^{3+} . Given the very negative reduction potential of Zr, this direct process is very unlikely. EPR data in literature is not conclusive, and the existence of Zr^{3+} species is highly debatable. Upon migration to the inorganic node, a high potential electron is created that can now effectively reduce a molecule (e.g. O_2) absorbed on the node. In order to

make the cycle complete, an electron donor (e.g. a solvent molecule) should refill the created hole on the linker.

Several problems arise unfortunately when looking at the pristine UiO-66 material. The band gap is determined by the linker as discussed in section 2.4.3 and is about 4 eV. This corresponds to about 310nm, which is in the UV region. So in order to use UiO as a green, solar-light active catalyst, modifications are necessary. Moreover, from the same section it can be deduced that a transfer from the linker to the inorganic node will be very difficult, since the empty Zr d states still lie more than 1 eV higher than the empty linker band. This lack of overlap impedes the electron to travel efficiently to the node.

In literature, several researchers have studied the photocatalytic activity of UiO-66 and related materials. Exploration of the UiO-66 materials for light-harvesting and photocatalytic applications started with Garcia and co-workers [149] on hydrogen generation using the amino-functionalised material. They showed that the NH_2 group allows to shift the absorption spectrum towards the visible range, solving the problem of the large band gap, which was afterwards applied to Cr(VI) reduction and oxidation of alcohols [150], a series of aerobic organic transformations [151] and CO_2 reduction [152] by other groups. The latter study also provided the first experimental insight in the mechanism and processes during irradiation of the UiO-66 and gave the first evidence for a charge transfer from the linker towards the Zr corners. Shen et al. [153] studied the electronic effect of ligand substituents on the photocatalytic activity of the UiO-66 framework and found that the corresponding rates linearly correlate with their Hammett coefficients. They proposed that the functional groups would promote charge transport and separation of the carriers in the framework.

The use of a mixed linker approach has recently been reported to improve the performance in the photocatalytic oxidation of alcohols. [154] Recent studies on the periodic UiO-materials confirmed the experimental band gap modulations via calculations based on Density Functional Theory (DFT). Flage-Larsen and co-workers employed both semi-local and hybrid functionals to model the band gap modulation of the parent UiO-66 material and its NO_2 and NH_2 linker-substituted variants. [155] The resulting band gap reduction could be explained based on lone-pair interaction with the bulk material. Recently, Musho et al. [156] examined the same set of materials, and the band gap modulation could be explained based on projected density of states of the periodic materials, and excited-state simulations of the linker components. Similar studies on the Ti-MIL-125 MOF have been reported

by Hendon and co-workers, showing the possibilities of this engineering approach. [157] Moreover, Musho et al. used the band structures of pristine and linker-functionalized UiO-66 to calculate electron mobilities and found that these decrease if functional groups are added. They also found that the functional group increased the charge density and hence concluded that charge transport in UiO-66 should be tunnelling based, admitting that considerations beyond ground stated DFT calculations are required to account for higher order quantum mechanical interactions. Also Sun et al. discuss the charge transfer in MOFs as a charge hopping process versus the classic band transport picture. [158]

By only functionalizing the linkers, the changes to the electronic structure are merely limited to the HOCO states. It offers an interesting pathway to tune the light absorption properties as will be shown in chapter 5, however the LUCO states and hence the ΔE_{LMCT} (see chapter 2) is altered only marginally, limiting the overall activity. In order to improve this, changes to the metal node are necessary. This work will study changes to the metal node as a possible pathway in chapter 7 and also look at the possibility of electronic structure engineering via introduction of defects in chapter 8. We will introduce the current literature in the third part of this thesis where we concern ourselves with these two pathways to improve the charge transfer efficiency.

4

Experimental and computational methods

4.1 Experimental methods

Experimental techniques for the study of materials evolve constantly and offer ever more possibilities to gain understanding at a fundamental level. In this section, a non-exhaustive overview of some of the major techniques used in this work will be given. First the often used characterization techniques and the specifications of the equipment in our laboratory will be provided. A short introduction to spectroscopy will then be given since these measurements represent the most important set of techniques used in this thesis. Finally, an overview of the photocatalytic set-up is provided.

4.1.1 Characterization

XRD

Powder X-ray diffraction (PXRD) is a technique that uses monochromatic X-rays to obtain information on the crystal structure of a material. The elastic scattering of the X-rays results from the electrons in the solid that interfere constructively and give rise to reflections corresponding to the different crystal planes, following Bragg's law:

$$2d_{hkl}\sin\theta = n\lambda \quad (4.1)$$

with d_{hkl} the spacing between two planes with Miller indices hkl and θ the angle between the incoming x-rays and the normal plane.

Equipment Ambient-temperature PXRD patterns were recorded on a Thermo Scientific ARL XTra diffractometer operating at 40 kV and 40mA using Cu K α radiation ($\lambda = 1.5406 \text{ \AA}$).

N₂-sorption

A central technique used to characterize porous materials is the adsorption of N₂ at low temperature. Measuring from low pressure to atmospheric pressure gives insight in the porous structure and the total internal surface of the materials. The latter one is obtained using a Langmuir approach, which is valid since the materials at hand are microporous.

Equipment The sorption isotherms were measured on a Belsorp Mini apparatus, operating at 77 K.

XPS

X-ray Photoelectron Spectroscopy is a surface sensitive technique based on the photo-electric effect to study the elemental composition of a sample. Moreover, information on the chemical and electronic state of the different elements can be obtained.

Equipment All measurements were recorded on a X-ray photoelectron spectroscopy S-Probe XPS spectrometer with monochromated Al (1486 eV) exciting radiation from Surface Science Instruments (VG). Powder was positioned on the holder using conducting tape. In order to minimize charging an electron flood gun of 3 eV was used as a neutralizer. All spectra are calibrated towards a C 1s peak position of adventitious carbon at 284.6 eV

SEM/TEM-EDX

Electron microscopy is a very powerful technique to study materials at the nanoscale. Within these techniques, the general idea is to illuminate the sample with a beam of accelerated electrons. Since electrons have a shorter wavelength than photons, the resolving power of an electron microscope is much larger than a standard light microscope. In this work, both Scanning Electron microscopy (SEM) is used and Transmission Electron Microscopy (TEM). Measuring of the characteristic x-rays emitted from the illuminated

sample via an Energy-dispersive X-ray Detector (EDX) yields qualitative and quantitative information on the elemental composition of the sample and allows for an elemental mapping.

Equipment A field emission scanning electron microscope (FEI Quanta 200) operated at low vacuum was used, equipped with an energy dispersive spectrometer for EDX elemental mapping. Samples were measured with an electron beam of 15kV.

(Bright-field scanning) transmission electron microscopy (BF-STEM) and energy dispersive X-ray spectroscopy (EDX) was performed on a JEOL JEM-2200FS high resolution scanning transmission electron microscope equipped with an EDX spectrometer with a spatial resolution of 0.13 nm, image lens spherical aberration corrector, electron energy loss spectrometer (filter) and an emission field gun (FEG) operating at 200 KeV.

4.1.2 Optical spectroscopy

The study of light-matter interactions to probe the electronic structure of a material is called spectroscopy. When light interacts with the materials surface, several processes can occur as shown in figure 4.1. Light can reflect off a surface with a well defined angle, equal to the angle of the incident light, regardless the orientation of the surface. On a perfect smooth surface (e.g. a mirror), light will reflect in a coherent way and this phenomenon is called specular reflection. On the other hand, since most materials have a rough surface, light will be reflected at several angles, referred to as diffuse reflectance. When light interacts with matter it can scatter incoherently and with loss of intensity.

Next to reflection and scattering, absorption and transmission can occur. When light is transmitted through the sample, no energy-loss is observed. On the other hand, the energy can be absorbed and transformed in to another form of energy, which is the process of absorption.

Transmission is defined as the amount of light (flux) measured after its passage through the sample as compared to the flux of incident light as given by:

$$T = \frac{\Phi_e^t}{\Phi_e^i} \quad (4.2)$$

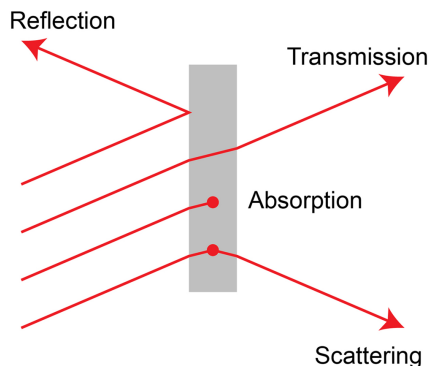


Figure 4.1: Different fundamental processes when light interacts with matter. Absorption is the transfer of the photon energy to electronic energy in the material. Reflection represents a change in light direction at a defined angle whilst scattering is light reflecting in any direction. Finally, transmission represents the passage of energy through the material without loss of energy. (figure adapted from [159])

Absorption is then defined relative to the transmittance via:

$$A = -\log T = \log\left(\frac{\Phi_e^i}{\Phi_e^t}\right) = \varepsilon c l \quad (4.3)$$

with ε the molar attenuation coefficient, c the concentration of the absorbing species and l the path length of the light. This relationship is called the Bouguer-Lambert-Beer (BLB) law.

When the energy of the light is above a certain threshold, the material can absorb the incident light. This is caused by a transition between two energy levels as already introduced in the previous chapter. Figure 4.2 shows schematically this process on the left. Here we see a material in its singlet ground state. The energy difference between the HOMO and the LUMO (or VB and CB in solid state materials) is the minimum amount of energy a photon should have to be able to excite the material, thus explaining the threshold value. After absorption, the material can go back to the ground state by emitting a photon of the same energy if no dissipation processes occur.

Unfortunately this way of representing the electronic transitions is much too simple to understand the complete picture of an electronic transition. Figure 4.2 shows on the right a much more evolved representation between two principal quantum states. These states are eigenfunctions of the electronic

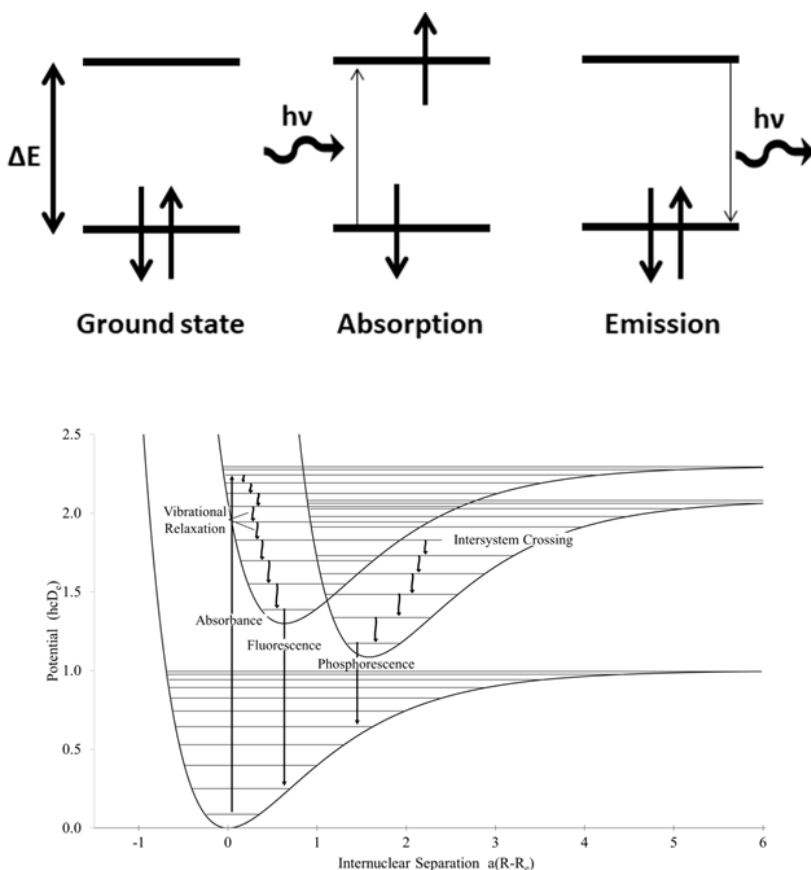


Figure 4.2: Schematic representation of the light absorption process. (figure adapted from [160])

Hamiltonian within the Born-Oppenheimer approximation and are represented here in function of the nuclear coordinates. A transition between these levels usually needs a photon with an energy in the UV/VIS range. Moreover, within the electronic states, vibrational and rotational energy levels are embedded. The former one is the subject of IR spectroscopy, which is a powerful technique to study the structure of a molecule, whilst the latter one needs microwave radiation to see transitions of these levels. Figure 4.2 only shows vibrational levels, since they are important to understand several features in the measured spectra. Allowed electronic excitations can occur between different vibrational levels hence explaining the peak broadening observed in the experimental spectra. Internal conversion of the energy can lead to a loss of energy and hence emission is usually found at higher wavelengths. Furthermore, if the excited state is long lived, relaxation of the nuclei

can occur, which is not described within the BO-approximation.

Since the motion of the nuclei is much slower than the electronic motion, we can say in a crude approximation that electronic absorption spectroscopy deals with vertical excitations, meaning that no relaxation of the excited state occurs. If we on the other hand study emission, these effects become important and a correct theoretical description is much more evolved.

The previous description was far from exhaustive and the interested reader is referred to general introductory books on spectroscopy for a more detailed description. [161]

UV/VIS absorption spectroscopy

Diluted liquid samples are usually measured in transmission mode. A quartz cuvette is used and the ratio between the incident light and the flux measured after passing through the sample is measured. According to BLB this defines the amount of light absorbed in the material as introduced above.

For solid state samples in powder form, diffuse reflection is usually measured instead of absorption. Since a powder is not a smooth surface, but rather an ensemble of randomly oriented crystallites, specular reflection is less meaningful to observe. The setup uses an integrating sphere, where all the reflected light is collected and integrated to obtain a reflectance spectrum.

Since reflectance and scattering is not easily separated, it is very difficult to obtain information about the absorption of the material. Via a series of approximations, Kubelka and Munk defined the following function:

$$F(R) = \frac{(1 - R)^2}{2R} = \frac{K}{S} \quad (4.4)$$

relating the reflectance R to an absorption coefficient (K) and a scattering factor (S).

The Kubelka-Munk function is a highly approximate way of converting reflection data to absorption data. The equation is only valid if the sample layer is sufficiently thick so that the reflectance is independent of the sample thickness. An important issue moreover is that the S factor should scale linearly in the studied wavelength region and is hence independent of the incident photon energy, only then, the $F(R)$ scales with the absorption factor K and can be interpreted in terms of an absorption spectrum. In order to

achieve this, the crystallite size is very important to consider.

Band gap determination Via the absorption spectrum, the band gap can be estimated in several ways. The easiest method is an extrapolation of the absorption edge, which usually gives a very good estimation and is eg. used by Musho et al. for UiO-66. [156].

A more advanced method was proposed by Tauc, and further developed by Davis and Mott. They show that the optical absorption strength depends on the difference between the photon energy and the band gap as related via the following equation:

$$(\alpha h\nu)^{1/n} = A(h\nu - E_g) \quad (4.5)$$

with α the absorption coefficient, E_g the band gap energy and A a proportionality constant. The values for n depend on the type of transition and equals $1/2$ for a direct allowed transition, which is important for this work.

The basic procedure for a Tauc analysis is plotting the $(\alpha h\nu)^{1/n}$ in function of the energy. With a very good data set, n can be determined by comparing the goodness-of-fit but this is seldom a reliable method.

Equipment Solid-state UV/vis measurements were done on a Varian Cary 500 dual-beam UV/vis/near-IR spectrophotometer using an internal 110mm BaSO₄-coated integrating sphere. Liquid experiments were carried out in solvent (DMF) on a PerkinElmer Lambda 900 UV/vis/NIR spectrometer.

Photoluminescence

Much more information on the electronic structure can be obtained by measuring the emission properties of a material, since now not only vertical transitions are probed. A typical photoluminescence (PL) study comprises two types of spectra. If one excites the material at a fixed wavelength and collects the light emitted by the material, an emission spectrum is obtained. On the other hand, if one probes the emission of the sample at a fixed wavelength whilst scanning the excitation wavelengths, a so-called excitation spectrum is obtained.

Equipment For both emission and excitation spectra, a FS920 of Edinburgh Instruments is used. A high pressure xenon arc lamp of 450 W is used as light source. This lamp is able to emit light in the broad range of of 250 nm

to 900 nm (be it not always with the same intensity). The excitation wavelength is selected through a double excitation monochromator (to limit stray light and improve resolution). The sample compartment can be extended with a cryo-probe to cool down the samples and improve resolution of the spectra. Within the sample chamber, a set of lenses focusses both the incoming light and the emitted light by the sample. The incident light passes through a semi-transparent mirror in order to measure the incoming photon-flux. The emitted light passes through another monochromator before being measured by a point detector (a Hamatsu 928 photomultiplier tube).

4.1.3 Gas phase photocatalysis setup

Within this thesis, gas phase breakdown of several VOC's was tested. A batch reactor designed by the Lumilab group of Prof. Poelman, optimised to study breakdown reactions of ethanol was used. Moreover, a collaboration with the group of Prof. Lenaerts at the university of Antwerp allowed for the study of flow reactions in the breakdown of acetaldehyd. Both ethanol and acetaldehyde are simple organic molecules and are used often as a model for larger VOC molecules.

Batch reactor

The setup of the batch reactor is shown in figure 4.3. The sample is first coated onto a glass substrate before it is mounted vertically inside the reaction chamber. The spin coating was performed by dissolving 0.05g of material in 1ml of i-PrOH. Three consecutive coating steps of 200 μ L were performed at 3000 rpm for 10 sec. The reaction chamber could be put under vacuum to choose a specific atmosphere. For the EtOH breakdown an atmosphere of Ar/O₂ was chosen to prevent overlap of the N₂ mass peak with the EtOH peak. After the sample was mounted, the chamber was set under vacuum (10⁻⁷ bar) and the sample heated to 90°C to dry overnight and remove any residual i-PrOH from the sample.

After the drying step, the chamber was filled with the Ar/O₂ atmosphere and the measurement could start. For a typical measurement, 6 μ L of EtOH (273 ppm) was introduced in the reaction chamber. After an equilibration step of 30min, UV illumination started with a 100W Hg-arc, containing major 254 nm and 365 nm lines.

The analysis of the chamber atmosphere containing the different reactants and breakdown products was performed using a QMS200 OmniStar by Pfeiffer Vacuum. The system is a quadrupole MS and is equiped with two detec-

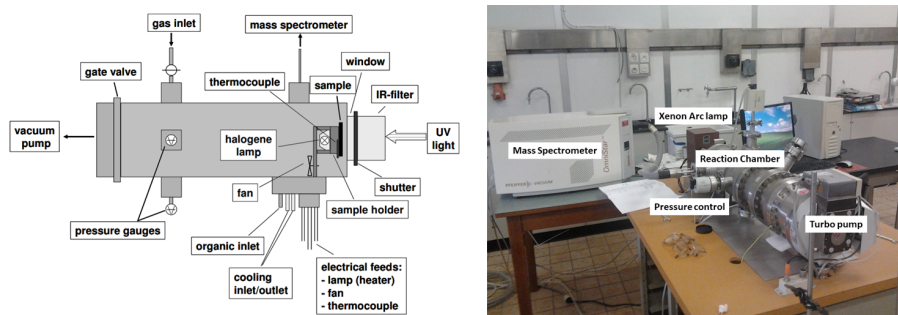


Figure 4.3: Schematic representation of the batch photocatalytic reactor adapted from the PhD thesis of dr. Eufinger (left). Picture of the actual setup (right).

tors, a Faraday cup and a channeltron detector, allowing to measure masses in the range 0-200 Dalton. The intensity of the peaks of several crucial masses are followed in function of the time (Multiple Ion Detection) and could be converted to a quantitative concentration (Multiple Concentration Detection) via a calibration matrix containing the known values of the Ar/O₂ concentrations.

Continuous flow

The photocatalytic performance of the samples towards the degradation of gas phase acetaldehyde is tested using the photocatalytic test setup described in detail by Tytgat et al. [162]. All samples were first suspended in water (20 mg powder + 2 mL water) and stirred ultrasonically for 30 min. On two silicon wafers (2.5 x 1.5 cm²), 500 μ L of the suspension was drop casted. The slides were left to dry in an oven at 90°C for 2h. The photodegradation experiments are conducted in a flat plate photoreactor equipped with a 25W UV-TL-lamp (3.2 mW/cm², λ_{max} =365 nm) and is operated in continuous flow mode. The photoreactor consists of a slit shaped reactor volume with dimensions 80 x 15 x 2 mm³. The schematic design is shown in figure 4.4. In the reactor slit a silicon wafer loaded with 5 mg of sample is placed. The reactor is sealed by a quartz plate and is made air tight with a tension ring. Acetaldehyde (C₂H₄O) is selected as test pollutant. A synthetic gas mixture of dry air (Air Liquide) and acetaldehyde (Air Liquide, 1% in N₂) was mixed by mass flow controllers resulting in an acetaldehyde gas concentration of 35 ppmv and a total flow of 400 cm³ min⁻¹.

Each photodegradation experiment consisted of 4 subsequent phases: (1) 10

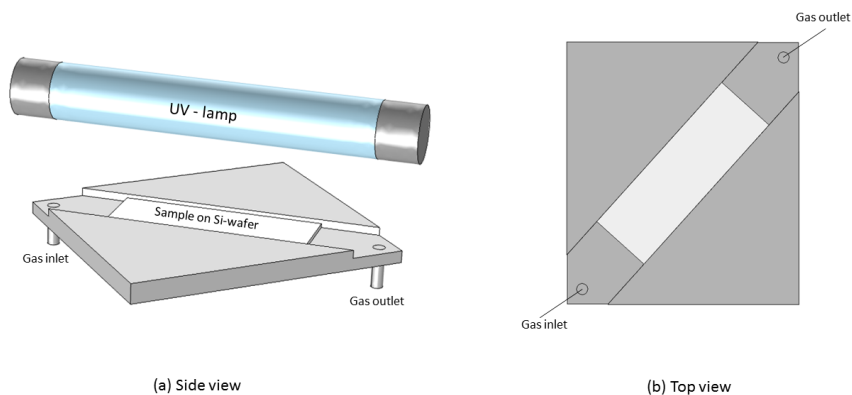


Figure 4.4: Schematic representation of the continuous flow photocatalytic reactor

min gas flow ($400 \text{ cm}^3 \text{ min}^{-1}$) in bypass, (2) 15 min gas flow through the dark reactor in order to achieve adsorption/desorption equilibrium, (3) 20 min gas flow through the reactor under UV-illumination and (4) 5 min air flow (flush phase) through the dark reactor. Before the experiment starts the samples are pretreated with UV for 30 minutes. For the long term stability measurement phase (3) is extended to 13 h. During these different phases detection of acetaldehyde and carbon dioxide in the gas effluent was carried out using a NicoletTM 380 FTIR spectrometer (Thermo Fisher Scientific) with ZnSe windows and a 2 m heated gas cell. Spectra were recorded in a range of $4000\text{--}400 \text{ cm}^{-1}$. The used $\nu_{\text{C}_2\text{H}_4\text{O}}$ and ν_{CO_2} stretch band positions of acetaldehyde and CO_2 are located at 2728 and 2360 cm^{-1} respectively. The peak heights at these wavenumbers are correlated with concentrations using a calibration curve.

4.2 Computational modelling

Although experimental observations are historically at the basis of scientific research, computational methods have evolved fast and are becoming more and more omnipresent. Computational research allows to study and understand the properties of a material at a molecular level and obtain information on a hitherto unreachable level for experimental techniques. Nowadays one can even predict features and help experimentalists in choosing the right directions, e.g. via high throughput screening or related techniques. In current

research projects, both experimental and computational methods are used in synergy to obtain a complete understanding of matter and its interactions.

Throughout the years, computational methods have been evolving at a peerless speed thanks to methodological improvements and the unstoppable rise in computer power. A complete overview is outside of the scope of this work. We will briefly introduce the methodologies used in this work and will refer the interested reader to specialised publications.

4.2.1 Quantum description of matter

Since the early developments of a quantum theory of matter, our understanding of its fundamental constituents has since then evolved tremendously. Although many assumptions need to be made, the success of the theory in describing many properties of molecular and solid state systems still accounts for its popularity. The fundamental equation that needs to be solved is the time-dependent Schrödinger equation dating back to 1926:

$$i\hbar \frac{\partial}{\partial t} |\Psi(t)\rangle = \hat{H} |\Psi(t)\rangle \quad (4.6)$$

with \hat{H} the Hamiltonian, describing all fundamental interactions of a quantum system. For a system of positive nuclei and negative electrons, this Hamiltonian contains all attractive and repulsive Coulombic interactions as well as the kinetic energy of the particles. Because \hat{H} is independent of time, one can find a series of stationary solutions to the Schrödinger equation, known as the time-independent Schrödinger equation and represented by:

$$\hat{H} |\psi_n\rangle = E_n |\psi_n\rangle \quad (4.7)$$

By solving this equation, one obtains a series of stationary Eigenfunctions, with corresponding Eigenvalues, representing the energies of the system E_n .

An important approximation that has to be made in order to solve these equations is the Born-Oppenheimer (BO) approximation. One can formally divide the Schrödinger equation in a part depending on the nuclear coordinates and a part depending on the electronic coordinates. If one performs this separation, a cross-term arises coupling the motion of the nuclei to that of the electrons. The BO approximation now states that owing to the difference in time scale of the motions of the electrons and nuclei one can neglect this term and separate the equation in two independent equations, one for the nuclei, and one for the electrons. Solving the many-body problem now boils down

to solving the electronic Schrödinger equation for different sets of nuclear configurations.

Although this approximation greatly reduces the problem, even within the BO approximation only a limited set of systems can be solved analytically. For complex many-body systems, more approximations have to be introduced, and the development of these is at the heart of quantum chemistry.

The methods can be divided in two main classes, wavefunction based methods and density based methods. The basis of the former one is the Hartree-Fock (HF) method. Within this method, the wavefunction is approximated by a single Slater determinant of single particle wavefunctions. Using this solution as an Ansatz, many post-HF methods have been developed to deal more exactly with electronic correlation and provide a better description of the molecules. On the other hand, Density Functional based methods focus on the electron density rather than on the many-particle wavefunction as will be introduced in the next section.

4.2.2 Density Functional Theory

Density Functional theory (DFT) is an alternative and formally exact Ansatz in quantum mechanics where not the wavefunction is the central quantity, but rather the electron density $\rho(\mathbf{r})$. We now don't have to deal with a complicated wavefunction and the associated coupled differential Schrödinger equations to solve. Hohenberg and Kohn proved that there is a relationship between the electron density, the external potential and the ground state energy of an electronic system. They prove that this ground state energy is an unique functional of $\rho(\mathbf{r})$. [163] Moreover, they show that by minimizing this functional with respect to $\rho(\mathbf{r})$, given an external potential, the ground state energy of the system is obtained. They summarize these findings in the by now famous Hohenberg-Kohn theorems:

- **Theorem 1** For any system interacting in an external potential $V_{\text{ext}}(\mathbf{r})$, this potential is determined uniquely by the ground state particle density $\rho(\mathbf{r})$.
- **Theorem 2** An universal functional $E[\rho(\mathbf{r})]$ can be found for any $V_{\text{ext}}(\mathbf{r})$. The exact ground state energy of the system is now the minimum of this functional with the corresponding ground state density $\rho_0(\mathbf{r})$

The energy functional contains purely electronic terms and external contributions and is by its nature exact for a system of N electrons. Unfortunately, an exact expression of the functional has not yet been found and also here we

need to make approximations to make the theory workable. The most used scheme is the iterative method by Kohn and Sham who circumvent the problem of not knowing the kinetic energy functional (finding a good functional has proven to be notoriously difficult in orbital-free DFT [164]) by adopting a fictitious non-interacting reference system without electron-electron repulsion terms and for which the $\rho_0(\mathbf{r})$ equals the density of the interacting system. They reintroduced orbitals, now called Kohn-Sham (KS) orbitals, to rewrite the energy functional. [165] These KS orbitals are subjected to the orthogonalization conditions of the set of single-electron wavefunctions of the fictitious system they introduced. Using this construction, a Kohn-Sham Hamiltonian is constructed with corresponding Eigenvalue equation which can be solved iteratively. In their formalism, there remains however one term which cannot be solved exactly, being the exchange-correlation energy. The development of expressions for this functional is a study on its own and still occupies many researchers across the world. Numerous benchmark studies have been performed and uncountable reviews have been written. [166–168]

The approaches to define this functional have made an enormous progress through the past decades. The increasing complexity (and mostly accuracy) is represented in Jacob's ladder. [169] One of the best known functionals is developed by Becke (exchange part) and Lee-Yang-Parr (other correlation) and is called the B3LYP functional. Part of the success of this hybrid functional is the introduction of a small amount of HF exchange, which is formally exact.

Although reintroducing orbitals may sound quite contradictory, the expressions still are computationally less demanding than corresponding post-HF methods, allowing the study of much larger systems and is why DFT still enjoys a widespread popularity. A physical interpretation of KS-orbitals, albeit often used in literature, has faced a longstanding controversy. [170–177] Although the KS-orbitals are by definition fictitious, in practice it is found that they resemble the Hartree-Fock orbitals quite well and allow for a qualitative interpretation of e.g. HOMO-LUMO orbitals, Ionization Potentials,... For this reason, this qualitative interpretation will be used within this work.

4.2.3 Time-Dependent DFT

DFT is a ground state theory and as a consequence cannot be used for calculating the energy of an excited state. Runge and Gross however proposed a theory that can be seen as the extension of Hohenberg-Kohn to excited states, providing the theoretical basis for time-dependent density functional theory (TD-DFT), for which an iterative scheme similar to the Kohn-Sham method can be derived. [178] The method that is implemented in most quan-

tum chemical codes is based on the formulation of Casida using a linear response formulation.

From solving the Casida equations, we obtain the different excitation energies with corresponding oscillator strengths. The latter one represent a measure for the strength of a certain transition, being between almost 0 for a quantum-mechanically forbidden transition and 1 for a fully allowed transition. The oscillator strength is related to the dipole strength of a certain transition and the molar absorption coefficient. The latter value allows a direct comparison with experiment. The computed oscillator strength f is coupled to the experimental molar absorptivity ϵ via:

$$\begin{aligned} f_{i,max} &\sim \tilde{\nu} \cdot D_{i,max} \\ D_{i,max} &\sim \epsilon_i^{max} \cdot \frac{1}{\tilde{\nu}} \end{aligned} \quad (4.8)$$

These equations show that the dimensionless oscillator strength at the maximum of the absorption ($f_{i,max}$) is proportional at a certain energy to the frequency ($\tilde{\nu}$) and the dipole strength D , which in turn can be linked to the molar absorptivity ϵ . In this thesis, we will consistently use these equations in order to compare directly calculated and experimental intensities.

In order to make a visible interpretation possible, the transitions are typically broadened using a Gaussian or pseudo-Voigt type distribution. In this work we use a Gaussian distribution (Eq. 5.1), with a standard deviation of $\sigma=0.4$ eV for comparison with the experimental spectra:

$$f(\nu) = f^{max} \exp \left(- \left(\frac{\nu - \tilde{\nu}}{\sigma} \right)^2 \right) \quad (4.9)$$

TDDFT allows to calculate excited states for systems of relatively large size at a feasible computational cost, which is why the theory has known such popularity. [179] TDDFT is particularly effective when studying low-lying valence excited states of molecular systems [180] Seminal work of Barone and co-workers has revealed that TD-DFT is able to provide accurate one-photon excitation and emission properties of organic molecular systems, even including vibrational coupling. [181] It has been reported that the main line shape of the electronic spectra is reasonably reproduced by the majority of modern DFT functionals, whereas the main difference between theory and experiment originates from the choice of the selected DFT functional. [182, 183] Moreover, effects of the molecular environment and dynamic effects of the structure are essential when comparison with experiment is foreseen. [184]

The dynamic effects are due to the inherent flexibility and vibrational motions of the molecule under investigation. It is now accepted that averaging over different configurations - generated during a molecular dynamics (MD) simulation - leads to reliable dynamic estimations of transition properties in good agreement with experimental data. This dynamic approach has been applied to successfully characterize halochromic dyes [185] and carbonaceous compounds present as reaction intermediates in a zeolite-catalyzed process [186] and given this success, dynamic averages will also be presented in this work. The dynamic simulations will provide insight in the key geometrical characteristics that are responsible for the changes in transition positions and intensities.

Software For all static calculations, the Gaussian09 software package was used. [187] The specific levels of theory are provided in the results chapters. Periodic calculations were performed by co-workers (Danny E.P. Vanpoucke and Arthur De Vos) within the VASP package. [188]

4.2.4 Dynamic methodology

It should be noted that the statical calculation of materials properties in their optimum geometry at 0K is impossible to verify experimentally. Since experiments are performed at a finite temperature, the molecule will be able to move around in its potential well and adopt different molecular conformations. Molecular dynamics (MD) is one of the techniques allowing to study the dynamical behaviour of a molecular system. The idea is rooted in classical physics, using Newton's equations of motion to describe the motion of the nuclei:

$$M_i \ddot{\mathbf{R}}_i = \mathbf{F}_i = -\nabla_i V \quad (4.10)$$

with M_i the mass of a nucleus i and \mathbf{R}_i its coordinate vector.

There exist many MD approaches that differ in their description of the potential energy V and hence forces \mathbf{F} felt by the nuclei. The simplest method is to represent all atoms by point charges that are connected with springs. In this Molecular Mechanics approach the quantum nature of the electron clouds is however neglected and extensive parametrisation is needed to obtain reasonable descriptions of a system. Another method, the one used in this work, constructs the PES via DFT calculations. By using equation 4.10, the program evaluates the energies and forces on all the atoms at each consecutive point in time and calculates the acceleration, velocity and a new position for every

atom. In this scheme, the electronic calculation is decoupled from the nuclear motion and hence is referred to as Born-Oppenheimer MD (BOMD).

From statistical physics we learn that by solving the equations of motion presented before results in sampling of the micro canonical ensemble. In this ensemble, the number of particles N , the volume V and the total energy E are conserved, which is known as the NVE ensemble. From an experimental point of view the energy is not easy to keep constant. However e.g. the temperature and the volume can be kept constant, and this NVT ensemble is more convenient when experiment and theory are compared. Several thermostats are available in literature in order to sample the NVT ensemble and in this work we use the Constant Velocity Rescaling algorithm (CSVR) [189] and a Nosé-Hoover thermostat. [190–192]

With increasing complexity, the computational time needed for an MD simulation can also increase rapidly. However the modelling of a complex environment, e.g. a polar solvent, is much better sampled and understood when explicit interactions are modelled since a much larger part of the phase space is explored. Thanks to the increasing computational power and the methodological improvements made, MD is nowadays starting to become more omnipresent in computational research. For more information on advanced dynamical methods, we recommend the reader to the excellent book by Frenkel and Smit. [193]

Software For Molecular Dynamics simulations, we used the CP2K software package. [194]

Averaging of excitation wavelengths

Also for the calculation of excited states, MD can improve a lot upon the static values at equilibrium geometry. The experimental absorption spectrum is measured at a finite temperature, hence, the molecule will change to different conformations and occupy the whole phase space around the potential well minimum. By performing MD simulations, we can sample the ground state PES as introduced in the previous section. A methodology proposed by Barone et al. [184] then puts forward the idea of calculating the excitation wavelengths of the different geometries obtained in the MD sampling and consequently averaging them out for a defined period of time. This methodology is schematically shown in figure 4.5.

It is now accepted that averaging over different configurations generated during a MD simulation leads to reliable dynamic estimations of transition prop-

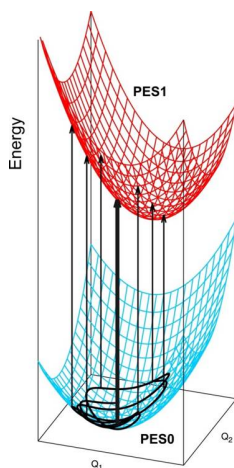


Figure 4.5: Schematic representation of the dynamic methodology to improve upon the static the TDDFT results.

erties in good agreement with experimental data. The dynamic simulations will provide insight in the key geometrical characteristics that are responsible for the changes in transition positions and intensities. [181–184, 186, 195]

Choice of model system

Throughout this thesis, a bottom-up approach was followed to gain stepwise information on the electronic structure and behaviour of the frameworks. Since current computational methodology to study excited states in periodic models is only emerging, good model systems are definitely needed. As a starting point, the smallest constituents (i.e. linkers and nodes) are treated separately and studied via ground state DFT and TDDFT calculations in the different chapters. A good description of these building blocks in terms of electronic and vibrational structure is of paramount importance to understand the full framework since, as we will show, their contributions to the electronic structure can be treated largely additively. Next, advanced cluster models comprising an inorganic node and several linkers are built. These systems are at the limit of computational feasibility for TDDFT in the implementation we used but allow for the study of their excited states. Finally, the full periodic models were studied using ground state DFT calculations. Here, the excitations observed in the cluster models can be qualitatively linked to the observations made in the periodic data.

A full detailed description of the models is given in the methodology section of each results chapter.

Part II

Understanding intrinsic light absorption

5

Intrinsic light-absorption in MOFs

Within this thesis, the interaction of light with the stable UiO-66 MOF will be investigated. In order to achieve a full understanding of the light-absorption process, a combined experimental and computational approach will be followed. This understanding is needed to engineer in a careful and deliberate way the electronic structure of UiO-66.

This chapter takes a closer look at how MOF materials with a 0D topology, of which UiO-66 is a prototypical example, interact with light. Understanding the electronic structure of the materials and their constituents is of paramount importance to engineer their light responsive properties. Within this chapter, a detailed study of the influence of several organic functional groups allowed to identify promising candidates for the visible light responsiveness of UiO-66. Moreover, thanks to the use of cluster models and periodic calculations, we obtained insight in the electronic characteristics of the material, allowing us to make a detailed scheme on how to improve this property for the UiO.

Directly following this chapter, we provide a detailed study of the importance of dynamical effects on the light-responsiveness of UiO-66. The dynamics of a molecule at finite temperature can severely influence the absorption properties. A link between the vibrational and electronic spectra of several linkers important in UiO synthesis is discussed, showing that a restriction of some vibrational modes due to inclusion in the framework results in differences in absorption.

5.1 Introduction

As introduced in chapter 3, most MOFs need to be specifically tuned to be viable for photocatalytic applications. The electronic structure of the materials studied in this work show a complex quasi-localised band structure, offering interesting properties of their electronic structure by adjusting the constituting parts. However, in the pristine material, large band gaps and bad orbital overlaps are impeding efficient photocatalytic activity. In order to improve this, one needs to first understand the influence of the different modifications that can be made to the frameworks. In this chapter, we focus on modifications made to the linkers and their influence on the intrinsic light-absorption properties of the materials. The aim of the first section is to provide insight in the optical characteristics of substituted UiO-66-X frameworks using advanced *ab initio* methods, in direct comparison to experimental measurements. Since we only concern the absorption properties of the framework as such, without e.g. including adsorbed guest molecules, we refer to ‘intrinsic’ light absorption properties in this work.

The modular nature of MOFs makes it possible to design the materials at a molecular level and tune their properties for a specific application. We also can modify the different constituents separately, since they contribute additively to the materials as corroborated throughout this work. The modification of the linkers will be a first step toward the engineering of the electronic structure. In order to provide a detailed description of how linker functionalisation changes the electronic structure of UiO-66, a bottom-up approach was followed. Within this methodology, we start from the smallest entities, namely the pure linkers, whereby we compare our computational results directly to the measured UV/Vis spectra. Next, we construct extended cluster models of one inorganic node with two linkers attached and 10 formic acid capping groups. Finally, the full periodic material will be studied.

We use the aforementioned TDDFT methodology, allowing to calculate excited states for systems of relatively large size at a feasible computational cost, which is why the theory has known such popularity. [179] TDDFT is particularly effective when studying low-lying valence excited states of molecular systems [180] Seminal work of Barone and co-workers has revealed that TDDFT is able to provide accurate one-photon excitation and emission properties of organic molecular systems, even including vibrational coupling. [181] It has been reported that the main line shape of the electronic spectra is reasonably reproduced by the majority of modern DFT functionals, whereas the main difference between theory and experiment originates from the choice of the selected DFT functional. [182, 183] Moreover, effects of the molecular

environment and dynamic effects of the structure are essential when comparison with experiment is foreseen. [184] The dynamic effects are due to the inherent flexibility and vibrational motions of the molecule under investigation. It is now accepted that averaging over different configurations - generated during a molecular dynamics (MD) simulation - leads to reliable dynamic estimations of transition properties in good agreement with experimental data. Some of the co-authors of the work in this chapter previously applied a dynamic approach to successfully characterize halochromic dyes [185] and carbonaceous compounds present as reaction intermediates in a zeolite-catalyzed process [186] and given this success, dynamic averages will also be presented here and in the next chapter. The dynamic simulations will provide insight in the key geometrical characteristics that are responsible for the changes in transition positions and intensities.

Moreover, a deeper understanding of the band gap modulation upon linker functionalization will be obtained, comparing the experimental UV/Vis spectra directly with the theoretical calculations on the fully periodic frameworks for a range of functionalizations. Semilocal DFT functionals are known to underestimate the band gap, we performed calculations with the hybrid HSE functional [196–199]. This functional has already been used to calculate the band gap of UiO-66-NH₂ and UiO-66-NO₂ frameworks and showed excellent agreement with the experimental values.

The results of this chapter are published in:

Understanding Intrinsic Light Absorption Properties of UiO-66 Frameworks: A Combined Theoretical and Experimental Study

K. Hendrickx, D.E.P. Vanpoucke, K. Leus, K. Lejaeghere, A. Van Yperen-De Deyne, V. Van Speybroeck, P. Van Der Voort and K. Hemelsoet, *Inorg. Chem.*, **2015**, 54, 10701-10710

Contribution: I performed the linker and cluster calculations and wrote the manuscript

5.2 Materials and methods

In this section, the detailed experimental and computational procedures used in this chapter will be given. For a more detailed introduction of some of the major techniques used, the reader is referred to chapter 4 of the introductory chapters.

5.2.1 Experimental Details

Linker synthesis

All linkers, except SH functionalized BDC, are commercially available (Sigma Aldrich, TCI) and were used without further purification. The 2,5-dimercapto terephthalic acid (BDC-2,5SH), was synthesized according to a three step procedure described by Otto et al. [200] Only during the final step of the synthesis, a slightly modified procedure was utilized. In the first step diethyl 2,5-dihydroxy terephthalate (5g) was mixed with 1,4-diazabicyclo[2.2.2]octane (9g) in 50 mL dimethylacetamide (DMA). This mixture was placed in an ice bath while a mixture of dimethylthiocarbamoylchloride (9.5 g) in 25mL DMA was added dropwise under argon atmosphere. Hereafter, the resulting mixture was stirred for 16 hours at room temperature, with the formation of a white opaque solid after already 30 minutes of reaction. Afterwards, the solid was collected by filtration and washed thoroughly with distilled water (250 mL). In a second step the product was placed in a vessel, heated to 215°C and held at that temperature for 20 minutes. To purify the product obtained from the second step, a recrystallization was performed with 2,2,4-trimethylpentane/toluene (60/40). The obtained crystals were filtered off and washed with isobutene. The 2,5-bis(dimethylthiocarbamoylsulfanyl)terephthalic acid diethyl, obtained after step 2, was refluxed under an argon atmosphere in a degassed 1.3M KOH solution for 3 hours. Afterwards, the solution was cooled in ice and was acidified using concentrated HCl, which was followed by the formation of a yellow precipitate. Hereafter an extraction with ethylacetate was performed to remove residual salts and to purify the obtained 2,5-dimercapto terephthalic acid. In Fig. 5.1 the ^1H NMR spectrum of the 2,5-dimercapto terephthalic acid is presented after synthesis. As can be seen clearly from this figure, one singlet is observed at 8.03 ppm for the synthesized SH material, which can be assigned to the equivalent aromatic protons.

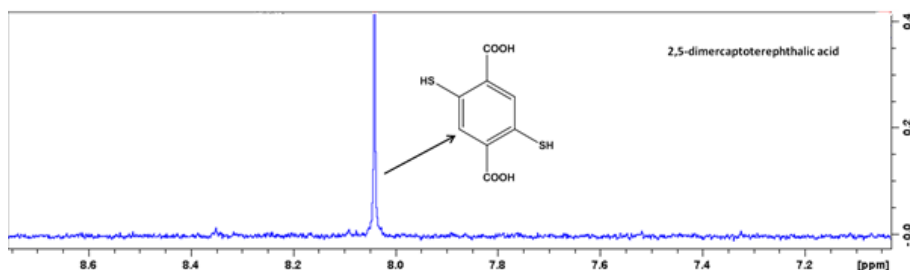


Figure 5.1: ^1H NMR spectrum of the synthesized $\text{H}_2\text{BDC-2,5SH}$ linker

MOF synthesis

UiO-66-X was synthesized following the general procedure described in section 2.4.2. For all the materials, the XRD diffractogram is identical, proving that they are isostructural, can be found in figure 5.2.

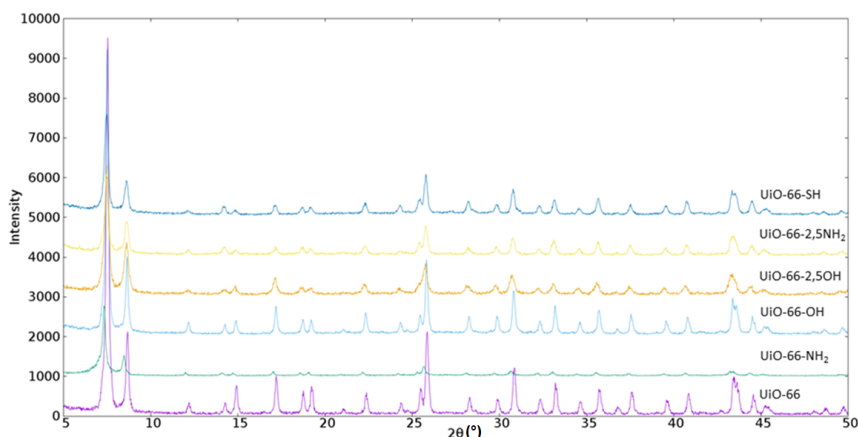


Figure 5.2: XRD diffractogram of all linker functionalized materials

Characterization

MOF materials were characterized by XRD and N₂-absorption measurements using the equipment introduced in chapter 4

UV/Vis absorption measurements were carried out in liquid and solid state conditions according to the methods described in the same chapter. The spectrum of BDC-2,5SH showed the appearance of an extra band when dissolved in DMF, probably forming an adduct with the solvent. For a better comparison, the spectrum of this product was measured in methanol, showing only one clearly defined peak. Band gaps were extracted by extrapolating the cut-off wavelength to the x-intercept, similar to Musho et al. [156]

5.2.2 Computational methodology

Geometry generation and excited-state calculations on linker and cluster models

Static calculations on the linkers and clusters were done in Gaussian09 (G09) [187] using DFT. Gas phase linker models as shown in figure 5.3 are considered. We performed an initial assessment study of the influence of basis set and DFT functional on the calculated excitation wavelengths of a typical linker. The complete set is provided in table 5.1. Our results point towards the hybrid B3LYP [201,202] functional in combination with a Pople 6-311+G(d,p) basis set [203] as appropriate for the study at hand. This level of theory was selected for both optimization of the structures and the TDDFT calculations. This method was previously shown to provide reliable absorption data of organic structures of similar size. [204]

Solvent effects (N,N-Dimethylformamide, DMF) were included during TDDFT calculations using a bulk solvent model, in particular a Polarizable Continuum Model ($\epsilon=37.219$) within the integral equation formalism [205], as is implemented in the G09 package.

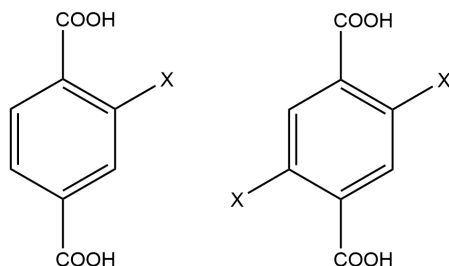


Figure 5.3: Two types of linkers considered in this chapter.
X=H,OH,SH, NH₂

The cluster models consist of 1 metal node ($\text{Zr}_6\text{O}_4(\text{OH})_4$) and 2 linkers. The 10 remaining coordination sites are terminated by formic acid (HCOO^-) anions. The resulting stoichiometry of the cluster model is given by:



Since Zr atoms are not included in the Pople basis set, the cluster calculations were performed using a triple- ζ Def2TZVP basis set [206], and the same DFT

	B3LYP (nm)	CAM-B3LYP (nm)
Experiment	371	
cc-pVDZ	343.63	316.04
cc-pVTZ	348.49	320.84
cc-pVQZ	350.13	322.21
cc-pV5Z	n.a.	323.12
aug-cc-pVDZ	352.03	323.32
aug-cc-pVTZ	351.94	323.51
aug-cc-pVQZ	n.a.	323.59
6-31G	364.61	330.7
6-31G(d)	343.12	331.07
6-31G(d,p)	361.34	331.1
6-31+G	368.79	334.15
6-31+G(d)	366.52	335.57
6-31+G(d,p)	366.39	335.48
6-311G	366.05	332.81
6-311G(d,p)	365.36	335.71
6-311+G	369.73	335.18
6-311+G(d,p)	369.27	338.36

Table 5.1: First vertical excitation energy testing various basis sets and two functionals for H₂BDC-2,5OH with PCM solvent model

functional. The clusters are optimized, retaining the metal node geometry as in the periodic structure, only optimizing the linkers position (resulting in a slight torsion, depending on the functional group).

The optimized ground state structures were employed to derive absorption data of the involved linkers and cluster models of the UiO-66 MOFs. Vertical transitions can be considered as an initial approximation for experimental UV/Vis spectra and can provide clear insight in relative trends when investigating the influence of linker substitution. [185] The computationally obtained transitions were broadened using a Gaussian distribution (Eq. 5.1),

with a standard deviation of $\sigma=0.4$ eV for comparison with the experimental spectra:

$$f(\nu) = f^{max} \exp \left(- \left(\frac{\nu - \tilde{\nu}}{\sigma} \right)^2 \right) \quad (5.1)$$

The percentages of orbital contributions were calculated using a Mulliken type approach, using the orbital coefficients and the overlap matrix as implemented in the Chemissian program.

Charge calculations on the linker systems were done using the Horton program. [207] In this program, an iterative Hirshfeld scheme [208] is implemented, applying the classical Hirshfeld scheme in a self-consistent way. This method has been assessed extensively in literature for different systems to test for basis set and level of theory sensibility, dependence on molecular geometry etc. [209–211] This scheme has been successfully implemented for periodic systems [212, 213] as a module in the HIVE v 3.x package, allowing comparison with the simulations on the fully periodic frameworks. [214]

Band structure calculations on the fully periodic models

All periodic calculations were performed within the VASP package [188, 215, 216], using the PBE functional [217]. The plane wave basis set had a kinetic energy cut-off of 500 eV, and a Γ -centred $3 \times 3 \times 3$ k-point set was used to sample the first Brillouin zone. All structures were relaxed using a conjugate gradient method with the energy convergence criterion set to 10^{-7} eV. As a result, the maximum force on an atom at the end of a relaxation is $< 1 \text{ meV}/\text{\AA}$. During the structure optimization we constrained the cell volume to that of the pure UiO-66 MOF, taken from Valenzano and co-workers [121]. Only the cell shape and internal positions were optimized, to reduce computational cost, and assuming the band structure does not change significantly on a qualitative scale with volume optimization. The resulting structures retained their fcc nature with only small distortions of the lattice parameters ($< 0.1 \text{\AA}$) and lattice angles ($< 0.5^\circ$). The lattice parameters can be found in table 5.2.

All calculations were performed using the primitive fcc unit cell containing 6 Zr atoms (i.e. 1 Zr-O cluster) and 6 linkers. As such, the cell of the unfunctionalized UiO-66 material contained 114 atoms, which increased up to 126 depending on the functionalization. The PBE density of states (DOS) was obtained using a $5 \times 5 \times 5$ k-point grid, and a PBE band structure was obtained along the high-symmetry lines Γ -X, Γ -L, and Γ -K. Since PBE is known to underestimate the band gap, we performed the computationally very expensive

	a (Å)	b(Å)	c(Å)	α (°)	β (°)	γ (°)
UiO-66	20.9784	20.9784	20.9784	60	60	60
UiO-66-OH	20.96793	20.96793	20.96793	60.0484	59.9484	60.0022
UiO-66-2,5OH	20.95334	20.95334	20.95334	60.1160	58.8911	59.9976
UiO-66-SH	20.92152	20.92152	20.92152	60.2332	59.9756	60.092
UiO-66-2,5SH	20.91721	20.91721	20.91721	60.3375	59.7742	59.8274

Table 5.2: Lattice parameters for the primitive cell (**fcc**) obtained after relaxation under fixed volume constraint. (UiO-66 = 2308.112907 Å³) The parameters for the primitive cell are published in the CCDC database (structures 1412526-1412530).

HSE06 [196–199] calculations. The HSE06 DOS was obtained by performing a single static run, starting from the PBE electron density. To make the calculations computationally feasible, the k-point set used for the HF exact exchange part of the functional was reduced to the Γ -point only and the remaining DFT contributions were calculated on a 3x3x3 k-point grid.

5.3 Results and Discussion

5.3.1 Experimental Results

The main linkers studied in this work are schematically represented in Scheme 5.3. For the NH₂ and OH functionalization, both mono- and difunctionalized linkers are commercially available while the SH linker was synthesized in our lab following the procedure as described above. Taking the BDC as a reference and placing one carboxylic group at position 1, the functionalizations are at position 2, or 2 and 5. Henceforth, we will label the mono-functionalized BDC as BDC-X and di-functionalized BDC as BDC-2,5X (X=NH₂, OH, SH). The investigated functional groups all exhibit electron donating character.

Fig. 5.4 A shows the experimental absorption spectra of the solvated (DMF) linkers BDC, BDC-NH₂, BDC-2,5NH₂, BDC-OH, BDC-2,5OH, BDC-2,5SH. The pristine BDC (X=H) does not absorb in the visible range of the spectrum, whilst clear absorption bands do appear for the BDC-X linkers. The shift of the BDC-OH linker remains modest (± 32 nm), but, for the other linkers, a shift of about 70–80 nm is observed, and BDC-2,5NH₂ has a band shifted for 150 nm compared to the parent BDC linker. The BDC-SH material was not studied experimentally, but is included in the theoretical calculations for comparison with the other mono-functionalized variants. Fig. 5.4

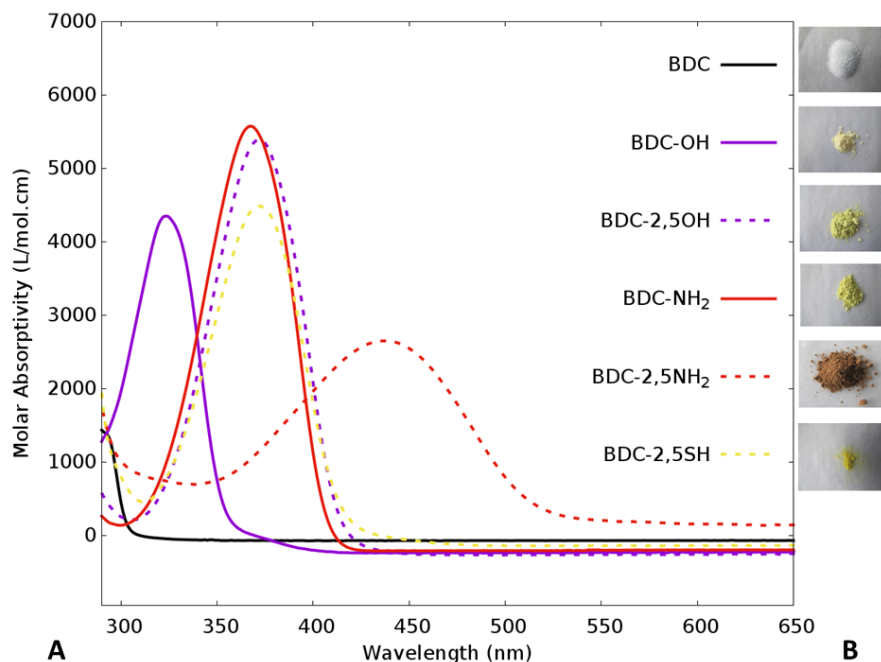


Figure 5.4: A: experimental linker spectra and B: photographs of pure linker

B clearly shows an intensifying color upon changing the functionalization, ranging from white over light yellow to dark yellow. The larger shift of the disubstituted linkers in comparison to the mono-substituted variants is similar for all functional groups (about 50-70 nm). The interesting possibilities of these doubly functionalized linkers are unmistakable and have already been exploited by e.g. Sun et al. to make a mixed UiO-66-NH₂/UiO-66-2,5NH₂ MOF. [152]

5.3.2 Theoretical Absorption Spectra and Charge Analysis

To obtain further insight into the molecular origin of the absorption spectra, a variety of theoretical calculations were performed. In Fig. 5.5, the static TDDFT results are compared for every separate linker with the experimental linker and MOF spectrum. Herein, only the transitions to the first excited state are included, since the higher excitations are in the UV region. Fig. 5.5 demonstrates the ability of static TDDFT calculations to predict the experimental absorption band of the isolated linkers with high accuracy. Both the

excitation wavelength and oscillator strength are computed with good accuracy when compared with experiment.

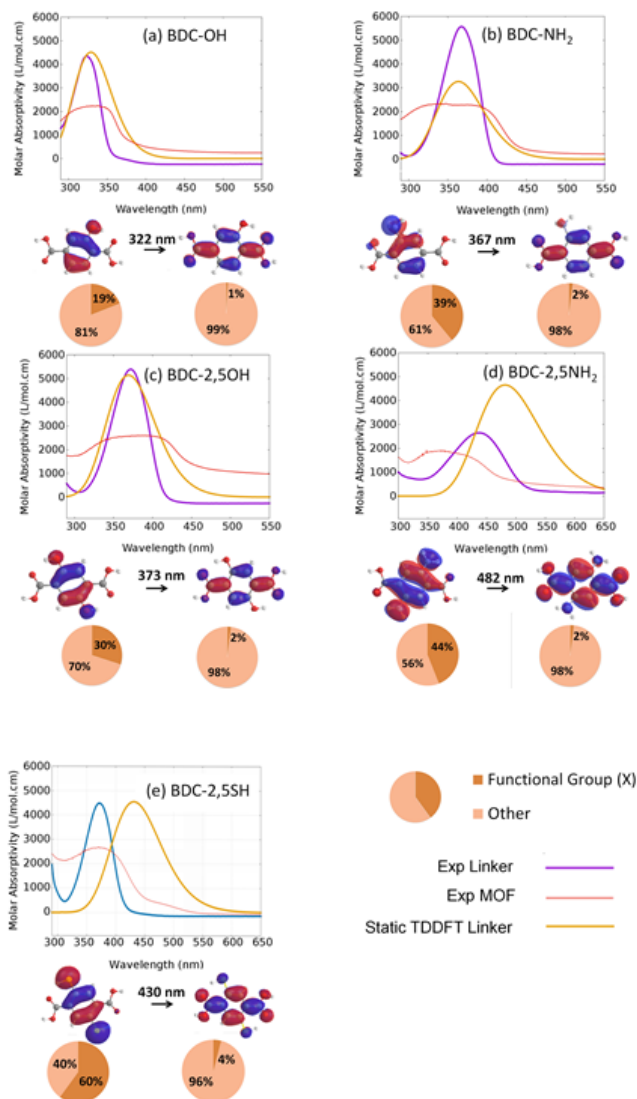


Figure 5.5: Plot of the experimental UV/Vis spectrum (blue line) and the TDDFT calculations on the isolated linkers (orange line). The arbitrarily scaled experimental DRS MOF spectra are added for comparison (red line). The orbitals of the ground state and the excited state (HOMO and LUMO) are depicted and the contributions of the functional group vs. the ring system is provided in the pie plots. For the 2,5X structures (b,d and e), the cumulative effect of the two functional groups is reported.

X	GS charge	ES charge	Δ
H ₂ BDC-X			
NH ₂	-0.14(3)	0.15(9)	0.30
OH	-0.17(4)	-0.02(9)	0.14
SH	0.03(8)	0.96(9)	0.93
H ₂ BDC-2,5X			
NH ₂	-0.14(0)	0.03(3)	0.17
OH	-0.18(7)	-0.06(9)	0.12
SH	0.033(2)	0.26(1)	0.23

Table 5.3: Iterative Hirshfeld charges of the substituents obtained for the Ground State (GS) and Excited State (ES) densities, obtained using B3LYP/6-311+G(d,p) and a PCM solvent model.

Analysis of the orbitals involved in the excitation indicates that the HOMO-LUMO excitation is the dominant contribution. The corresponding orbitals are incorporated in Fig. 5.5, showing that the contribution of the functional groups almost vanishes in the LUMO orbitals. For example, the functional group in the case of the BDC-SH linker constitutes up to 54% of the HOMO orbital, whereas this is reduced to only 2% when inspecting the LUMO. Since the first excited state is mainly composed out of this LUMO, the functional groups have almost no influence in this state.

In order to further quantify this effect, we performed Hirshfeld-charge calculations, based on the ground state and excited state electronic densities. The most important results are shown in Table 5.3. For the mono-functionalized linkers, we find a large charge shift in the ring system, with the order $\text{OH} < \text{NH}_2 < \text{SH}$. This order is consistent with the drop in electronegativity [218] ($\text{EN}(\text{O}) > \text{EN}(\text{N}) > \text{EN}(\text{S})$). The same trend is found for the doubly functionalized linker. However, since electron donating substituents have a para directing influence on the electronic structure of the aromatic system, there is a small counteracting influence, and hence the contribution per substituent is smaller.

In conclusion, the following general observations can be made based on the analysis of the theoretical calculations on the organic linker models. The different functionalities have an increasing electron donating effect on the aromatic ring, shifting the absorption maximum in the following order: $\text{H} < \text{OH} < \text{NH}_2 < \text{SH}$. Static calculations accurately predict the peak position

and intensity of the OH functionalized linkers, but for the other systems, dynamic effects are suggested to be taken into account. The TDDFT based method yields accurate results and the experimental values were reproduced well. For the NH_2 linkers, and in particular the difunctionalized variant, the calculated values overestimate the experimental absorption maxima.

5.3.3 Electronic absorption spectra of inorganic-organic cluster models

In literature, it has been suggested that the photocatalytic activity of the UiO-66 materials can be attributed to a Ligand to Metal Charge transfer (LMCT) process. In this process, light is absorbed via the (NH_2) -functionalized linker, after which an energy transfer takes place toward the inorganic nodes. In this way, the absorbed energy can be used to initiate redox reactions at these reactive sites. It has however been proven by now that this transfer is quite inefficient (see chapter 3) In order to investigate possible LMCT effects theoretically, we constructed inorganic-organic clusters based on the periodic structures. This procedure was already followed to study e.g. reactivity in the UiO-66 materials. [219]

Calculations on the full cluster model yield similar trends for the absorption wavelengths and intensities as compared to the pure linker calculations. This is no surprise as we show that the linker functionalization is the origin of the visible absorption band. The results are shown in table 5.4.

	λ (nm)	f
H	276	0.020
OH	332	0.155
2,5OH	369	0.123
NH_2	375	0.1425
2,5 NH_2	482	0.144
SH	363	0.047
2,5SH	431	0.068

Table 5.4: Wavelength (λ) and oscillator strength (f) of the first excitation in the cluster models, using B3LYP/def2TZVP

Fig. 5.6 shows the HOMO, LUMO and LUMO+1 orbitals in the case of the BDC-2,5OH linker. As was the case with the linker studies (Fig. 5.5), the HOMO-LUMO orbitals are found to play the major role in the visible light excitation, considering both the oscillator strength f and the wavelength λ .

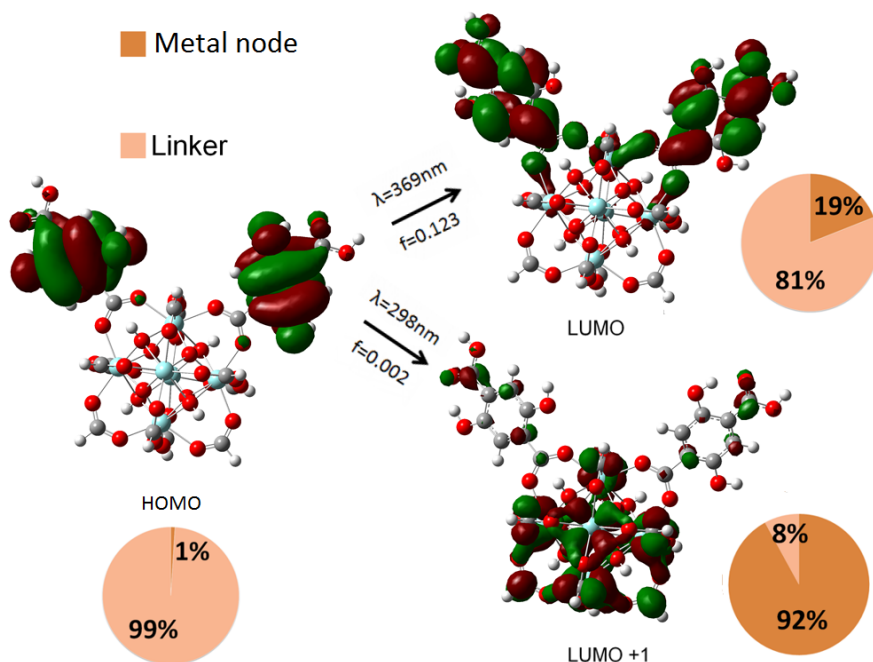


Figure 5.6: Scheme representing the first and second excitation for the cluster model with BDC-2,5OH linkers (resulting in following stoichiometry: $\text{Zr}_6\text{O}_4(\text{OH})_4(\text{HCOO})_{10}(\text{BDC-2,5OH})_2$). TDDFT calculations are performed using B3LYP/def2TZVP as level of theory.

Hence, the peak positions of these calculations yield the same trends as found with the linker calculations (cfr. table 5.4). A similar static analysis of the orbital contributions as on the bare linkers was performed as well. This shows that the HOMO orbitals are localized on the linkers and exciting the system at 369 nm causes a shift of about 19% of the orbital contributions to the inorganic cluster (see Fig. 5.6). If we look at the excitation involving the HOMO to LUMO+1 transition (at 298 nm in case of BDE-2,5OH, see (Fig. 5.5), the contribution of the linkers almost completely disappears, resulting theoretically in a large shift of orbital contribution towards the inorganic metal nodes. However, the calculated oscillator strength of this excitation is almost zero and hence as almost no contribution in the total excitation spectra. These results indicate that the LMCT only limitedly occurs in these systems upon visible light radiation. If we look e.g. at the BDC-OH linker on this cluster, the same general behaviour can be observed, but the first excitation only has an orbital shift of 10% in stead of the 20% observed in the doubly functional-

ized system.

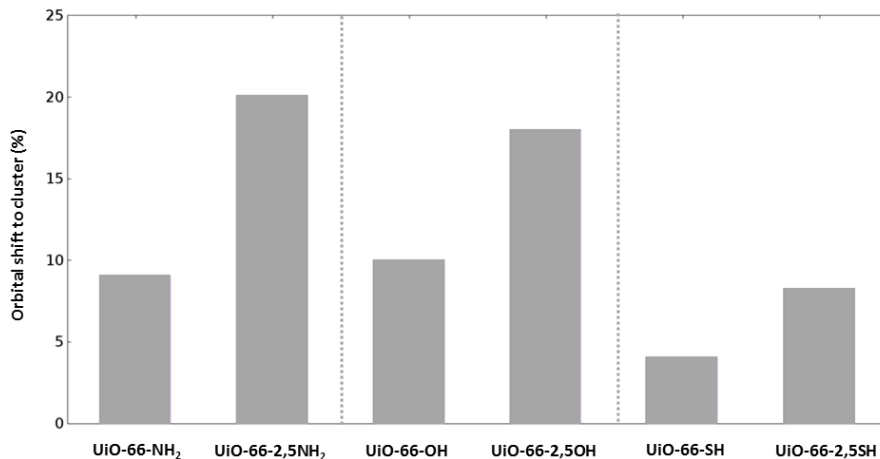


Figure 5.7: LMCT transfer in the first (HOMO to LUMO) excitation for all clusters; representing the transfer of orbital contributions from the organic linker to the inorganic metal node.

Fig. 5.7 summarizes the transfer of orbital contribution in the first (HOMO to LUMO) excitation for all inorganic-organic clusters. These data represent the LMCT transfer from the organic linker to the inorganic Zr-O node upon excitation expressed in terms of the shift in orbital contribution. As a general trend, we observe that multiple substitution has an extra electron-donating influence in these cluster models. This effect can (partially) explain the higher catalytic activity as observed by Sun et al. [152] The use of doubly functionalized linkers or a mixed-linker approach can hence be beneficial when developing a new photocatalyst.

5.3.4 Band gap alterations

Experimental determination of the band gaps can be done in several ways as explained in chapter 4. We chose to follow the simple reasoning of extrapolating the absorption edge as a good and easy approximation as shown by Musho et al. [156]

The experimental UV/Vis spectra shown in Figure 5.5 indicate that the pure linker peaks overlap with the absorption maxima of the corresponding UiO-

66-X materials. On the other hand, the spectra of the periodic materials show significant broadening. This immediately becomes clear when we compare the pure linker powders with the frameworks, as shown in figure 5.8. The color variations indicate that the electronic band structure around the band gap is significantly modified.

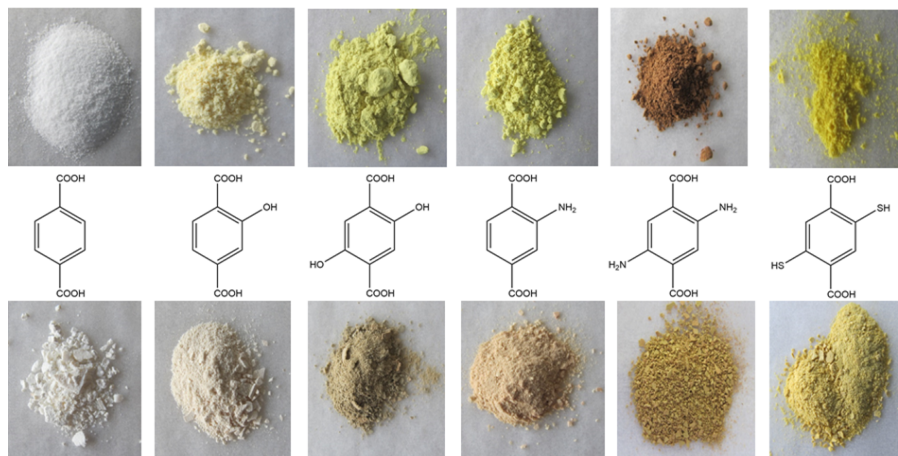


Figure 5.8: Experimental MOF powders (lower row) and the original linkers (top)

This is indeed supported by the periodic simulations of the UiO-66-X materials. In all cases, a direct band gap was found. Comparison of the PBE and HSE06 DOS shows them to present the same qualitative picture, while quantitatively the main difference is the larger band gap for the HSE06 DOS. The calculated band gaps for the different functionalized UiO-66 MOFs are compared to our experimentally determined values in Figure 5.9. All of the calculated data are reported in the next section, table 5.5. It is clear that although the PBE values significantly underestimate the experimental band gaps, they do represent the experimentally observed trends. The HSE06 band gaps, on the other hand, also show good quantitative agreement with experiment. These accurate data indicate that linker functionalization can lead to band gaps ranging between 4.0 and 2.2 eV and that engineering of the band gap of the UiO-66 materials is possible.

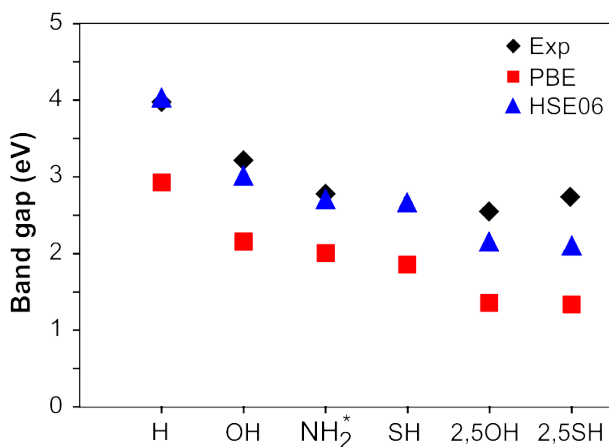


Figure 5.9: Band gaps for various functionalized UiO-66 materials.

5.3.5 Geometry of linkers in Gas phase vs framework

Organic linkers embedded in MOFs, by their very nature, are expected to be quite comparable to their free molecular counterparts. Although the lattice introduces some constraints on their geometry, their electronic structure is expected to be more or less unaltered apart from possible charge transfer pathways that become available upon coordinating with a metal node. Comparison of the embedded linkers and the free molecular linkers indicates that the geometry of the functional groups is retained even after structure optimization in the periodic systems (see table 5.5).

Moreover, the calculated Hirshfeld-I charges show that despite the variation in type and number of functional groups, the total linker charges as well as the charges of the Zr atoms barely vary among the different functionalized UiO materials. This means that without excitation of the electronic structure, the different functionalizations of the linkers do not influence the electronic structure of the ZrO clusters. To obtain a more detailed understanding of the electronic structure of the functionalized UiO-66 materials, their densities of states (DOS) and band structures are investigated below.

5.3.6 Density of state and band structure analysis

Careful comparison of the different densities of state shows that the electronic structure of both the functionalized and unfunctionalized UiO-66 are

quite similar. However, contrary to the unfunctionalized material, UiO-66-X materials possess a filled band within the original band gap, which can be referred to as a filled gap state. This therefore corresponds to the new valence band, lowering the effective band gap substantially. In contrast, the energy difference corresponding to the band gap of the host material remains roughly constant for all functional groups (3.0 eV for PBE and 4.0 eV for HSE06, table 5.6).

Table 5.5: Comparison between linkers in the UiO-66 framework, and free molecular linkers (between brackets). The bond length, r_X , and the bond angle, α_X , of the functional group as well as the Hirshfeld-I charges of the functional group, C_X , the linker, C_l , and the Zr atoms, C_{Zr} , are presented. The UiO-66 results are obtained using the PBE functional, and under fixed-volume constraint of the unit cell (*cf.* methods section), while the molecular results are obtained using the B3LYP functional.

	$r_X(\text{\AA})$	$\alpha_X(^{\circ})$	$C_X(e)$	$C_l(e)$	$C_{Zr}(e)$
UiO-66	1.089 (1.082)	–	–	–1.558	3.060
UiO-66-OH	1.348 (1.342)	105.5 (108.1)	-0.124 (-0.174)	-1.556 (-0.978)	3.063 (–)
UiO-66-2,5OH	1.354 (1.339)	105.9 (110.3)	-0.124 (-0.187)	-1.566 (-0.999)	3.065 (–)
UiO-66-SH	1.755 (1.777)	94.8 (99.4)	0.081 (0.038)	-1.560 (-0.992)	3.063 (–)
UiO-66-2,5SH	1.759 (1.776)	96.5 (96.4)	0.083 (0.033)	-1.560 (-0.980)	3.064 (–)

	band gap (eV)		ΔE (eV)		gap state width (eV)		gap state occupation (#e)	
	PBE	HSE06	PBE	HSE06	PBE	HSE06	PBE	HSE06
UiO-66	2.92	4.03	2.92	4.03	—	—	—	—
UiO-66-OH	2.15	3.01	3.04	4.00	0.07	0.20	12	12
UiO-66-2,5OH	1.35	2.15	3.00	3.89	0.10	0.22	12	12
UiO-66-SH	1.85	2.66	3.00	4.02	0.22	0.35	12	12
UiO-66-2,5SH	1.33	2.10	3.01	4.00	0.23 & 0.22	0.36 & 0.35	12 \times 2	12 \times 2

Table 5.6: Comparison of PBE and HSE06 values for the band gap, the energy difference related to the host material (ΔE), the width of the gap state and its occupation for the different UiO-66-X frameworks.

In case of the doubly functionalized UiO-66-2,5SH material, a second band is also identified just above the valence band of the host material (cf. table 5.6). This is not the case for the PBE DOS of UiO-66-2,5OH, although the HSE06 DOS indicates that this band might overlap with the top of the valence band. We will however not discuss this band further, as it does not influence the spectroscopic properties of UiO-66-X.

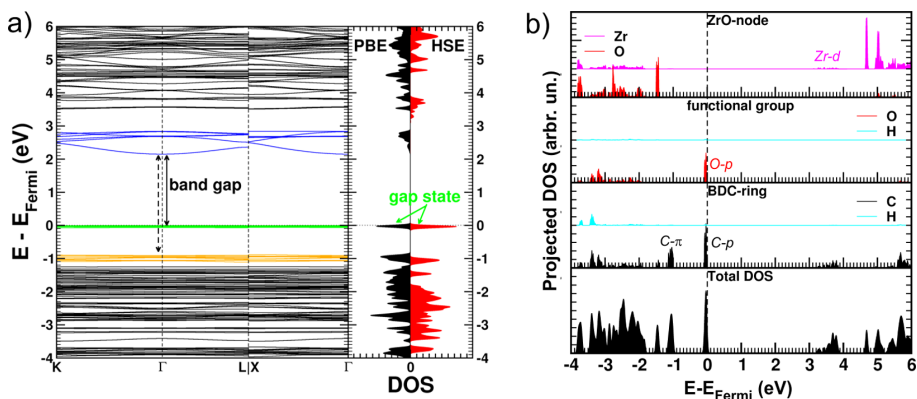


Figure 5.10: DOS of UiO-66-2,5OH and projected DOS

Projected densities of state (PDOS) provide more insight in the origin of distinct bands, by projecting the corresponding orbitals on the different atoms. This is illustrated in Fig.5.10b for the UiO-66-OH material, but similar conclusions are valid for the other functionalized UiO-66 materials. The electron densities for these bands are plotted in figure 5.11.

We find that the gap state has a recognizable fingerprint for each UiO-66-X: it is mainly of a p character associated with the C atoms of the ring and the S/O atom of the functional group(s). This indicates that the functional group forms a bond with the π -orbitals of the linker ring. Importantly, the occupation remains the same: 2 electrons per functional group in the system, indicative of the bond between the functional group and the ring. The width of the functionalization-induced band depends on the employed functional and on the type of the functional group, but not on the number of functional groups on the linker (cf. 5.6). The π -orbitals of the linker ring themselves give rise to the top levels of the valence band. In contrast, the conduction band is rather insensitive to the functional group: the conduction band character mainly corresponds to that of the Zr d -electrons or to delocalized orbitals over the entire linkers.

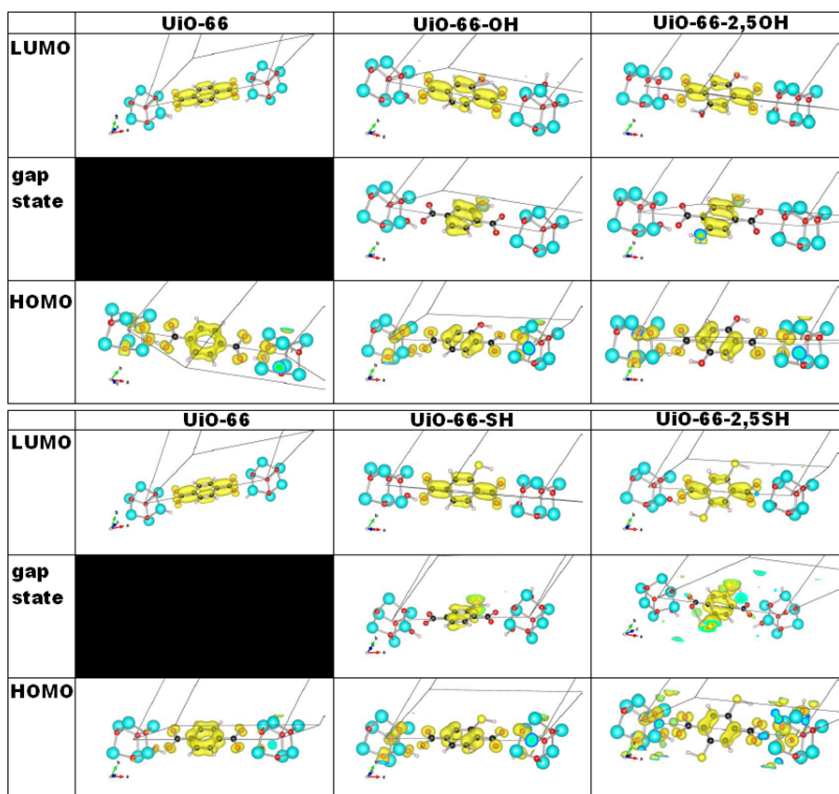


Figure 5.11: Electron density of the states associated with the HOMO, LUMO and gap state(s) for different functionalized UiO-66. Electron densities are obtained using the PBE functional in periodic calculations. For clarity only one linker and two Zr-clusters are shown.

We conclude that the band gap of the host material remains largely the same, but upon functionalization, the π -orbital splits into two bands. One of these bands remains in position, while the other band, which contains contributions of the functional group, moves upward, giving rise to a fully filled gap state and a reduced effective band gap. As a consequence, exciting the linker electrons from this newly split off gap state is much easier and explains the decreasing trend in the band gaps upon functionalization (see Fig.5.9).

5.4 Conclusion

This chapter provided a detailed study of the optical absorption properties of functionalized UiO-66-type MOFs. A full understanding is needed when one wants to modify the frameworks to obtain a better performance, which will be the subject of the later chapters of this thesis. We investigated UiO-66 using experimental UV/Vis measurements combined with theoretical simulations. The BDC linker unit was mono- or bifunctionalized with various electron donating substituents, i.e., OH, NH₂ and SH, and the resulting effect on the absorption properties was examined. The effect of the nanoporous framework was directly assessed via simulations on the solvated linkers, extended clusters and the fully periodic material.

Theoretical absorption spectra of the various functionalized linkers were obtained using time-dependent density functional theory (TDDFT) with the hybrid B3LYP functional. Vertical transition energies of the substituted linkers already provided a good agreement with experiment, in particular for the OH-substituted linkers. The correct trend was obtained for the mono-functionalized cases, meaning that the absorption maximum increases from OH to NH₂ to SH. Interpretation of the orbitals involved in the main transition clearly pointed towards a charge transfer from the functional group to the aromatic ring of the linker molecule.

In a next phase, inorganic-organic clusters were considered to examine the amount of charge transfer between the organic linkers and the metal nodes. Static TDDFT simulations on an extended cluster model indicated that the corresponding first excitation is found at almost the same wavelength as for the linker situation. In this transition, there is a small transfer of orbital contribution to the metal nodes, but the LUMO orbital involved in the excitation is still mainly located on the linker units. The amount of transfer is functionalization dependent and showed to be the largest (however still limited) in the case of BDC-2,5NH₂.

Fully periodic models were also employed to corroborate our findings. In addition to PBE, the hybrid HSE06 functional was used to investigate the electronic structure of the functionalized Zr(UiO-66)-type metal organic frameworks. The existence of a gap state within the band gap of the unfunctionalized UiO-66 was shown to be the reason of the observed band gap modulation. The HSE06 calculations on the fully periodic models provided band gaps in excellent agreement with the experimental values. The band gaps ranged between 4.0 and 2.2 eV, indicating that linker functionalization is indeed an excellent procedure to modify the band gap of the metal organic framework.

The simulations suggest that materials containing the same type of linkers would show similar behaviour. However, we believe that more research is warranted to investigate whether MOF materials with the same organic linkers but varying inorganic units would give similar absorption properties.

6

Vibrational fingerprint

6.1 Introduction

In the previous section, we discussed the influence of functional groups on the light-absorption properties of UiO-66 materials. Distinct influences are found from the nuclear dynamics on the calculated excitation energies. This study followed the procedure as proposed by the group of Barone et al., who demonstrated that averaging over different configurations generated during an MD simulation leads to reliable dynamic estimations of transition properties in good agreement with experimental data [220–223]. Such methodology was previously successfully applied for a large variety of systems, ranging from small gas phase molecules over solvated dyes to dyes occluded in a porous zeolitic environment [220,224–226]. In the majority of the studies, the electronic transitions are calculated using TD-DFT in its linear response formulation, since it offers a good accuracy/computational cost ratio [227,228].

The aim of this chapter is to gain a better understanding of which vibrational modes affect calculated electronic transitions in UiO-type materials. To this end, we will compare static excitation energies with dynamic averages, obtained using distorted geometries generated during MD runs. This is done for 9 UiO-type frameworks, bearing a variety of organic linkers as shown in 6.1, to study induced effects on the excitation spectra. The top figure represents BDC and BPDC (4,4'-biphenyl-dicarboxylate) linkers present in the pristine UiO-66 and UiO-67 materials and some other functionalized derivatives. These structures have previously been synthesized by various groups,

and their absorption properties and/or photocatalytic performance have been tested as described in the previous chapter. [121,149,152]. Additionally, figure 6.1 includes 2 aliphatic linker models, constituting UiO-66-oxal and UiO-66-CC. These hypothetical UiOs are included as they can provide more insight in the framework motions due to their reduced set of possible vibrations. Due to their reduced conjugation compared to the aromatic linkers, these materials are not expected to absorb in the visible range. All frameworks share the same octahedral $\text{Zr}_6\text{O}_4(\text{OH})_4$ inorganic building unit. Herein we want to explore which vibrational modes impact the observed absorption spectrum. We will employ an analysis method recently proposed in the CMM group, which is based on a comparison of the velocity power spectra (VPS) with the power spectra of the transition energies (the so-called ϵPS) [229]. By comparison with both power spectra, the vibrational fingerprint of the excitation energies can be unraveled. Here, the influence of the UiO framework will be explicitly included via MD simulations on the fully periodic structure. By comparing vibrational spectra of the pure linker versus the fully periodic UiOs, the influence of the UiO framework on the characteristic vibrational frequencies and absorption properties can be directly assessed. This is the first time the procedure based on the comparison of power spectra is used on large extended systems such as the UiO materials.

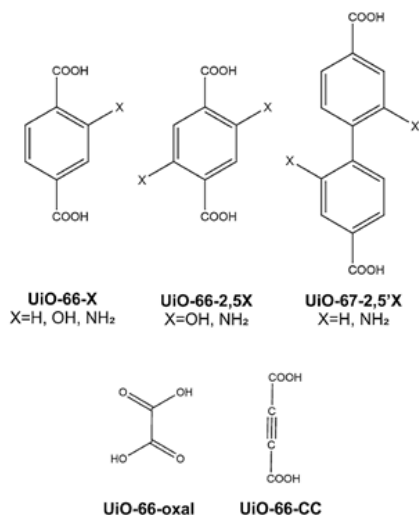


Figure 6.1: Linkers studied in this chapter

The complete understanding of the light absorption properties is important for the further development of these frameworks as photoactive materials.

Overall, elucidating the vibrational features of complex materials offers detailed molecular-scale information. It is well known that IR spectroscopy can be of great help in the characterization of MOF materials [230]. In addition to numerous experimental studies, theoretical examinations are ideally suited to provide very detailed information on the geometrical structure of the constituent atoms and building units of the porous materials. Thus far, vibrational frequencies based on static quantum-mechanical calculations within the harmonic oscillator approximation are usually employed [231]. The calculated frequencies can be scaled to reproduce well-known characteristic peaks, in order to account for lack of anharmonicity and errors due to the employed level of theory. For the UiO-66- and UiO-67-type materials, IR spectra were obtained using such a static *ab initio* approach [121, 232]. Valenzano et al. found a good agreement between harmonic frequencies of the hydroxylated and dehydroxylated UiO-66 framework and experimental FTIR data. The theoretical periodic data allowed to assign the main IR peaks, and moreover, changes in the skeletal modes (between 400 and 800 cm^{-1}) suggested clear distortions of the inorganic ZrO units upon (de)hydration [121]. From the same group, a similar study on the UiO-67 material appeared, assigning the observed IR peaks in detail. [232]

More recently, VPS derived from MD simulations have become an interesting alternative to static frequencies, including the anharmonicity of the surface as well as temperature effects in a natural way. To date, VPS of zeolitic materials have been calculated successfully to elucidate the framework vibrations [9], but this is not yet a routine strategy for MOFs. Leus et al. [233] reported VPS of Au nanoparticles loaded in UiO-66, which were found to be in good agreement with experimental spectra. Furthermore, Greathouse and Allendorf [234] obtained VPS from force field data in order to discuss the slow torsional motion (40 cm^{-1}) of the aromatic rings in IRMOF-1 which they validated via NMR measurements. The provided vibrational fingerprint of the set of isorecticular UiOs will contribute to previous investigations. A detailed analysis of the VPS and the link with the excitation properties is missing so far.

The results of this chapter are based on:

Vibrational fingerprint of the absorption properties of UiO-type MOF materials

A. Van Yperen-De Deyne, K. Hendrickx, L. Vanduyfhuys, G. Sastre, P. Van Der Voort, V. Van Speybroeck and K. Hemelsoet, *Theor. Chem. Acc.*, **2016**, 135:102

Contribution: I performed part of the calculations and analysis, and co-wrote the manuscript

6.2 Methodology

6.2.1 Ab initio molecular dynamics

Ab initio optimizations and molecular dynamics (AIMD) simulations on both the isolated linkers and full periodic UiO-type frameworks were carried out using the CP2K software package [194]. They were performed using the PBE functional. Empirical dispersion corrections (DFTD3) were added to include long-range van der Waals interactions [235]. These ab initio simulations were done with the Gaussian and plane waves (GPW) method [236], using a DZVP Gaussian basis set and a plane wave basis set with a cutoff of 350 Ry using the Goedecker-Teter-Hutter pseudopotentials [237, 238]. For the AIMD simulations, the systems were initially heated to the desired temperature of 300 K using a CSVR thermostat [189], followed by MD runs using a Nosé-Hoover thermostat consisting of 5 coupled heat baths [190, 191]. The total sampling time of the NVT simulations at 300 K was 35 ps for the gas phase linkers and 27 ps for the full UiO frameworks using a 0.5-fs time step. Fully equilibrated trajectories of 20 ps were found sufficient for the computation of resolved power spectra. Subsequently, snapshots were taken every 5 fs (resulting in 4000 snapshots) and used as input for a static TDDFT calculation to derive dynamic averages of the excitation energy. This methodology and similar level of theory (employing BLYP instead of PBE) have proven to yield accurate results for these types of systems [185]. For the gas phase linkers, a cubic box [cell length 17.0 Å (UiO-66) or 22.0 Å (UiO-67)] was employed, which is sufficiently large to avoid interactions between the molecules. The MOF frameworks were simulated starting from a trigonal unit cell. The AIMD simulations on the entire UiOs were preceded by a cell and geometry optimization, performed at the level of theory described above. In the case of the original UiO-66 framework, this cell contains 114 atoms, i.e., 6 linkers and one Zr-O building block.

6.2.2 Calculation of VPS and ϵ PS

A velocity power spectrum (VPS) generated by a MD simulation contains all information about the internal vibrational modes (associated with vibrational coordinates Q_i) with frequencies ω_i (see below) and hence expresses the change of the molecular structure during the MD run. [239,240] The VPS is defined as: [240]

$$I_{VPS}(\omega) = \sum_{\alpha=x,y,z} \sum_{l=1}^N \left| \int v_{l,\alpha}(t) \exp(-i\omega t) dt \right|^2 \quad (6.1)$$

for a system with N nuclei and where $v_{l,\alpha}$ is the α^{th} Cartesian component of the velocity of the l^{th} nucleus. The VPS shows high intensities at frequencies corresponding to the vibrational energy levels. It contains all information about the internal motions of the studied systems.

Sampling of the ground state PES and subsequent computation of the vertical excitation energy for distinct snapshots creates a time series of $\epsilon(n)$ values. The excitation energy ϵ hence becomes an implicit function of time and similar to the VPS, the corresponding power spectrum of the excitation energy (ϵ PS) is defined as

$$I_{\epsilon PS}(\omega) = \left| \int \epsilon(t) \exp(-i\omega t) dt \right|^2. \quad (6.2)$$

The ϵ PS is characteristic for fluctuations in ϵ . In ref. [229] it was reported that one needs to examine the overlap between $I_{\epsilon PS}$ and I_{VPS} to determine the correlations between internal motions and the electronic spectrum generated by the vertical transition energy ϵ . Peaks coinciding in both spectra do not contribute to the shift in the dynamic average compared to the static value. This shift is caused by higher order, in particular quadratic, terms. The quadratic contributions can be identified by comparing the VPS with the ϵ PS where the frequency axis is now scaled with 1/2. In case of an overlap in this situation, the corresponding vibrational mode contributes to the difference between the static and dynamic excitation energy.

6.3 Results

6.3.1 Dynamic vs Static excitation energies

We start the analysis of the light absorption properties of the UiO-type materials under investigation by examining the calculated excitation energies of the organic units. Table 6.1 lists the first excitation energies of the linkers,

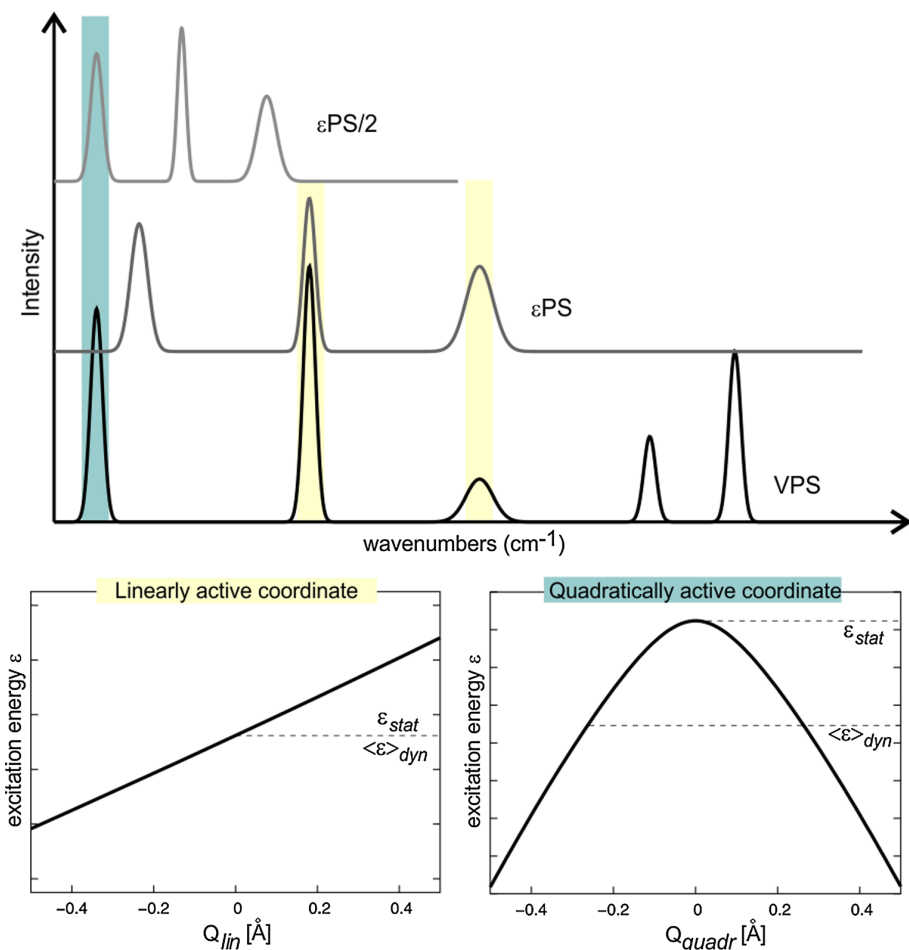


Figure 6.2: Schematic representation of the computational analysis tool based on VPS and ϵ PS. **a** Comparison of VPS with ϵ PS and ϵ PS with a scaling of the frequency axis of 1/2 allows to identify linearly or quadratically active modes. **b** The linearly active coordinate does not lead to a shift between the dynamic average $\langle \epsilon \rangle_{dyn}$ and static ϵ_{stat} excitation energy. **c** The quadratically active coordinate leads to a shift between the dynamic average $\langle \epsilon \rangle_{dyn}$ and static ϵ_{stat} excitation energy

calculated using a static calculation ('static') or via the averaging procedure as explained in the computational details ('dynamic'). The dynamic averages result from AIMD runs using the gas phase linker or the full periodic MOF material. During the periodic MD simulations, the organic linkers experience

interactions with the other linkers or inorganic units in the unit cell. The resulting dynamically obtained average excitation energy of the extracted organic linker includes both the induced effects of the periodic lattice and of the harmonic and anharmonic nuclear motions. Inspection of Table 1 reveals that when comparing the excitation energies based on the different geometries, no general trend can be derived for this set of isoreticular MOFs. For instance, the dynamic averages are not necessarily larger compared to the static values. Nevertheless, the following observations can be made. First, the static excitation energies of the linkers obtained from a direct gas phase optimization ('gas phase/static') or extracted from the optimized periodic MOF ('periodic/ static') differ very minorly. This indicates that during geometry optimization of the full UiO frameworks, the linkers are not substantially altered as compared to an optimization of the isolated linker. Only in case of the BDC-2,5NH₂ linker a large difference is found, which can be attributed to the different orientation of the hydrogen atoms of the NH₂ substituents. In case of the static optimization, the hydrogens are located in the plane of the aromatic ring, whereas this is not the case for the linker extracted from the optimized UiO-66-2,5NH₂ material. Second, the dynamic averages obtained from the AIMD runs show larger differences when comparing the gas phase (gas phase dynamic) and extracted ('periodic/dynamic') linkers. The difference ranges between 2 and 34 nm. This already indicates that, as expected, the geometrical structure of the linkers is influenced by the periodic MOF framework during an MD simulation.

Table 6.1 lists the first excitation energies of the linker units, calculated using a static calculation or via averaging. The dynamic averages result from either AIMD runs using the gasphase linker or full periodic MOF material. For four selected materials, AMD simulations using the full periodic MOF material have also been carried out.

A final important observation from Table 6.1 is that the static and dynamic excitation energies can differ substantially, in particular for the periodic data. For example, for the UiO-66-OH and UiO-66-2,5OH materials, the dynamic AIMD values are 19 and 29 nm larger compared to their static results, respectively. These shifts are due to changes in the geometrical structures induced during the dynamic simulations and will be examined in detail in Sects. 4.2 and 4.3 by linking the excitation energies to the vibrational features of the material. In addition to the calculated excitation energies, also the intensities of the electronic transitions can be taken into account. The dynamic averages are systematically lower compared to the static intensities, as shown in Fig. 4.

From Fig. 4, the bathochromic shift upon using a electron-donating sub-

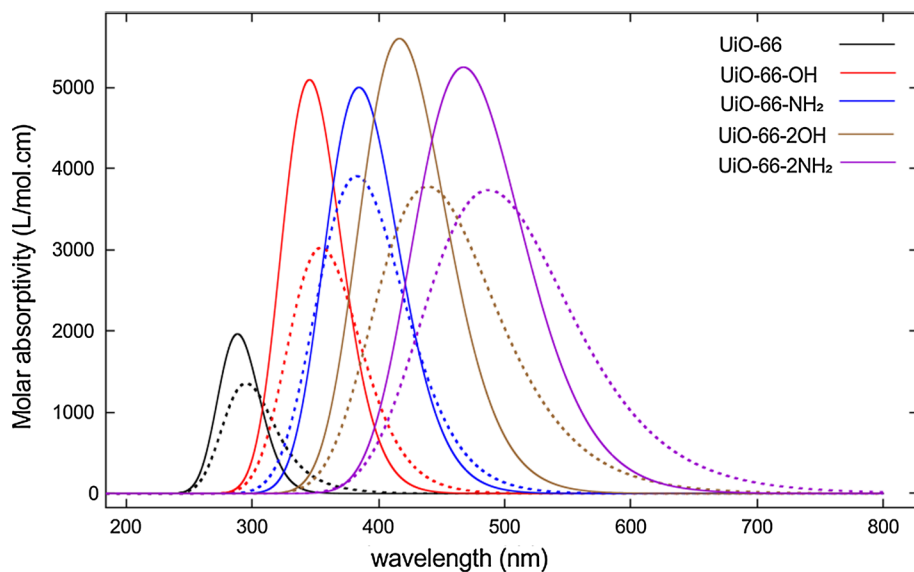


Figure 6.3: Comparison of the excitation spectra calculated on the linkers extracted from the periodic frameworks using static (full curves) and dynamic (dotted curves) methodologies. The intensities are expressed in L/mol.cm. The wavelength values of the peaks are indicated in Table 6.1 static ('periodic/ static') and dynamic ('periodic/dynamic')

stituent is also clearly observable, in line with previous findings on these UiO-type materials [23]. The origin of the vertical transitions can be investigated based on the involved orbitals of the linkers. We previously reported that for the UiO-66-variants, the transition is mainly due to a HOMO to LUMO excitation, in which the contribution of the functional group almost vanishes in the LUMO orbital [23]. A similar observation can be made in the case of the longer BPDC-2,5'NH₂ linker, where the contribution of the electron-donating substituents reduces from 33 % in the HOMO to 1 % in the LUMO (see Fig. 5). The optimized gas phase BPDC linkers (shown in Fig. 5) are nonplanar in the ground state, exhibiting a dihedral angle of 30.1 and 52.2 ° of the two aromatic rings for BPDC and BPDC-2,5'NH₂, respectively. The additional NH₂ substituents increase the deviation from planarity. Some of the presenting authors previously investigated the influence of the torsional angle on the excitation energy in the case of a bipyridine-based linker [62]. For biphenyl, it is well described in the literature that the dihedral angle between the phenyl linkers is nonzero [36]. Importantly, this deviation from planarity in case of the BPDC linkers hampers the conjugation and the

calculated excitation energies are hence not necessarily larger compared to their BDC counterparts (as indeed seen in Table 1).

	static		dynamic		experiment ^a	
	gasphase AI	periodic AI	periodic A	gasphase ^b AIMD	periodic ^b AIMD	periodic ^c AMD
Uio-66-H	285	288		285	288	325
Uio-66-OH	339	345	-	337	372	-
Uio-66-NH ₂	389	385		383	391	355
Uio-66-2,5OH	411	417	-	412	467	-
Uio-66-2,5NH ₂	528	467	-	470	478	-
Uio-66-oxal	-	341	-	-	356	-
Uio-66-CC	-	341		-	345	331
Uio-67-H	314	318		281	305	-
Uio-67-2,5'NH ₂	387	383	-	378	384	-

Table 6.1: Vertical excitation energies computed using TD-DFT (B3LYP/6-311+G(d,p)). The experimental values refer to absorption maxima and are taken from the previous chapter. All values are in nm.

^a From chapter 5. ^b Mean average using 2000 snapshots. ^c Mean average using 5000 snapshots.

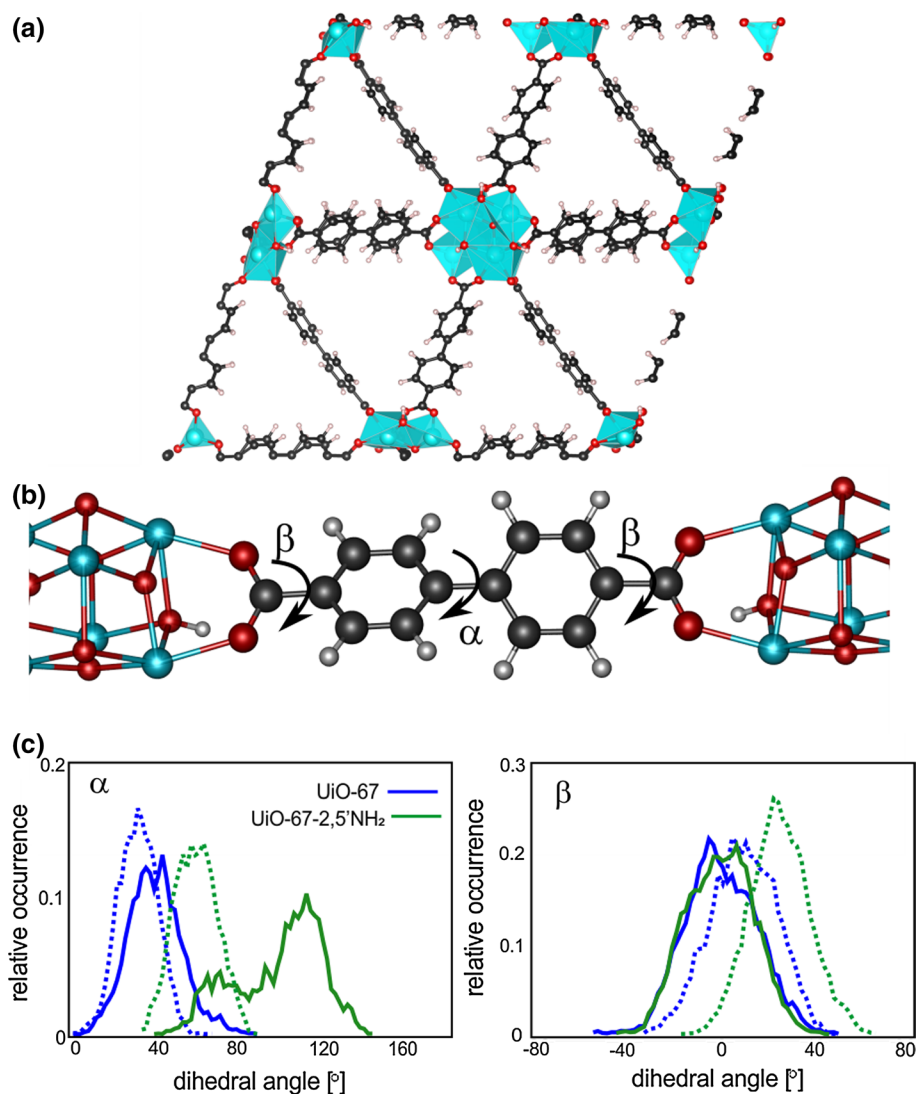


Figure 6.4: (a) Periodic structure of the UiO-67 porous framework. (b) Detailed view on the BPDC linker anchored at the inorganic Zr-O units. Dihedrals α and β represent the torsional angle between the two aromatic rings and the dihedral angle between a phenylic and carboxylic part, respectively. (c) Relative occurrence of the dihedral angles α and β as calculated from the MD simulations using the fully periodic UiO-67 (in blue) and UiO-67-NH₂ (in green) frameworks. Full curves obtained from gas phase MD and dotted curves from periodic MD simulations

Moreover, when anchored in the UiO-67 (Fig. 6.4a) this torsional dihedral will be influenced. Notably, also the dihedral angle between the phenylic groups and the carboxylic parts of the linker influences the conjugation of the system. Both dihedral angles (α and β) are indicated in Fig. 6.4b. During the MD simulations, the spread in the values for these dihedral angles becomes substantially larger due to the increased temperature. Their distribution for the UiO-67 and UiO-67-2,5'-NH₂ materials, obtained during the gas phase and periodic MD simulations are displayed in Fig. 6.4c. It is observed that for UiO-67 the angles α and β behave similarly when comparing the gas phase (full curves) and periodic (dotted curves) MD simulations. The dihedrals vary around an average value with ranges of about 60 and 80 ° for α and β , respectively. For the functionalized linker, the dihedral angles are significantly larger due to the sterical hinder caused by the amine groups. For the gas phase BPDC-NH₂ linker, the barrier between the two symmetry-related structures can be overcome during the MD simulations at 300 K, resulting in the observed peaks at 70 and 110 ° (which essentially represent the same structure).

For the gas phase MD simulations, the average of β is approximately zero, similar to the BDC linkers as can be deduced from figure 6.5. When placed in the framework, however, the carboxylic groups are bound to the inorganic clusters and thus much more rigid. Therefore, the dihedral angle between carboxyl group and the phenyl linkers is nonzero in the periodic simulations. This effect is even more pronounced for the NH₂-functionalized UiO-67 material, due to the larger torsional angle α between the phenyl rings.

6.3.2 Vibrational analysis

The MD trajectories are used to calculate VPS spectra, providing insight in the vibrational modes of the UiOs. A detailed analysis of the vibrational motions of all investigated structures is outside the scope of this paper, and therefore, only the main features are described. Figure 6.6 depicts the VPS of the prototype UiO-66 material computed using the periodic MD trajectory. To gain more insight in the origin of the calculated VPS, partial VPS spectra, separating, e.g., the contributions from the linker and the inorganic Zr-O unit, are also shown. The clear peak at 3731 cm⁻¹ corresponds with the OH stretching frequency in the Zr₆O₄(OH)₄ units, denoted as the μ_3 -OH. This value can be related with the experimental value of 3676 cm⁻¹ reported by Lamberti et al., who combined static periodic B3LYP calculations with experimental data to report vibrational data of the UiO-66 [19] and UiO-67 [39] materials. The CH stretching frequencies of the aromatic BDC linker

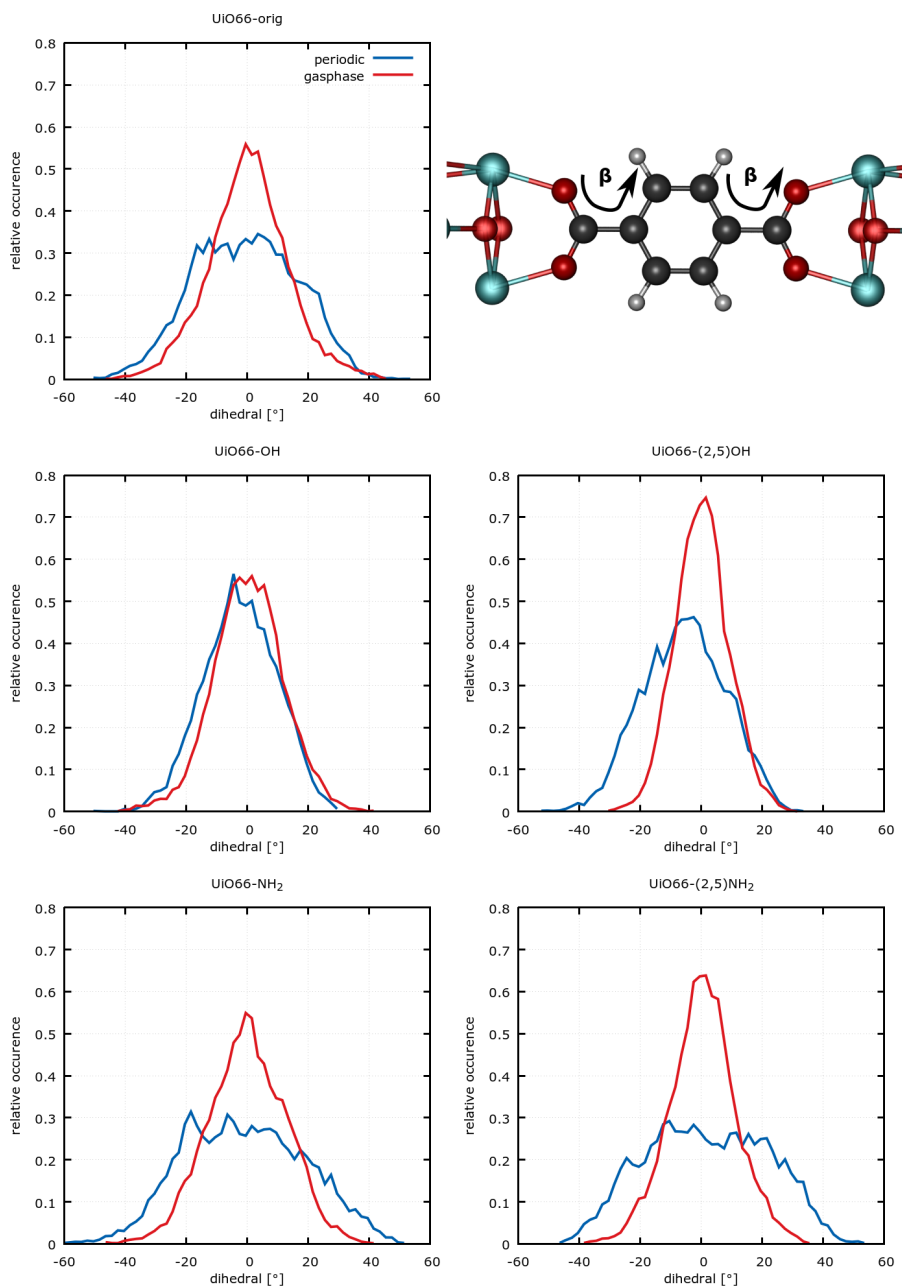


Figure 6.5: Distribution of the dihedral angle β over the MD trajectories for the UiO-66 and functionalized materials.

are located between 3100 and 3200 cm^{-1} , but these are not expected to be of further importance in our discussion relating the vibrational motions to the changes in the excitation energy. The skeletal vibrations are situated at lower frequencies, i.e., between 400 and 1600 cm^{-1} , and clearly these are dominated by the linker contributions. These contributions can mainly be assigned to various kinds of ring vibrations, including out-of-plane vibrations (i.e., at 400 cm^{-1}), distortions and C-C stretches. The partial VPS show that the vibrations of the Zr_6 -octahedron units are found between 400-470 and 650-850 cm^{-1} .

The VPS of UiO-66 also reveals three main peaks at very low wave numbers, i.e., at 38, 50 and 60 cm^{-1} (see Fig. 6.6 b). These so-called soft modes are associated with the carboxylate torsion and other global modes of the organic linkers, as made clear via PCA and visualized in Fig. 6.6c. These modes have an important influence on the calculated absorption properties, as shown hereafter. The VPS provide an interesting way to compute these modes. The selected test set allows to investigate the influence of both linker substitution and usage of extended linkers. Changes in the linker functionalization are most clearly observed in the stretching region above 3000 cm^{-1} as shown in Fig. 6.7a.

Importantly, the calculated $\nu(\text{O-H})$ stretching frequencies of the OH-substituted UiO-66s are found between 3250 and 3450 cm^{-1} , indicative of mild hydrogen bonding in these structures. This is also revealed when comparing the VPS calculated from the MD of the gas phase linker with the VPS calculated for the linker extracted from the MD of the periodic UiO framework, as illustrated in Fig. 6.7b for UiO-66-2,5OH.

For the gas phase MD, a substantial shift of the OH frequency is found compared to the periodic simulations. This is due to a stronger hydrogen bond with the carboxylic oxygens, reducing the strength of the observed OH bond more in the case of gas phase simulations. Inspection of the relevant geometrical parameters does, however, not result in changes between the values obtained from a static optimization and from dynamic averages. Use of the longer BPDC linkers results in VPS which are very similar to the spectra of the UiO-66 materials. Detailed investigation shows that the VPS of the UiO-67 framework show an extra peak at 1188 cm^{-1} , which must be attributed to a collective mode of the BPDC linker, in excellent agreement with the theoretical value of 1180 cm^{-1} reported by Chavan et al. [39].

In analogy with the VPS of UiO-66, the VPS of UiO-67 shows dominant peaks at low frequencies. Due to the occurrence of the biphenylic unit, a variety of

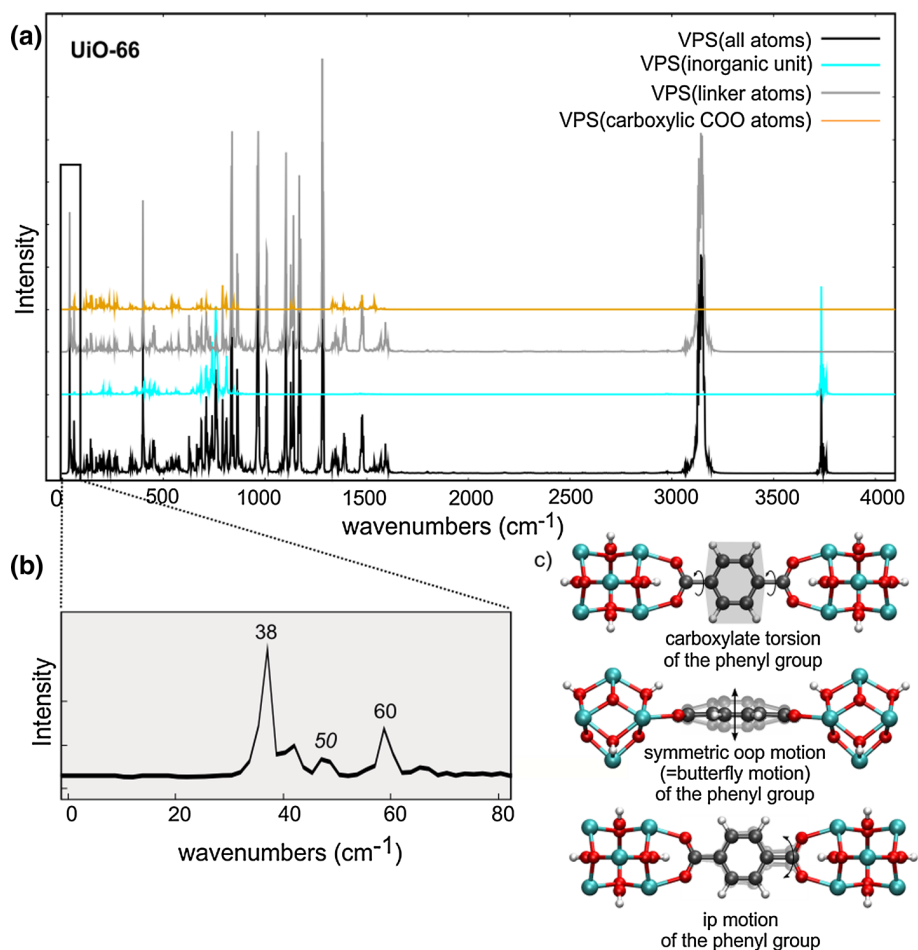


Figure 6.6: (a) Power spectra computes using MD of the fully periodic UiO-66 framework (black). Partial spectra using only the information from atom of the inorganic (cyan), organic (grey) and carboxylic (orange) units. (b) Detail of the VPS of the periodic UiO-66: the region below 80 cm^{-1} , indicative of the soft modes, is shown. (c) Representation of the characteristic soft modes, corresponding with global motions of the aromatic linker.

low-frequency modes including a butterfly mode, torsions over α and β is present in the range below 70 cm^{-1} . The VPS of the two models systems, UiO-66-oxal and UiO-66-CC still showed a lot of vibrational peaks in the skeletal region below 900 cm^{-1} . Notably, the first peak of UiO-66, located

around 38 cm^{-1} and corresponding with a global torsion of the organic aromatic linker is now absent. A peak around 68 cm^{-1} represents a global translation of the central CC out of the carboxylic plane, motions which are indeed still present in both model systems. The $\text{C}\equiv\text{C}$ stretching mode in case of UiO-66-CC is found at 2255 cm^{-1} .

6.3.3 VPS vs. ϵ PS

To gain more insight into the motions contributing to the shift between the static and dynamic excitation energies, the VPS must be compared directly with the ϵ PS (see Sect. 6.2). The ϵ PS reveal the modes that are characteristic for changes in the computed excitation energy. All power spectra based on the periodic MD show dominant features at low-frequency modes, i.e., below 100 cm^{-1} . These modes correspond with the global motions of the aromatic/aliphatic linkers, as visualized in Fig. 6.6c for the aromatic BDC unit. In the model case of UiO-66-oxal, such modes are less present, which has clearly its influence on the ϵ PS, yielding more pronounced peaks at higher frequencies. Other contributions to the ϵ PS resulting from these organic moieties are the vibrations located between 1400 and 1600 cm^{-1} , representing, e.g., a variety of ring distortions in case of the aromatic units. Figure 6.9 shows the ϵ PS and VPS in case of (a) UiO-66, (b) UiO-66-CC, (c) UiO-66-2,5OH and (d) UiO-67, in line with the conceptual Fig. 6.2. Detailed inspection reveals that although a correlation between the ϵ PS and VPS can overall be found, the complexity of the VPS hampers straightforward unraveling which vibrational modes are represented and a PCA is performed. In what follows, the main observations are summarized for the four case studies shown in Fig. 6.9.

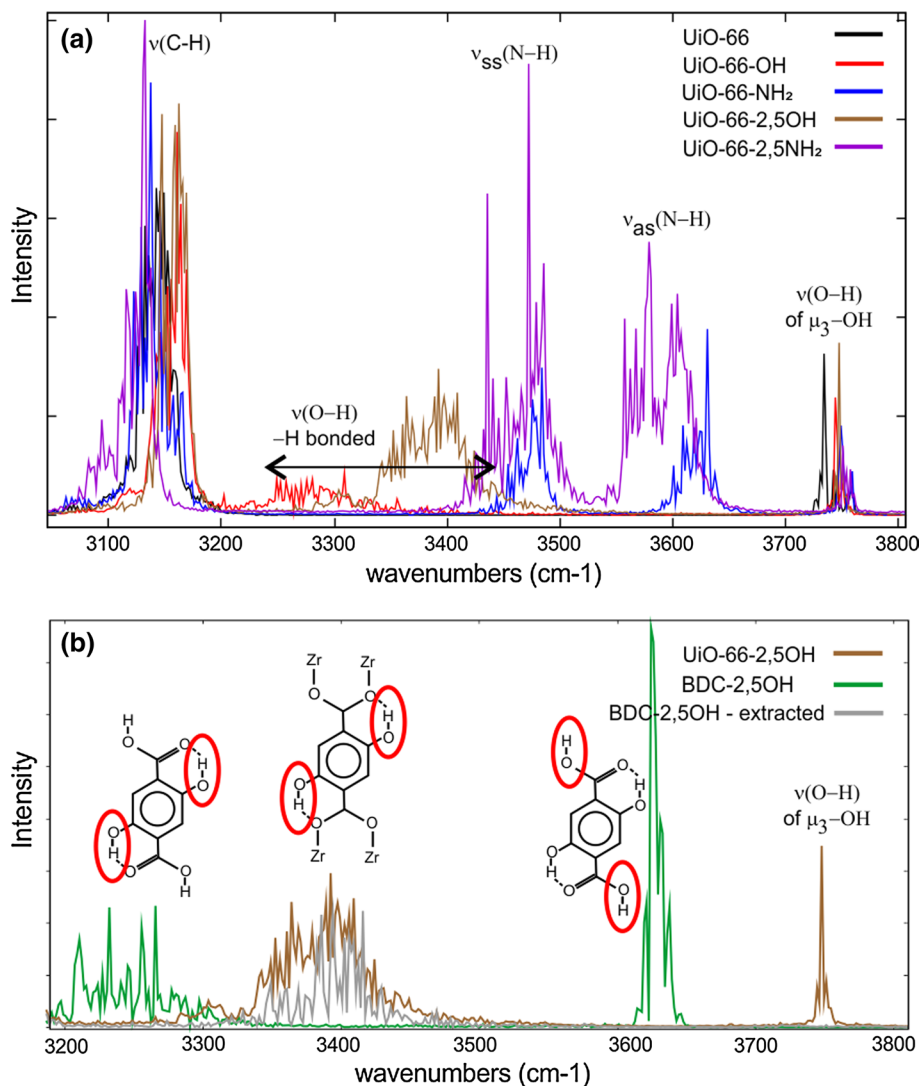


Figure 6.7: (a) Periodic structure of the UiO-67 porous framework. (b) Detailed view on the BPDC linker anchored at the inorganic Zr-O units. Dihedrals α and β represent the torsional angle between the two aromatic rings and the dihedral angle between a phenylic and carboxylic part, respectively. (c) Relative occurrence of the dihedral angles α and β as calculated from the MD simulations using the fully periodic UiO-67 (in blue) and UiO-67-NH₂ (in green) frameworks. Full curves obtained from gas phase MD and dotted curves from periodic MD simulations

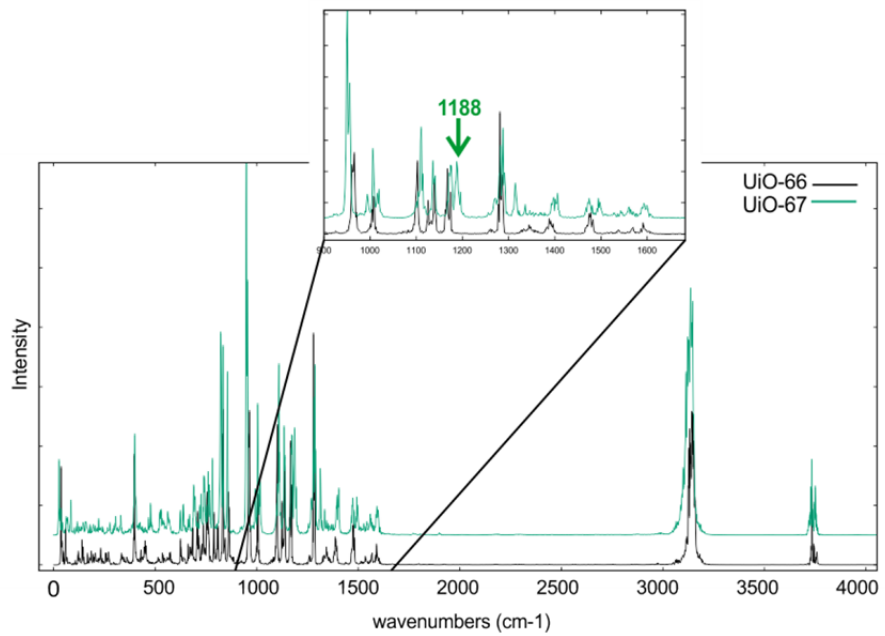


Figure 6.8: Comparison between the VPS of UiO-66 and UiO-67 from the periodic MD simulations.

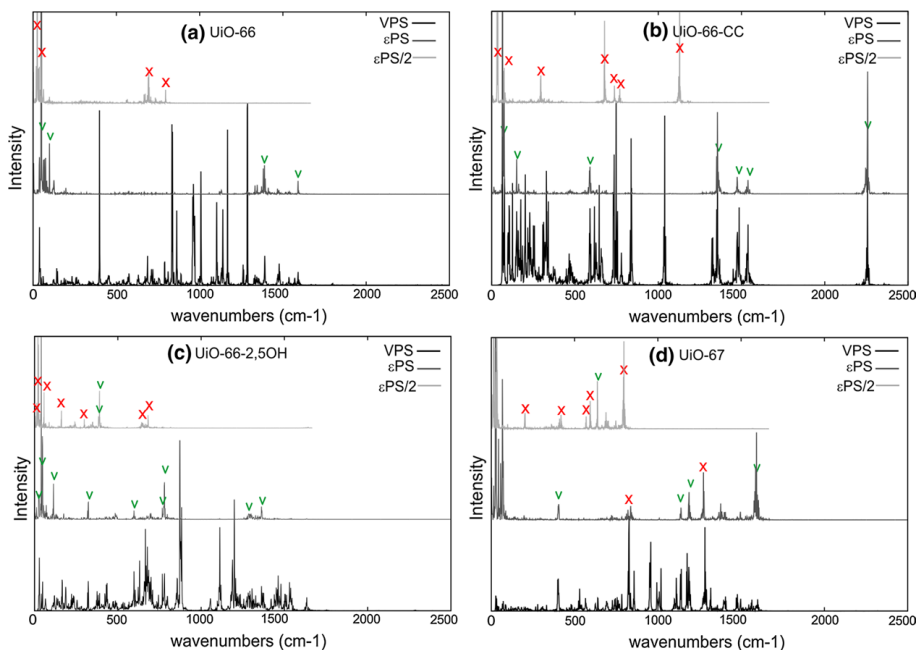


Figure 6.9: Power spectra of selected UiO frameworks: (a) UiO-66, (b) UiO-66-CC, (c) UiO-66-2,5OH and (d) UiO-67. Partial VPS from the periodic AIMD data, using only the linker atoms (black), ϵ PS (dark gray) and ϵ PS with scaling of the frequency axis by 1/2 (light gray). A green tick indicates a correlation between the power spectra, whereas a red cross indicates no correlation is found. The TD-DFT simulations are solely performed on the linkers (either obtained from the gas phase MD or extracted from the periodic MD), and hence, the partial VPS using the linker atoms are employed (see Fig. 6.6 for UiO-66). For the simulation of the VPS, the hydrogen atoms are neglected since their contribution to the VPS is dominant, while their influence on the π -system is very small

In case of the original UiO-66 material (Fig. 6.9a), the ϵ PS look rather simple, featuring a main peak around 50 cm^{-1} , a smaller one at 38 cm^{-1} and some minor contributions between 60 and 125 cm^{-1} and around 1300 - 1600 cm^{-1} . Close comparison between the ϵ PS and the VPS reveals that all the peaks above 1300 cm^{-1} coincide in both power spectra. All these modes correspond with various in-plane ring vibrations. This indicates a linear dependency of the excitation property on changes in these coordinates. When averaging during the MD sampling, no net influence is observed on the average dynamic excitation energy compared to the static value. But, comparing the ϵ PS with the ϵ PS/2 (2 upper curves in Fig. 6.9a) reveals that several low-frequency modes have both a linear and quadratic behavior since the spectra have coinciding peaks. Table 2 identifies the PCA coordinates for which the Q_i PS show high overlap with the scaled and unscaled ϵ PS. Q_2 and Q_3 are nearly degenerate with main peaks at 50 and 60 cm^{-1} , with additional peaks for Q_3 . Due to this degeneracy, these modes are not simple linear or quadratic modes. They are instead a mixture of a butterfly motion quadratic and an in-plane translation of the phenyl ring linear motion as shown in Fig. 6.6c. Although this degeneracy complicates the analysis, due to the presence of the peaks in both the scaled and nonscaled ϵ PS, we can safely conclude that the butterfly motion is quadratic and causes the absorption shift as seen in Table 6.1. Other modes, such as the global linker torsion (Q_1) and in-plane phenyl rotation (Q_{10}), have inherently both a quadratic and linear dependency, due to the saturation of the linker with hydrogen atoms in case of the linkers extracted from the periodic UiOs. In case of the MD simulations involving the gas phase BDC linker, the ϵ PS shows less activity in the low-frequency range. This indicates that no quadratic motions are found and, indeed, the static and dynamic excitation energy in case of the gas phase MD simulation is very similar (see Table 6.1).

The ϵ PS of the model framework UiO-66-CC show seven main peaks (see Fig. 6.9b). The highest peak is located at low wave numbers (i.e., at 65 cm^{-1}). Another peak in the ϵ PS are located at 2255 cm^{-1} , indicating that the $\text{C}\equiv\text{C}$ stretch of the model linker also impacts changes in the excitation energy. Again, for all peaks an overlap between the ϵ PS and VPS is found, demonstrating a linear correlation along these modes, and thus, a small overall shift is obtained between the dynamic average and static value of the excitation energy (the obtained shift indeed only equals 7 nm , see Table 6.1).

Due to the complexity of the VPS of UiO-66-2,5OH and UiO-67 (Fig. 6.9c, d), a PCA is performed. For the UiO-66-2,5OH framework, the excitation energy computed using a static or dynamic approach differs significantly in the case of the AIMD of the fully periodic MOF: a bathochromic shift of 29 nm is ob-

tained (see Table 6.1). As this shift is not observed in case of the AIMD of the gas phase BDC-2,5OH linker, an important effect of the periodic framework is suggested. In case of the periodic AIMD data, the PCA reveals the occurrence of a quadratic coordinate Q_{11} , of which the corresponding power spectrum (Q_{11} PS) exhibits peaks at 381 and 390 cm^{-1} . These peaks are also found in the ϵ PS with the frequency axis scaled with 1/2 (see Fig. 6.10). These peaks are due to a complicated motion, including the asymmetric out-of-plane motion of carbon and oxygen atoms of the BDC unit and OH substituents as shown in Fig. 6.10.

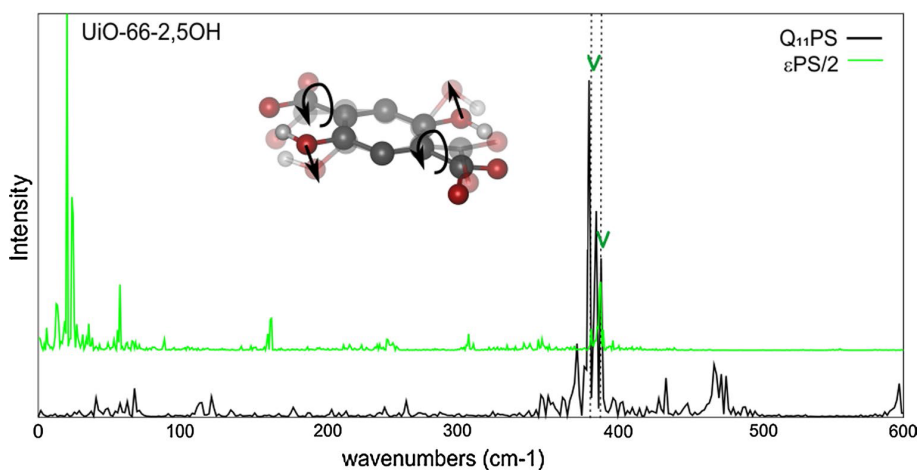


Figure 6.10: Comparison of the ϵ PS with scaling of the frequency axis by 1/2 and the Q_{11} PS obtained from the PCA in case of UiO-66-2,5OH. The corresponding motion is visualized (hydrogen atoms are omitted for clarity). The periodic AIMD data were used

This vibrational mode dominates the shift between the averaged dynamic and static excitation energy. For the gas phase AIMD data, all coordinates exhibit a linear behavior, rationalizing that the dynamic average almost equals the value obtained from the static optimization.

The UiO-67 framework offers another interesting case study. Clearly, motions affecting the central C-C bond disturb the π -system of the conjugated aromatic linker substantially. These modes are expected to have a significant influence on the resulting excitation energy. The analysis of the ϵ PS involving the gas phase AIMD is already rather complicated due to the large number of peaks, confirming that many vibrations impact the excitation energy. The

biphenylic unit results in a variety of motions that can occur, and importantly, many of them exhibit a quadratic behavior. Notably, the butterfly motion, torsion of the phenylic rings and ring vibrations (e.g., the in-plane ring vibration at 631 cm^{-1}) are dominant modes. Inclusion of the framework in the AIMD simulations leads to a rather similar picture, although fewer quadratic modes are obtained. The ϵ PS of the linkers extracted from the UiO-67 framework show 4 main contributions in the very lowfrequency range, i.e., below 70 cm^{-1} , but only one of these peaks is now quadratic. Using PCA, it can be concluded that this peak represents the global rotation of the biphenyl linker compared to the rest of the UiO-67 framework (i.e., rotating over the dihedral angle β , see Fig.6.4b). A second quadratic peak is found at 637 cm^{-1} and corresponds with an in-plane vibration of the aromatic rings. In these cases, the various quadratic contributions might compensate each other, and hence, the observed shift between the static and dynamic excitation energy is found to be relatively small (see Table 6.1). The case studies above indicate that the analysis based on power spectra can identify the vibrational modes that impact the calculated excitation energy.

6.4 Conclusions

In this chapter, theoretical simulations have been employed to assess which vibrational modes impact absorption properties of UiO-type metal-organic frameworks. The excitation energies have been calculated using TD-DFT on the organic linkers. Nine UiO-based frameworks have been tested, varying in linker substituents considering electron-donating OH and NH_2 substituents and linker length. In addition to the UiO-66 and UiO-67 materials and substituted derivatives, two model systems exhibiting a simplified linker have been considered. The impact of nuclear motions on the excitation properties have been accounted for by sampling the potential ground-state surface using *ab initio* molecular dynamics (AIMD) simulations. Subsequently, averaged dynamic absorption properties have been calculated and compared with absorption data from an optimized geometry. The sampling has been done for both the gas phase organic linker and the fully periodic UiO framework. Given the distinct simulations involving various sets of generated geometries, the analysis allows addressing the influence of the periodic framework, temperature and harmonic and anharmonic nuclear motions.

The absorption spectra of the mono- and disubstituted UiO-66 MOFs show a clear bathochromic shift upon substitution. In case of UiO-67, NH_2 substitution results in a similar modulation and also indicates that the contribution of the substituent to the LUMO nearly vanishes in the HOMO to LUMO

excitation. Velocity power spectra, calculated from the MD trajectories, provide vibrational information of the UiO materials. For the UiO-66-OH and UiO-66-2,5OH frameworks, the VPS provide insight into the hydrogen bonding in these materials and an influence of the framework is reported. The soft modes at low frequencies can be calculated for all UiOs with accuracy, providing characteristic values below 70 cm^{-1} for the global linker motions, such as ring torsions and butterfly motions.

The VPS are directly compared with the power spectra of the excitation energy ϵ PS to identify the dominant vibrational motion(s) responsible for changes in the spectroscopic property. Inspection of the ϵ PS reveals that for all periodic UiO frameworks, the low-frequency modes impact the calculated excitation energy. In case of the periodic UiO-66 material, the shift between the static and dynamic excitation energy mainly originates from the global butterfly motion of the organic linker. For the periodic UiO-66-2,5OH material, a more complicated motion, including out-of-plane movements of atoms of both the aromatic unit and the substituents, is identified. These shifts are not observed when the dynamics solely involve the gas phase organic linker, clearly pointing out the effect of the periodic UiO framework. For the UiO-67 material, the torsion between the phenylic rings also impacts the excitation energy. The computational tool based on power spectra allows to determine the vibrational fingerprint of excitation properties of nanoporous materials featuring global modes such as UiO frameworks. The resulting insights based on a combination of MD and TD-DFT simulations add to the complete understanding of the light absorption properties of these complex materials.

Part III

Improving photocatalytic properties

7

Improving charge transfer via metal doping

In the previous part of this thesis, a detailed study allowed to fully understand the electronic structure of the UiO-type materials. It was shown that light-absorption occurs via the organic linkers and that the addition of electron-donating groups is beneficial to extend the absorption window to the visible range. Unfortunately, the contribution of the inorganic node to the conduction band is negligible in the pristine material as shown via our cluster calculations in chapter 5, hence, an efficient charge transfer, required for efficient photocatalysis is limited in UiO-66. In order to improve this, the inorganic states need to be lowered to overlap with the LUMO linker states.

Within this part of the thesis, we will discuss two pathways to improve the energetic overlap of the inorganic node states with the linker states. In this chapter, we take a look at metal doping. We present a broadly applicable synthesis procedure to dope UiO-66 with a wide range of metals, with a special focus on lanthanides. A detailed spectroscopic study allows to construct charge-state transition levels for the whole lanthanide series and titanium with respect to the UiO host band structure. In order to obtain more insight in the electronic structure of these materials, DFT calculations are performed on a selected subset of materials.

Chapter 8 then will provide a detailed study of defect engineering as an alternative pathway for UiO electronic structure engineering. Although this

strategy is for now proposed purely theoretically, current developments in UiO defect engineering encourage us that also this pathway will soon be experimentally viable.

The results and text of this chapter are based on:

Exploring lanthanide doping in UiO-66: a combined experimental and computational study of the electronic structure properties

K. Hendrickx, J.J. Joos, A. De Vos, K. Lejaeghere, D. Poelman, P.F. Smet V. Van Speybroeck and P. Van Der Voort, submitted

Contribution: I performed the synthesis, characterization, spectroscopic measurements and cluster calculations and wrote the manuscript

7.1 Introduction

As has been introduced, one of the limiting problems of semi-conductor photocatalysts is the high electron-hole recombination rate. In MOFs, electrons are localized on distinct constituents. Hence, the photoreceptive system (or antenna) and the photocatalytically active centre are separated entities within the same crystalline material. In this way an efficient separation and transfer via a Ligand-To-Metal Charge Transfer (LMCT) can take place if the bands are well aligned. Moreover, the modular set-up allows for an orthogonal engineering of the electronic structure, since linker and node contributions can be treated additively.

UiO-66 in its pristine form is poorly suited for photocatalysis, however. Besides its large band gap, impeding excitation with light in the visible region of the spectrum as discussed in the previous chapters, the major problem is the inefficient charge transfer between linker and node. From figure 7.1 it can be deduced that a transfer from the linker to the inorganic node will be very difficult, since the empty Zr d states lie more than 1 eV higher than the empty linker band (ΔE_{LMCT}). This lack of overlap impedes the electron to travel efficiently to the node as we have discussed in chapter 3. In order to improve LMCT, changes to the LUCO states (Lowest Unoccupied Crystalline Orbital) are necessary. Introduction of Ti in the Zr node, via postsynthetic exchange, [241, 242] strongly improves the catalytic activity of the material due to the appearance of low lying d states in the DOS.

Introduction of Ti in the Zr node, via postsynthetic exchange, [241,242] strongly

improves the catalytic activity of the material due to the appearance of low lying d states in the DOS. Sun et al. demonstrated that Ti doping of UiO-66 lead to an enhanced photocatalytic performance for CO₂ reduction and H₂ evolution under visible light irradiation. [243] In order to elucidate the mechanism, they performed DFT calculations and found the appearing of Ti 3d band at the lower end of the conduction band. Moreover they performed EPR measurements and found the appearance of a Zr³⁺ signal in the spectrum. Their findings already lead to the idea of Ti acting as a mediator to transfer the electron from the linker to Zr but are not conclusive. Lee and co-workers performed similar catalytic experiments on a Ti-doped BDC-NH₂/BDC-2,5NH₂ mixed-linker UiO-66 and found a better performance compared to the mono-functionalized UiO-66-NH₂ material and most of the common literature catalysts. [244] Via PL spectroscopy and UV photo-electron spectroscopy they constructed an energy band diagram which shows a more efficient transfer from the linker via the node to CO₂ thanks to a better alignment of the conduction band minima. A consecutive study by Wang et al. [245] tested several Ti dopant concentrations in the degradation of methylene blue. They performed a detailed morphological study and found a decrease in crystallinity when the Ti concentrations are too high. Next, Nasalevich and co-workers [147] discussed three existing isostructural MOFs composed of d⁰ metals (Ti⁴⁺, Zr⁴⁺, and Hf⁴⁺) and confirmed that only the Ti materials show a large LMCT. Via EPR and other time-dependent spectroscopic techniques, they concluded that almost no reduced Zr or Hf species could be found when exciting the UiO material. Also computationally, several authors explored the electronic changes in the materials. Yang and co-workers explored the materials properties (bulk moduli,...) and optical properties of a series of Ti and Hf doped UiOs. Yasin et al. recently performed a high throughput screening of the band gaps and constructed ternary plots of the band gap in function of the Zr, Ti and Hf concentration. [246, 247] A recent study using transient absorption spectroscopy corroborated the aforementioned studies and the authors propose a mechanism where Ti acts as a mediator for the electron transfer from the organic linker to a Zr ion. [248]

In light-based applications, special attention goes to the series of lanthanide (Ln) metals. Their bright emission forms the basis of many lighting applications, and their specific electronic structure is ideally suited for catalytic fine chemistry. [249–251] Also within MOF research, Ln-based materials have emerged in recent years. [252–254] As Ln ions are inserted in a crystalline framework, they are heterogenized, facilitating the processing steps for several applications. Moreover, the orbital overlap between the antenna and the Ln ion is ensured since they are part of the same rigid framework. The latter is of paramount importance to provide an efficient pathway for the charge

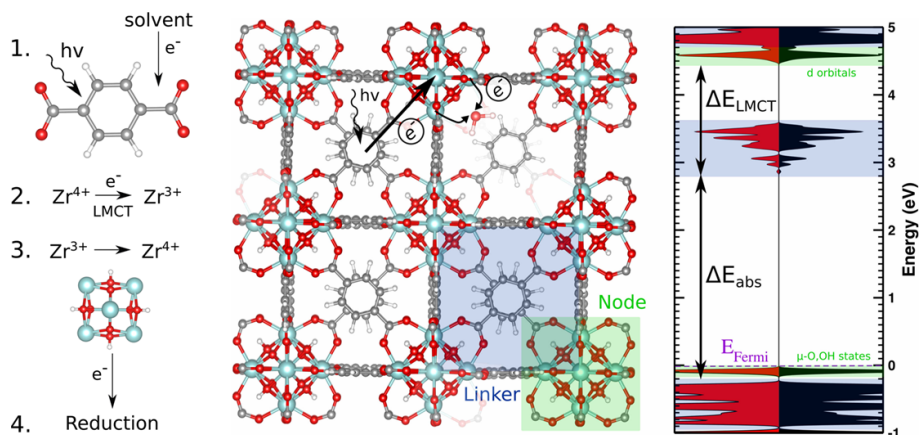


Figure 7.1: Basic steps occurring in a UiO-66 photocatalytic process (left): light absorption(1), LMCT (2) and reduction process (3,4). The middle and right figure show a model of the UiO-66 material and the corresponding DOS of the material. Green indicates bands that have mainly node-contributions whilst blue indicates that mostly linker states can be found. The figure is adapted from [126]

carriers to move in the framework. Unfortunately, difficult syntheses and limited stability restrict the use of Ln MOFs. [255] In order to overcome this problem, we propose an approach inspired by solid state lanthanide chemistry where a stable robust carrier material (e.g. a metal oxide) is doped with a small amount of lanthanide ions in a high-temperature process. Within this work, we adopt a microwave-based methodology to dope UiO-66, a robust MOF, with several lanthanide and transition metal ions and investigate the electronic properties of the new materials. So far, this doping strategy to alter the electronic properties was only used to introduce isovalent atoms. However, thanks to the highly exchangeable nature of the constituents in MOF materials, we show that this methodology can be extended towards many more metals. The doping of a robust MOF with low concentrations of Ln dopant ions leads to a whole new series of materials which may advance a wide range of applications, ranging from lighting to photocatalysis. Given the stability of the parent material, evaluation in different chemical environments and under different ambient conditions is possible whilst retaining the Ln-specific properties.

Within this chapter we use for the first time a systematic experimental method to incorporate lanthanide ions in the UiO-66 framework and probe the electronic properties of these new materials. Although we provide insight into the

electronic transitions (which result in their absorption/emission behaviour) using demanding first-principles computational techniques, we also establish a more empirical model by exploiting recurrent features of the lanthanides. Indeed, systematic behaviour emerges across the lanthanide series independent of the chemical environment as all ions act chemically very similar. This behaviour results in a typical ‘zig-zag’ curve across the lanthanide series that displays the charge-state transition levels for lanthanide impurities in crystalline materials. Thanks to the systematics, the location of the charge-state transition levels for all lanthanides can be predicted when one knows the location of at least one such level for one lanthanide ion. [256–258] In this work, the systematic properties of the lanthanide ions are used to construct band diagrams of Ln-doped UiO-66, containing all fourteen Ln (2+/3+) and (3+/4+) charge state transition levels, based on a small set of experimental absorption and photoluminescence (PL) spectra. To our knowledge, this is the first time a complex hybrid carrier material is evaluated using this methodology. Furthermore, a Density Functional Theory (DFT) study of some of the selected materials corroborates the findings of the empirical model and helps to understand the electronic structure changes observed for the different doped frameworks. It bridges the gap between our novel Ln-MOFs and the existing isovalently doped materials.

7.2 Materials and methods

7.2.1 Synthesis

UiO-66 was synthesized based on a general procedure by Biswas and co-workers as discussed in section 2.4. The doping of the UiO-66 framework was performed using a post-synthetic metal ion exchange procedure based on procedures developed by Lau et al. [259] and Tu et al. [260] using different metal precursors.

In this chapter, we dope UiO-66 with isovalent ions (Ti^{4+} ($\text{TiCl}_4(\text{THF})_2$) and Hf^{4+} ($\text{HfCl}_4(\text{THF})_2$)) and lanthanides (Ce^{4+} ($\text{Ce}(\text{NH}_4)_2(\text{NO}_3)_6$), Eu^{3+} ($\text{EuCl}_3 \cdot x\text{H}_2\text{O}$), Yb^{3+} ($\text{YbCl}_3 \cdot 6\text{H}_2\text{O}$) and Nd^{3+} ($\text{NdCl}_3 \cdot 6\text{H}_2\text{O}$)). To compare the spectroscopic properties of the pure UiO materials and doped materials, a pure cerium based UiO was also prepared. Synthesis of UiO-66(Ce) was based on a procedure by Lammert et al. [119]

Titanium precursor

$\text{TiCl}_4(\text{THF})_2$ was synthesized by means of a slightly modified literature method. [241, 259] In a 250 mL round-bottomed flask, TiCl_4 (1.5 ml, 13.7 mmol) was carefully added to 25 mL anhydrous dichloroethane under argon atmosphere. The light yellow clear solution was cooled to 0 °C in an ice bath before slowly adding 4.3 mL (52.4 mmol) of anhydrous tetrahydrofuran (THF), resulting in a clear, dark yellow-brown solution. Next, the product was precipitated by adding 50 mL of anhydrous n-hexane. The resulting yellow powder was filtered off on a membrane filter and washed with n-hexane (2·25 mL) and dried under vacuum overnight. The $\text{TiCl}_4(\text{THF})_2$ was used immediately for post-synthetic exchange. The powder could be stored for a few days under inert atmosphere but then starts to decompose slowly with formation of HCl.

Doping procedure

The procedure starts with 0.5 mmol (0.12 g, equiv. based on organic linkers) UiO-66 that was dispersed in DMF and put for 10 minutes in the ultrasonic bath. After adding 0.5 mmol metal precursor, the resultant mixture was transferred to a microwave tube, sealed with a Teflon cap and heated to 120 °C for 4 h. All samples had a 1 minute pre-stirring step and the MW power was 250 Watt. Hereafter, the powder was filtered off, washed several times with fresh DMF and stirred over night in 50 mL MeOH. The resultant UiO-66(Zr/M) was dried under vacuum at 80 °C.

Synthesis UiO-66(Ce)

This synthesis is taken from Lammert et al. [119]. 213 μmol of linker (BDC or fumaric acid) was introduced into a glass tube and dissolved in N,N-dimethyl formamide (DMF) (1.2 mL). After 10 min ultrasonification, an aqueous solution of cerium(IV) ammonium nitrate (400 μL , 0.53 M) was added. The tube was heated under stirring in a heating block for 15 min to 100 °C. The resulting pale yellow precipitate was filtered off, washed several times with DMF and acetone and dried at 70 °C in dynamic vacuum.

7.2.2 Characterization

XRD, N_2 -sorption, XPS, UV/Vis and PL equipment were already introduced in chapter 4. Bright-field scanning transmission electron microscopy (BF-STEM) and EDX measurements were performed on a JEOL JEM-2200FS high resolution scanning transmission electron microscope equipped with an EDX spectrometer with a spatial resolution of 0.13 nm, image lens spherical aberration

corrector, electron energy loss spectrometer (filter) and a field emission gun (FEG) operating at 200 keV.

7.2.3 Empirical model for charge-state transition levels

Lanthanide ions show similar properties irrespective of their chemical environment. [261] The 4f valence electrons are well shielded from the exterior of the atom by the filled 5s and 5p shells, implying that a lanthanide ion shows similar properties irrespective of its chemical environment. [261] A well-known example are the $4f^N-4f^N$ luminescence spectra that are lanthanide-specific, but change very little with the environment. This insensitivity to the environment leads to a systematic behaviour across the lanthanide series resulting in a typical ‘zig-zag’ curve for various physical properties as a function of the 4f occupation number of the lanthanides. Such curves are often constructed in Ln-doped oxide materials to predict charge-transition states of the whole series compared to the band edges of the host electronic structure (Host Referred Binding Energy, HRBE) using experimental spectroscopic data. This methodology is reviewed in [256–258] and is known to give transition level locations of lanthanide impurities in inorganic crystals within accuracies of a few 100 meV². Recently, an extension of the empirical rules was proposed towards titanium. [262] Given the importance of Ti doping in UiO-66 and the current interest for photocatalytic applications, we include it in our empirical model as well. This offers a way to verify the model and make the bridge between isovalent transition metal dopants and the Ln series.

7.2.4 Computational details

In addition to the empirical model used to construct the Ln charge state transition levels, we also opted to further unravel the electronic properties of a carefully selected subset of samples by using Density Functional Theory (DFT) based methods. Since the behaviour of Ln ions is notoriously difficult to predict with DFT, we only performed UiO-66:Ln calculations with Ce⁴⁺. Because Ce⁴⁺ contains no 4f or 5d electrons, the electron correlation is limited and DFT has been shown to provide reasonable qualitative results. [263,264] Periodic calculations revealed the band structures of the pristine UiO-66, UiO-66(Ti), UiO-66(Hf) and UiO-66(Ce) material. These band structure calculations are ground state calculations. Because excited state calculations on periodic systems are still challenging within current computational models, we performed Time-Dependent DFT (TDDFT) calculations

on some well-defined clusters. These calculations allowed us to study the possible excitations and yielded qualitative information on the orbitals involved.

Periodic models

Periodic calculations were performed on a 4-node unit cell within the VASP package [188, 215], using the Projector Augmented Wave approach (PAW) [216] with the recommended high precision GW PAW potentials [167] and the PBE functional [217]. Although PBE is known to underestimate band gaps severely, it has been observed in numerous studies that it reproduces trends correctly as shown earlier in this work. The plane wave basis set had a kinetic energy cut-off of 700 eV, and a Γ -only grid was used to sample the first Brillouin zone. The equilibrium volume was obtained using a Rose-Vinet equation-of-state fit (9 points between -4% and 4% of the equilibrium volume) [265] and the structures were relaxed at this volume, using an ionic energy criterion of 10^{-4} eV and an electronic convergence criterion of 10^{-7} eV. Densities of states (DOS) were calculated using a Γ -centred $2 \times 2 \times 2$ grid.

Calculations on cluster models

Calculations on cluster models were done in Gaussian09 [187] using DFT on a series of simplified model systems. Both clusters with stoichiometry $\text{Zr}_{6-x}\text{X}_x\text{O}_4(\text{OH})_4(\text{HCOO})_{12}$ and $\text{Zr}_{6-x}\text{X}_x\text{O}_4(\text{OH})_4(\text{HCOO}^-)_{10}(\text{HBDC})_2$ were used to investigate the influence of the dopant ion. In the previous chapters we have shown that the combination of the B3LYP [201, 202] functional with a triple- ζ Def2TZVP basis set [206] is a good choice for these cluster calculations and hence we applied the same settings in this work. Geometry optimization of the clusters was performed on the same level.

Two types of calculations were performed: ground-state DFT and Time-Dependent DFT (TDDFT). In order to mimic the cluster after excitation and LMCT of the framework, we performed ground-state DFT calculations on the model cluster with one extra electron. [266] In this way, the system is forced in a doublet spin state and a charge of -1. This allowed us to look into the ideal case where the electron efficiently transfers to the inorganic node, and to study the potential preferential sites in these nodes for the electron to reside. Actual modeling of excited states is computationally much more demanding. TDDFT within its linear-response formulation offers a way to calculate vertical transition energies, which can be linked to experimental UV/Vis spectra. [180, 227, 267] To visually improve the similarity with the experimental

spectra, a Gaussian distribution ($\sigma=0.4$ eV) was used to broaden the theoretical transition energies.

7.3 Results and discussion

The first part of this work describes the synthesis and characterization of the different doped UiO-66 samples in detail and provides an overview of the discussed samples in this work. Secondly, spectroscopic techniques are used to probe the electronic structure of the samples. Next, using the experimental data, we reconstruct the typical lanthanide ‘zig-zag’ curve of the (2+/3+) and (3+/4+) charge state transition levels relative to the UiO-66 band diagram. Finally, via DFT calculations on cluster and periodical models, more insight is obtained in the charge transfer processes in titanium- and lanthanide-doped materials.

7.3.1 Synthesis and Characterization

We synthesized UiO-66 doped with 5 different lanthanide and transition metal ions using a post-synthetic cation exchange method. (see table 7.1). Post-synthetic cation exchange is a synthetic technique that allows the modification of existing stable materials and the production of systems with otherwise unreachable compositions. [241, 268] It is only in the last decade that the cation techniques applied to other inorganic materials [269–271] came into use within MOF chemistry. Compared to a conventional solvothermal approach, which is an energy and time consuming process, the use of a microwave-assisted approach as proposed for UiO-66 by Tu et al. [260] allows for a drastic reduction in synthesis time from about a week to only a few hours to obtain a similar loading. We based our procedure on this doping strategy and extended its application to the incorporation of lanthanide ions as dopant in the framework.

A thorough experimental characterization was performed on all samples shown in table 7.1 and the data are provided in supporting information (section S2). These data show that after the cation exchange, all samples retained their crystallinity and porosity. Moreover, the shift of the low angle diffraction peaks and the fact that no new peaks are observed in the XRD diffractogram can suggest that dopant ions are included on a Zr site and that no other Ti-O or Ln-O species are formed. Nitrogen sorption measurements indicate that the original UiO material is well preserved since the materials retain their high surface area (figure 7.3). However, the observed reduction can be due to a partial blocking of the pores through e.g. absorbed metal precursors.

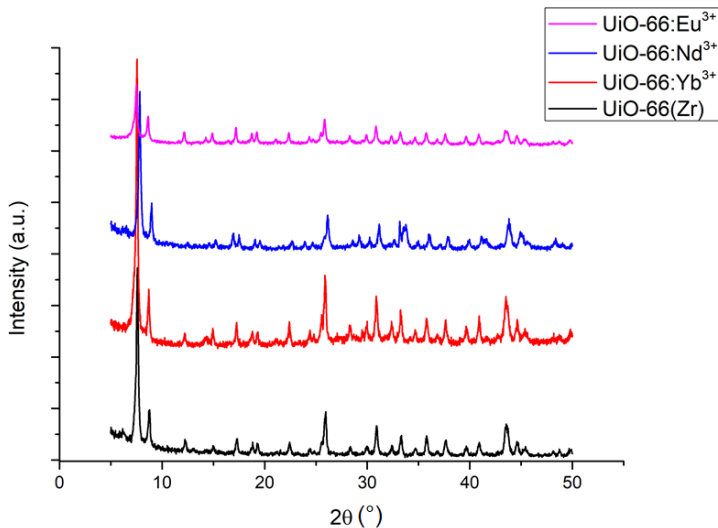


Figure 7.2: XRD diffractograms of pristine UiO-66 compared to different Ln-doped frameworks

Whether dopant ions are inserted on a Zr position in the metal node or are adsorbed at a defect site is nevertheless still subject of much debate. [272] Direct proof however is very hard to obtain and this matter still remains open for discussion. A combination of two effects can also occur and can explain the seemingly contradictory results.

The distribution of the dopant ions was verified using BF-STEM EDX measurements. Figure 7.5 shows that the Ce^{4+} ions are distributed quite homogeneously and no cluster formation is observed. We however notice that some surface enrichment can be seen, probably due to the diffusion limitations of the precursor in the material. Similar measurements were performed on $\text{Eu}^{3+}/\text{Yb}^{3+}$ doped samples (figures 7.6 and 7.7). In the following sections, our focus will be mainly on the Ce^{4+} - and Eu^{3+} - doped materials. This gives sufficient information to construct the charge state transition zig-zag curve for both $2+/3+$ and $3+/4+$ transitions. Later in this work, they will be compared to our DFT calculations on the pristine UiO-66 and Ti^{4+} doped materials.

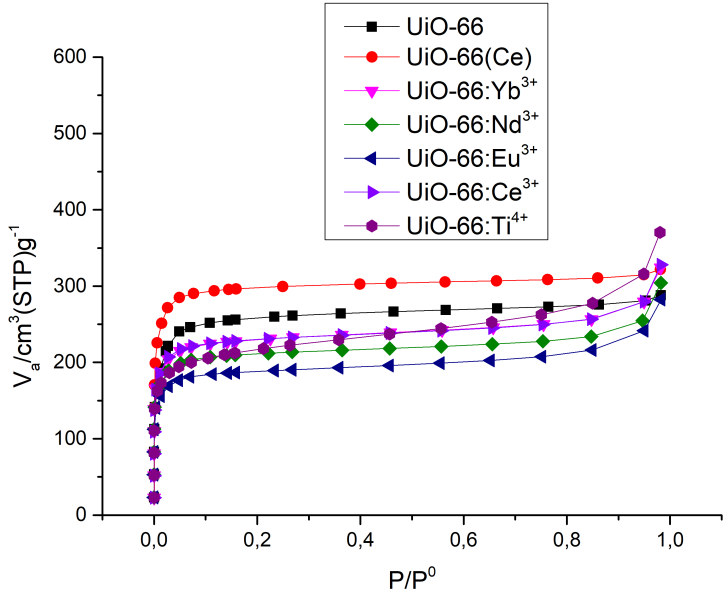


Figure 7.3: N_2 uptake of doped UiO-66 samples.

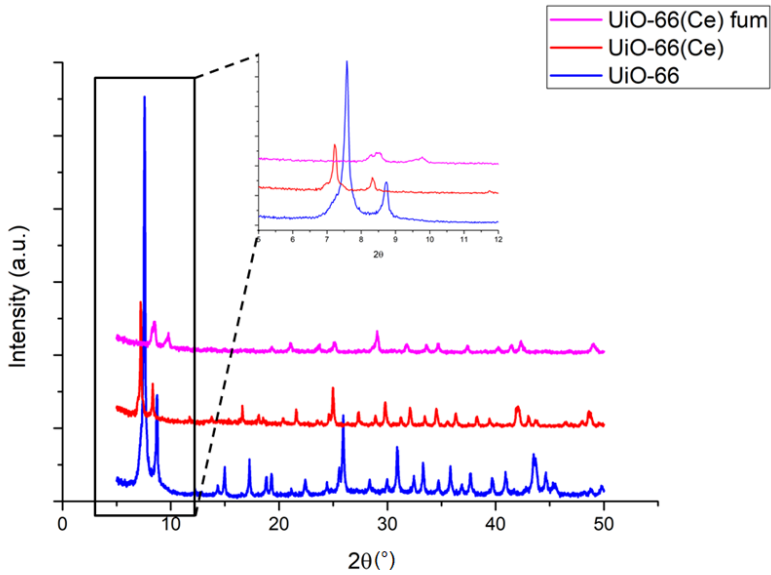


Figure 7.4: XRD diffractograms of UiO-66(Ce), UiO-66:Ce⁴⁺ and UiO-66-fum(Ce)

Sample name	Metal ion concentrations	linker
UiO-66	100% Zr ⁴⁺	BDC
UiO-66(Ce)	100% Ce ⁴⁺	BDC
UiO-66:Ce ⁴⁺	1-5% Ce ⁴⁺	BDC
UiO-66-NH ₂ :Ce ⁴⁺	1-5% Ce ⁴⁺	BDC-NH ₂
UiO-66-fum:Ce ⁴⁺	1-5% Ce ⁴⁺	Fum
UiO-66:Nd ³⁺	1-5% Nd ³⁺	BDC
UiO-66:Eu ³⁺	1-5% Eu ³⁺	BDC
UiO-66:Yb ³⁺	1-5% Yb ³⁺	BDC
UiO-66:Ti ⁴⁺	5% Ti ⁴⁺	BDC
UiO-66-NH ₂ :Ti ⁴⁺	5% Ti ⁴⁺	BDC-NH ₂

Table 7.1: Overview of samples studied in this work. The doped samples are indicated as UiO-66:Xⁿ⁺. Ion concentrations are obtained by fitting of the (TEM/SEM)-EDX results and are prone to large errors. However, similar loadings for all samples were obtained. The loading of the UiO-66:Ti⁴⁺ was verified via Inductive Coupled Plasma Optical Emission Spectroscopy (ICP-OES). BDC is the benzene-1,4-dicarboxylic acid linker, BDC-NH₂ is 2-amino-benzene-1,4-dicarboxylic acid and Fum represents fumaric acid.

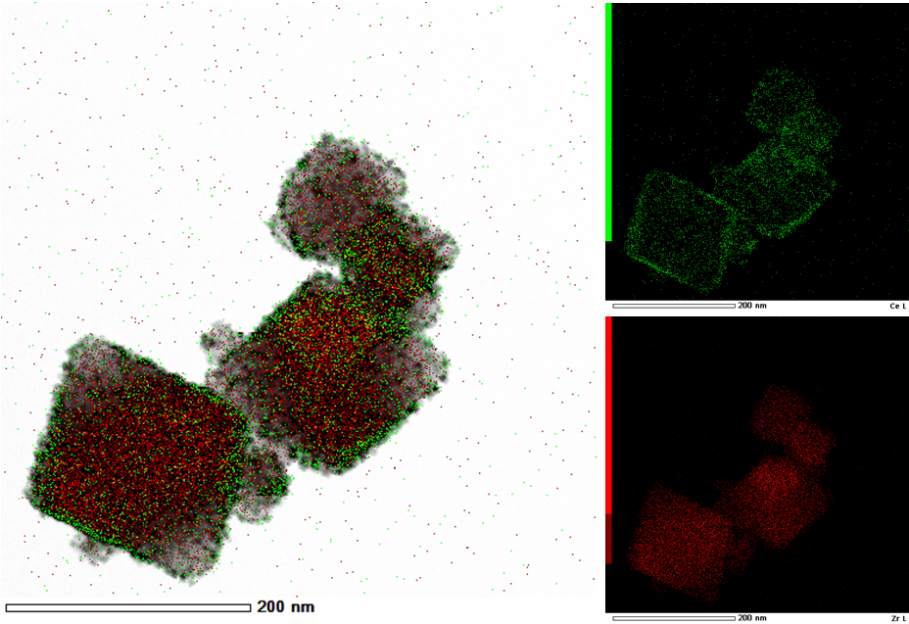


Figure 7.5: BF-STEM EDX profiles of Ce atoms (green) and Zr atoms (red) within a UiO-66:Ce⁴⁺ sample.

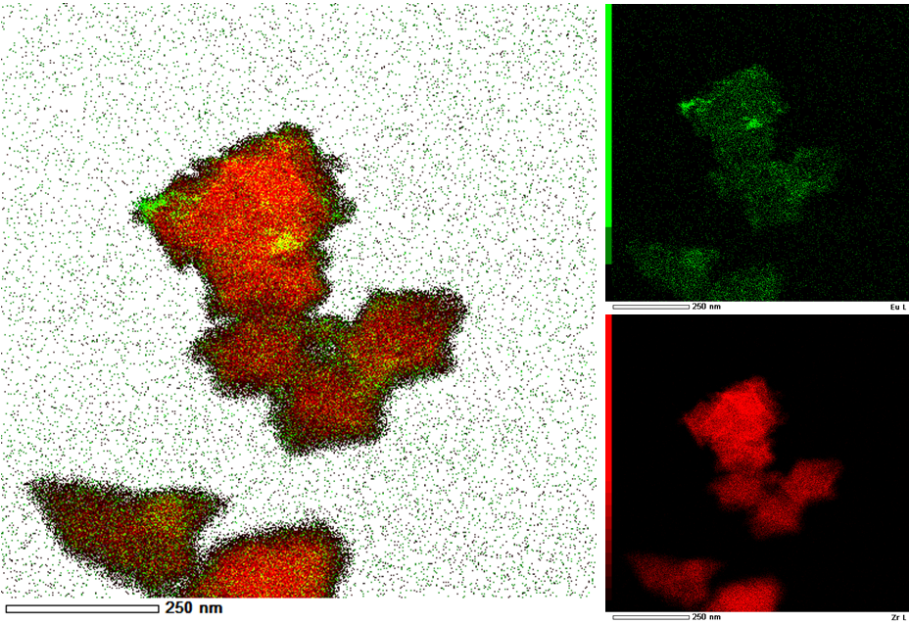


Figure 7.6: BF-STEM EDX profiles of Eu (green) and Zr (red)

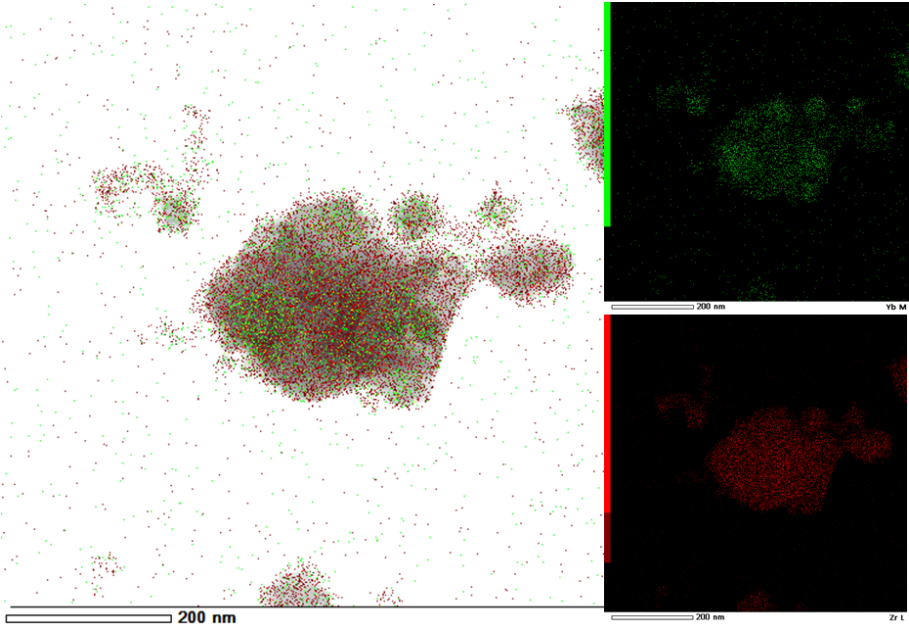


Figure 7.7: BF-STEM EDX profiles of Yb (green) and Zr (red)

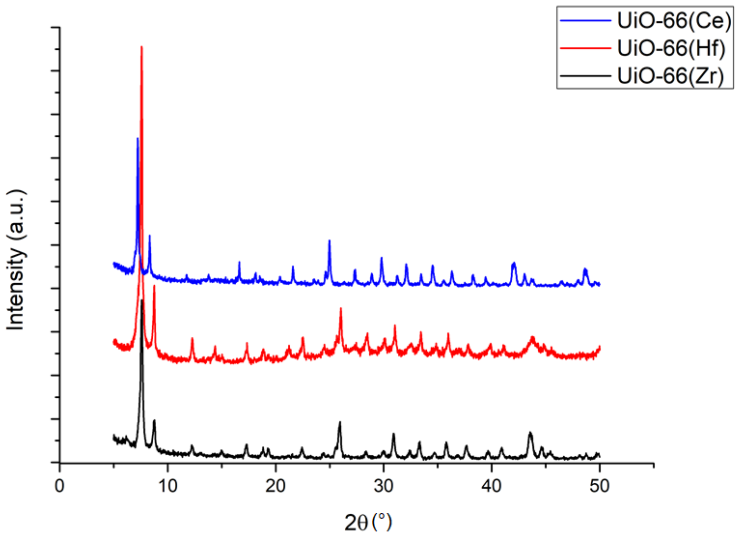


Figure 7.8: XRD diffractograms of the three pure UiO materials: UiO-66(Zr), UiO-66(Ce) and UiO-66(Hf)

7.3.2 Spectroscopy

UV/Vis and photoluminescence (PL) measurements were performed to probe the electronic structure of the UiO materials. The former give information on direct transitions, directly related to the band gap of the material. Interpretation of the latter is more involved, since excited state relaxations and inter-system conversions are can occur before a photon is emitted by the material. Combination of the two techniques allows to understand on a fundamental level the electronic structure of the materials and provides the necessary information for the construction of the Ln zig-zag curve.

UV/Vis measurements of doped UiO-66: X^{n+}

When assessing the electronic properties of photoactive doped UiO materials, it is instructive to compare the new materials to the known titanium-doped UiO-66. Figure 7.9 shows the UV/Vis Kubelka-Munk function of pristine UiO-66 and UiO-66: Ti^{4+} and of their amino-functionalized counterparts obtained from Diffuse Reflectance measurements. The largest shift of the absorption edge is due to the amine group of the linker-functionalized material (region **B** in fig. 7.9). (see chapter 5) Comparing UiO-66 to UiO-66: Ti^{4+} material, we observe a shift and broadening of the UV edge due to the strong Ti-O-Zr interactions (region **A** in fig. 7.9). The interaction of the metal node with the linker also leads to a shift of the NH_2 absorption of the amine-functionalized materials (region **C** in fig. 7.9). The influence of the nearby metal node on the absorption maximum of the linker (regions **A** and **C**) has been observed and discussed in literature [243, 245] and will be discussed in more detail later in the computational section of this work.

Figure 7.10 shows the UV/Vis spectra of UiO-66: $^{4+}$ and UiO-66-X(Ce) (X=BDC, fum) materials compared to the pristine UiO-66 and UiO-66- NH_2 materials. We find that independent of the chosen linker (fumaric acid or BDC) the absorption edge of UiO-66-X(Ce) is the same. This indicates that the main absorption in this material is due to a node-based transition rather than a linker transition like in pristine UiO-66. Moreover, the change in band gap is coincidentally about the same as induced by addition of a NH_2 functional group to the linker. We will show in the computational section that this is because insertion of cerium in the inorganic node introduces a new band within the band gap of the pristine UiO-66, similar to what happens in aminofunctionalized UiO-66.

Contrary to the pure cerium materials, the doped UiO-66: Ce^{4+} shows an edge at 4 eV corresponding to the BDC linker transition, similar to pristine

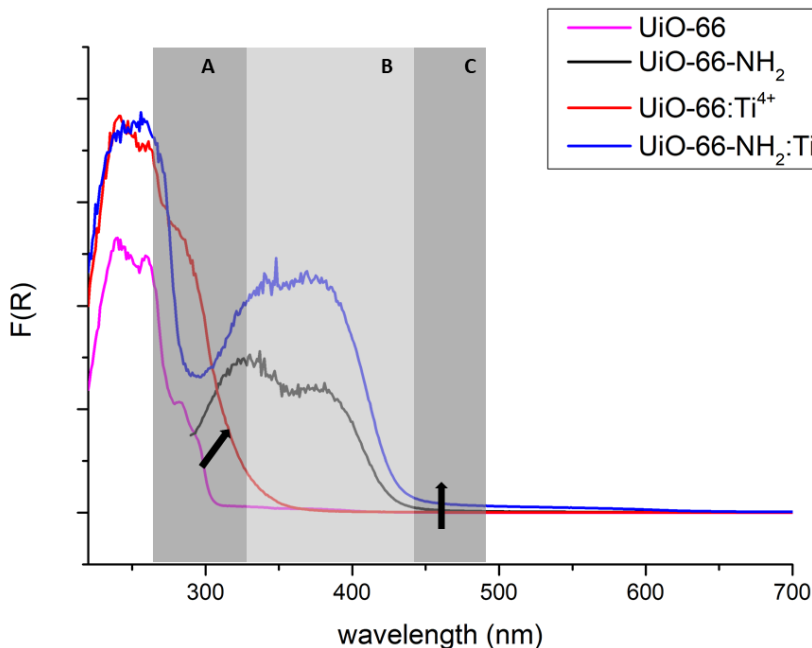


Figure 7.9: UV/Vis spectra in Kubelka-Munk units of pristine UiO-66 and UiO-66-NH₂ materials compared to Ti-doped frameworks. Band **A** shows how the excitation of the aromatic system is influenced by the metal node. The black arrow indicates the shift caused by the changing coordination of the linker. Band **B** corresponds to the absorption of the NH₂ group. Band **C** shows the change in the NH₂ absorption due to the interaction with Ti. Here again, the arrow indicates the shift caused by the titanium.

UiO. However, a new broad band arises in the spectrum, starting at 2.5 eV, which we attribute to a charge transfer process. This band is most likely due to the Ce⁴⁺-O²⁻ LMCT process. The position of this band will be used to construct the charge state transition level curve for the (3+/4+) transition further on.

UV/Vis reflectance spectra of the UiO-66:Yb³⁺ and UiO-66:Nd³⁺ materials are given in figure 7.11. This data is given merely for completeness but is not used in the subsequent discussion.

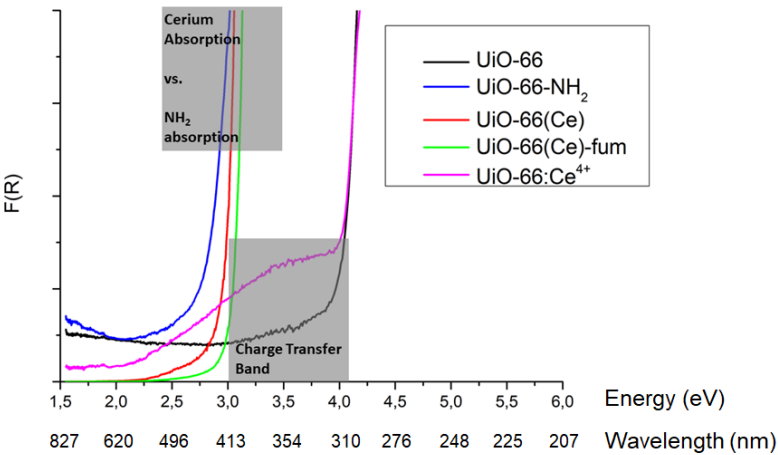


Figure 7.10: UV/Vis spectra of a series of different Ce^{4+} UiO samples compared to pristine UiO-66 and UiO-66- NH_2 . For the nomenclature, see table 7.1.

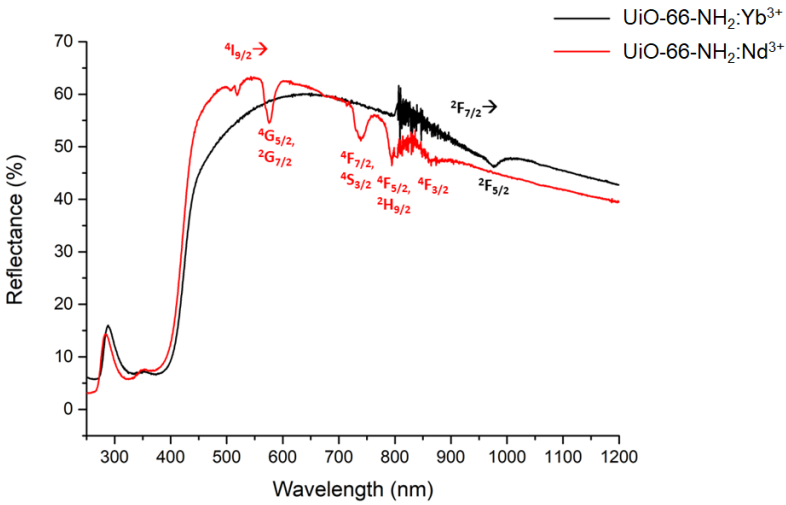


Figure 7.11: UV/Vis reflectance spectra for Nd^{3+} and Yb^{3+} materials

Photo-Luminescence measurements

Eu^{3+} represents one of the spectroscopically most investigated lanthanide ions due to its characteristic red luminescence lines. [273] A typical Jablon-

ski diagram of a generic Eu^{3+} -doped material is presented in figure 7.13 and shows the different pathways that can occur after absorption of a photon by the material. The excited linker can quickly decay to its ground state (fluorescence) or the electron can be transferred via an Intersystem Crossing (ISC) to a triplet state and then to the Eu^{3+} impurity. From there it decays from different levels to the ground state, giving rise to characteristic peaks in the emission spectrum.

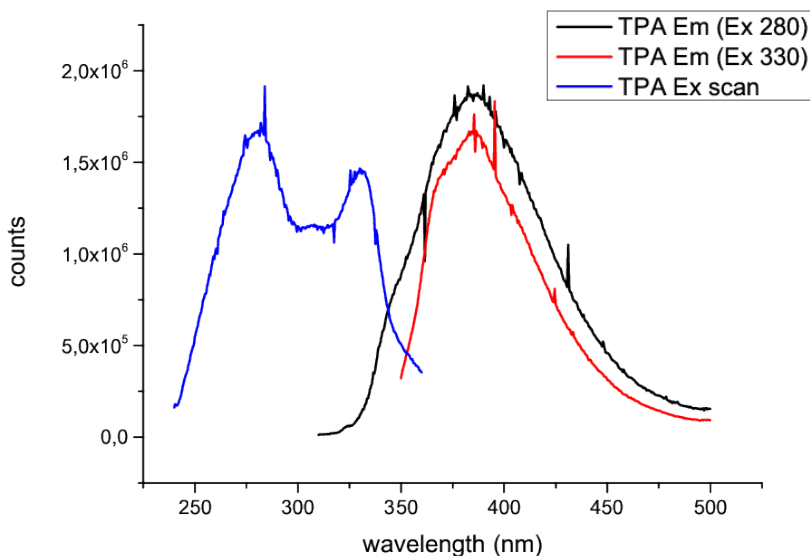


Figure 7.12: Excitation and emission spectrum of pure terephthalic acid (BDC linker). A broad emission band centered around 400nm is observed.

Figure 7.15 shows the emission and excitation spectra of the UiO-66:Eu^{3+} sample. The red line shows a broad linker emission band (see supporting information section S3) ranging to about 550nm followed by the characteristic Eu^{3+} intraconfigurational $4f^6$ lines. [273, 274] By measuring the excitation spectrum for emission at two different wavelengths, we can investigate the mechanisms leading to this specific emission. At 460 nm, only linker emission is found and no Eu^{3+} emission. The excitation spectrum for emission at this wavelength hence shows the characteristic broad band absorption which is also observed for pristine UiO-66 (fig. 7.14) and which corresponds to photon absorption of the linker followed by fluorescent decay. If we however look at the spectrum measured at an emission of 615.5nm, corresponding to the $^5\text{D}_0$

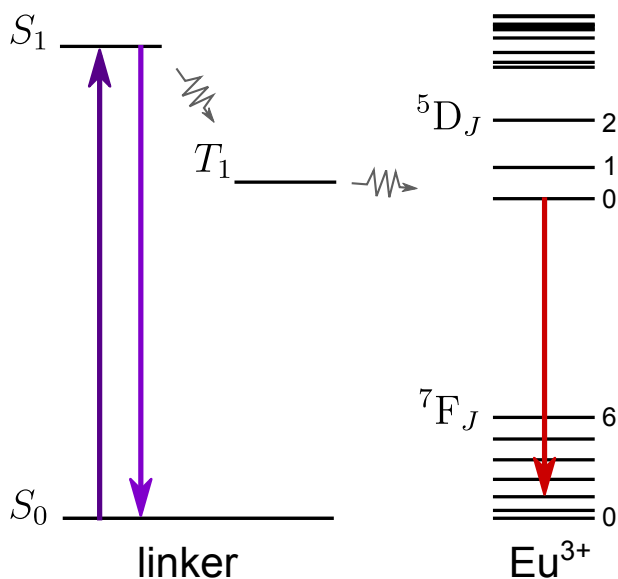


Figure 7.13: A simplified Jablonski diagram showing the energy transfer processes in a generic Eu^{3+} doped MOF. The solid lines indicate the absorption or emission of a photon, wavy lines represent non-radiative transitions (Intersystem crossing or energy transfer)

→ 7F_2 transition of Eu, more features arise. The narrow lines correspond to direct excitation channels of the Eu atoms with following fluorescent decay. More interesting is the broad band which we attribute to a charge transfer band. We attribute this excitation to the $\text{O}^{2-}-\text{Eu}^{3+}$ LMCT and the value of the edge (300nm, 4.1 eV) will be used to position the (2+/3+) transition levels of all other lanthanides in the next section.

7.3.3 Charge-state transition levels

The limited sensitivity of lanthanides to the chemical environment leads to a systematic behaviour across the lanthanide series resulting in a typical ‘zig-zag’ curve for various physical properties across the Ln series. Such curves are often constructed in Ln-doped oxide materials to predict the charge state transition energies of the whole series compared to the band edges of the host electronic structure (Host Referred Binding Energy, HRBE) by means of only a few experimental data points. The LMCT offset obtained from the UV/Vis data (2.5 eV) positions the Ce(3+/4+) level with respect to the HOCO of the pristine UiO-66 band structure. The position of this data point (circled

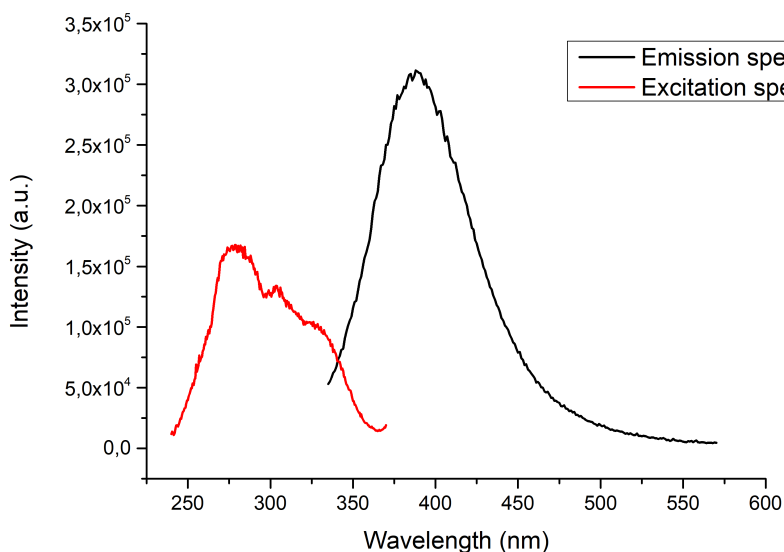


Figure 7.14: Photoluminescence emission and excitation spectrum of pristine UiO-66

dot of the black curve in figure 7.16) fixes the relative energies of the other lanthanides (black line in fig. 7.16). Rogers et al. found that the $\text{Ti}^{(3+/4+)}$ transition level can be found at approximately the same binding energy value as the $\text{Eu}^{(2+/3+)}$ transition level. [262] Because of the relevance of Ti-doped UiO-66, this transition level was also added to the diagram (Fig. 7.16).

Positioning of the $(2+/3+)$ transition curve (blue line in figure 7.16) was possible from the PL measurements performed on UiO-66:Eu^{3+} . The LMCT was found to occur at 4.1 eV and fixes the $\text{Eu}(2+/3+)$ charge state transition energy for Eu (circled blue square in figure 7.16) and as a result the complete $2+/3+$ curve.

The Coulomb correlation energy for Eu, which is typically used as the lanthanide of reference, amounts to 6.87 eV, a typical value calculated for oxides. The correspondence with typical literature values (e.g. Dorenbos et al. [275]) confirms our correct interpretation of the excitation/emission spectra. This value allows to calculate the location of the vacuum level in the band diagram and hence calculate all binding energies relative to this values (Vacuum-Referred Binding Energy, VRBE).

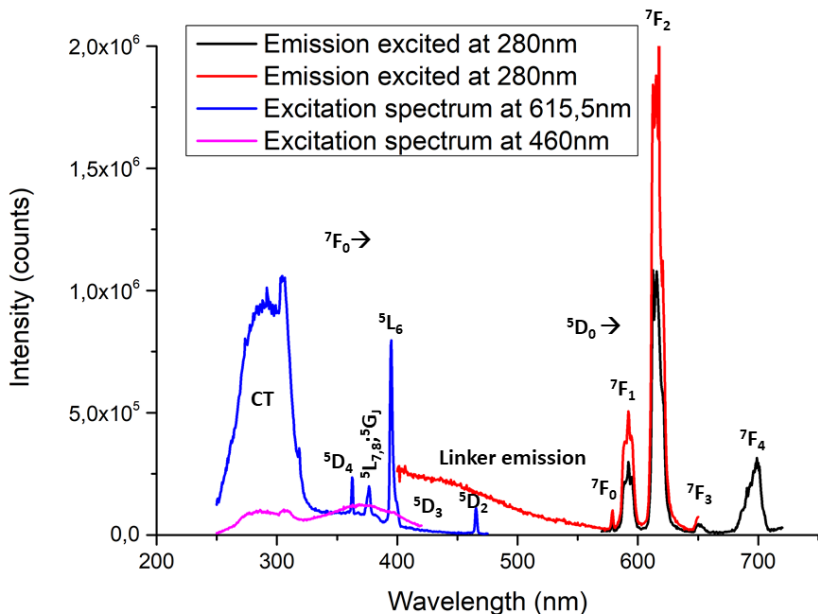


Figure 7.15: Europium emission and excitation spectrum of UiO-66:Eu³⁺

From the diagram in fig. 7.16, it is observed that the Ti^(3+/4+) level and hence the LMCT of Ti⁴⁺ is resonant with the material's HOCO-LUCO gap, explaining the improved electron mobility observed for this material after excitation. The overlap between the Ti^(3+/4+) level and the LUCO of UiO-66 is believed to be the cause for the increased photocatalytic activity for UiO-66:Ti⁴⁺, since an excited electron of the linker has sufficient energy to move to the dopant ion. Following the same reasoning, all Ln ions with charge state transition levels near or below the UiO-66 LUCO region could potentially be the target of an LMCT process upon excitation of the UiO host (e.g. Pr, Sm or Tb). In order to validate this assumption, the transfer is investigated in the next section via absolute luminescence intensity measurements. Further on, DFT calculations will be performed on Ti- and Ce-doped samples to corroborate our findings.

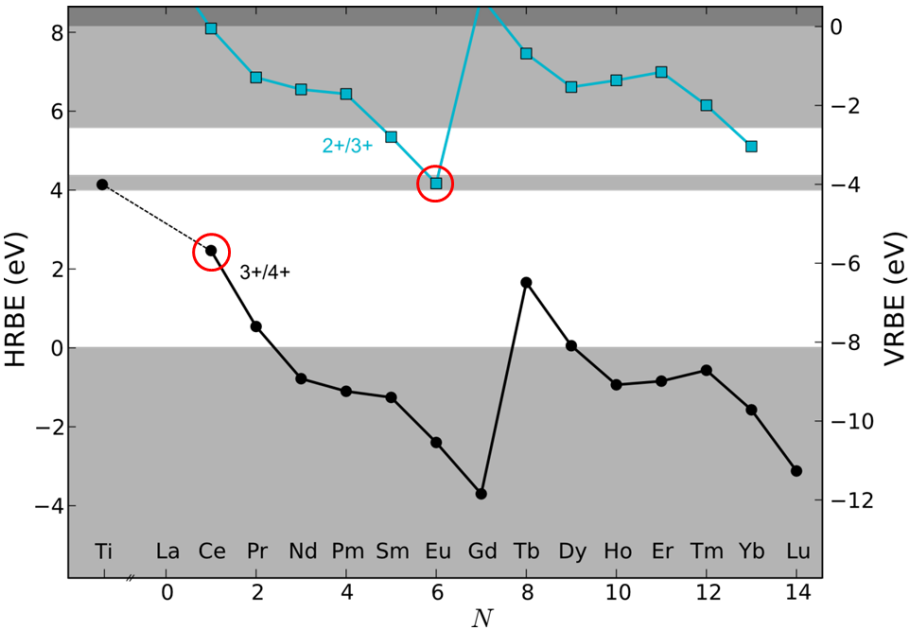


Figure 7.16: Overlay of the band diagram of UiO-66 (grey) with the charge state transition levels for the lanthanide series for both (3+/4+) transitions (black zig-zag curve) and (2+/3+) transitions (blue zig-zag curve) incorporated as impurities in the UiO-66 host. The curves are calibrated using the LMCT absorption edges obtained for UiO-66:Ce⁴⁺ (3+/4+) and UiO-66:Eu³⁺ (2+/3+) as indicated by the red circles. Titanium can also be included using a recently proposed expansion of the empirical model. [262] Values are referred to the vacuum (VRBE, Vacuum-Referred Binding Energy) or relative to the host material (HRBE, Host-Referred Binding Energy)

Absolute intensities

From the PL measurements, we know that the unfunctionalized linker shows a broad band emission, centred around 400 nm (see supporting information section S3). This band is due to the recombination of the exciton, centred on the linker, with emission of a photon. The doped UiO materials aim to impede this direct recombination pathway by inducing energy transfer to the metal ions. The opening of the new decay channel competes with the direct recombination, resulting in a decrease of the linker emission band. The more efficient the LMCT process, the larger the reduction of the linker emission, offering a method to assess the efficiency of the energy transfer via LMCT.

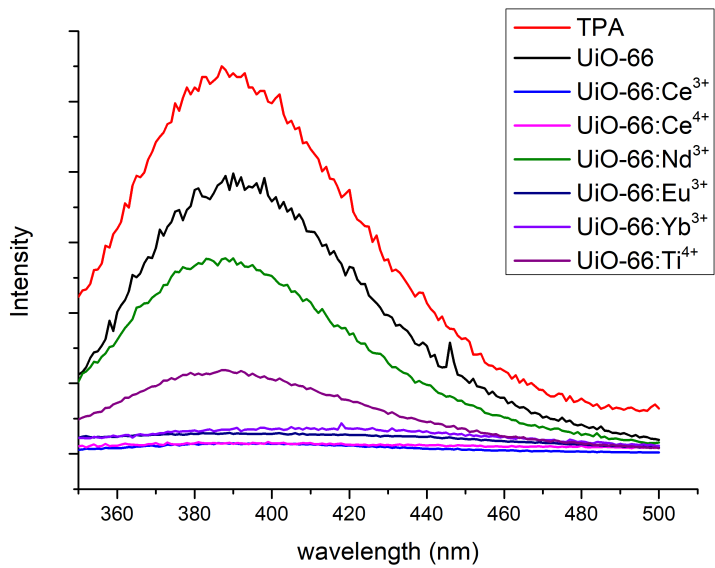


Figure 7.17: Intensity of the linker emission band at 395nm for the different doped UiO materials, excited at 300nm.

The most simple semi-quantitative method to compare absolute emission intensities of powder samples consists of measuring an ‘infinitely’ thick sample. This is done by using a filled cup that is placed in the standard PL set-up. Since the incoming light beam illuminates the entire sample, the emission can be compared amongst different samples in the same set-up.

Table 7.2 shows the integrated intensities of the linker emission band of the different doped UiO samples. They are normalized to the pure UiO-66 emis-

Sample	Integrated intensity (%)
UiO-66	100
UiO-66:Ce ⁴⁺	6
UiO-66:Nd ³⁺	71
UiO-66:Eu ³⁺	12
UiO-66:Yb ³⁺	14
UiO-66:Ti ⁴⁺	31

Table 7.2: Integrated intensities of the linker emission band between 350 and 500nm excited at 300nm. The results are normalized to the UiO-66 emission.

sion and are based on the emission spectra provided in supporting information (section S3). One can observe that by doping the material, the resulting linker emission diminishes, suggesting that it is now in competition with alternative pathways. We see that Ti⁴⁺, Eu³⁺, Yb³⁺ and Ce⁴⁺ all lead to a drastic decrease in intensity. For Ti and Eu we already discussed their beneficial influence on the charge transfer pathway in UiO-66. Indeed, table 7.2 corroborates that an efficient LMCT can take place and the emission intensity drops substantially. For the Ce⁴⁺ sample, almost a complete loss of the emission peak is found. This could also be attributed to a fast energy transfer, but possibly followed by fast energy dissipation via nonradiative pathways, for which Ce⁴⁺ is notorious. [276, 277]

We also have a look at the other lanthanides not thoroughly discussed in the previous sections. About the same drop in intensity as for Eu³⁺ and Ce⁴⁺ can be found for Yb³⁺. Figure 7.16 shows that the interband transition of the host material resonates with the (2+/3+) charge state transition level of the Yb ion, opening a decay pathway via this channel and hence lowering the linker-based emission peak. On the other hand, incorporation of Nd³⁺ leads to a much smaller decrease in intensity. This trend corresponds to the observations in figure 7.16, where e.g. Yb has a charge state transition level near the UiO LUCO whilst the Nd^(2+/3+) charge state transition occurs at a much higher energy, meaning that a Nd charge transition will likely not occur.

Figure 7.16 shows that many more possibilities arise for an efficient LMCT, since also e.g. Sm and Tb show charge state transition levels within the UiO-66 band gap. Further investigations of the different Ln-doped UiO-66 materials can yield more insight in the decay pathways and could lead to materials

with improved luminescent properties or increased photocatalytic activity. However, as the results show, the resonance of the Eu or Yb charge state transitions with the HOCO-LUCO energy gap indicates that these doped materials would be first of choice for a further study.

7.3.4 Computational assessment

Cluster models

In order to gain more insight at a fundamental level, a DFT study was performed on a selected subset of the samples. As introduced before, excited state calculations on periodic systems are still challenging for current computational models. We therefore performed TDDFT calculations on some well-defined clusters. We focused on isovalent dopant ions (Ti or Hf) because isovalent substitution in UiO-66 is by now sufficiently understood to serve as a reference and does not offer computational difficulties. In addition, ground state calculations were performed on isovalently substituted UiO-66 with a single negative charge (and doublet spin state). This can serve as a model of the cluster after charge transfer from the linker has occurred. Observation of the SOMO (Singly Occupied Molecular Orbital) yields insight in the localization of this excess negative charge. Periodic data are presented afterwards and offer insights in the ground state electronic structure, which can be qualitatively linked to the observed changes in the experimental data.

First, we performed calculations on a series of simplified cluster models, consisting of one inorganic node, terminated with formic acid, resulting in a total stoichiometry of $\text{Zr}_{6-n}\text{M}_n\text{O}_4(\text{OH})_4(\text{HCOO})_6$ with M being Ti^{4+} or Hf^{4+} . Figure 7.18 shows three cluster models. Left, we show a node built from 6 Zr atoms. The SOMO orbital shows that the extra electron is uniformly distributed over the whole node. The same is true for node depicted in the middle of the figure, where the uppermost atom is replaced by a hafnium atom. If we however insert a titanium atom on the same spot (right figure), the electron now is localized on the empty 3d orbitals of the Ti atom.

Even though TDDFT calculations on these small clusters, without aromatic linkers, are severely simplified model systems, inspection of the spectra obtained this way shows some interesting results. The hafnium doped node shows an almost identical spectrum as the pristine Zr node. On the contrary, a peak arises around 320nm caused by the inserted Ti (fig.7.19). Depending on the number of Ti atoms present in the cluster, the oscillator strength of this transition rises and hence the absorption in the spectrum. It should be noted that the 100% titanium UiO has not yet been synthesised as such and

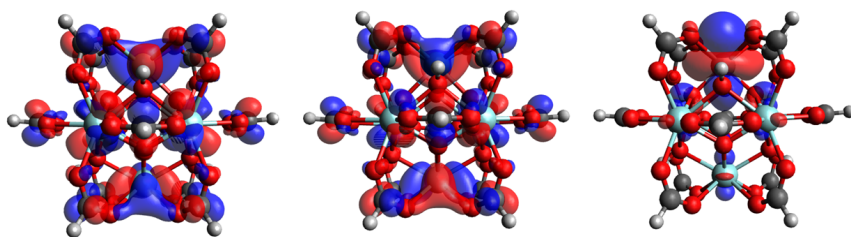


Figure 7.18: Cluster models of $\text{Zr}_6\text{O}_4(\text{OH})_4(\text{HCOO})_{12}$ (left), $\text{Zr}_5\text{Hf}_1\text{O}_4(\text{OH})_4(\text{HCOO})_{12}$ (middle, Hf is the top metal atom) and $\text{Zr}_5\text{Ti}_1\text{O}_4(\text{OH})_4(\text{HCOO})_{12}$ (right, Ti is the top metal atom) calculated at the B3LYP/DEF2TZVP level with a -1 charge and doublet spin state. These models show the localization of the additional electron on the titanium 3d shell (right)

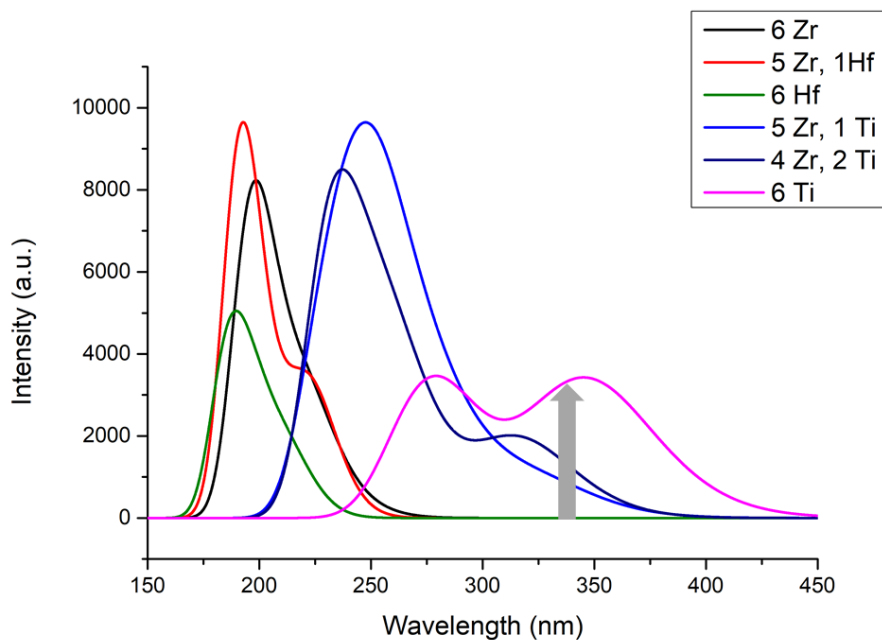


Figure 7.19: TDDFT spectra for simple formic acid terminated clusters with 1 or more Zr replaced by Hf or Ti. The grey arrow indicates the new peak rising as a function of the number of Ti atoms in the cluster and corresponds to an $\text{O}^{2-}-\text{Ti}^{4+}$ excitation.

has to be considered as a limiting case to compare with the other materials. Closer investigation of this transition learns that it concerns a transition from

oxygen-centred p-orbitals (oxygen from the formate anions) towards the Ti 3d orbitals. This shift can be linked to the shift observed experimentally in the A region of figure 7.9. Moreover, this LMCT band is predicted around 4 eV, which corresponds with both experimental (fig. 7.9) and empirical results (fig. 7.16).

The simple cluster models allow to identify the absorption pathways arising upon doping the UiO material. However, the artificial replacement of the linkers by formate anions results in the loss of linker states and is thus a severe approximation. This is why we also studied more complex clusters containing 1 Ti atom, in which two formate capping molecules were replaced by HBDC linkers, terminated by a hydrogen to secure charge balance. The general cluster structure is shown in figure 7.20 where the green atom indicates the dopant and the *R*-group can be H or NH₂. Since much interest has gone to the amine-functionalized variants, showing an even larger increase in photocatalytic activity, we also include an amine modified cluster model in our calculations. The resulting spectra are shown in figure 7.20.

We notice that the results are qualitatively similar to those of fig. 7.19. If we take a closer look at the three main features in the spectrum and couple these to the corresponding orbital transitions (see figure 7.21) we find some characteristic behaviour. Region **A** of fig. 7.19 corresponds to the classical HOMO-LUMO excitation of the linker. The shift of this peak upon inclusion of a titanium atom corresponds to the shift of absorption edges observed experimentally for these materials (indicated as region A in figure 7.9). In region **B**, not only the BDC-NH₂ absorption arises as a small peak just below 400nm, but also a clear absorption caused by the included Ti. In this transition the most important contribution to the orbitals is moved from the p-orbitals of the oxygen atoms of the surrounding carboxylate groups to the Ti 3d orbital (figure 7.21B). This transition is similar to the one observed in the small cluster models shown in figure 7.19. Finally, region **C** in figure 7.19 contains a feature only observed in the amino-functionalized material which has not been reported thus far. It shows a transition between the aromatic ring of the linker, more specifically the HOMO of the complete cluster, and a Ti 3d orbital. This transition only occurs when both an amine group and a Ti atom are present in the system. This gives an indication to why amine-functionalized UiO-66:Ti⁴⁺ shows the largest photocatalytic activity in literature. [243,244]

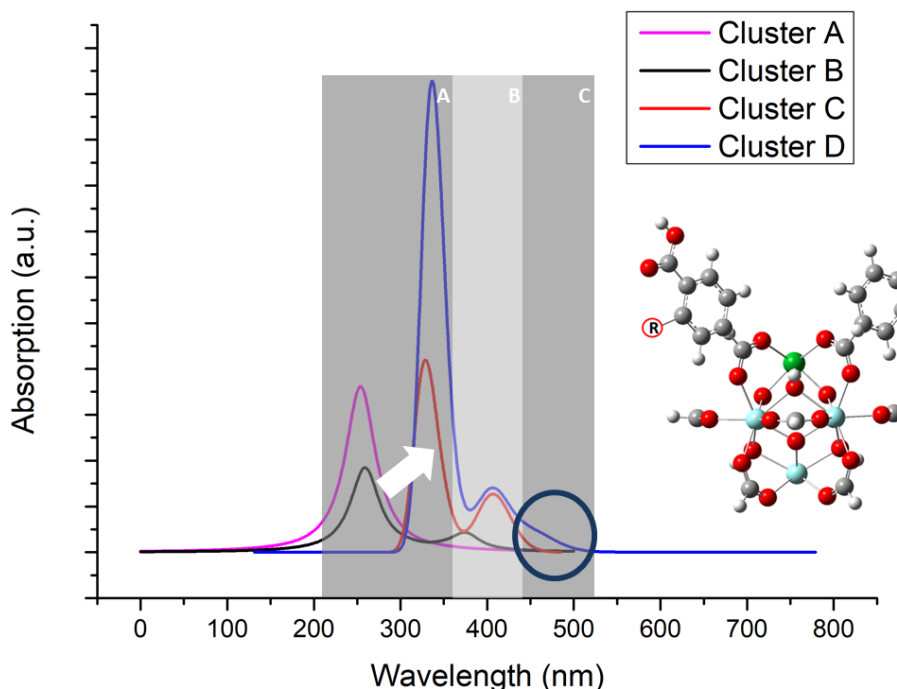


Figure 7.20: TDDFT absorption spectrum (B3LYP/6-311+G(d,p), 30 states) for extended cluster models. (left) The basic cluster model has a stoichiometry of $\text{Zr}_5\text{XO}_4\text{OH}_4(\text{HCOO})_{10}(\text{BDC-R})_2$ with $\text{R} = \text{H}, \text{NH}_2$ and $\text{X} = \text{Zr}, \text{Ti}$ (right). For the shaded regions **A**, **B** and **C**, see text.

Periodic models

In order to gain further insight at a fundamental level, a DFT study was performed on isovalently substituted UiO-66 and UiO-66(Ce) using a periodic model. Figure 7.22 shows the DOS for the four considered structures, consisting of pure Zr, Hf, Ti or Ce nodes. Pure UiO-66(Ti) has not been synthesised as such and has to be considered as a limiting case to compare with the other materials.

As shown by fig. 7.22, the DOS of the Zr and Hf material show almost no difference at all, since the electronic characteristics of the bare ions are very similar. This behaviour was also found experimentally by Nasalevich and co-workers [147] and in the previous section displaying our cluster calculations. On the other hand, introducing titanium in the metal node alters the LUCO states of the material by introducing 3d states that are sufficiently low in energy to go below the linker-based band forming the LUCO of the pristine

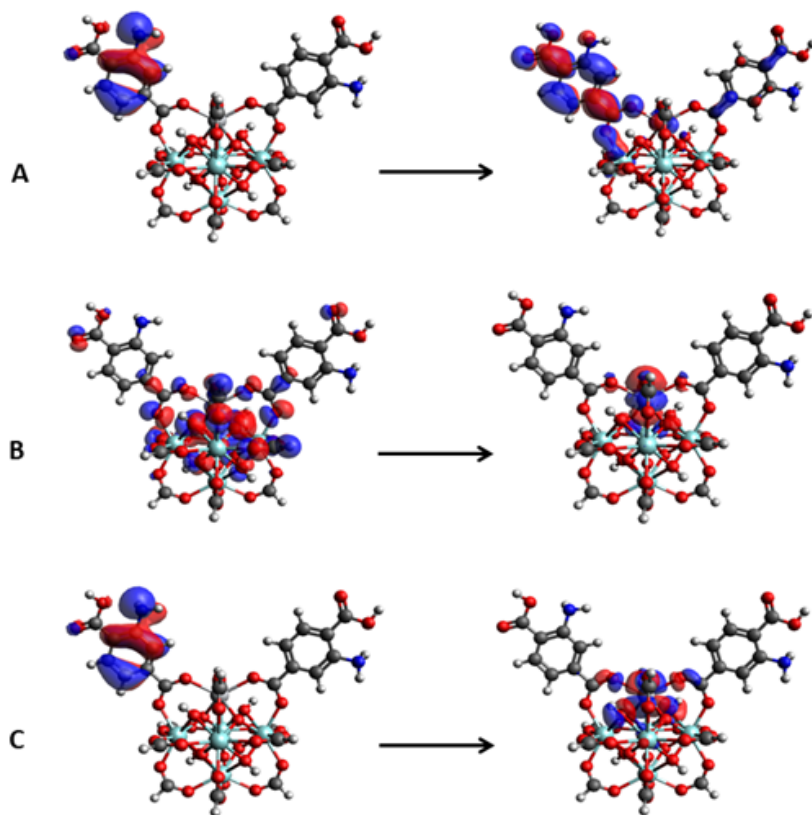


Figure 7.21: Orbitals contributing to the three main excitations observed in the spectrum of figure 7.20 for cluster D.

UiO-66. The overlap between the Ti 3d and the linker orbitals gives evidence for the better charge transfer possibilities of the material, explaining the increased photocatalytic activity observed for this material.

Periodic calculations on the UiO-66(Ce) show the appearance of a broad band within the original HOCO-LUCO gap of the material. This band consists of the empty 4f orbitals of the Ce ions. In the 4+ state, these orbitals are completely empty and hence form the new LUCO state of the material. Therefore, the LUCO changes from ligand-based to metal-based, similar to the Ti-doped material, although no energetic overlap between the new and original LUCO states is now observed. The gap state caused by the introduced cerium occurs at the same energy as the state introduced by an amine group in UiO-66-NH₂ as previously observed. [?] Note that although the effect on

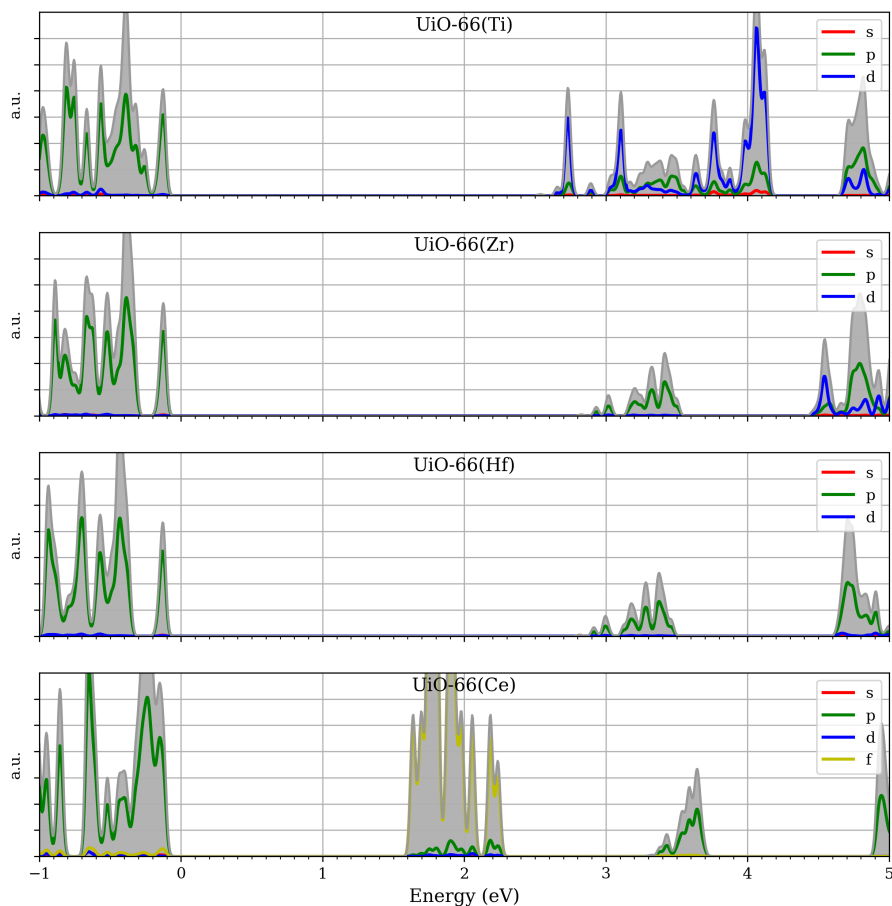


Figure 7.22: DOS of (from top to bottom) UiO-66(Ti), UiO-66(Zr), UiO-66(Hf) and UiO-66(Ce)

the overall band gap is comparable as observed in fig. 7.10, both excitations are physically different. The amine group creates a new HOCO state, since this band is completely filled, and results in a linker-based absorption. In contrast, cerium brings down the LUCO state and an excitation to a cerium level is observed.

The Ce f band can be qualitatively linked to the results obtained in the previous subsections of this work. The broad band observed in the absorption spectrum of figure 7.10 was already attributed to a charge transfer channel. The appearance of the empty 4f band of Ce in the DOS within the band gap of the pristine UiO-66 is energetically reachable for an electron that has been excited to the linker LUMO via an energy transfer process. Moreover, the lo-

cation of this 4f band shows a good correspondence with the thermodynamic ($3+/4+$) charge state transition level shown in figure 7.16. The occurrence of 4f levels in the band gap of UiO-66 indicates that Ce can take different charge states depending on the Fermi level location and that a charge transfer transition, measurable by optical spectroscopy, is to be expected. Equivalently, this means that a charge-state transition level will be present in the band gap. This is in correspondence with the empirical model (Fig. 7.16). The location of the Kohn-Sham single-particle levels (Fig. 7.22) is not exactly the same as the location of the charge-state transition level. This is however not to be expected given their different physical meaning [?, ?, ?, ?]

7.4 Catalysis

In order to support our discussion of the electronic structure of the doped UiO materials and their influence on the electron mobility, a catalytic study would be needed to further corroborate some of our findings and predictions. We performed photocatalytic measurements using a batch and a flow reactor set-up for the gas-phase degradation of several VOCs but unfortunately the overall activity was very limited as compared to liquid-phase reactions which are more common for these materials in literature. However, UiO materials show a large absorption capacity for these volatile organic compounds, offering possibilities for combined absorption/degradation materials for these pollutants.

In order to test the activity of the samples, a long batch run was performed for the degradation of ethanol. Three representative samples are presented in figure 7.23. Pristine UiO-66 did not show any degradation after a 7 hours run. On the contrary, we observe a small degradation of EtOH when performing the runs with Ti-doped samples. For comparison, a run using the P25 reference catalyst shows a much faster degradation within the same time window. However, the results already give an indication that both linker- and node-functionalization are great tools to improve the photocatalytic activity.

To conclude this chapter, the obtained results in the the flow reactor for the breakdown of acetaldehyd are provided in table 7.3. The flow set-up allows for a fast screening of several samples.

From this table, we can see that although some breakdown is measured in each cycle, the results are all worse than the Ti doped samples. The best performing Cerium material appears to be the UiO-66(Ce^{4+}) structure. Further

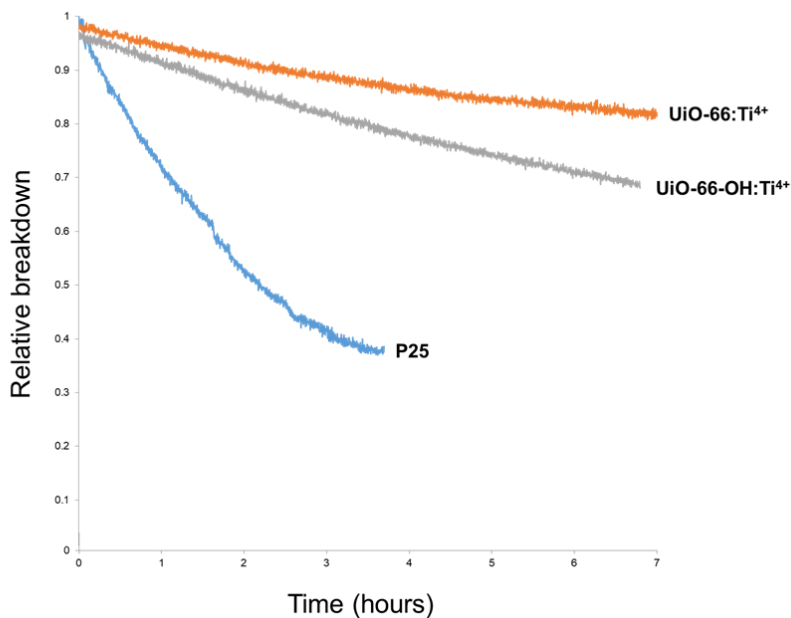


Figure 7.23: Run to compare activities of two titanium doped samples: UiO-66:Ti⁴⁺ and UiO-66-OH:Ti⁴⁺. Pristine UiO-66 showed no degradation. For comparison, a run using P25 (TiO₂) is added as a reference.

Sample	AcAl breakdown (ppm) (%)
UiO-66	0.0
UiO-66-NH ₂	0.0
UiO-66:Ti ⁴⁺	0.8
UiO-66-NH ₂ :Ti ⁴⁺	1.0
UiO-66:Ce ⁴⁺	0.1
UiO-66-NH ₂ :Ce ⁴⁺	0.2
UiO-66(Ce ⁴⁺)	0.5

Table 7.3: Amount of acetaldehyde that has been broken down within 1 cycle (20min).

catalytic tests also including e.g. humid air should be carried out. Also, the reaction time was only 20 minutes for each run, which appears to be limited if we compare to the batch reactor results.

From this section we can conclude that the preliminary catalytic results are

promising, but that further detailed study of the reaction conditions is needed.

7.5 Conclusion

Lanthanide MOFs represent an interesting class of materials with specific electronic properties exploitable for luminescent and photocatalytic applications. Unfortunately, pure Ln-MOFs are notoriously unstable and difficult to synthesise. In this work, a simple microwave-assisted synthesis methodology is proposed for the fast incorporation of transition metal and lanthanide cations in the robust UiO-66 material, opening an entire new set of highly stable materials with unprecedented electronic properties. Combining spectroscopic data with computational results allowed to understand the changes in electronic structure of the different materials in a synergistic way. By using experimentally observed LMCT values in Ce- and Eu-doped UiO samples, a charge state transition curve for both the (2+/3+) transition and the (3+/4+) transition was constructed with respect to the band structure of the host material for the entire Ln series (see fig. 7.16). Absolute intensity measurements confirmed this model showing that for dopants with transition levels resonant to the HOCO-LUCO gap of the UiO-66 an extra decay pathway becomes available. Further confirmation was obtained using DFT calculations. For isovalently substituted samples, only Ti shows a LMCT pathway whilst pure Zr or Hf nodes do not. This is because Ti 3d levels overlap energetically with the linker LUMO state whilst Hf and Zr states only occur in a higher energy range. Cerium insertion in the node introduces an empty 4f band within the pristine UiO-66 band gap. Similar charge transitions were observed for Yb and Eu, identifying these Ln-based material as prime candidates in further catalytic studies. Moreover, the general applicability of our synthesis procedure combined with the stability of the proposed materials may encourage researchers to conduct further studies and open up a new chapter in Ln-MOF luminescence and photocatalytic studies.

8

Improving charge transfer via defect engineering

8.1 Introduction

The previous chapter described the use of metal dopants to reduce the ΔE_{LMCT} and engineer the electronic structure to improve the inefficient charge transfer of the pristine material. In this chapter, we discuss missing linker defects as an alternative pathway to engineer the electronic structure of UiO-66(Zr) and thus its photocatalytic activity. To the best of our knowledge, this work is the first thorough discussion of the influence of different defect structures on the electronic structure of MOFs and the intentional use of defects to engineer it.

Defect engineering is a rising topic within MOF research and offers interesting new opportunities. [278, 279] Both missing linker and missing cluster defects can occur in UiO and appear to yield stable frameworks. Lillerud et al. showed that defects are inherently present in UiO-66 frameworks under normal synthesis conditions. They moreover succeeded in designing synthesis procedures to obtain a defect-free UiO-66(Zr) [280] or to incorporate additional defects. [281] The incorporation of multiple types of defects in a highly controllable manner [280–282] was found to lead to different mechanical properties, [283] catalytic behavior, [128, 219, 284–286] and absorption properties. [287, 288]

Defects are inherently part of any material. Although producing defects requires energy, their formation is favored entropically. Depending on the conditions, the formation free energy of a defect at finite temperature can therefore be sufficiently low to enable its creation. While the synthesis of a defect-free UiO-66(Zr) crystal is possible [280] and can be an objective, defects may also be desirable as they introduce properties that the perfect crystalline material does not possess. Without missing linkers, the Zr atoms in the octahedral nodes are fully coordinated and are not as accessible as active sites. Moreover, missing linkers alter the node structure and thus the corresponding electronic properties. This is of interest for photocatalytic applications of UiO-66(Zr) and will be the subject of this chapter.

The results and text of this chapter are based on:

Missing Linkers: An Alternative Pathway to UiO-66 Electronic Structure Engineering

A. De Vos, K. Hendrickx, P. Van Der Voort, V. Van Speybroeck and K. Lejaeghere, *Chem. Mater.*, **2017**, 29, 3006-3019

Contribution: I performed the cluster calculations and partially wrote the manuscript

8.2 Results and discussion

8.2.1 Defect structures

A (missing linker) defect structure is created by removing a number of benzene dicarboxylate linkers, BDC^{2-} , from the pristine UiO-66. We look at defect structures created by removing one, two, or three linkers from a four-node unit cell. In order to describe the calculations in a systematic way, we opted to introduce a general notation to uniquely define UiO-66 defect structures. Our notation improves upon previous classifications recently proposed in the literature, [128, 283, 289] since the structural characteristics of the defect configuration can be deduced from the name.

There are many ways to remove linkers from a UiO-66 crystal. The number of symmetrically inequivalent ways that linkers can be removed depends on the number of removed linkers and the size of the unit cell. We introduce a general, transparent notation here that depends on the size of the unit cell and thus accounts for the periodicity of the defect structure. It is also easily

extended toward larger unit cells.

When l linkers are removed from an n -node unit cell, we can note the resulting defect structure as $(\text{CN}(1)_\alpha, \text{CN}(2)_\beta, \dots, \text{CN}(n)_\nu)_{\{i\}}$, representing the structure of the material from the point of view of the nodes. Each node configuration, CN_α , is described by its coordination number (CN), to which a subscript is added (α, \dots, ν) to differentiate between nodes with the same coordination number but with a different symmetry. The subscript set $\{i\}$ indicates the $\binom{l}{2}$ interlinker distances between the centers of the l removed linkers and serves to remove any remaining ambiguity. These indices are expressed in terms of coordination shell numbers: 245, for example, means that there are three missing linkers that are second-, fourth-, and fifth-nearest neighbours. Because our notation fully determines the defect structure, the order of the node configurations does not matter. By convention, we order by increasing coordination number and then by alphabetical subscript.

shell	ILD (-)
1	0.354
2	0.500
3	0.612
4	0.707
5	0.866

Table 8.1: Subscript used in our defect structure notation to indicate the distance between the centers of the removed linkers. This interlinker distance (ILD) has been normalized with respect to the lattice constant of the four-node unit cell of UiO-66. It does not take into account potential relaxation caused by removing linkers.

This work considers unit cells with four Zr nodes per unit cell, removing up to three linkers. The possible node configurations and interlinker distances are listed in Figure 8.1 and Table 8.1, respectively. In contrast to the available notations, our notation, e.g. $(10_a, 10_a, 12, 12)_4$, shows at first sight that two linkers are removed from a four-node unit cell with the second linker in the fourth coordination shell of the first, leaving nodes of both 12 and 10_a node configurations.

To ensure neutrality of the inorganic node, the removed negative charge can be compensated by adding a negative ligand [289,290] or by removing a positive proton from the node. [283,291,292] Bristow et al. [289] compared differ-

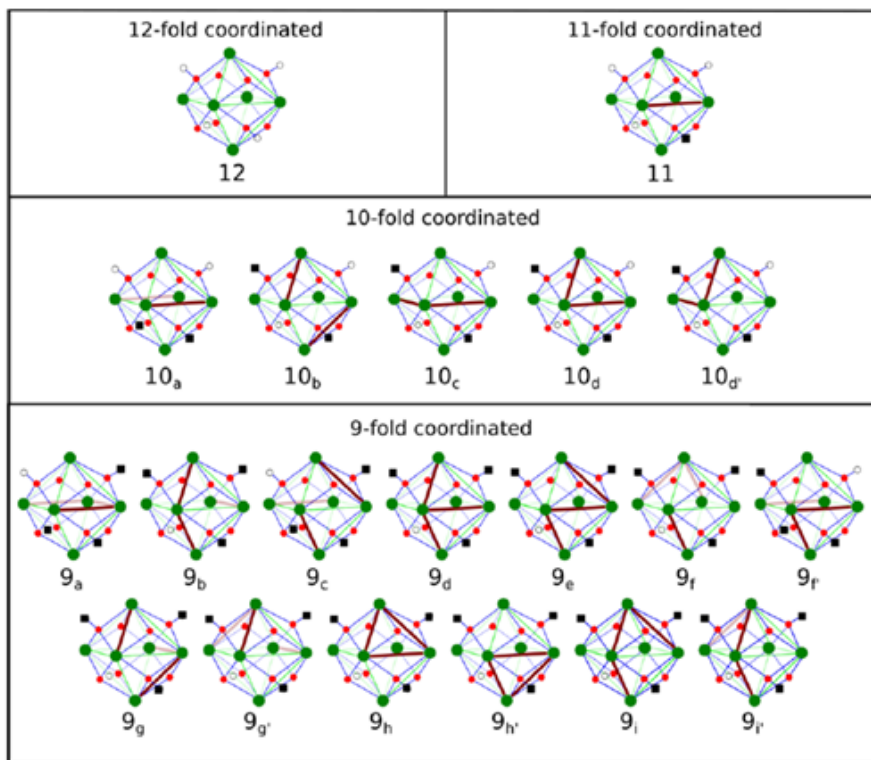


Figure 8.1: Node configurations created by removing zero, one, two or three linkers. Zr atoms are represented in green, O atoms in red and H atoms in white. Red lines indicate where a linker is missing and black squares indicate a removed hydrogen atom to ensure charge neutrality.

ent charge compensation methods for the one-defect structure, (11,11,12,12), and concluded that the acetate capping mechanism (CH_3COO^-), which closely resembles the missing BDC^{2-} linker, was the most stable. However, the acetate cap effectively shields the Zr electrons from potential reactants. In contrast, undercoordinated Zr sites provide more efficient active sites for catalysis. They are created by removing a proton from the inorganic node, for example through reaction with the acetate termination, leaving the node free of both acetate cap and proton. During the process of alternating capping and decapping of the node, the bare node is expected to play the most important role in photocatalytic reactions. In this work, we will therefore only consider deprotonated nodes.

8.2.2 Electronic properties

As explained before, in an ideal photocatalyst, the excited linker electrons should be easily transferred to the node's unoccupied d orbitals. Such an efficient charge transfer requires reducing ΔE_{LMCT} (see Figure 2.17). One possible route is to substitute Zr by other metals as described in the previous chapter. On the other hand, because the removal of linkers alters the nodes, it may lower the unoccupied d orbitals as well. In the next sections, we discuss the DOS of all defect structures created by removing one, two, or three linkers from a four-node unit cell, focusing on the change in the unoccupied d orbitals. To assess the impact of LMCT on the d orbitals, we also performed cluster calculations.

Density of states

A selection of the most relevant DOS is shown in Figure 8.2. Some trends among the different defect structures can be identified. The density of states of the one-defect structure, (11,11,12,12), is almost identical to that of the defect-free UiO-66(Zr), for example (see Figure 8.2). More importantly, the lowest unoccupied d orbitals in the DOS are unchanged. The environment of the Zr atoms in the 11-fold coordinated nodes is apparently not altered sufficiently to influence the character and position of the lowest unoccupied d orbitals, leaving ΔE_{LMCT} unaltered.

Although the removal of one linker introduces charge fluctuations, there is no locally amplified effect between neighboring Zr atoms, with charge imbalances on each face of the node's octahedron canceling out. The only difference in electronic structure between the defect-free and the one-defect structure is seen at the top of the HOCO, where the exact ordering of linker and node states moreover depends slightly on the level of theory. [147, 155, 293] There, the $\mu_3\text{-OH}_2\text{O}$ node states split off a filled gap state because the linker removal lifts the equivalence of the different oxygen atoms. Although this lowers the effective band gap of the material, it does not change the linker excitation energy, ΔE_{abs} , as the linker states are unaltered (see Figure 8.2).

The DOS of the two-defect structures show a similar $\mu_3\text{-OH}_2\text{O}$ node state splitting, again leaving ΔE_{abs} unaltered. More importantly, however, some defect structures also exhibit modified unoccupied d orbitals, decreasing ΔE_{LMCT} . This is the case for all defect structures that contain a 10-fold coordinated node, while no change is seen when only 11-fold coordinated nodes are present. The largest shift of the lowest unoccupied d orbitals is seen for the $(10_d', 11, 11, 12)_1$ (see Figure 8.2) and $(10_d, 11, 11, 12)_1$ defect structures. For both 10_d and $10_d'$

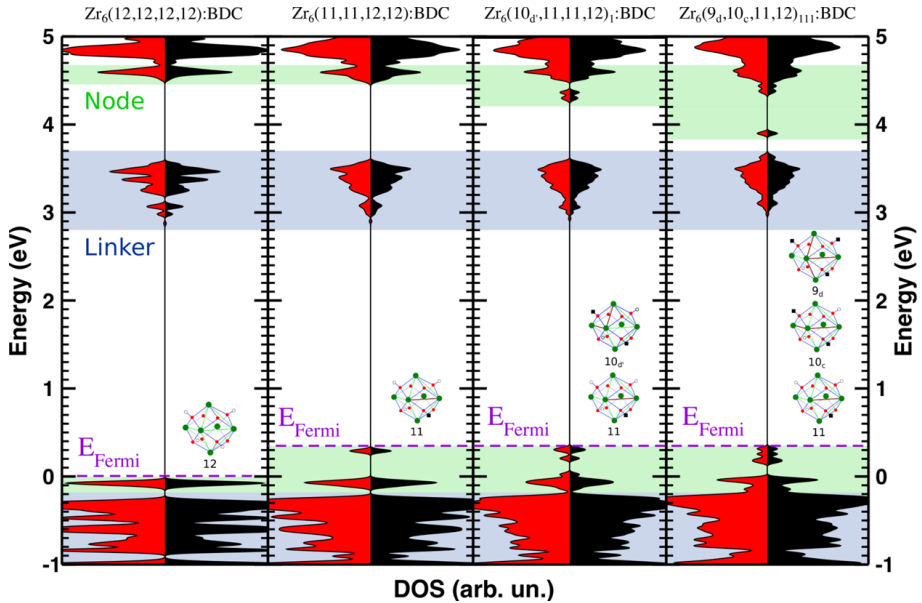


Figure 8.2: Density of states of the pristine, one-, two-, and three-defect structure where all missing linkers were connected to a single node. Red and black curves represent different spin channels, and all DOS are aligned with respect to the pristine μ -OH,O node states. Blue and green indicate linker and node states, respectively.

nodes, the removed linkers are adjacent and connected to the same Zr atom. This suggests that a strongly localized distortion of the environment of the Zr atoms substantially lowers the energy of the d orbitals, potentially improving the photocatalytic activity.

Finally, among three-defect structures, a lowering of the lowest unoccupied d orbitals is quite common, decreasing ΔE_{LMCT} while ΔE_{abs} remains constant. This is partly because many of these defect structures contain 10-fold coordinated nodes. The 9-fold coordinated nodes moreover affect the unoccupied d orbitals as well. Defect structures $(9_d, 10_c, 11, 12)_{111}$ (see Figure 8.2) and $(9_h, 11, 11, 11)_{111}$ show the lowest unoccupied d orbitals and smallest ΔE_{LMCT} , outperforming two-defect structures with 10_d or $10_d'$ nodes. These three-defect structures contain 9-fold coordinated nodes where the environment of the Zr atoms is locally strongly distorted. In the 9_d node, three linkers are missing from a single Zr atom, while for 9_h the three linkers are removed from a single octahedral face of the node.

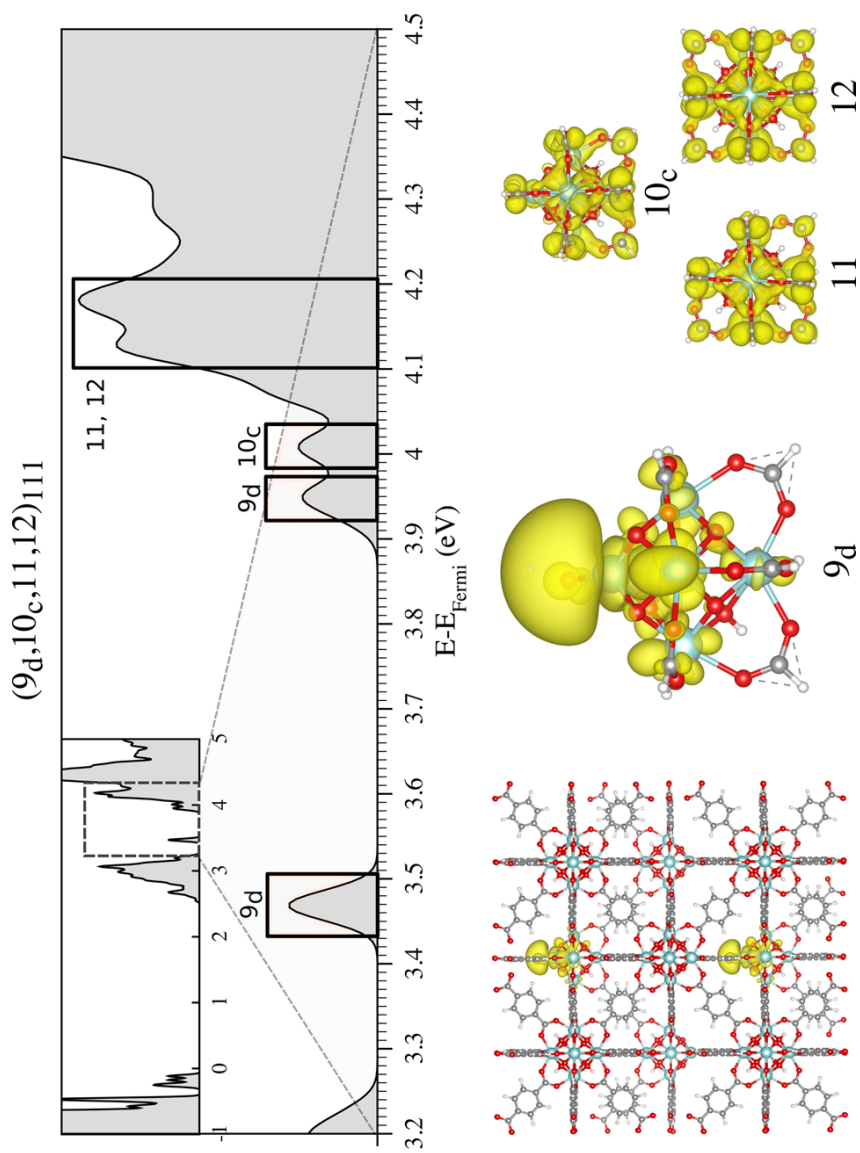


Figure 8.3: (Top) Density of states of the $(9_d, 10_c, 11, 12)_{111}$ defect structure, decomposed in terms of Zr unoccupied d orbitals. (Bottom) Contour plots of the lowest-energy d orbital centered on the 9_d node (left) and the SOMOs of formate capped 9_d , 10_c , 11 and 12 nodes (right)

The position of the unoccupied d orbitals in the DOS, related to ΔE_{LMCT} , is not the only relevant quantity. It is also interesting to see what these d orbitals look like in real space. Such a visualization gives a first impression of how electrons, transferred from the excited linker states, are localized on the target nodes. Figure 8.3 shows the example of a $9_d, 10_c, 11, 12_{111}$ defect structure where the unoccupied d orbitals are localized on different node types. Both defect-free and 11-fold coordinated nodes are characterized by d-states spread over the entire node, while the d orbitals are much more localized in 10- and 9-fold coordinated nodes. In the latter case, the d orbitals are lower in energy and located at sites where the linkers have been removed, ideal for a photocatalytic reaction.

Besides missing linkers, Lillerud et al. recently also discussed the presence of missing nodes as one of the major defect types in UiO-66(Zr). [281] However, removing a complete node has a similar effect on the electronic structure as removing linkers (see Figure 8.4), since the removed node itself does not affect the electronic structure and the edges of the defect consist of nodes with one additional linker missing.

The above observations show that changes in the Zr unoccupied d orbitals are driven by the local environment of the nodes. The behavior of the d orbitals can therefore be deduced to a large extent from the type of nodes present in the defect structure. When only 11-fold coordinated nodes are available, almost no change is seen compared to pristine UiO-66(Zr). However, when more linkers per node are removed, the d orbitals lower in energy and the electron localizes near the site of the missing linkers. The observed energy lowering and electron localization moreover suggest an improved photocatalytic activity. Note that the strongest effects are not necessarily seen for the lowest-energy node types. However, several low-energy nodes also display a noticeable change in the lowest unoccupied d orbitals. One could moreover wonder how important the role of nodes with multiple missing linkers is for photocatalysis, since removing a single linker already suffices to generate an active site. Indeed, the removal of each additional linker generates a supplementary energy cost, but it leads to nodes with increased charge transfer capabilities. In addition, specialized synthesis procedures exist to introduce more defects, [219] leading to lower coordinated nodes with more favorable properties. The 10-fold and 9-fold coordinated nodes are therefore expected to play an important role in the material's photocatalytic activity, be it by nature or by design.

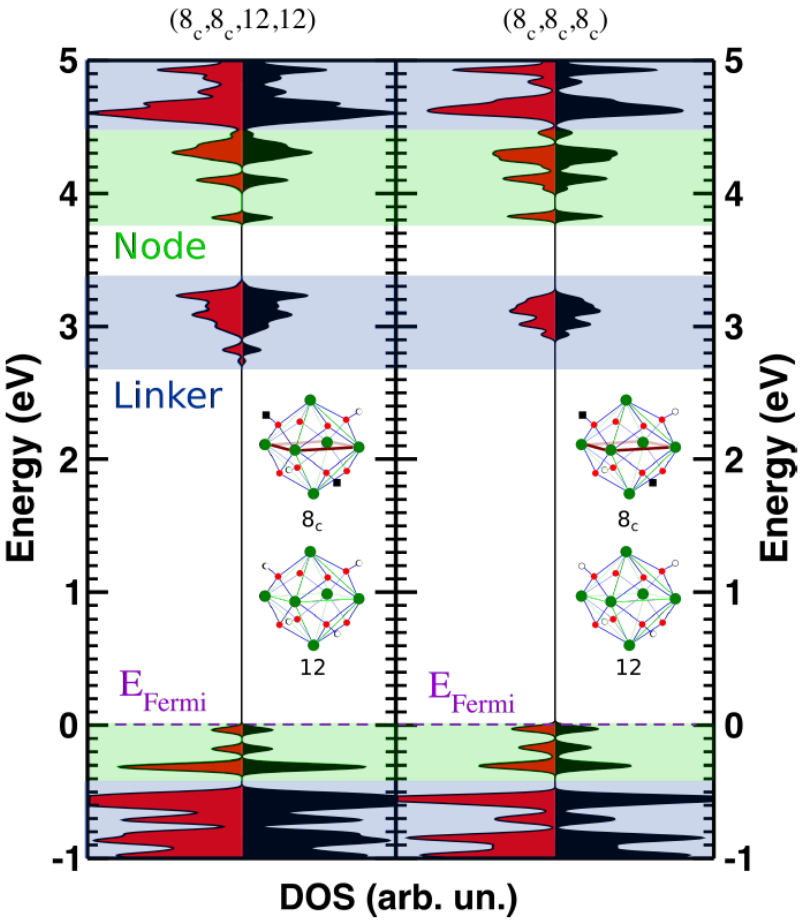


Figure 8.4: Removal of a node from the 4-node unit cell (right) compared to a 4-defect structure in which the linkers are removed to created corresponding node configurations present in a missing node defect structure (left). Red and black curves represent different spin channels and all DOS are aligned with respect to the pristine μ -OH,O node states. Blue and green indicate linker and node states, respectively

Singly Occupied Molecular Orbitals

In an idealized process, a separation of the exciton occurs via a migration of the electron to the unoccupied Zr d orbitals. Although our periodic calculations provide much insight in the ground state electronic structure of UiO-66 materials, it is also instructive to consider what happens after this

ligand-to-metal charge transfer occurs. To obtain more insight into the behaviour of the system after charge transfer, calculations were performed on isolated nodes, replacing linkers by formate termination groups. Indeed, our periodic analysis shows that the properties of individual nodes are to a large extent indicative of the overall properties of the material. The excited cluster is mimicked via ground state DFT calculations, adding one extra electron to the cluster by artificially imposing a -1 charge and a doublet state. While the LUCO in periodic calculations is localized on the linkers (see Figure 2.17), these states are not present in a node cluster model, so the targeted Zr node orbitals become the lowest unoccupied states. This negatively charged model system therefore represents the idealized situation in the framework after excitation and charge transfer.

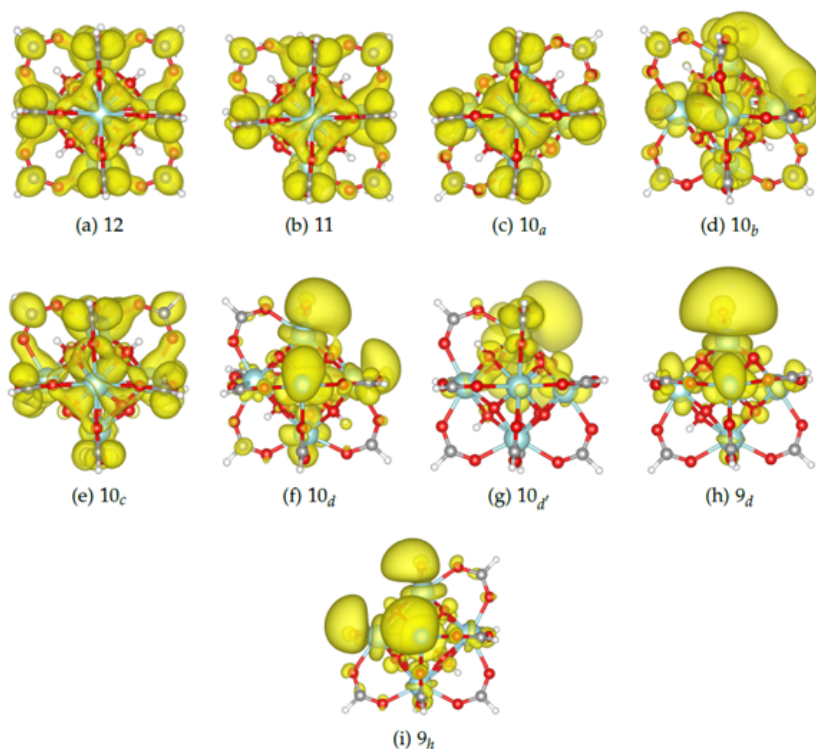


Figure 8.5: The SOMO of calculated cluster configurations with one surplus electron.

Analysis of the orbital contributions to the newly created singly occupied molecular orbital (SOMO) gives information on the sites where the electron preferentially resides. For this analysis, we consider a representative set of

node types, the 12, 11, $10_{a-d'}$, 9_d , and 9_h node configurations, to cover the most important structural features present in the different defect structures. Figure 8.3 and Figure 8.5 allow us to identify the general trends in the changing orbital contributions.

The node with only one defect shows almost no changes in orbital contributions compared to the perfect 12-fold configuration. The extra electron gets delocalized over the whole node. This means that transfer of the electron to a reactant approaching the defect will hardly be improved via a singly defected node. The node configurations with two missing linkers show larger differences in orbital contributions and a less uniform distribution throughout the inorganic node. The effect is again the most pronounced in nodes $10_{d-d'}$, where two linkers are missing from a single Zr atom (see Figure 8.5). The orbital contributions of the thrice defected Zr atoms to the SOMO, present in the 9-fold coordinated nodes, increase even further. These cluster-based SOMOs resemble the unoccupied d orbitals of the periodic calculations (see Figure 8.3), where d orbitals are highly localized on defected nodes with the highest contributions on the lowest coordinated Zr (see Figure 8.3(left)). One can calculate the contributions of an atomic orbital χ_μ to the SOMO via a Mulliken approach:

$$\% = C_\mu^2 + C_\mu \sum_{\nu \neq \mu} C_\nu S_{\nu\mu} \quad (8.1)$$

with C_μ the expansion coefficient of the SOMO in terms of atomic orbital χ_μ and $S_{\nu\mu}$ the overlap between two atomic orbitals χ_μ and χ_ν .

In general, we observe that the contributions from the Zr atoms, compared to the other atoms in the node, increase as the number of defects on the node becomes larger. If one looks at the calculated orbital contributions of node 9_d , for example, the thrice defected Zr atom accounts for half of the orbital contributions to the SOMO. Together with the singly defected Zr atoms in that node type, this amounts up to almost 80% of the SOMO contributions. This shows that when an electron can migrate to a defected node, it will preferably reside on the most defected Zr atom. The preferential localization of the excited electron thus enhances the possibility for a reaction to occur at a defect site, since the electron will be more accessible for approaching reactants.

	$\text{Zr}^{3\times}(\%)$	$\text{Zr}^{2\times}(\%)$	$\text{Zr}^{1\times}(\%)$	$\text{Zr}^{0\times}(\%)$	$\Sigma \text{Zr}(\%)$
12	-	-	-	6.3	38
11	-	-	4.5	6.8	36
10a	-	-	4	16.5	49
10b	-	-	-	12.3	64
10c	-	2	4.5	7	32
10d	-	27	19	7.7	88
10d'	-	35	15.5	6.3	85
9d	49	-	10	7	93
9h	-	21.7	-	9.3	93

Table 8.2: Orbital contributions of Zr-centred atomic orbitals to the SOMO, calculated via a Mulliken approach. Contributions from all Zr types (e.g. Zr^3 represents a thrice defected Zr atom, Zr^0 is a Zr atom with full 8-fold coordination) present in a certain node configuration are shown, normalized to the number of zirconiums of that type.

TDDFT calculations

Similar to the methodology followed in the previous chapters we also studied the actual excited states via TDDFT. The calculated spectra for the studied defect clusters are provided in figure 8.6. Though we see that the shifts do change within the presented series, the differences are too small to compare with our experimental data. Since no new information could be obtained from these calculations we merely present them for completeness and will not provide an extensive treatment.

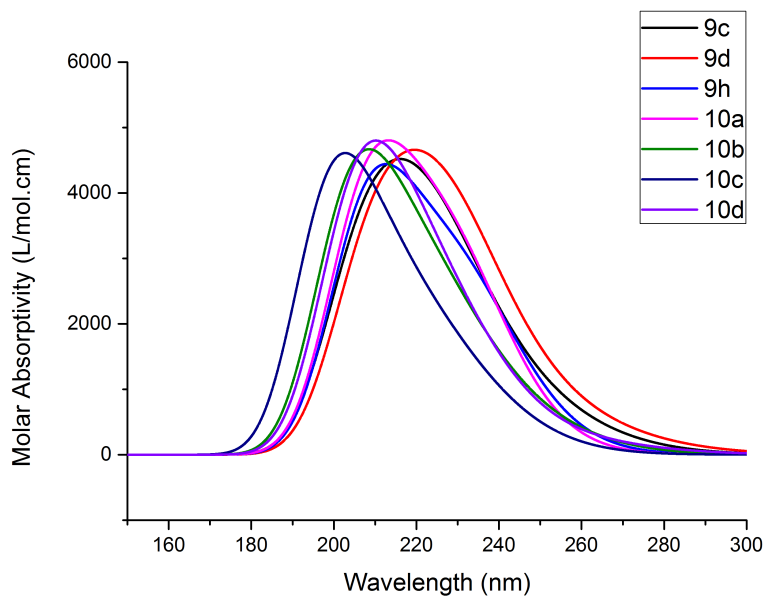


Figure 8.6: TDDFT results for different defect nodes

8.3 Conclusions

When designing UiO-66 frameworks for photocatalysis, different pathways are available to engineer their absorption and charge transfer capabilities. Moreover, thanks to the largely independent behaviour of linkers and inorganic nodes, these effects can be studied separately. This chapter discusses the influence of missing linker defects on the electronic structure of UiO-66-type frameworks. Missing linker defects mostly affect the local node geometry and therefore offer an alternative route to node modification, which was thus far only achieved through metal substitution.

The electronic properties were shown to be determined by the node configurations present in the unit cell. Linker removal results in a change of the environment of the affected Zr atoms, which often lowers their unoccupied d orbitals (ΔE_{LMCT}) and increases charge transfer likelihood, therefore improving the photocatalytic activity. On the other hand, the linker states remain almost constant for all defect structures (ΔE_{abs}), corroborating the idea of orthogonal tuning of the electronic structure. We showed that the effect of missing linkers on the unoccupied d orbitals is highly dependent on the number of defects and their configuration. It was observed that only when two or more missing linkers are removed from the same node, a noticeable energy lowering of the d orbitals is obtained. This lowering was found to be the largest when the removed linkers are connected to a single Zr atom, as this drastically changes the environment of that atom.

Furthermore, we investigated the localization of the excited electron after LMCT by means of a simple cluster model. We showed that for a sufficient number of missing linkers, the excited electron will preferentially be located on the lowest coordinated Zr atoms, in line with the periodic results, which is beneficial for further catalytic steps with the material.

9

Conclusions and perspectives

9.1 Conclusions

One of the major scientific challenges of the 21st century is the change from energy intensive and polluting processes to green and sustainable alternatives. A promising approach is the conversion of solar energy, an abundant and incessant energy source, into chemical energy via photocatalytic processes. MOFs offer an interesting platform, since their inherent modular nature resembles that of the natural photo-active complexes and results in a unique electronic structure. The materials studied in this work show a complex quasi-localised band structure, offering interesting possibilities their electronic structure by adjusting the constituting parts. However, in the pristine material, large band gaps and bad overlaps are impeding efficient photocatalytic activity. In order to improve this, one needs to understand first the influences of the different modifications that can be made to the frameworks.

In chapters 5 and 6, we focussed on modifications made to the linkers and their influence on the intrinsic light-absorption properties of the materials. We investigated the optical characteristics of substituted UiO-66-X frameworks using *ab initio* methods, in direct comparison to experimental measurements. We proposed a bottom-up approach and studied the complex electronic structure of the frameworks by first studying its smallest constituents (linkers, metal nodes) and reconstructing part by part the periodic framework. We found that the band gap decrease relates to the choice of substituents and discuss this in function of a gap-state, inserted by the electron-

donating group. Inspection of the orbitals contributing to the different electronic transitions showed that LMCT is very ineffective in these materials. Furthermore, via advanced MD simulations, we showed that vibrations of the linkers in several UiO-type materials change the absorption wavelength. We also discussed the changes upon inclusion of a free linker inside the framework.

The next part of the thesis, starting with chapter 7 discussed several strategies to improve the charge transfer characteristics of the UiO materials. First, we applied a microwave-assisted metal exchange methodology to construct a series of doped UiO frameworks (Ti, Hf, Eu, Yb, Nd, Ce). This methodology allows to do post-synthetic metal-exchange in robust MOFs much faster than with conventional autoclaves. Synthesis times and required energy could be greatly reduced, from 5 days in a muffle furnace towards 4h in a microwave. Characterization of these doped materials is very hard. Although we obtained structural information through a big set of techniques, more specialised analysis is necessary to gain information about the actual surrounding of the lanthanide ions and their distribution within the UiO-66 framework.

Via a combined experimental and computational study we studied the influence of the dopants to the electronic properties of the material. The understanding of the electronic structure is of paramount importance not only for the use of UiO-66(Zr/Ti) in photocatalytic applications, but also gives important input for their use in other electronic applications. A spectroscopic study of the Ln-doped materials allowed us to construct via simple empirical models the charge-state transition curve for the whole Ln series with respect to the host band structure. Further experimental and computational studies confirmed this model. After the mechanistic investigation, the materials were tested in a photocatalytic batch and flow reactor for their use in VOC breakdown reactions. Although their activity is very low, we show clearly that the doping of the framework is essential to observe catalytic activity.

In chapter 8, we present a theoretical study of defects and discuss their possibilities as a completely different pathway to engineer the electronic structure of UiO-66. The electronic properties were shown to be determined by the node configurations present in the unit cell. Linker removal results in a change of the environment of the affected Zr atoms, which often lowers their unoccupied d orbitals (ΔE_{LMCT}) and increases charge transfer likelihood, therefore improving the photocatalytic activity. On the other hand, the linker states remain almost constant for all defect structures (ΔE_{abs}). Furthermore, we investigated the localization of the excited electron after

LMCT by means of a simple cluster model. We showed that for a sufficient number of missing linkers, the excited electron will preferentially be located on the lowest coordinated Zr atoms, in line with the periodic results, which is beneficial for further catalytic steps with the material.

Generally, this work shows that thanks to the decoupling between node- and linkerbased effects on the electronic properties of UiO-66 type frameworks, a set of possible routes can be deduced for a careful engineering of the electronic structure of 0D MOFs with similar structures as UiO-66 (e.g. MOF-5). Combining the knowledge of linker functionalization, metal-doping and defect engineering can now pave the way for a more fundamental reasoning when MOFs are designed for their use in electronic applications.

9.2 Perspectives

The possibilities of carefully engineered MOFs for electronic applications are still exploited to a too small extent. We hope that we convinced the reader by now that the unique structure of MOFs can give new perspectives to tailored photocatalysis and luminescence applications. In addition, the electronic structure engineering may also be of broader use in promising new fields such as semiconducting [294] or conductive MOFs [158] and dynamic magnetic frameworks. [73]

Starting from this research, it would be advisable to first obtain more structural information on the inclusion of the dopant ions in the framework. It is a very hard task, but from the data presented in this work, no conclusive image could be put forward. A suggestion would be to perform high resolution x-ray measurements at a synchrotron radiation source (XRD, XANES, EXAFS,...)

When no doubt remains about the structures of the doped UiO, this study can be continued and more fundamental information can be obtained. For example the interplay between defects and the doped materials can be investigated, especially for the luminescence properties of the Ln ions. Moreover combination of the fingerprint methodology and defect studies with far-IR and advanced spectroscopic techniques could in my opinion advance the field of defect engineering.

The extension of the models put forward in this thesis to other materials with similar structures could be very relevant to verify the suggestion that elec-

tronic structure engineering via our methodology can be straightforwardly extended to these structures. If this would be the case, a prediction of relevant structures could be combined with the lanthanide empirical model and be an interesting guidance for experimentalists to design a MOF material with engineered electronic characteristics.

Also the photocatalysis should be extended to different reactions, since the gas phase reactions appear to be too low in activity. Higher concentrations of dopants, or e.g. moisture in the reaction chamber could improve the results. Evaluating the materials in more high-end liquid phase reactions could also be of great interest since proof-of-concept reactions (methylene blue degradation, Cr(VI) reduction,...) appeared to be very active.



Supplementary Information

Supplementary Information of Chapter 2

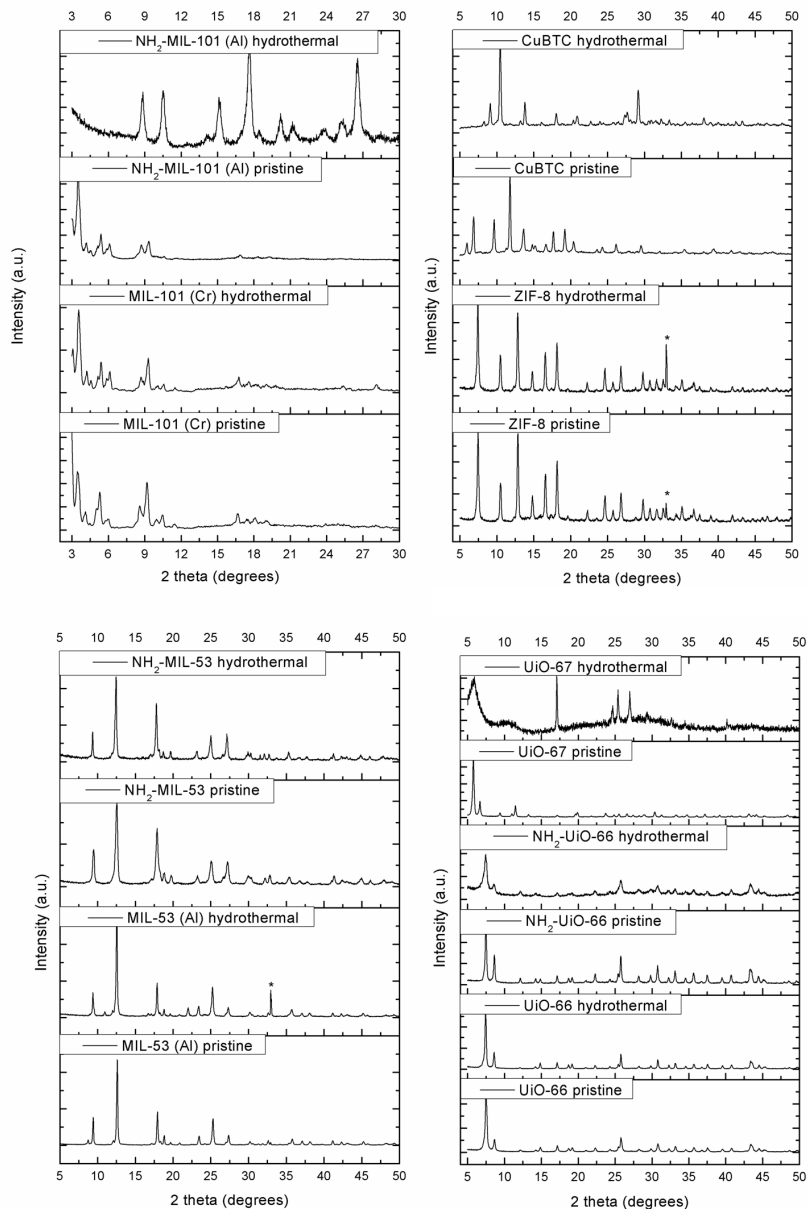
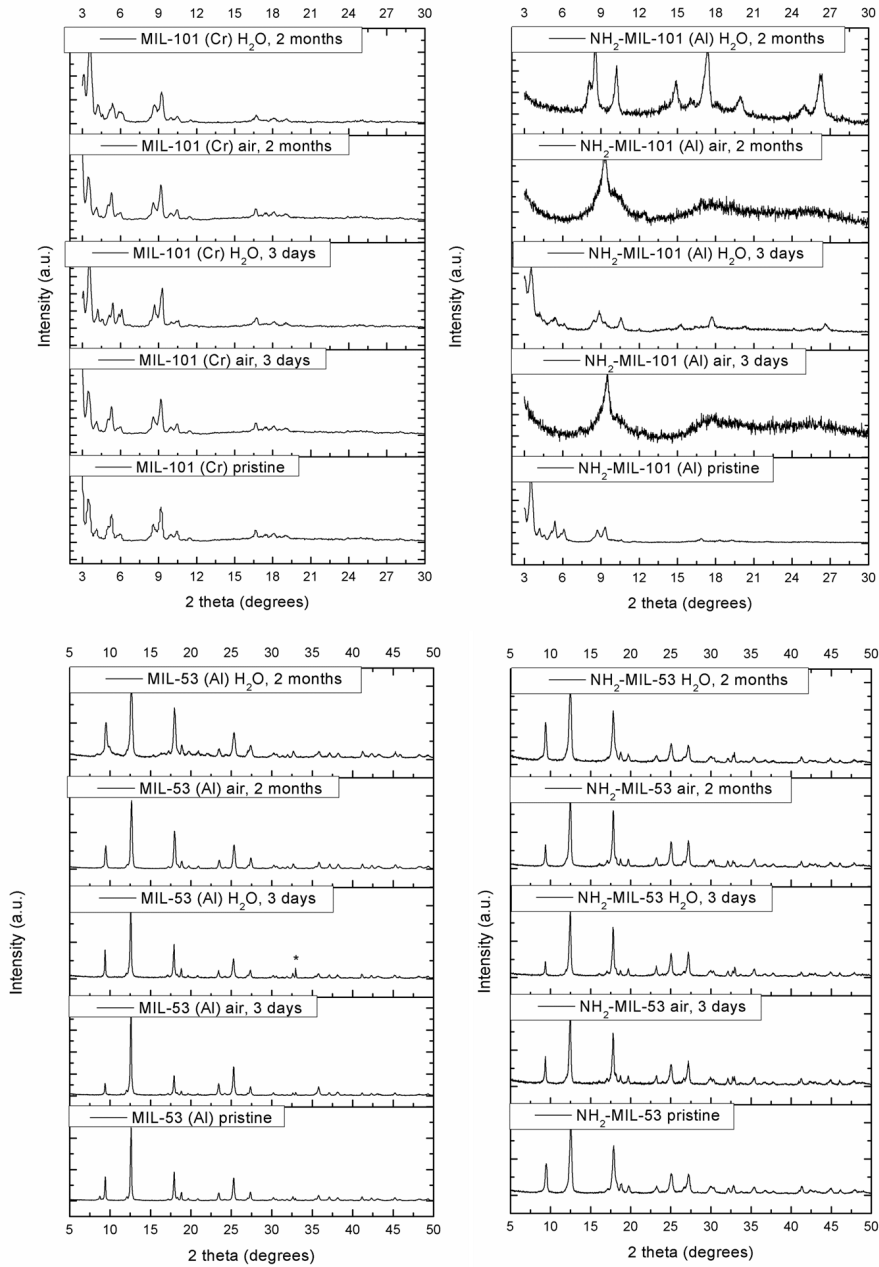
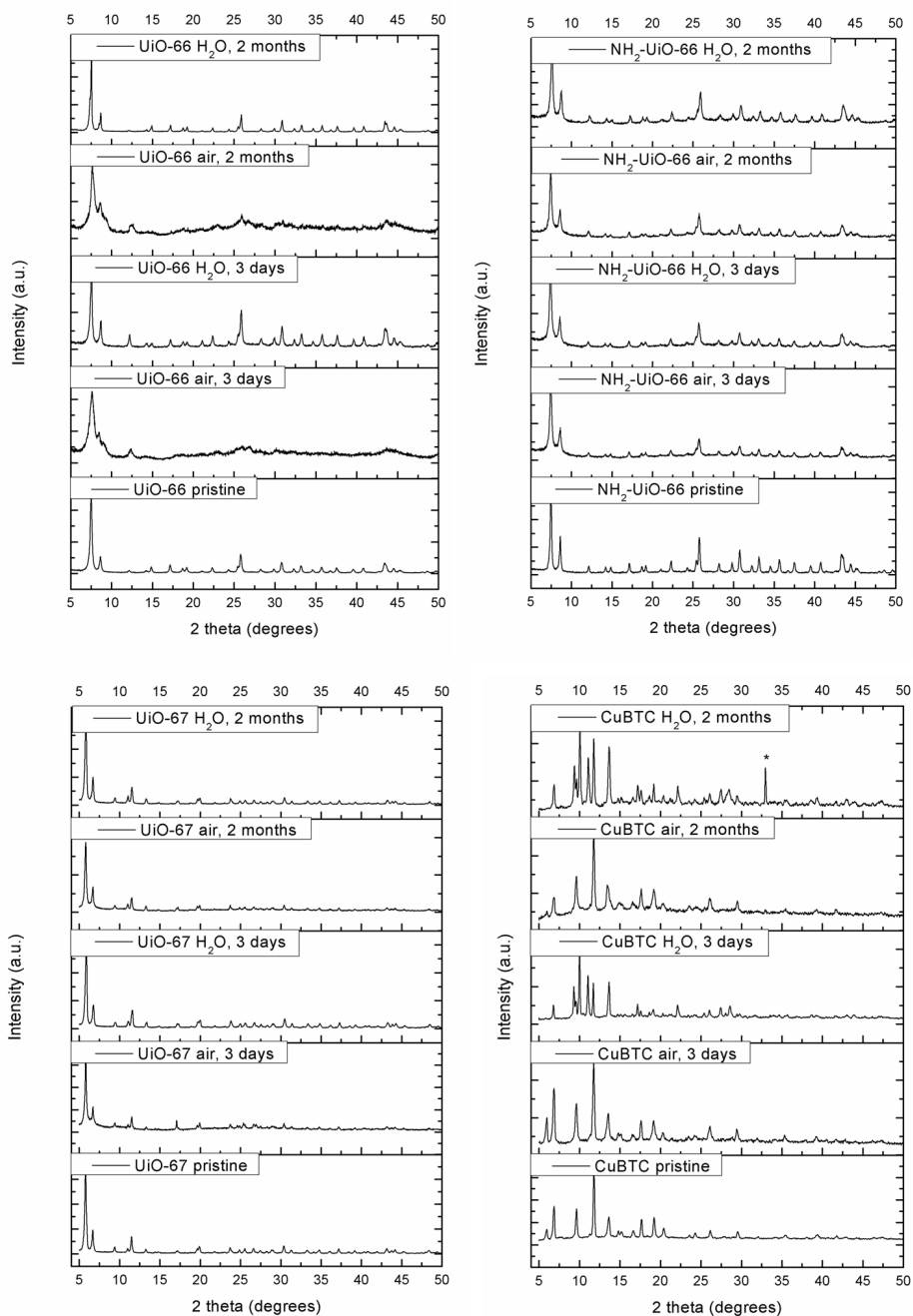
Supporting information

Figure S1. XRPD patterns of all the pristine MOF materials and after the hydrothermal treatment (*is due to the background of the sample holder at an angle of 32.9°).





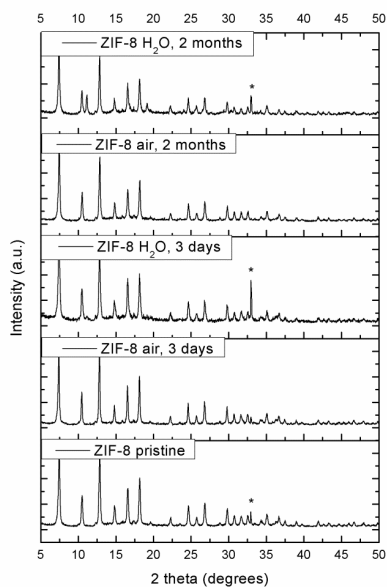
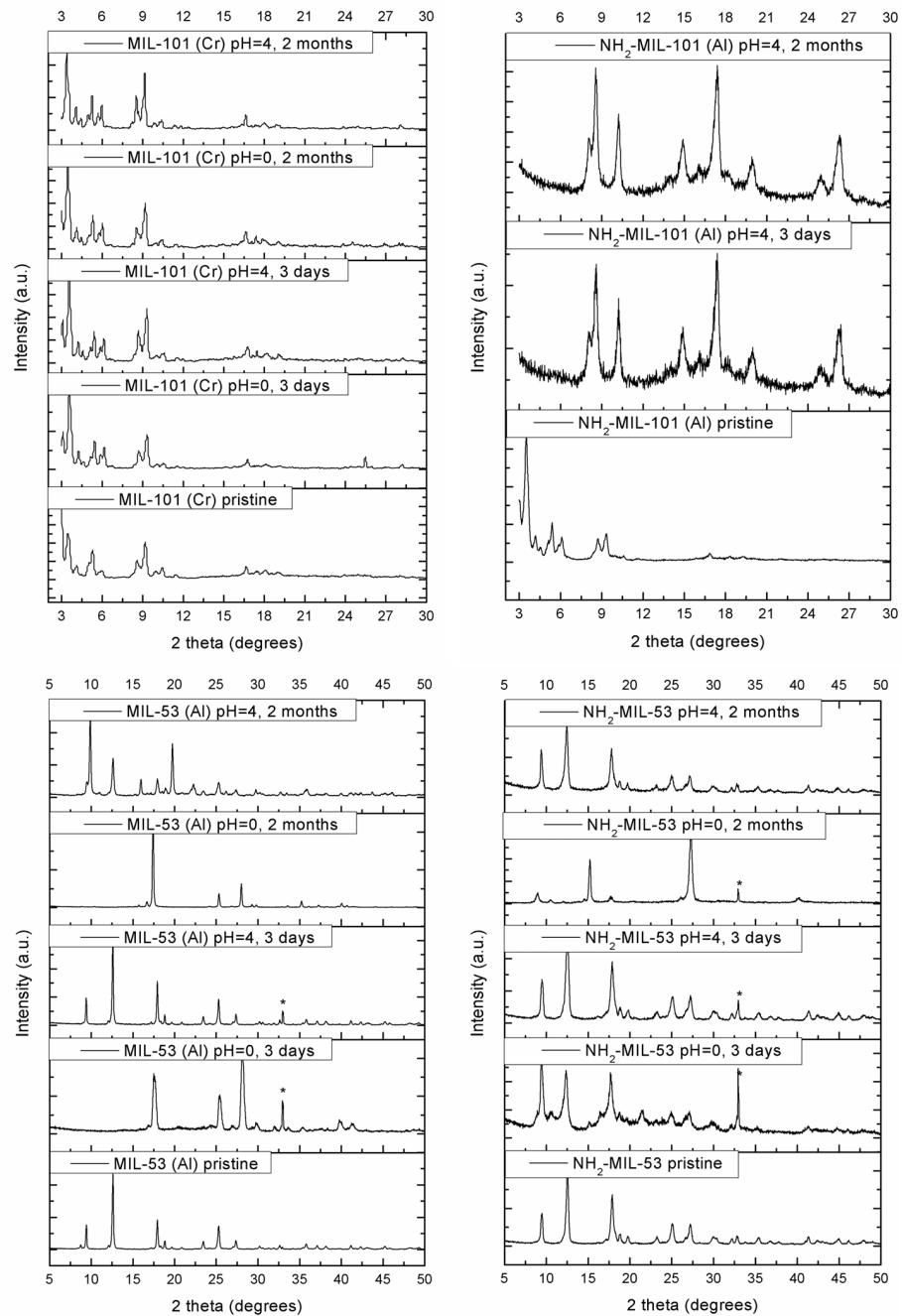


Figure S2. XRPD patterns of all the pristine MOF materials and after exposure to water or air for 3 days to 2 months (*is due to the background of the sample holder at an angle of 32.9°).



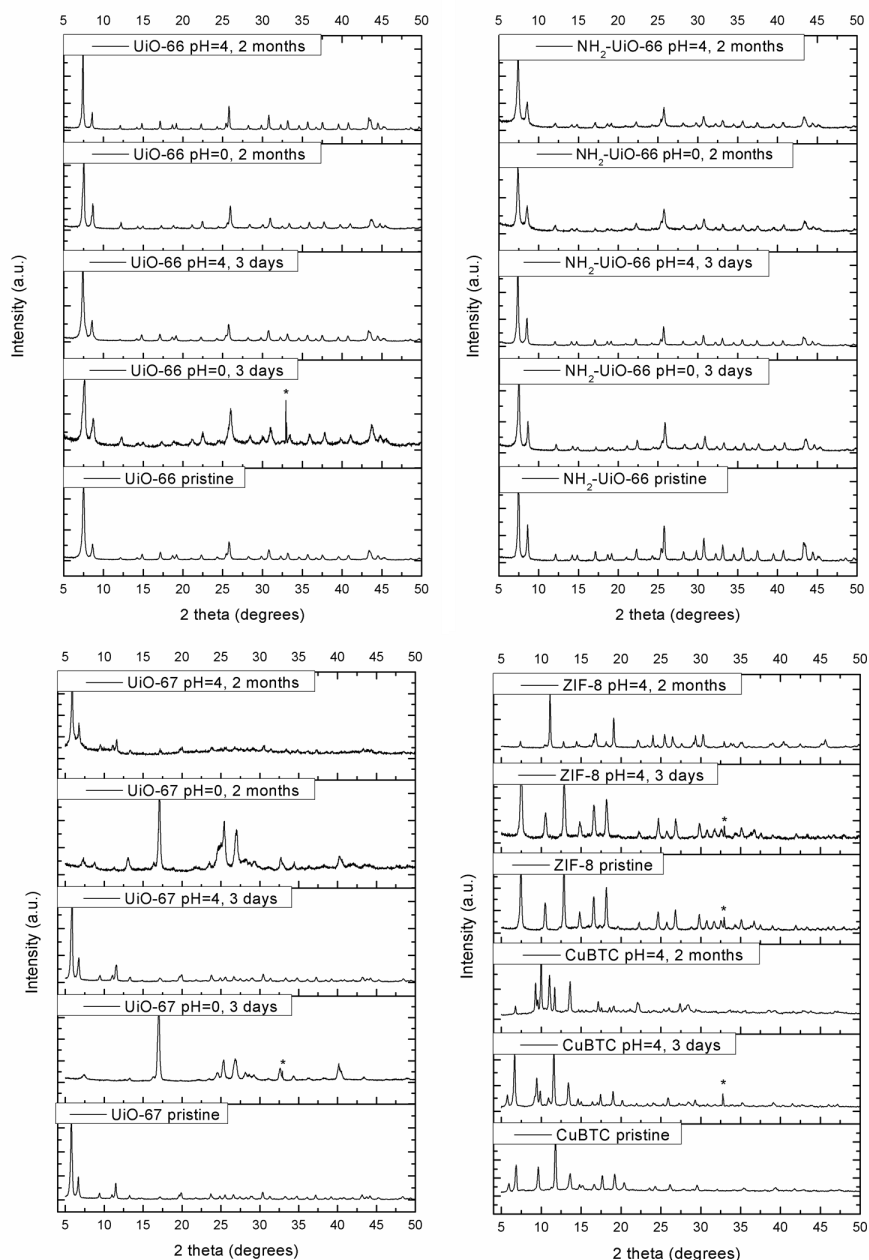


Figure S3. XRPD patterns of all the pristine MOF materials and after exposure to acidic conditions (pH=0 and pH=4) for 3 days to 2 months (*is due to the background of the sample holder at an angle of 32.9°).

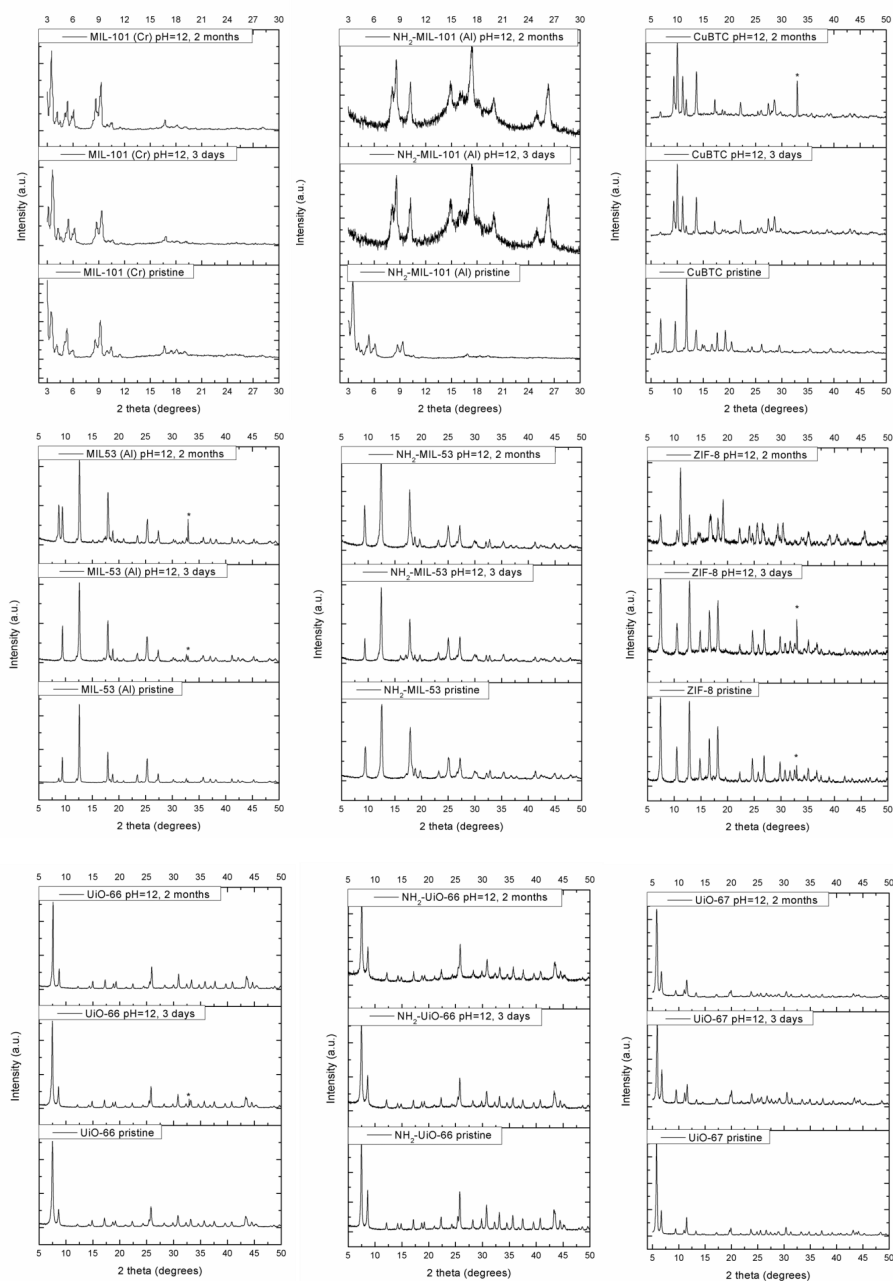


Figure S4. XRPD patterns of all the pristine MOF materials and after exposure to basic conditions (pH=12) for 3 days to 2 months (*is due to the background of the sample holder at an angle of 32.9°).

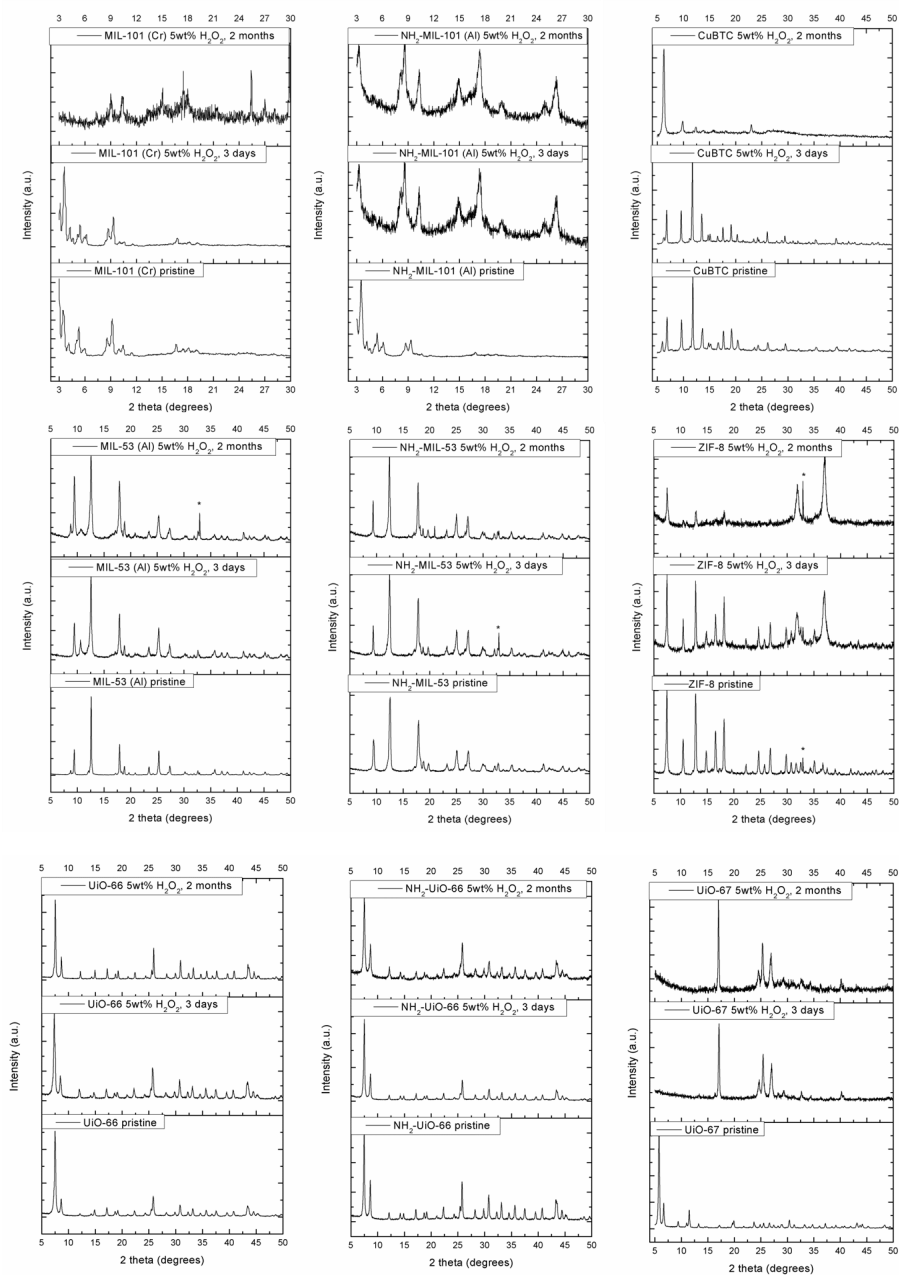


Figure S5. XRPD patterns of all the pristine MOF materials and after exposure to oxidative conditions (5 wt% H_2O_2) for 3 days to 2 months (*is due to the background of the sample holder at an angle of 32.9°).

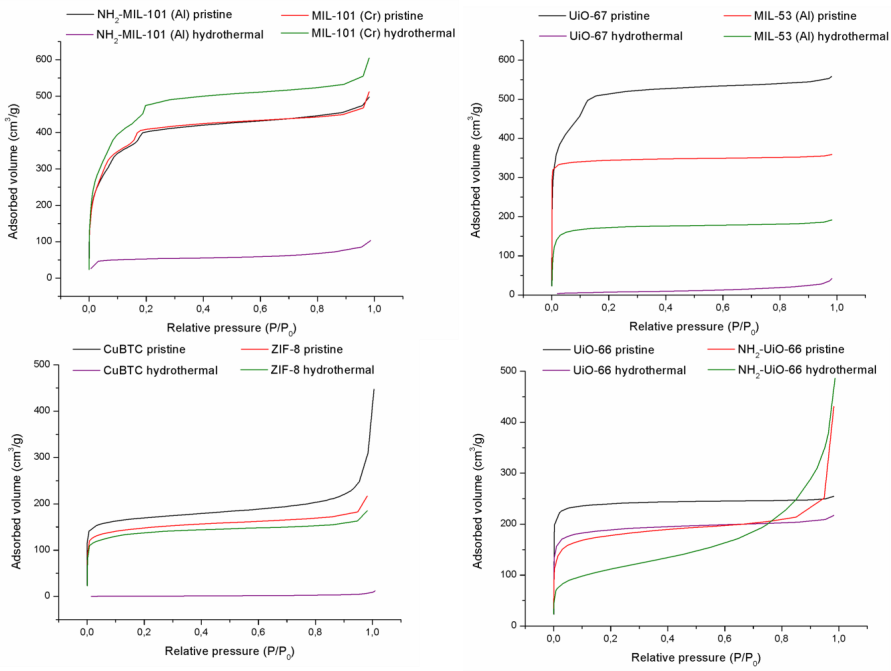
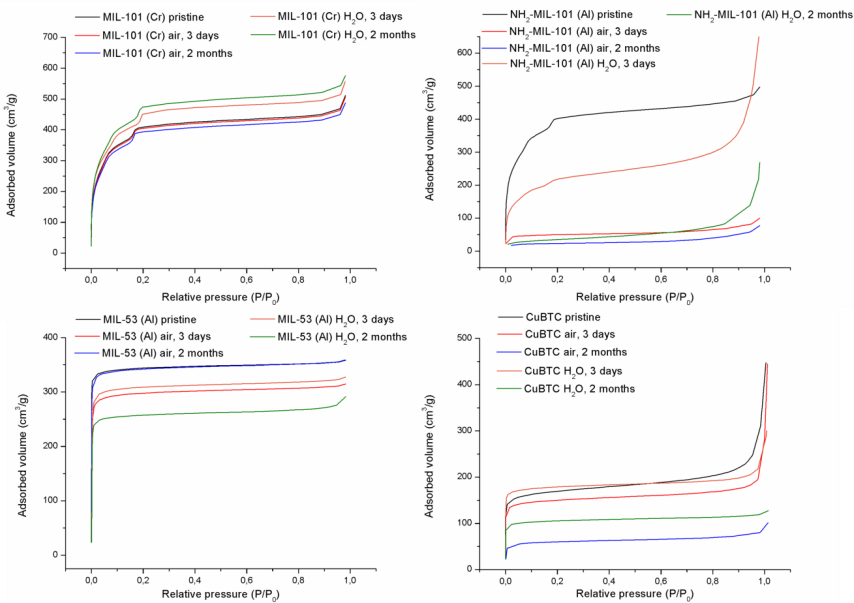


Figure S6. Nitrogen adsorption isotherms of all the pristine MOF materials and after the hydrothermal treatment



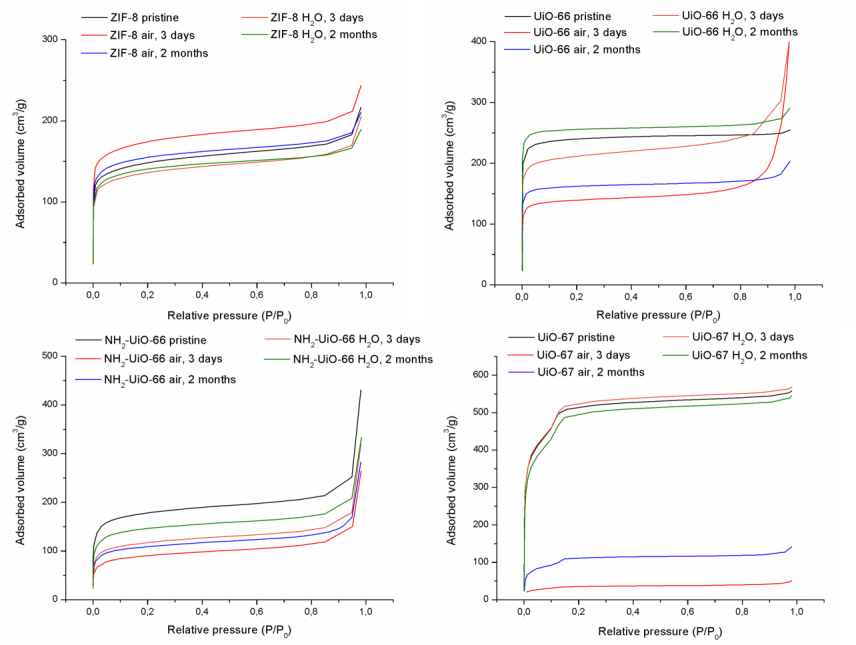
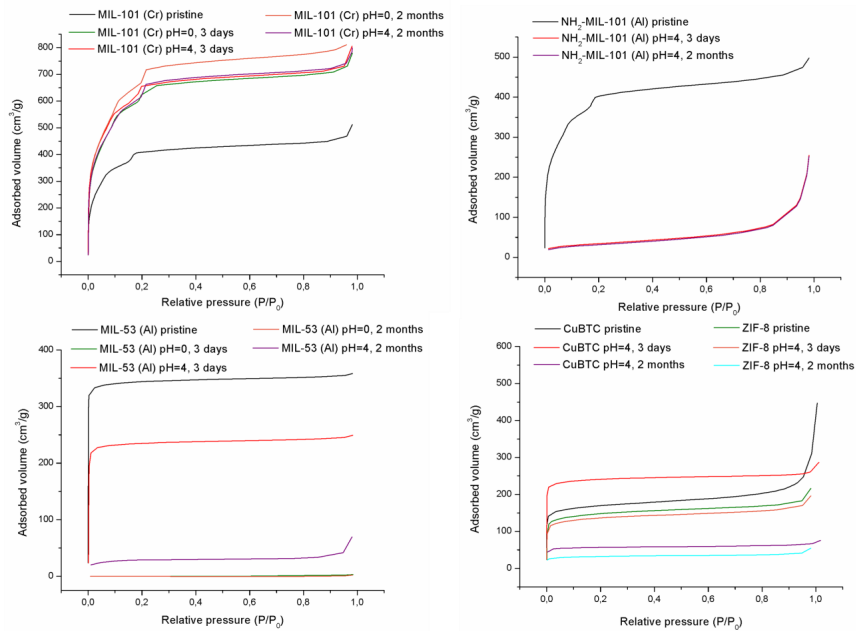


Figure S7. Nitrogen adsorption isotherms of all the pristine MOF materials and after exposure to water or air for 3 days to 2 months.



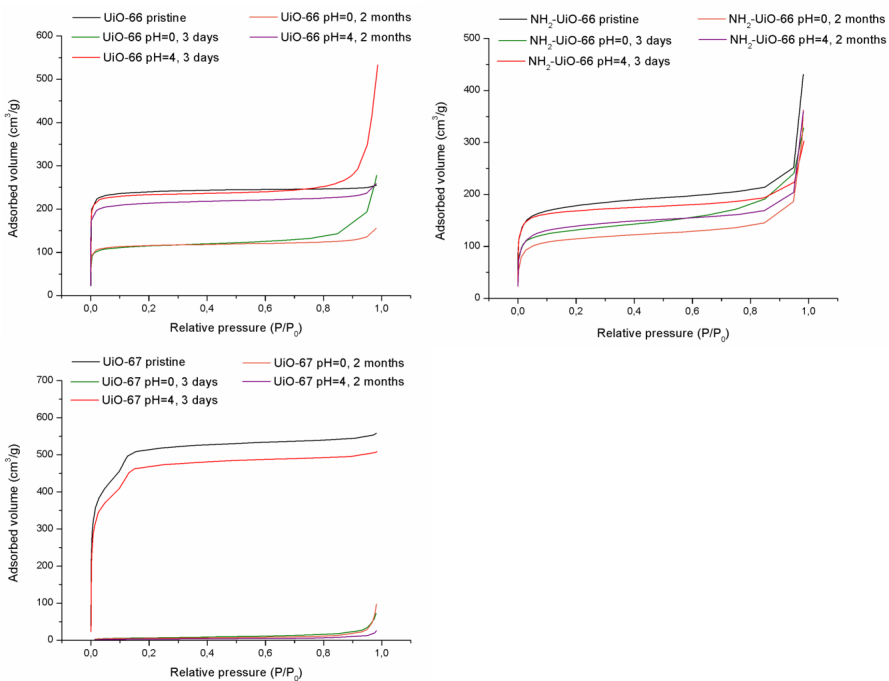


Figure S8. Nitrogen adsorption isotherms of all the pristine MOF materials and after exposure to acidic conditions (pH=0 and pH=4) for 3 days to 2 months.

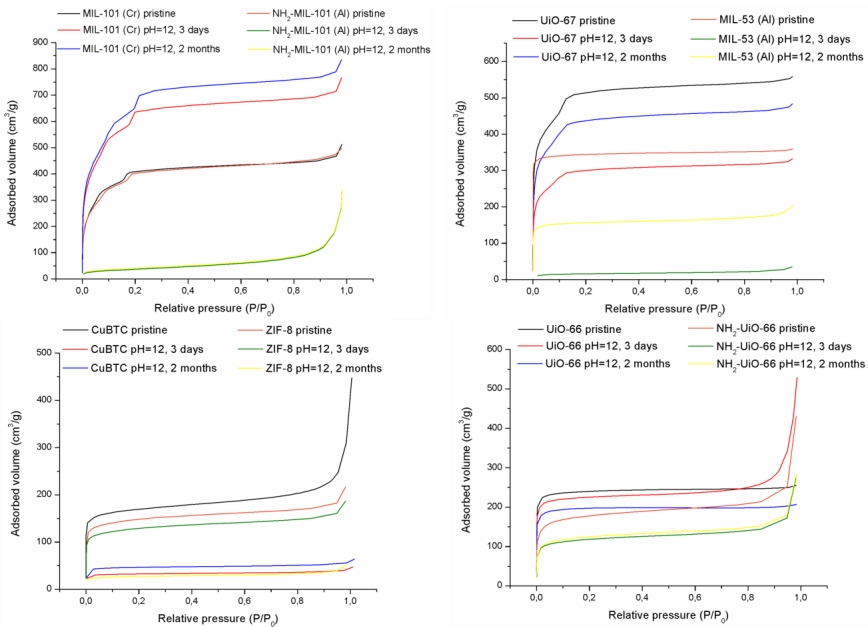


Figure S9. Nitrogen adsorption isotherms all the pristine MOF materials and after exposure to basic conditions (pH=12) for 3 days to 2 months.

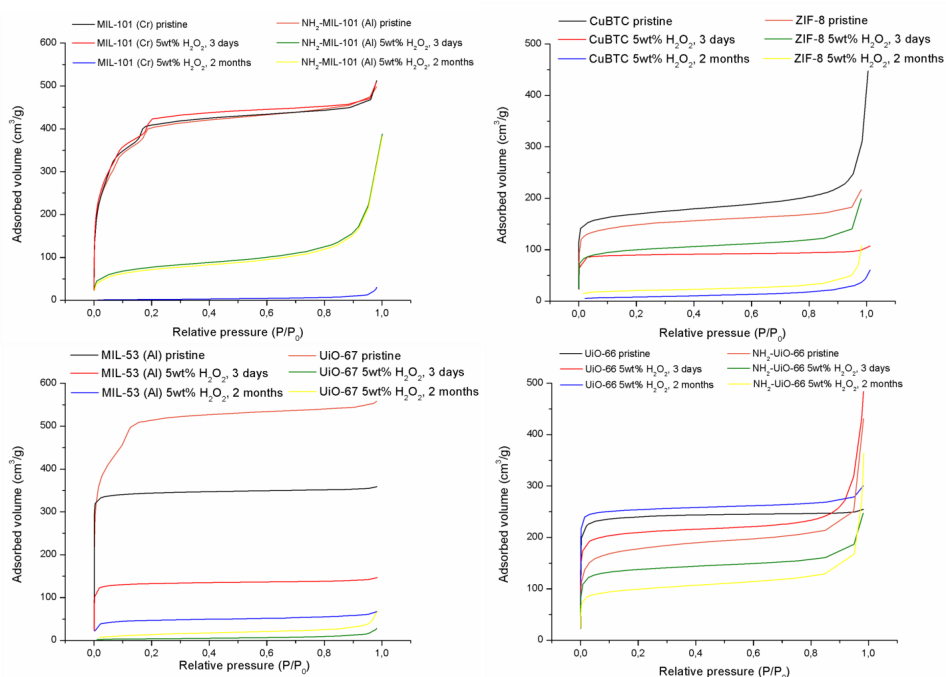
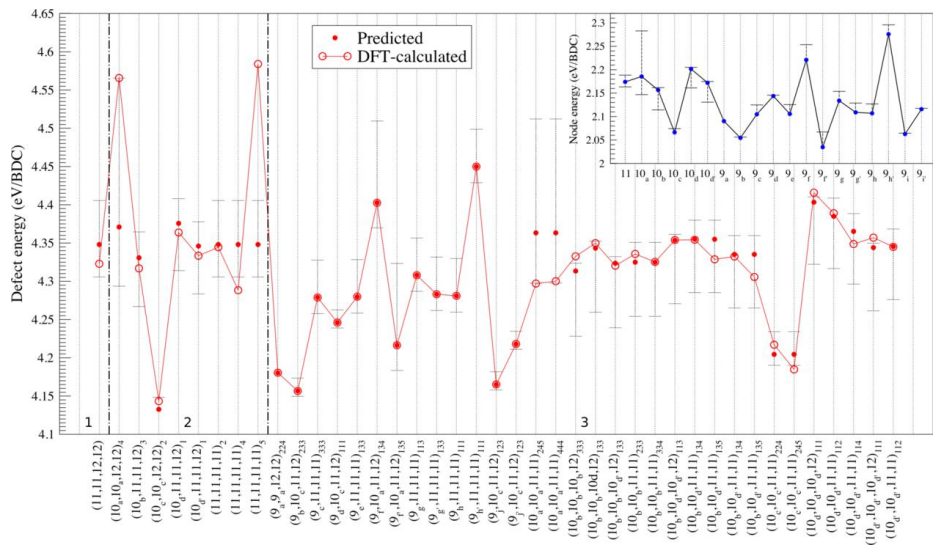


Figure S10. Nitrogen adsorption isotherms of all the pristine MOF materials and after exposure to oxidative conditions (5 wt% H₂O₂) for 3 days to 2 months.

Supplementary Information of Chapter 8



Defect energies for all missing linker defect structures normalized with respect to the number of missing linkers per unit cell. The connected open circles indicate the calculated values, and the solid markers represent the predicted defect energies from the least-squares fitted node energies. These fitted node energies, normalized to the number of missing linkers on each node, are shown in the inset. Error bars express the sensitivity of the fit and essentially represent the effect of different linker orientations. They are determined as the range of possible node energies when fitting to different sets of reference data (subsets of one-, two-, or three-defect structures separately and combinations of these subsets).



List of Publications

Publications in international peer-reviewed journals

1. K. Hendrickx, J.J. Joos, A. De Vos, K. Lejaeghere, D. Poelman, P.F. Smet V. Van Speybroeck and P. Van Der Voort *Exploring lanthanide doping in UiO-66: a combined experimental and computational study of the electronic structure properties*, submitted
2. G. Wang, K. Leus, K. Hendrickx, J. Wieme, H. Depauw, Y. Liu, V. Van Speybroeck and P. Van Der Voort, *A series of sulfonic acid functionalized mixed-linker DUT-4 analogues: synthesis, gas sorption properties and catalytic performance*, Dalton Transactions, **2017**, 43, 14356-14364 IF: 4.029, 9/66 [Q1]
3. A. De Vos, K. Hendrickx, P. Van der Voort, V. Van Speybroeck, K. Lejaeghere *Missing linkers: an alternative pathway to UiO-66 electronic structure engineering*, Chemistry of Materials, **2017**, 29, 3006-3019 IF: 9.407, 4/273 [Q1]
4. S. Clerick, K. Hendrickx, V. Van Speybroeck, P. Van der Voort, *Heterogeneous Ru(III) oxidation catalysts via 'click' bidentate ligands on a Periodic Mesoporous Organosilica support*, Green Chemistry, **2016**, 18,6035-6045 IF: 8.506, 16/163 [Q1]

5. K. Leus, T. Bogaerts, J. De Decker, H. Depauw, K. Hendrickx, H. Vrielinck, V. Van Speybroeck, P. Van der Voort, *A systematic study of the chemical and hydrothermal stability of some 'stable' Metal Organic Frameworks*, Microporous and Mesoporous Materials, **2016**, 226, 110-116
IF: 3.349, 10/71 [Q1]
6. J. Ouwehand, J. Lauwaert, D. Esquivel, K. Hendrickx, V. Van Speybroeck, J.W. Thybaut, P. Van der Voort, *Facile synthesis of cooperative acid-base catalysts by clicking cysteine and cysteamine on an ethylene-bridged periodic mesoporous organosilica*, European Journal of Inorganic Chemistry, **2016**, 13-14, 2144-2151
IF: 2.942, 13/65 [Q1]
7. A. Van Yperen-De Deyne, K. Hendrickx, L. Vanduyfhuys, G. Sastre, P. Van der Voort, V. Van Speybroeck, K. Hemelsoet, *Vibrational fingerprint of the absorption properties of UiO-type MOF materials*, Theoretical Chemistry Accounts, **2016**, 135 (4), 102
IF: 1.806, 92/144 [Q3]
8. K. Hendrickx, D.E.P. Vanpoucke, K. Leus, K. Lejaeghere, A. Van Yperen-De Deyne, V. Van Speybroeck, P. Van der Voort, K. Hemelsoet, *Understanding Intrinsic Light Absorption Properties of UiO-66 Frameworks: A Combined Theoretical and Experimental Study*, Inorganic Chemistry, **2015**, 54 (22), 10701-10710
IF: 4.820, 4/46 [Q1]
9. K. Hendrickx, B. Braida, P. Bultinck, P. C. Hiberty, *More insight in multiple bonding with valence bond theory*, Computational and Theoretical Chemistry, **2015**, 1053, 180-188
IF: 1.368, 96/136 [Q3]
10. B. Braida, K. Hendrickx, D. Domin, J.P. Dinnocenzo, P. C. Hiberty, *Multicenter Bonding in Ditetrayanoethylene Dianion: A Simple Aromatic Picture in Terms of Three-Electron Bonds*, **2013**, 9(5), 2276-2285
IF: 5.309, 3/34 [Q1]

Conference contributions

Invited talks (presenter is underlined)

1. Orthogonal band gap engineering of UiO-66 frameworks through active control of defects
K. Lejaeghere, A. De Vos, K. Hendrickx, S.M.J. Rogge, P. Van der Voort,

V. Van Speybroeck

EMN Meeting 2016 on Active Matter, Las Vegas, USA, October 10-14, 2016

Oral presentations(presenter is underlined)

1. Heterogeneous Ru(III) oxidation catalysts via ‘click’ bidentate ligands on a Periodic Mesoporous Organosilica support
S. Clerick, E. De Canck, K. Hendrickx, V. Van Speybroeck, P. Van der Voort, Multifunctional, Hybrid and Nanomaterials, 5th International conference, Lisbon, Portugal, March 06-10, 2017
2. Understanding Light-Absorption in MOFs: Combined Experimental and Theoretical Study of UiO-66 Type Frameworks
K. Hendrickx, A. De Vos, K. Hemelsoet, P. Van der Voort, V. Van Speybroeck
5th International Conference on Metal-Organic Frameworks & Open Framework Compounds, Long Beach, USA, September 11-15, 2016
3. Orthogonal band gap engineering in Zr based MOFs
A. De Vos, K. Hendrickx, S.M.J. Rogge, K. Lejaeghere, V. Van Speybroeck
IAP-WP2 meeting, Zwijnaarde, Belgium, June 16, 2016
4. Metal-Organic Frameworks: When the whole is more than the sum of its parts.
D. Vanpoucke, K. Hendrickx, B. Bueken
General Scientific Meeting of the Belgian Physical Society, Gent, Belgium, May 18, 2016
5. Engineering light-absorption in MOFs: Combined experimental and theoretical study of UiO-66
K. Hendrickx, K. Hemelsoet, D.E.P. Vanpoucke, P. Van der Voort, V. Van Speybroeck
Modeling Photoactive Molecules, Nantes, France, April 21-24, 2015
6. Engineering light-absorption in functionalized UiO-66 frameworks
K. Hendrickx, K. Hemelsoet, D.E.P. Vanpoucke, P. Van der Voort, V. Van Speybroeck
N3C, Noordwijkerhout, The Netherlands, March 02-04, 2015

Poster presentations (presenter is underlined)

1. Defect engineering of UiO-66 using 4-sulfobenzoic acid
X. Feng, K. Hendrickx, G. Wang, K. Leus, V. Van Speybroeck, P. Van der Voort
 N3C, Noordwijkerhout, The Netherlands, March 06-08, 2017
2. Understanding Light-Absorption in MOFs: Combined Experimental and Theoretical Study of UiO-66 Type Frameworks
K. Hendrickx, A. De Vos, K. Hemelsoet, P. Van der Voort, V. Van Speybroeck
 Chemical Research in Flanders (CRF-1), Blankenberge, Belgium, October 24-26, 2016
3. Understanding intrinsic light absorption properties of UiO-66 frameworks: A combined theoretical and experimental study
 K. Hendrickx, A. De Vos, K. Iejaeghere, P. Van Der Voort, V. Van Speybroeck
 Annual IAP meeting, Liège, Belgium, September 12, 2016
4. Generation of S-containing bidentate ligands on a Periodic Mesoporous Organosilica (PMO) support: heterogenization of Ru(III) as a selective oxidation catalyst in water
S. Clerick, E. De Canck, K. Hendrickx, V. Van Speybroeck, P. Van der Voort
 Doctoral Symposium, Faculty of Sciences, Ghent, Belgium, March 03, 2016
5. Understanding intrinsic light absorption properties of UiO-66 frameworks: A combined theoretical and experimental study
 K. Hendrickx, D.E.P. Vanpoucke, K. Leus, K. Iejaeghere, A. Van Yperen-De Deyne, V. Van Speybroeck, P. Van der Voort, K. Hemelsoet
 IAP Annual Meeting, Hasselt, Belgium, September 11, 2015
6. Understanding Experiments: the Power of First Principle Simulations of Metal-Organic Frameworks
 D.E.P. Vanpoucke, K. Hendrickx, B. Beuken, D. De Vos, K. Hemelsoet, P. Van der Voort, V. Van Speybroeck
 IAP Annual Meeting, Hasselt, Belgium, September 11, 2015

Master's thesis

'A simple strategy based on valence bond theory to describe multiple bonding'

K. Hendrickx

Master's thesis performed at the Ghent Quantum Chemistry Group (GQCG),

Ghent University and the Laboratoire du Chimie Théorique, Université de Pierre et Marie Curie (Paris VI), 2012-2013

Promoters: prof. dr. Patrick Bultinck, dr. Benoît Braïda

Bachelor's thesis

'In search of the nature of bonding in the π -stacked $TCNE_2^{2-}$ di-anion dimer'

K. Hendrickx

Bachelor's thesis performed at the Laboratoire du Chimie Théorique, Université de Pierre et Marie Curie (Paris VI) and the Laboratoire du Chimie Physique, Université de Paris-Sud (Paris XI) 2010-2011

Promoters: dr. Benoît Braïda, dr. Philippe Charles Hiberty

Bibliography

- [1] U.S. Energy Information Administration, “World energy outlook 2016,” .
- [2] D. Ravelli, D. Dondi, M. Fagnoni, and A. Albini, “Photocatalysis. a multi-faceted concept for green chemistry,” *Chem. Soc. Rev.*, vol. 38, no. 7, pp. 1999, 2009.
- [3] A. Werner, “Beitrag zur konstitution anorganischer verbindungen,” *Z. Anorg. Chem.*, vol. 3, no. 1, pp. 267–330, 1893.
- [4] P. Muller, “Glossary of terms used in physical organic chemistry (IUPAC recommendations 1994),” *Pure Appl. Chem.*, vol. 66, no. 5, pp. 1077–1184, 1994.
- [5] L. McCusker, F. Liebau, and G. Engelhardt, “Nomenclature of structural and compositional characteristics of ordered microporous and mesoporous materials with inorganic hosts (IUPAC recommendations 2001),” *Pure Appl. Chem.*, vol. 73, no. 2, pp. 381–394, 2009.
- [6] A. F. Cronstedt, “Om en obekant bärg art, som kallas zeolites,” *Akad. Handl. Stockholm*, , no. 18, pp. 120, 1756.
- [7] H. de Sainte Claire Deville, “Reproduction de la lévyne,” *C. R. Hebd. Seances Acad. Sci.*, vol. 54, pp. 324, 1862.
- [8] Ch. Baerlocher and L. B. McCusker, “Database of zeolite structures, available at: <http://www.iza-structure.org/databases/> (august 9, 2015),” .
- [9] V. Speybroeck, K. Hemelsoet, L. Joos, M. Waroquier, R. G. Bell, and R. C. A. Catlow, “Advances in theory and their application within the field of zeolite chemistry,” *Chem. Soc. Rev.*, vol. 44, no. 20, pp. 7044–7111, 2015.
- [10] C. E. Wilmer, M. Leaf, C. Lee, O. K. Farha, B. G. Hauser, J. T. Hupp, and R. Q. Snurr, “Large-scale screening of hypothetical metal-organic frameworks,” *Nat. Chem.*, vol. 4, no. 2, pp. 83–89, 2011.

- [11] A. Lipson, "<http://www.andrewlipson.com>," .
- [12] O. M. Yaghi, M. O’Keeffe, N. W. Ockwig, H. K. Chae, M. Eddaoudi, and J. Kim, "Reticular synthesis and the design of new materials," *Nature*, vol. 423, no. 6941, pp. 705–714, 2003.
- [13] M. Eddaoudi, J. Kim, N. Rosi, D. Vodak, J. Wachter, M. O’Keeffe, and O. M. Yaghi, "Systematic design of pore size and functionality in isorecticular MOFs and their application in methane storage," *Science*, vol. 295, no. 5554, pp. 469–472, 2002.
- [14] M. G. Goesten, F. Kapteijn, and J. Gascon, "Fascinating chemistry or frustrating unpredictability: observations in crystal engineering of metal-organic frameworks," *Crystengcomm*, vol. 15, no. 45, pp. 9249–9257, 2013.
- [15] Y. Kinoshita, I. Matsubara, T. Higuchi, and Y. Saito, "The crystal structure of Bis(adiponitrilo)copper(I) nitrate," *B. Chem. Soc. Jpn.*, vol. 32, no. 11, pp. 1221–1226, 1959.
- [16] C. Biondi, M. Bonamico, L. Torelli, and A. Vaciago, "On the structure and water content of copper(II) tricyanomethanide," *Chem. Commun. Lond.*, vol. 0, no. 10, pp. 191, 1965.
- [17] E.A. Tomic, "Thermal stability of coordination polymers," *J. Appl. Polym. Sci.*, vol. 9, no. 11, pp. 3745–3752, 1965.
- [18] S.M.J. Rogge, A. Bavykina, J. Hajek, H. Garcia, A.I. Olivos-Suarez, A. Sepúlveda-Escribano, A. Vimont, G. Clet, P. Bazin, F. Kapteijn, M. Daturi, E.V. Ramos-Fernandez, F.X. Llabrés i Xamena, V. Van Speybroeck, and J. Gascon, "Metal-organic and covalent organic frameworks as single-site catalysts," *Chem. soc. rev.*, vol. 46, no. 11, pp. 3134–3184, 2017.
- [19] B. F. Hoskins and R. Robson, "Infinite polymer frameworks consisting of three dimensionally linked rod-like segments," *J. Am. Chem. Soc.*, vol. 111, no. 15, pp. 5962–5964, 1989.
- [20] H. Li, M. Eddaoudi, M. O’Keeffe, and O. M. Yaghi, "Design and synthesis of an exceptionally stable and highly porous metal-organic framework," *Nature*, vol. 402, no. 6759, pp. 276–279, 1999.
- [21] S. R. Batten, N. R. Champness, X-M. Chen, J. Garcia-Martinez, S. Kitagawa, L. Öhrström, M. O’Keeffe, M. Suh, and J. Reedijk, "Terminology

- of metal-organic frameworks and coordination polymers (IUPAC recommendations 2013),” *Pure Appl. Chem.*, vol. 85, no. 8, pp. 1715–1724, 2013.
- [22] A. J. Howarth, Y. Liu, P. Li, Z. Li, T. C. Wang, J. T. Hupp, and O. K. Farha, “Chemical, thermal and mechanical stabilities of metal-organic frameworks,” *Nat. Rev. Mater.*, vol. 1, no. 3, pp. 15018, 2016.
- [23] Y. J. Colón and R. Q. Snurr, “High-throughput computational screening of metal-organic frameworks,” *Chem. soc. rev.*, vol. 43, no. 16, pp. 5735–5749, 2014.
- [24] S. Cantrill, “Metal-organic frameworks: The big indoors,” *Nat. Chem.*, vol. 4, no. 7, pp. 516–516, 2012.
- [25] S. Kitagawa, R. Kitaura, and S-i. Noro, “Functional porous coordination polymers,” *Angew. Chem. Int. Ed.*, vol. 43, no. 18, pp. 2334–2375, 2004.
- [26] G. Férey, “Hybrid porous solids: past, present, future,” *Chem. soc. rev.*, vol. 37, no. 1, pp. 191–214, 2007.
- [27] “Thematic issue: Metal-organic frameworks,” Thematic issue on Metal-Organic Frameworks *Chemical reviews*, vol. 112, no. 2, pp. 673–1268, 2012.
- [28] H-C. Zhou and S. Kitagawa, “Metal-Organic frameworks (MOFs),” *Chem. soc. rev.*, vol. 43, no. 16, pp. 5415–5418, 2014.
- [29] I. Huskić, I. Pekov, S. Krivovichev, and T. Frisic, “Minerals with metal-organic framework structure,” *Sci. Adv.*, vol. 2, no. 8, pp. e1600621, 2016.
- [30] M. Sadakiyo, T. Yamada, K. Honda, H. Matsui, and H. Kitagawa, “Control of crystalline Proton-Conducting pathways by Water-Induced transformations of Hydrogen-Bonding networks in a Metal-Organic framework,” *J. Am. Chem. Soc.*, vol. 136, no. 21, pp. 7701–7707, 2014.
- [31] S. Miyatsu, M. Kofu, A. Nagoe, T. Yamada, M. Sadakiyo, T. Yamada, H. Kitagawa, M. Tyagi, V. Sakai, and O. Yamamuro, “Proton dynamics of two-dimensional oxalate-bridged coordination polymers,” *Phys. Chem. Chem. Phys.*, vol. 16, no. 32, pp. 17295–17304, 2014.
- [32] A.C. McKinlay, R. E. Morris, P. Horcajada, G. Férey, R. Gref, P. Couvreur, and C. Serre, “BioMOFs: Metal-Organic frameworks for biological and medical applications,” *Angew. Chem. Int. Ed.*, vol. 49, no. 36, pp. 6260–6266, 2010.

- [33] C. Volkringer, T. Loiseau, N. Guillou, G. Férey, D. Popov, M. Burghammer, and C. Riekel, "Synthesis and structural characterization of metal-organic frameworks with the mellitate linker $M_2(OH)_2[C_{12}O_{12}H_2] \cdot 2H_2O$ ($M = Al, Ga$, in) MIL-116," *Solid State Sci*, vol. 26, pp. 38–44, 2013.
- [34] J. An, O. K. Farha, J. T. Hupp, E. Pohl, J. I. Yeh, and N. L. Rosi, "Metal-adeninate vertices for the construction of an exceptionally porous metal-organic framework," *Nat. Commun*, vol. 3, pp. 604, 2012.
- [35] S-Y. Ding and W. Wang, "Covalent organic frameworks (COFs): from design to applications," *Chem. soc. rev.*, vol. 42, no. 2, pp. 548–568, 2012.
- [36] X. Feng, X. Ding, and D. Jiang, "Covalent organic frameworks," *Chem. soc. rev.*, vol. 41, no. 18, pp. 6010–6022, 2012.
- [37] P. J. Waller, F. Gaándara, and O. M. Yaghi, "Chemistry of covalent organic frameworks," *Acc. Chem. Res.*, vol. 48, no. 12, pp. 3053–3063, 2015.
- [38] C.S. Diercks and O. M. Yaghi, "The atom, the molecule, and the covalent organic framework," *Science*, vol. 355, no. 6328, pp. eaal1585, 2017.
- [39] N. Huang, P. Wang, and D. Jiang, "Covalent organic frameworks: a materials platform for structural and functional designs," *Nat. Rev. Mater.*, vol. 1, no. 10, pp. 16068, 2016.
- [40] Y. Wan and D. Zhao, "On the controllable Soft-Templating approach to mesoporous silicates," *Chem. Rev.*, vol. 107, no. 7, pp. 2821–2860, 2007.
- [41] P. Van Der Voort, D. Esquivel, E. De Canck, F. Goethals, I. Van Driessche, and F. Romero-Salguero, "Periodic mesoporous organosilicas: from simple to complex bridges; a comprehensive overview of functions, morphologies and applications," *Chem. soc. rev.*, vol. 42, no. 9, pp. 3913–3955, 2013.
- [42] W. Xin and Y. Song, "Mesoporous carbons: recent advances in synthesis and typical applications," *Rsc Adv.*, vol. 5, no. 101, pp. 83239–83285, 2015.
- [43] R. ChakraB.y, P. Mukherjee, and P. J. Stang, "Supramolecular coordination: Self-Assembly of finite two- and Three-Dimensional ensembles," *Chem. Rev.*, vol. 111, no. 11, pp. 6810–6918, 2011.

- [44] R. J. Kuppler, D. J. Timmons, Q-R. Fang, J-R. Li, T. A. Makal, M. D. Young, D. Yuan, D. Zhao, W. Zhuang, and H-C. Zhou, "Potential applications of metal-organic frameworks," *Coordin. Chem. Rev.*, vol. 253, no. 23-24, pp. 3042–3066, 2009.
- [45] G. Maurin, A. Serre, C. and Cooper, and G. Férey, "The new age of MOFs and of their porous-related solids," *Chem. soc. rev.*, vol. 46, no. 11, pp. 3104–3107, 2017.
- [46] O. K. Farha, I. Eryazici, N. Jeong, B. G. Hauser, C. E. Wilmer, A. A. Sarjeant, R. Q. Snurr, S. T. Nguyen, Ö. A. Yazaydin, and J. T. Hupp, "Metal-Organic framework materials with ultrahigh surface areas: Is the sky the limit?," *J. Am. Chem. Soc.*, vol. 134, no. 36, pp. 15016–15021, 2012.
- [47] Anna G. Slater and Andrew I. Cooper, "Function-led design of new porous materials," *Science*, vol. 348, no. 6238, 2015.
- [48] J-R. Li, R. J. Kuppler, and H-C. Zhou, "Selective gas adsorption and separation in metal-organic frameworks," *Chem. soc. rev.*, vol. 38, no. 5, pp. 1477–1504, 2009.
- [49] N. L. Rosi, J. Eckert, M. Eddaoudi, D.T. Vodak, J. Kim, M. O’Keeffe, and O. M. Yaghi, "Hydrogen storage in microporous Metal-Organic frameworks," *Science*, vol. 300, no. 5622, pp. 1127–1129, 2003.
- [50] L. J. Murray, M. Dincă, and J. R. Long, "Hydrogen storage in metal-organic frameworks," *Chem. soc. rev.*, vol. 38, no. 5, pp. 1294, 2009.
- [51] M. Suh, H. Park, T. Prasad, and D-W. Lim, "Hydrogen storage in Metal-Organic frameworks," *Chem. Rev.*, vol. 112, no. 2, pp. 782–835, 2012.
- [52] Y. He, W. Zhou, G. Qian, and B. Chen, "Methane storage in metal-organic frameworks," *Chem. soc. rev.*, vol. 43, no. 16, pp. 5657–5678, 2014.
- [53] K. Sumida, D.L. Rogow, J. A. Mason, T. M. McDonald, E. D. Bloch, Z. R. Herm, T-H. Bae, and J. R. Long, "Carbon dioxide capture in Metal-Organic frameworks," *Chem. Rev.*, vol. 112, no. 2, pp. 724–781, 2012.
- [54] M. J. Katz, J. E. Mondloch, R. K. Totten, J. K. Park, S. T. Nguyen, O. K. Farha, and J. T. Hupp, "Simple and compelling biomimetic Metal-Organic framework catalyst for the degradation of nerve agent simulants," *Angew. Chem. Int. Ed.*, vol. 53, no. 2, pp. 497–501, 2014.

- [55] J. B. DeCoste and G. W. Peterson, "Metal-Organic frameworks for air purification of toxic chemicals," *Chem. Rev.*, vol. 114, no. 11, pp. 5695–5727, 2014.
- [56] H. Jasuja, G. Peterson, J. Decoste, M. Browe, and K. S. Walton, "Evaluation of MOFs for air purification and air quality control applications: Ammonia removal from air," *Chem. Eng. Sci.*, vol. 124, pp. 118–124, 2015.
- [57] B. Li, H-M. Wen, W. Zhou, and B. Chen, "Porous Metal-Organic frameworks for gas storage and separation: What, how, and why?," *J. Phys. Chem. Lett.*, vol. 5, no. 20, pp. 3468–3479, 2014.
- [58] B. Li, H. Wang, and B. Chen, "Microporous Metal-Organic frameworks for gas separation," *Chem. Asian J.*, vol. 9, no. 6, pp. 1474–1498, 2014.
- [59] P. Horcajada, Tamim Chalati, C. Serre, B. Gillet, C. Sebrie, T. Baati, J. F. Eubank, D. Heurtaux, P. Clayette, C. Kreuz, J-S. Chang, Y. Hwang, V. Marsaud, P-N. Bories, L. Cynober, S. Gil, G. Férey, P. Couvreur, and R. Gref, "Porous metal-organic framework nanoscale carriers as a potential platform for drug delivery and imaging," *Nat. Mater.*, vol. 9, no. 2, pp. 172–178, 2009.
- [60] M-X. Wu and Y-W. Yang, "Metal-Organic Framework (MOF)-Based Drug/Cargo delivery and cancer therapy," *Adv. Mater.*, vol. 29, no. 23, pp. 1606134, 2017.
- [61] S. Keskin and S. Kizilel, "Biomedical applications of metal-organic frameworks," *Industrial Eng. Chem. Res.*, vol. 50, no. 4, pp. 1799–1812, 2011.
- [62] A. Corma, H. García, and F.X. Llabrés i Xamena, "Engineering metal organic frameworks for heterogeneous catalysis," *Chem. Rev.*, vol. 110, no. 8, pp. 4606–55, 2010.
- [63] J. Gascon, A. Corma, F. Kapteijn, and F.X. Llabrés i Xamena, "Metal-organic framework catalysis: Quo vadis?," *Acs Catal.*, vol. 4, no. 2, pp. 361–378, 2014.
- [64] H. Noh, Y. Cui, A. W. Peters, D. R. Pahls, M. A. Ortuño, N. A. Vermeulen, C. J. Cramer, L. Gagliardi, J. T. Hupp, and O. K. Farha, "An exceptionally stable Metal-Organic framework supported Molybdenum(VI) oxide catalyst for cyclohexene epoxidation," *J. Am. Chem. Soc.*, vol. 138, no. 44, 2016.

- [65] T. Bogaerts, A. Van Yperen-De Deyne, Y-Y. Liu, F. Lynen, V. Van Speybroeck, and P. Van Der Voort, "Mn-salenMIL101(Al): a heterogeneous, enantioselective catalyst synthesized using a 'bottle around the ship' approach," *Chem. Commun.*, vol. 49, no. 73, pp. 8021–8023, 2013.
- [66] A. Dhakshinamoorthy and H. Garcia, "Catalysis by metal nanoparticles embedded on metal-organic frameworks," *Chem. soc. rev.*, vol. 41, no. 15, pp. 5262–5284, 2012.
- [67] C. Rösler and R. A. Fischer, "Metal-organic frameworks as hosts for nanoparticles," *Crystengcomm*, vol. 17, no. 2, pp. 199–217, 2014.
- [68] F-X. Coudert, "Responsive Metal-Organic frameworks and framework materials: Under pressure, taking the heat, in the spotlight, with friends," *Chem. Mater.*, vol. 27, no. 6, pp. 1905–1916, 2015.
- [69] P. K. Kundu, G. L. Olsen, V. Kiss, and R. Klajn, "Nanoporous frameworks exhibiting multiple stimuli responsiveness," *Nat. Commun.*, vol. 5, pp. 3588, 2014.
- [70] M.D. Allendorf, C.A. Bauer, R.K. Bhakta, and R.J.T. Houk, "Luminescent metal-organic frameworks," *Chem. soc. rev.*, vol. 38, no. 5, pp. 1330–1352, 2009.
- [71] W. P. Lustig, S. Mukherjee, N. D. Rudd, A. V. Desai, J. Li, and S. K. Ghosh, "Metal-organic frameworks: functional luminescent and photonic materials for sensing applications," *Chem. soc. rev.*, vol. 46, no. 11, pp. 3242–3285, 2017.
- [72] M. Kurmoo, "Magnetic metal-organic frameworks," *Chem. soc. rev.*, vol. 38, no. 5, pp. 1353, 2009.
- [73] E. Coronado and G. Espallargas, "Dynamic magnetic MOFs," *Chem. soc. rev.*, vol. 42, no. 4, pp. 1525–1539, 2012.
- [74] D. Liu, K. Lu, C. Poon, and W. Lin, "Metal-organic frameworks as sensory materials and imaging agents," *Inorg. Chem.*, vol. 53, no. 4, pp. 1916–24, 2013.
- [75] Q. Zhang and J. M. Shreeve, "Metal-Organic frameworks as high explosives: A new concept for energetic materials," *Angew. Chem. Int. Ed.*, vol. 53, no. 10, pp. 2540–2542, 2014.
- [76] K. A. McDonald, S. Seth, and A. J. Matzger, "Coordination polymers with high energy density: An emerging class of explosives," *Cryst Growth Des.*, vol. 15, no. 12, pp. 5963–5972, 2015.

- [77] C. Combelles, B. M. Yahia, L. Pedesseau, and M.-L. Doublet, "Design of electrode materials for Lithium-Ion batteries: The example of Metal-Organic frameworks," *J. Phys. Chem. C*, vol. 114, no. 20, pp. 9518–9527, 2010.
- [78] S. Bai, X. Liu, K. Zhu, S. Wu, and H. Zhou, "Metal-organic framework-based separator for lithium-sulfur batteries," *Nat. Energy*, vol. 1, no. 7, pp. 16094, 2016.
- [79] P. Ramaswamy, N. E. Wong, and G. K. H. Shimizu, "MOFs as proton conductors - challenges and opportunities," *Chem. soc. rev.*, vol. 43, no. 16, pp. 5913–5932, 2014.
- [80] MOFapps, "<http://www.mofapps.com>," .
- [81] MOFtechnologies, "<http://www.moftechnologies.com>," .
- [82] NuMat Technologies, "<http://www.numat-tech.com>," .
- [83] N. Czaja, A. Trukhan and U. Müller, "Industrial applications of metal-organic frameworks," *Chem. soc. rev.*, vol. 38, no. 5, pp. 1284–1293, 2009.
- [84] P. Silva, S. Vilela, J. Tomé, and F. Paz, "Multifunctional metal-organic frameworks: from academia to industrial applications," *Chem. Soc. Rev.*, vol. 44, no. 19, 2015.
- [85] B. Yilmaz, N. Trukhan, and U. Müller, "Industrial outlook on zeolites and metal-organic frameworks," *Chinese J. Catal.*, vol. 33, no. 1, pp. 3–10, 2012.
- [86] J-Z. Gu, W-G. Lu, L. Jiang, H-C. Zhou, and T-B. Lu, "3D porous Metal-Organic framework exhibiting selective adsorption of water over organic solvents," *Inorg. Chem.*, vol. 46, no. 15, pp. 5835–5837, 2007.
- [87] P. Küsgens, M. Rose, I. Senkovska, H. Fröde, A. Henschel, S. Siegle, and S. Kaskel, "Characterization of metal-organic frameworks by water adsorption," *Micropor. Mesopor. Mat.*, vol. 120, no. 3, pp. 325–330, 2009.
- [88] J. J. Low, A. I. Benin, P. Jakubczak, J. F. Abrahamian, S. A. Faheem, and R. R. Willis, "Virtual high throughput screening confirmed experimentally: Porous coordination polymer hydration," *J. Am. Chem. Soc.*, vol. 131, no. 43, pp. 15834–42, 2009.
- [89] K. Tan, N. Nijem, P. Canepa, Q. Gong, J. Li, T. Thonhauser, and Y. J. Chabal, "Stability and hydrolyzation of metal-organic frameworks

- with Paddle-Wheel SBUs upon hydration,” *Chem. Mater.*, vol. 24, no. 16, pp. 3153–3167, 2012.
- [90] H. Choi, J. Kim, J. Moon, Y. Kim, C. Choi, H. Lim, E. Kim, S-W. Rha, C. Park, H. Seo, and D. Oh, “Unusual dominant course of left circumflex coronary artery to right coronary artery territory with absent right coronary artery,” *J. Cardiol.*, vol. 55, no. 1, pp. 117–119, 2010.
- [91] J. Ehrenmann, S. K Henninger, and C. Janiak, “Water adsorption characteristics of MIL-101 for Heat-Transformation applications of MOFs,” *Eur. J. Inorg. Chem.*, vol. 2011, no. 4, pp. 471–474, 2011.
- [92] G. Akiyama, R. Matsuda, and S. Kitagawa, “Highly porous and stable coordination polymers as water sorption materials,” *Chem. Lett.*, vol. 39, no. 4, pp. 360–361, 2010.
- [93] D. Bazer-Bachi, L. Assié, V. Lecocq, B. Harbuzaru, and V. Falk, “Towards industrial use of metal-organic framework: Impact of shaping on the MOF properties,” *Powder Technol.*, vol. 255, pp. 52–59, 2014.
- [94] K. Park, Z. Ni, A. P. Côté, J. Choi, R. Huang, F. J. Uribe-Romo, H. K. Chae, M. O’Keeffe, and O. M. Yaghi, “Exceptional chemical and thermal stability of zeolitic imidazolate frameworks,” *Proc. National Acad. Sci.*, vol. 103, no. 27, pp. 10186–10191, 2006.
- [95] Y-K. Seo, J. Yoon, J. Lee, Y. Hwang, C-H. Jun, J-S. Chang, S. Wuttke, P. Bazin, A. Vimont, M. Daturi, S. Bourrelly, P. L. Llewellyn, P. Horcajada, C. Serre, and G. Férey, “Energy-Efficient dehumidification over hierachically porous Metal-Organic frameworks as advanced water adsorbents,” *Adv. Mater.*, vol. 24, no. 6, pp. 806–810, 2012.
- [96] J. E. Mondloch, M. J. Katz, N. Planas, L. Semrouni, D. and Gagliardi, J. T. Hupp, and O. K. Farha, “Are Zr_6 -based MOFs water stable? linker hydrolysis vs. capillary-force-driven channel collapse,” *Chem. Commun.*, vol. 50, no. 64, pp. 8944–8946, 2014.
- [97] I. Kang, N. Khan, E. Haque, and S. Jhung, “Chemical and thermal stability of isotypic Metal-Organic frameworks: Effect of metal ions,” *Chem. Eur. J.*, vol. 17, no. 23, pp. 6437–6442, 2011.
- [98] S. Biswas and P. Van Der Voort, “A general strategy for the synthesis of functionalised UiO-66 frameworks: Characterisation, stability and CO_2 adsorption properties,” *Eur. J. Inorg. Chem.*, vol. 2013, no. 12, pp. 2154–2160, 2013.

- [99] M. J. Katz, Z. J. Brown, Y. J. Colón, P. W. Siu, K. A. Scheidt, R. Q. Snurr, J. T. Hupp, and O. K. Farha, "A facile synthesis of UiO-66, UiO-67 and their derivatives," *Chem. Commun.*, vol. 49, no. 82, 2013.
- [100] D. Jiang, A. D. Burrows, Y. Xiong, and K. J. Edler, "Facile synthesis of crack-free metal-organic framework films on alumina by a dip-coating route in the presence of polyethylenimine," *J. Mater. Chem.*, vol. 1, no. 18, pp. 5497–5500, 2013.
- [101] M. Hartmann and M. Fischer, "Amino-functionalized basic catalysts with MIL-101 structure," *Micropor. Mesopor. Mat.*, vol. 164, pp. 38–43, 2012.
- [102] D. J. Tranchemontagne, J. R. Hunt, and O. M. Yaghi, "Room temperature synthesis of metal-organic frameworks: MOF-5, MOF-74, MOF-177, MOF-199, and IRMOF-0," *Tetrahedron*, vol. 64, no. 36, pp. 8553–8557, 2008.
- [103] T. Loiseau, C. Serre, C. Huguenard, G. Fink, F. Taulelle, M. Henry, T. Bataille, and G. Férey, "A rationale for the large breathing of the porous aluminum terephthalate (MIL-53) upon hydration," *Chem. Eur. J.*, vol. 10, no. 6, pp. 1373–1382, 2004.
- [104] A. F. Gross, E. Sherman, and J. J. Vajo, "Aqueous room temperature synthesis of cobalt and zinc sodalite zeolitic imidizolate frameworks," *Dalton Trans.*, vol. 41, no. 18, pp. 5458–5460, 2012.
- [105] J. B. DeCoste, G. W. Peterson, H. Jasuja, G. T. Glover, Y.-g. Huang, and J. S. Walton, "Stability and degradation mechanisms of metal-organic frameworks containing the $\text{Zr}_6\text{O}_4\text{OH}_4$ secondary building unit," *J. Mater. Chem.*, vol. 1, no. 18, pp. 5642–5650, 2013.
- [106] G. Férey, C. Mellot-Draznieks, C. Serre, F. Millange, J. Dutour, S. Surblé, and I. Margiolaki, "A chromium Terephthalate-Based solid with unusually large pore volumes and surface area," *Science*, vol. 309, no. 5743, pp. 2040–2042, 2005.
- [107] J. Ren, H. W. Langmi, B. C. North, M. Mathe, and D. Bessarabov, "Modulated synthesis of zirconium-metal organic framework (Zr-MOF) for hydrogen storage applications," *Int. J. Hydrogen Energ.*, vol. 39, no. 2, pp. 890–895, 2014.
- [108] D.-Y. Hong, Y. Hwang, C. Serre, G. Férey, and J.-S. Chang, "Porous chromium terephthalate MIL-101 with coordinatively unsaturated sites: Surface functionalization, encapsulation, sorption and catalysis," *Adv. Funct. Mater.*, vol. 19, no. 10, pp. 1537–1552, 2009.

- [109] T. Wittmann, R. Siegel, N. Reimer, W. Milius, N. Stock, and J. Senker, "Enhancing the water stability of Al-MIL-101-NH₂ via postsynthetic modification," *Chem. Eur. J.*, vol. 21, no. 1, pp. 314–323, 2015.
- [110] I. Bezverkhyy, G. Ortiz, G. Chaplais, C. Marichal, G. Weber, and J-P. Bellat, "MIL-53(Al) under reflux in water: Formation of γ -AlO(OH) shell and H₂BDC molecules intercalated into the pores," *Micropor. Mesopor. Mat.*, vol. 183, pp. 156–161, 2014.
- [111] D-D. Zu, L. Lu, X-Q. Liu, D-Y. Zhang, and L-B. Sun, "Improving hydrothermal stability and catalytic activity of Metal-Organic frameworks by graphite oxide incorporation," *J. Phys. Chem. C*, vol. 118, no. 34, pp. 19910–19917, 2014.
- [112] D. Mustafa, E. Breynaert, Sneha R. Bajpe, J. A. Martens, and C.E.A. Kirschhock, "Stability improvement of Cu₃(BTC)₂ metal-organic frameworks under steaming conditions by encapsulation of a kegglin polyoxometalate," *Chem. Commun*, vol. 47, no. 28, pp. 8037–8039, 2011.
- [113] M. Kandiah, M. Nilsen, S. Usseglio, S. Jakobsen, U. Olsbye, M. Tilset, C. Larabi, E. Quadrelli, F. Bonino, and K. Lillerud, "Synthesis and stability of tagged UiO-66 Zr-MOFs," *Chem. Mater.*, vol. 22, no. 24, pp. 6632–6640, 2010.
- [114] X. Zhao, D. Liu, H. Huang, W. Zhang, Q. Yang, and C. Zhong, "The stability and defluoridation performance of MOFs in fluoride solutions," *Micropor. Mesopor. Mat.*, vol. 185, pp. 72–78, 2014.
- [115] C. Mottillo and T. Friščić, "Carbon dioxide sensitivity of zeolitic imidazolate frameworks," *Angew. Chem. Int. Ed.*, vol. 53, no. 29, pp. 7471–7474, 2014.
- [116] J. H. Cavka, S. Jakobsen, U. Olsbye, N. Guillou, C. Lamberti, S. Bordiga, and K. P. Lillerud, "A new zirconium inorganic building brick forming metal organic frameworks with exceptional stability," *J. Am. Chem. Soc.*, vol. 130, pp. 13850–13851, 2008.
- [117] B. Bueken, F. Vermoortele, M. J. Cliffe, M. T. Wharmby, D. Foucher, J. Wieme, L. Vanduyfhuys, C. Martineau, N. Stock, F. Taulelle, V. Van Speybroeck, A. L. Goodwin, and D. De Vos, "A breathing zirconium Metal-Organic framework with reversible loss of crystallinity by correlated nanodomain formation," *Chem. Eur. J.*, vol. 22, no. 10, pp. 3264–3267, 2016.

- [118] Z. Hu, A. Nalaparaju, Y. Peng, J. Jiang, and D. Zhao, "Modulated hydrothermal synthesis of UiO-66(Hf)-Type Metal-Organic frameworks for optimal carbon dioxide separation," *Inorg. Chem.*, vol. 55, no. 3, pp. 1134–1141, 2016.
- [119] M. Lammert, M. T. Wharmby, S. Smolders, B. Bueken, A. Lieb, K. A. Lomachenko, D. De Vos, and N. Stock, "Cerium-based metal organic frameworks with UiO-66 architecture: synthesis, properties and redox catalytic activity," *Chem. Commun*, vol. 51, no. 63, pp. 12578–12581, 2015.
- [120] S-N. Kim, Y-R. Lee, S-H. Hong, M-S. Jang, and W-S. Ahn, "Pilot-scale synthesis of a zirconium-benzenedicarboxylate UiO-66 for CO₂ adsorption and catalysis," *Catal. Today*, vol. 245, pp. 54–60, 2015.
- [121] Valenzano L., Civalleri B., S. Chavan, S. Bordiga, M. H. Nilsen, S. Jakobsen, K. P. Lillerud, and C. Lamberti, "Disclosing the complex structure of uio-66 metal organic framework: A synergic combination of experiment and theory," *Chem. Mater.*, vol. 23, pp. 1700–1718, 2011.
- [122] Y. Bai, Y. Dou, L-H. Xie, W. Rutledge, J-R. Li, and H-C. Zhou, "Zr-based metal-organic frameworks: design, synthesis, structure, and applications," *Chem. soc. rev.*, vol. 45, no. 8, pp. 2327–67, 2016.
- [123] A. Schaate, P. Roy, A. Godt, J. Lippke, F. Waltz, M. Wiebcke, and P. Behrens, "Modulated synthesis of Zr-Based Metal-Organic frameworks: From nano to single crystals," *Chem. Eur. J.*, vol. 17, no. 24, pp. 6643–6651, 2011.
- [124] M.A. Nasalevich, M. van der Veen, F. Kapteijn, and J. Gascon, "Metal-organic frameworks as heterogeneous photocatalysts: advantages and challenges," *Crytengcomm*, vol. 16, no. 23, pp. 4919–4926, 2014.
- [125] S. Ling and B. Slater, "Unusually large band gap changes in breathing Metal-Organic framework materials," *J. Phys. Chem. C*, vol. 119, no. 29, pp. 16667–16677, 2015.
- [126] A. De Vos, K. Hendrickx, P. Van Der Voort, V. Van Speybroeck, and K. Lejaeghere, "Missing linkers: an alternative pathway to UiO-66 electronic structure engineering," *Chem. Mater.*, vol. 29, no. 7, pp. 3006–3019, 2017.
- [127] A. Wiersum, E. Soubeyrand-Lenoir, Q. Yang, B. Moulin, V. Guillermin, M. Yahia, S. Bourrelly, A. Vimont, S. Miller, C. Vagner, M. Daturi, G. Clet, G. Serre, C. and Maurin, and P. Llewellyn, "An evaluation of

- UiO-66 for Gas-Based applications,” *Chem. Asian J.*, vol. 6, no. 12, pp. 3270–3280, 2011.
- [128] M. Vandichel, J. Hajek, F. Vermoortele, M. Waroquier, D. De Vos, and V. Van Speybroeck, “Active site engineering in UiO-66 type metal-organic frameworks by intentional creation of defects: a theoretical rationalization,” *ChrystEngComm*, vol. 17, no. 2, pp. 395–406, 2014.
- [129] W-W. Zhao, C-Y. Zhang, Z-G. Yan, L-P. Bai, X. Wang, H. Huang, Y-Y. Zhou, Y. Xie, F-S. Li, and J-R. Li, “Separations of substituted benzenes and polycyclic aromatic hydrocarbons using normal- and reverse-phase high performance liquid chromatography with UiO-66 as the stationary phase,” *J. of Chromatogr. A*, vol. 1370, pp. 121–128, 2014.
- [130] I. Stassen, M. Styles, T. Assche, N. Campagnol, J. Fransaer, J. Denayer, J-C. Tan, P. Falcaro, D. De Vos, and R. Ameloot, “Electrochemical film deposition of the zirconium Metal-Organic framework UiO-66 and application in a miniaturized sorbent trap,” *Chem. Mater.*, vol. 27, no. 5, pp. 1801–1807, 2015.
- [131] L. Shen, W. Wu, R. Liang, R. Lin, and L. Wu, “Highly dispersed palladium nanoparticles anchored on UiO-66(NH₂) metal-organic framework as a reusable and dual functional visible-light-driven photocatalyst,” *Nanoscale*, pp. 9374–9382, 2013.
- [132] J. Hajek, B. Bueken, M. Waroquier, D. De Vos, and V. Van Speybroeck, “The remarkable amphoteric nature of defective UiO-66 in catalytic reactions,” *Chemcatchem*, vol. 9, no. 12, pp. 2203–2210, 2017.
- [133] J. Barber, “Photosynthetic energy conversion: natural and artificial,” *Chem. Soc. Rev.*, vol. 38, 2009.
- [134] D. Gust, T. A. Moore, and A. L. Moore, “Solar fuels via artificial photosynthesis,” *Acc. Chem. Res.*, vol. 42, no. 12, pp. 1890–1898, 2009.
- [135] H.J.M. Hou, S. I. Allakhverdiev, M. M. Najafpour, and Govindjee, “Current challenges in photosynthesis: from natural to artificial,” *Front. Plant Sci.*, vol. 5, pp. 232, 2014.
- [136] A. Fujishima and K. Honda, “Electrochemical photolysis of water at a semiconductor electrode,” *Nature*, vol. 238, pp. 37–38, 1972.
- [137] H. Hennig, “Semiconductor photocatalysis: Principles and applications,” *Angew. Chem. Int. Ed.*, vol. 54, no. 15, pp. 4429–4429, 2015.

- [138] M.R. Hoffmann, S. T. Martin, W. Choi, and D. W. Bahnemann, "Environmental applications of semiconductor photocatalysis," *Chem. Rev.*, vol. 95, no. 1, pp. 69–96, 1995.
- [139] M. Fox and M. T. Dulay, "Heterogeneous photocatalysis," *Chem. Rev.*, vol. 93, no. 1, pp. 341–357, 1993.
- [140] D.M. Schultz and T. P. Yoon, "Solar synthesis: Prospects in visible light photocatalysis," *Science*, vol. 343, pp. 1239176, 2014.
- [141] X. Lang, X. Chen, and J. Zhao, "Heterogeneous visible light photocatalysis for selective organic transformations," *Chem. Soc. Rev.*, 2014.
- [142] H. Kisch, *Semiconductor Photocatalysis: Principles and Applications.*, Wiley-vch.
- [143] R. Ameta and S. C. Ameta, *Photocatalysis: Principles and Applications.*, CRC Press.
- [144] "<http://www.thesolarspark.co.uk>," .
- [145] S. Park, W. Chang, C. Lee, S. Park, H-Y. Ahn, and K. Nam, "Photocatalytic hydrogen generation from hydriodic acid using methylammonium lead iodide in dynamic equilibrium with aqueous solution," *Nat. Energy*, vol. 2, no. 1, pp. nenergy2016185, 2016.
- [146] J. Schneider and D. W. Bahnemann, "Undesired role of sacrificial reagents in photocatalysis," *J. Phys. Chem. Lett.*, vol. 4, no. 20, pp. 3479–3483, 2013.
- [147] M.A. Nasalevich, C. H. Hendon, J. G. Santaclara, K. Svane, B. van der Linden, S. L. Veber, M. V. Fedin, A. J. Houtepen, M. A. van der Veen, F. Kapteijn, A. Walsh, and J. Gascon, "Electronic origins of photocatalytic activity in d0 metal organic frameworks," *Sci. Rep.*, vol. 6, pp. 23676, 2016.
- [148] J.G. Santaclara, F. Kapteijn, J. Gascon, and M.A. van der Veen, "Understanding metal-organic frameworks for photocatalytic solar fuel production," *Crytengcomm*, vol. 19, no. 29, pp. 4118–4125, 2017.
- [149] C. Gomes Silva, I. Luz, F. X. Llabrés i Xamena, A. Corma, and H. García, "Water stable Zr-Benzenedicarboxylate Metal-Organic frameworks as photocatalysts for hydrogen generation," *Chem. Eur. J.*, vol. 16, no. 36, pp. 11133–11138, 2010.

- [150] L. Shen, Shijing L., Weiming W., Ruowen L., and Ling W., "Multifunctional NH_2 -mediated zirconium metal-organic framework as an efficient visible-light-driven photocatalyst for selective oxidation of alcohols and reduction of aqueous Cr(VI) ," *Dalton Trans.*, pp. 13649–13658, 2013.
- [151] Z. Long, S. Wang, Z. Ding, S. Wang, Y. Zhou, L. Huang, and X. Wang, "Amine-functionalized zirconium metal-organic framework as efficient visible-light photocatalyst for aerobic organic transformations," *Chem. Commun.*, vol. 48, pp. 11656–11658, 2012.
- [152] D. Sun, Y. Fu, W. Liu, Lin Y., D. Wang, L. Yang, X. Fu, and Z. Li, "Studies on photocatalytic CO_2 reduction over $\text{NH}_2\text{-UiO-66(Zr)}$ and its derivatives: Towards a better understanding of photocatalysis on Metal-Organic frameworks," *Chem. Eur. J.*, vol. 19, no. 42, pp. 14279–14285, 2013.
- [153] Lijuan S., Ruowen L., Mingbu L., Fenfen J., and Ling W., "Electronic effects of ligand substitution on metal-organic framework photocatalysts: the case study of UiO-66 ," *Phys. Chem. Chem. Phys.*, pp. 117–122, 2014.
- [154] T. Goh, C. Xiao, R. Maligal-Ganesh, X. Li, and W. Huang, "Utilizing mixed-linker zirconium based metal-organic frameworks to enhance the visible light photocatalytic oxidation of alcohol," *Chem. Eng. Sci.*, vol. 124, pp. 45–51, 2015.
- [155] E. Flage-Larsen, A. Røyset, J. H. Cavka, and K. Thorshaug, "Band gap modulations in UiO Metal-Organic frameworks," *J. Phys. Chem. C*, vol. 117, pp. 20610–20616, 2013.
- [156] T. Musho, J. Li, and N. Wu, "Band gap modulation of functionalized metal-organic frameworks," *Phys. Chem. Chem. Phys.*, vol. 16, no. 43, pp. 23646–23653, 2014.
- [157] C. Hendon, D. Tiana, M. Fontecave, C. Sanchez, L. D'arras, C. Sassoey, L. Rozes, C. Mellot-Draznieks, and A. Walsh, "Engineering the optical response of the Titanium-MIL-125 Metal-Organic framework through ligand functionalization," *J. Am. Chem. Soc.*, vol. 135, no. 30, pp. 10942–10945, 2013.
- [158] L. Sun, M. G. Campbell, and M. Dincă, "Electrically conductive porous Metal-Organic frameworks," *Angew. Chem. Int. Ed.*, vol. 55, no. 11, pp. 3566–3579, 2016.

- [159] “<http://www.renishaw.com/en/a-basic-overview-of-raman-spectroscopy-25805>,” .
- [160] “<https://commons.wikimedia.org/>,” .
- [161] N.J. Turro, V. Ramamurthy, and J.C. Scaiano, Eds., *Principles of Molecular Photochemistry, an Introduction*, University Science Books, 2009.
- [162] T. Tytgat, B. Hauchecorne, M. Smits, S. W. Verbruggen, and S. Lenaerts, “Concept and validation of a fully automated photocatalytic test setup,” *J. Lab. Aut.*, vol. 17, no. 2, pp. 134–143, 2012.
- [163] P. Hohenberg and W. Kohn, “Inhomogeneous electron gas,” *Phys. Rev.*, vol. 136, no. 3B, pp. B864–B871, 1964.
- [164] J. Xia, C. Huang, I. Shin, and E. A. Carter, “Can orbital-free density functional theory simulate molecules?” *J. Chem. Phys.*, vol. 136, no. 8, pp. 084102, 2012.
- [165] W. Kohn and L.J. Sham, “Self-Consistent equations including exchange and correlation effects,” *Phys. Rev.*, vol. 140, no. 4A, pp. A1133–A1138, 1965.
- [166] M. Korth and S. Grimme, “‘Mindless’ DFT benchmarking,” *J. Chem. Theory Comput.*, vol. 5, no. 4, pp. 993–1003, 2009.
- [167] K. Lejaeghere, G. Bihlmayer, T. Björkman, P. Blaha, S. Blügel, V. Blum, D. Caliste, I. E. Castelli, S. J. Clark, A. Corso, S.o de Gironcoli, T. Deutsch, J. K. Dewhurst, I. Di Marco, C. Draxl, M.in Dulak, O. Eriksson, J. A Flores-Livas, K. F. Garrity, L. Genovese, P. Giannozzi, M. Giantomassi, S. Goedecker, X. Gonze, O. Grånäs, E.K.U. Gross, A. Gulans, F. Gygi, D.R. Hamann, P.J. Hasnip, N.A.W. Holzwarth, D. Iusan, D. B. Jochym, F. Jollet, D. Jones, G. Kresse, K. Koepnik, E. Küçükbenli, Y. O. Kvashnin, I. L.M. Locht, S. Lubeck, M. Marsman, N. Marzari, U. Nitzsche, L. Nordström, T. Ozaki, L. Paulatto, C. J. Pickard, W. Poelmans, M. I.J. Probert, K. Refson, M. Richter, G-M.o Rignanese, S. Saha, M. Scheffler, M. Schlipf, K. Schwarz, S. Sharma, F. Tavazza, P. Thunström, A. Tkatchenko, M. Torrent, M. J. Vanderbilt, D.and van Setten, V. Speybroeck, J. M. Wills, J. R. Yates, G-X. Zhang, and S. Cottenier, “Reproducibility in density functional theory calculations of solids,” *Science*, vol. 351, no. 6280, 2016.
- [168] A.D. Laurent and D. Jacquemin, “TD-DFT benchmarks: A review,” *Int. J. Quant. Chem.*, vol. 113, no. 17, pp. 2019–2039, 2013.

- [169] J. P. Perdew, "Jacob's ladder of density functional approximations for the exchange-correlation energy," *AIP Conf. Proc.*, pp. 1–20, 2001.
- [170] R. Stowasser and R. Hoffmann, "What do the Kohn-Sham orbitals and eigenvalues mean?," *J. Am. Chem. Soc.*, vol. 121, no. 14, pp. 3414–3420, 1999.
- [171] S. Hamel, P. Duffy, M. E. Casida, and D. R. Salahub, "Kohn-Sham orbitals and orbital energies: fictitious constructs but good approximations all the same," *J. Electron. Spectrosc.*, vol. 123, no. 2-3, pp. 345–363, 2002.
- [172] L. Kleinman, "Significance of the highest occupied Kohn-Sham eigenvalue," *Phys. Rev. B*, vol. 56, no. 19, pp. 12042–12045, 1997.
- [173] J. P. Perdew, R. G. Parr, M. Levy, and J. L. Balduz, "Density-Functional theory for fractional particle number: Derivative discontinuities of the energy," *Phys Rev Lett*, vol. 49, no. 23, pp. 1691–1694, 1982.
- [174] P. Politzer and F. Abu-Awwad, "A comparative analysis of Hartree-Fock and Kohn-Sham orbital energies," *Theor. Chem. Acc.*, vol. 99, no. 2, pp. 83–87, 1998.
- [175] R. van Meer, O. V. Gritsenko, and E. J. Baerends, "Physical meaning of virtual Kohn-Sham orbitals and orbital energies: An ideal basis for the description of molecular excitations," *J. Chem. Theory Comput.*, vol. 10, no. 10, pp. 4432–41, 2014.
- [176] J-L. Bredas, "Mind the gap!," *Mater. Horizons*, vol. 1, no. 1, pp. 17–19, 2013.
- [177] G. Zhang and C. B. Musgrave, "Comparison of DFT methods for molecular orbital eigenvalue calculations," *J. Phys. Chem.*, vol. 111, no. 8, pp. 1554–1561, 2007.
- [178] M. A.L. Marques, C. A. Ullrich, F. Nogueira, A. Rubio, K. Burke, and E.K.U. Gross, *Time-Dependent Density Functional Theory*, vol. 55, Springer, 2004.
- [179] C. Adamo and D. Jacquemin, "The calculations of excited-state properties with Time-Dependent density functional theory," *Chem. Soc. Rev.*, vol. 42, no. 3, pp. 845–857, 2012.
- [180] A. Dreuw and M. Head-Gordon, "Single-Reference ab initio methods for the calculation of excited states of large molecules," *Chem. Rev.*, vol. 105, no. 11, pp. 4009–4037, 2005.

- [181] J. Boino, M. Biczysko, F. Santoro, and V. Barone, "General approach to compute vibrationally resolved One-Photon electronic spectra," *J. Chem. Theory Comput.*, vol. 6, no. 4, pp. 1256–1274, 2010.
- [182] V. Barone, M. Biczysko, J. Boino, L. Carta, and A. Pedone, "Environmental and dynamical effects on the optical properties of molecular systems by time-independent and time-dependent approaches: Coumarin derivatives as test cases," *Comput. Theor. Chem.*, vol. 1037, pp. 35–48, 2014.
- [183] A.D. Laurent, C. Adamo, and D. Jacquemin, "Dye chemistry with time-dependent density functional theory," *Phys. Chem. Chem. Phys.*, vol. 16, no. 28, pp. 14334–14356, 2014.
- [184] A. Pedone, G. Prampolini, S. Monti, and V. Barone, "Realistic modeling of fluorescent Dye-Doped silica nanoparticles: A step toward the understanding of their enhanced photophysical properties.," *Chem. Mater.*, vol. 23, no. 22, pp. 5016–5023, 2011.
- [185] T. De Meyer, K. Hemelsoet, L. Van der Schueren, E. Pauwels, K. De Clerck, and V. Van Speybroeck, "Investigating the halochromic properties of azo dyes in an aqueous environment by using a combined experimental and theoretical approach," *Chem. Eur. J.*, vol. 18, no. 26, pp. 8120–8129, 2012.
- [186] K. Hemelsoet, Q. Qian, T. De Meyer, K. De Wispelaere, B. De Sterck, B. M. Weckhuysen, M. Waroquier, and V. Van Speybroeck, "Identification of intermediates in zeolite-catalyzed reactions by in situ uv/vis microspectroscopy and a complementary set of molecular simulations," *Chem. Eur. J.*, vol. 19, no. 49, pp. 16595–16606, 2013.
- [187] M. J. Frisch, G. W. Trucks, H. B. Schlegel, G. E. Scuseria, M. A. Robb, J. R. Cheeseman, G. Scalmani, V. Barone, B. Mennucci, G. A. Petersson, H. Nakatsuji, M. Caricato, X. Li, H. P. Hratchian, A. F. Izmaylov, J. Boino, G. Zheng, J. L. Sonnenberg, M. Hada, M. Ehara, K. Toyota, R. Fukuda, J. Hasegawa, M. Ishida, T. Nakajima, Y. Honda, O. Kitao, H. Nakai, T. Vreven, J. A. Montgomery, Jr., J. E. Peralta, F. Ogliaro, M. Bearpark, J. J. Heyd, E. Brothers, K. N. Kudin, V. N. Staroverov, R. Kobayashi, J. Normand, K. Raghavachari, A. Rendell, J. C. Burant, S. S. Iyengar, J. Tomasi, M. Cossi, N. Rega, J. M. Millam, M. Klene, J. E. Knox, J. B. Cross, V. Bakken, C. Adamo, J. Jaramillo, R. Gomperts, R. E. Stratmann, O. Yazyev, A. J. Austin, R. Cammi, C. Pomelli, J. W. Ochterski, R. L. Martin, K. Morokuma, V. G. Zakrzewski, G. A. Voth, P. Salvador, J. J. Dannenberg, S. Dapprich, A. D. Daniels, Ö. Farkas, J. B.

- Foresman, J. V. Ortiz, J. Cioslowski, and D. J. Fox, "Gaussian09 Revision D.01," .
- [188] J. Hafner, "Ab-initio simulations of materials using vasp: Density-functional theory and beyond," *J. Comput. Chem.*, vol. 29, pp. 2044–2078, 2008.
- [189] G. Bussi, D. Donadio, and M.E. Parrinello, "Canonical sampling through velocity rescaling," *J. Chem. Phys.*, vol. 126, no. 1, pp. 014101, 2007.
- [190] S. Nosé, "A molecular dynamics method for simulations in the canonical ensemble," *Mol. Phys.*, vol. 52, no. 2, pp. 255–268, 1984.
- [191] S. Nosé, "A unified formulation of the constant temperature molecular dynamics methods," *J. Chem. Phys.*, vol. 81, no. 1, pp. 511, 1984.
- [192] W. G. Hoover and B. Holian, "Kinetic moments method for the canonical ensemble distribution," *Phys. Lett. A*, vol. 211, no. 5, pp. 253–257, 1996.
- [193] D. Frenkel, , and B. Smit, Eds., *Understanding Molecular Simulation (Second Edition)*, Academic Press, second edition edition, 2002.
- [194] J. Hutter, M. Iannuzzi, F. Schiffmann, and J. VandeVondele, "cp2k: atomistic simulations of condensed matter systems," *Wiley Interdisciplinary Reviews: Computational Molecular Science*, vol. 4, no. 1, pp. 15–25, 2014.
- [195] V. Barone, J. Boino, M. Biczysko, and F. Santoro, "Fully integrated approach to compute vibrationally resolved optical spectra: From small molecules to macrosystems," *J. Chem. Theory Comput.*, vol. 5, no. 3, 2009.
- [196] J. Heyd, G. E. Scuseria, and M. Ernzerhof, "Hybrid functionals based on a screened coulomb potential," *J. Chem. Phys.*, vol. 118, no. 18, pp. 8207–8215, 2003.
- [197] J. Heyd, J. E. Peralta, G. E. Scuseria, and R. L. Martin, "Energy band gaps and lattice parameters evaluated with the Heyd-Scuseria-Ernzerhof screened hybrid functional," *J. Chem. Phys.*, vol. 123, no. 17, pp. 174101, 2005.
- [198] J. Heyd, G. Scuseria, and M. Ernzerhof, "Erratum: Hybrid functionals based on a screened coulomb potential' [*J. chem. phys.*118, 8207 (2003)]," *J. Chem. Phys.*, vol. 124, no. 21, pp. 219906, 2006.

- [199] E.N. Brothers, A. F. Izmaylov, J.O. Normand, V. Barone, and G.E. Scuseria, "Accurate solid-state band gaps via screened hybrid electronic structure calculations," *J. Chem. Phys.*, vol. 129, no. 1, pp. 011102, 2008.
- [200] L. Vial, F. Ludlow, J. Leclaire, R. Pérez-Fernández, and S. Otto, "Controlling the biological effects of spermine using a synthetic receptor," *J. Am. Chem. Soc.*, vol. 128, no. 31, pp. 10253–10257, 2006.
- [201] Chengteh L., Weitao Y., and Robert G. P., "Development of the Colle-Salvetti correlation-energy formula into a functional of the electron density," *Phys. Rev. B*, vol. 37, no. 2, pp. 785–789, 1988.
- [202] A. D. Becke, "Density-functional thermochemistry. III. the role of exact exchange," *J. Chem. Phys.*, vol. 98, no. 7, pp. 5648–5652, 1993.
- [203] R. Krishnan, J. Binkley, R. Seeger, and J. Pople, "Self-consistent molecular orbital methods. XX. a basis set for correlated wave functions," *J. Chem. Phys.*, vol. 72, no. 1, pp. 650–654, 1980.
- [204] D. Jacquemin, E. Perpète, G. E. Scuseria, I. Ciofini, and C. Adamo, "TD-DFT performance for the visible absorption spectra of organic dyes: conventional versus Long-Range hybrids," *J. Chem. Theory Comput.*, vol. 4, no. 1, pp. 123–135, 2008.
- [205] J. Tomasi, B. Mennucci, and R. Cammi, "Quantum mechanical continuum solvation models," *Chem. Rev.*, vol. 105, no. 8, pp. 2999–3093, 2005.
- [206] F. Weigend and R. Ahlrichs, "Balanced basis sets of split valence, triple zeta valence and quadruple zeta valence quality for h to rn: Design and assessment of accuracy," *Phys. Chem. Chem. Phys.*, vol. 7, no. 18, pp. 3297–3305, 2005.
- [207] T. Verstraelen, "Horton," <http://theochem.github.com/horton/>, 2011.
- [208] P. Bultinck, C. Van Alsenoy, P. W. Ayers, and R. Carbó-Dorca, "Critical analysis and extension of the hirshfeld atoms in molecules," *J. Chem. Phys.*, vol. 126, no. 14, pp. 144111, 2007.
- [209] P. Bultinck, P. W. Ayers, S. Fias, K. Tiels, and C. Van Alsenoy, "Uniqueness and basis set dependence of iterative hirshfeld charges," *Chem. Phys. Lett.*, vol. 444, no. 1-3, pp. 205–208, 2007.
- [210] T. Verstraelen, P. W. Ayers, V. Van Speybroeck, and M. Waroquier, "The conformational sensitivity of iterative stockholder partitioning schemes," *Chem. Phys. Lett.*, vol. 545, pp. 138–143, 2012.

- [211] T. Verstraelen, E. Pauwels, F. De Proft, V. Van Speybroeck, P. Geerlings, and M. Waroquier, "Assessment of atomic charge models for Gas-Phase computations on polypeptides," *J. Chem. Theory Comput.*, vol. 8, no. 2, pp. 661–676, 2012.
- [212] D. Vanpoucke, P. Bultinck, and I. Van Driessche, "Extending hirshfeld-i to bulk and periodic materials," *J. Comput. Chem.*, vol. 34, no. 5, pp. 405–417, 2013.
- [213] D. Vanpoucke, I. Van Driessche, and P. Bultinck, "Reply to 'comment on "extending hirshfeld-i to bulk and periodic materials"'", *J. Comput. Chem.*, vol. 34, no. 5, pp. 422–427, 2013.
- [214] D. E. P. Vanpoucke, "HIVE v3.x," <http://D.vanpoucke.be/>, 2011.
- [215] G. Kresse and J. Furthmüller, "Efficiency of ab-initio total energy calculations for metals and semiconductors using a plane-wave basis set," *Comput. Mater. Sci.*, pp. 169–186, 1996.
- [216] G. Kresse and D. Joubert, "From ultrasoft pseudopotentials to the projector augmented-wave method," *Phys. Rev. B*, vol. 59, pp. 1758–1775, 1999.
- [217] J.P. Perdew, K. Burke, and M. Ernzerhof, "Generalized gradient approximation made simple," *Phys. Rev. Lett.*, vol. 77, no. 18, pp. 3865–3868, 1996.
- [218] L. Pauling, "The nature of the chemical bond. iv. the energy of single bonds and the relative electronegativity of atoms.," *J. Am. Chem. Soc.*, vol. 54, no. 9, pp. 3570–3582, 1932.
- [219] F. Vermoortele, M. Vandichel, B. Van de Voorde, R. Ameloot, M. Waroquier, V. Van Speybroeck, and D. E. De Vos, "Electronic effects of linker substitution on lewis acid catalysis with Metal-Organic frameworks," *Angew. Chem. Int. Ed.*, vol. 51, no. 20, pp. 4887–4890, 2012.
- [220] V. Barone, M. Biczysko, J. Bloino, L. Carta, and A. Pedone, "Environmental and dynamical effects on the optical properties of molecular systems by time-independent and time-dependent approaches: Coumarin derivatives as test cases," *Comput. Theor. Chem.*, vol. 1037, pp. 35–48, 2014.
- [221] M.E. Pavone, G. Brancato, G. Morelli, and V. Barone, "Spectroscopic properties in the liquid phase: Combining High-Level ab initio calcu-

- lations and classical molecular dynamics,” *Chemphyschem*, vol. 7, no. 1, pp. 148–156, 2006.
- [222] V. Barone, J. Bloino, S. Monti, A. Pedone, and G. Prampolini, “Theoretical multilevel approach for studying the photophysical properties of organic dyes in solution,” *Phys. Chem. Chem. Phys.*, vol. 12, no. 35, pp. 10550–10561, 2010.
- [223] N. Mitri, S. Monti, G. Prampolini, and V. Barone, “Absorption and emission spectra of a flexible dye in solution: A computational Time-Dependent approach,” *J. Chem. Theory Comput.*, vol. 9, no. 10, pp. 4507–4516, 2013.
- [224] T. De Meyer, K. Hemelsoet, L. Van der Schueren, E. Pauwels, K. De Clerck, and V. Van Speybroeck, “Investigating the halochromic properties of azo dyes in an aqueous environment by using a combined experimental and theoretical approach,” *Chem. Eur. J.*, vol. 18, no. 26, pp. 8120–8129, 2012.
- [225] K. Hemelsoet, Q. Qian, T. De Meyer, K. De Wispelaere, B. De Sterck, B. M. Weckhuysen, M. Waroquier, and V. Van Speybroeck, “Identification of intermediates in Zeolite-Catalyzed reactions by in situ UV/Vis microspectroscopy and a complementary set of molecular simulations,” *Chem. Eur. J.*, vol. 19, no. 49, pp. 16595–16606, 2013.
- [226] A. Pedone, G. Prampolini, S. Monti, and V. Barone, “Realistic modeling of fluorescent Dye-Doped silica nanoparticles: A step toward the understanding of their enhanced photophysical properties,” *Chem. Mater.*, vol. 23, no. 22, pp. 5016–5023, 2011.
- [227] E. Runge and E. K. Gross, “Density-functional theory for time-dependent systems,” *Physical Review Letters*, vol. 52, no. 12, pp. 997–1000, 1984.
- [228] M. A. Marques, C. A. Ullrich, F. Nogueira, A. Rubio, K. Burke, and E. K. Gross, *Time-Dependent Density-functional theory*, vol. 706 of *Lecture notes in physics*, 2006.
- [229] A. Van Yperen-De Deyne, T. De Meyer, E. Pauwels, A. Ghysels, K. De Clerck, M. Waroquier, V. Van Speybroeck, and K. Hemelsoet, “Exploring the vibrational fingerprint of the electronic excitation energy via molecular dynamics,” *J. Chem. Phys.*, vol. 140, no. 13, pp. 134105, 2014.

- [230] C. Lamberti, A. Zecchina, E. Groppo, and S. Bordiga, "Probing the surfaces of heterogeneous catalysts by in situ IR spectroscopy," *Chem. soc. rev.*, vol. 39, no. 12, pp. 4951, 2010.
- [231] S. O. Odoh, C. J. Cramer, D. G. Truhlar, and L. Gagliardi, "Quantum-Chemical characterization of the properties and reactivities of Metal-Organic frameworks," *Chem. Rev.*, vol. 115, no. 12, pp. 6051–6111, 2015.
- [232] S. Chavan, J. G. Vitillo, D. Gianolio, O. Zavorotynska, B. Civalieri, S. Jakobsen, M. H. Nilsen, L. Valenzano, C. Lamberti, K. Lillerud, and S. Bordiga, "H₂ storage in isostructural UiO-67 and UiO-66 MOFs," *Phys. Chem. Chem. Phys.*, vol. 14, no. 5, pp. 1614–1626, 2011.
- [233] K. Leus, P. Concepcion, M. Vandichel, M. Meledina, A. Grirrane, D. Esquivel, S. Turner, D. Poelman, M. Waroquier, V. Van Speybroeck, G. Van Tendeloo, H. García, and P. Van Der Voort, "Au@UiO-66: a base free oxidation catalyst," *Rsc Adv.*, vol. 5, no. 29, pp. 22334–22342, 2015.
- [234] J. A. Greathouse and M. D. Allendorf, "Force field validation for molecular dynamics simulations of IRMOF-1 and other isorecticular zinc carboxylate coordination polymers," *J. Phys. Chem. C*, vol. 112, no. 15, pp. 5795–5802, 2008.
- [235] S. Grimme, J. Antony, S. Ehrlich, and H. Krieg, "A consistent and accurate ab initio parametrization of density functional dispersion correction (DFT-D) for the 94 elements H-Pu," *J. Chem. Phys.*, vol. 132, no. 15, pp. 154104, 2010.
- [236] G. Lippert, J. Hutter, and M. Parrinello, "A hybrid gaussian and plane wave density functional scheme," *Mol. Phys.*, vol. 92, no. 3, pp. 477–487, 1997.
- [237] C. Hartwigsen, S. Goedecker, and J. Hutter, "Relativistic separable dual-space gaussian pseudopotentials from H to Rn," *Phys. Rev. B*, vol. 58, no. 7, pp. 3641–3662, 1998.
- [238] S. Goedecker, M. Teter, and M. Hutter, "Separable dual-space gaussian pseudopotentials," *Phys. Rev. B*, vol. 54, no. 3, pp. 1703–1710, 1996.
- [239] T. Verstraelen, M. Van Houteghem, V. Van Speybroeck, and M. Waroquier, "MD-TRACKS: A productive solution for the advanced analysis of molecular dynamics and monte carlo simulations," *Journal of Chem. Inf. Mod.*, vol. 48, no. 12, pp. 2414–2424, 2008.

- [240] M. Van Houteghem, T. Verstraelen, D. Van Neck, C. Kirschhock, J. A. Martens, M. Waroquier, and V. Van Speybroeck, "Atomic velocity projection method: A new analysis method for vibrational spectra in terms of internal coordinates for a better understanding of zeolite nanogrowth," *J. Chem. Theor. Comput.*, vol. 7, no. 4, pp. 1045–1061, 2011.
- [241] M. Kim, J. F. Cahill, H. Fei, K. A. Prather, and S. M. Cohen, "Post-synthetic ligand and cation exchange in robust Metal-Organic frameworks," *J. Am. Chem. Soc.*, vol. 134, no. 43, pp. 18082–18088, 2012.
- [242] S. J.D. Smith, B. P. Ladewig, A. J. Hill, C. Lau, and M. R. Hill, "Post-synthetic Ti exchanged UiO-66 Metal-Organic frameworks that deliver exceptional gas permeability in mixed matrix membranes," *Sci. Rep.*, vol. 5, pp. 7823, 2015.
- [243] D. Sun, W. Liu, M. Qiu, Y. Zhang, and Z. Li, "Introduction of a mediator for enhancing photocatalytic performance via post-synthetic metal exchange in metal-organic frameworks (MOFs)," *Chem. Commun*, vol. 51, no. 11, pp. 2056–2059, 2014.
- [244] Y. Lee, S. Kim, J. Kang, and S. M. Cohen, "Photocatalytic CO₂ reduction by a mixed metal (Zr/Ti), mixed ligand metal-organic framework under visible light irradiation," *Chem. Commun*, vol. 51, no. 26, pp. 5735–5738, 2015.
- [245] A. Wang, Y. Zhou, Z. Wang, M. Chen, L. Sun, and X. Liu, "Titanium incorporated with UiO-66(Zr)-type Metal-Organic framework (MOF) for photocatalytic application," *Rsc Adv.*, vol. 6, no. 5, pp. 3671–3679, 2015.
- [246] A. Yasin, J. Li, N. Wu, and T. Musho, "Study of the inorganic substitution in a functionalized uiO-66 metal-organic framework," *Phys. Chem. Chem. Phys.*, vol. 18, no. 18, pp. 12748–12754, 2016.
- [247] L-M. Yang, E. Ganz, S. Svelle, and M. Tilset, "Computational exploration of newly synthesized zirconium metal-organic frameworks UiO-66, -67, -68 and analogues," *J. Mater. Chem. C*, vol. 2, no. 34, pp. 7111–7125, 2014.
- [248] A. Santiago-Portillo, H. Baldovi, T. García, S. Navalon, P. Atienzar, B. Ferrer, M. Alvaro, H. Garcia, and Z. Li, "Ti as mediator in the photoinduced electron transfer of Mixed-Metal NH₂-UiO66(Zr/Ti). transient absorption spectroscopy study and application in photovoltaic cell," *J. Phys. Chem. C*, vol. 121, no. 12, pp. 7015–7024, 2017.

- [249] Y. Yaoguang, G. Chen, Y. Zhou, and Z. Han, "Recent advances in rare-earth elements modification of inorganic semiconductor-based photocatalysts for efficient solar energy conversion: A review," *J. Rare Earth*, vol. 33, no. 5, pp. 453–462, 2015.
- [250] G. S. Kumar and G. L. Devi, "Review on modified TiO₂ photocatalysis under UV/Visible light: Selected results and related mechanisms on interfacial charge carrier transfer dynamics," *J. Phys. Chem. A*, vol. 115, no. 46, pp. 13211–13241, 2011.
- [251] X. Qin, X. Liu, W. Huang, M. Bettinelli, and X. Liu, "Lanthanide-Activated phosphors based on 4f-5d optical transitions: Theoretical and experimental aspects," *Chem. Rev.*, vol. 117, no. 5, pp. 4488–4527, 2017.
- [252] P. Cheng, *Lanthanide Metal-Organic Frameworks*, Structure and Bonding. Springer, 2015.
- [253] H. Xu, C-S. Cao, X-M. Kang, and B. Zhao, "Lanthanide-based metal-organic frameworks as luminescent probes," *Dalton T*, vol. 45, no. 45, pp. 18003–18017, 2016.
- [254] C. Pagis, M. Ferbinteanu, G. Rothenberg, and S. Tanase, "Lanthanide-Based metal-organic frameworks: Synthetic strategies and catalytic applications," *Acs Catal.*, vol. 6, no. 9, pp. 6063–6072, 2016.
- [255] Y-T. Liang, G-P. Yang, B. Liu, Y-T. Yan, Z-P. Xi, and Y-Y. Wang, "Four super water-stable lanthanide-organic frameworks with active uncoordinated carboxylic and pyridyl groups for selective luminescence sensing of Fe³⁺," *Dalton Trans.*, vol. 44, no. 29, pp. 13325–13330, 2015.
- [256] P. Dorenbos, "A review on how lanthanide impurity levels change with chemistry and structure of inorganic compounds," *Ecs J. Solid State Sci. Tech.*, vol. 2, no. 2, pp. R3001–R3011, 2013.
- [257] J. J. Joos, D. Poelman, and P. F. Smet, "Energy level modeling of lanthanide materials: review and uncertainty analysis," *Phys. Chem. Chem. Phys.*, vol. 17, no. 29, pp. 19058–19078, 2015.
- [258] L. Seijo and Z. Barandiarán, *Ab Initio Calculations on Excited States of Lanthanide Containing Materials*, Handbook on the Physics and Chemistry of Rare Earths. Elsevier, 2016.
- [259] C. Lau, R. Babarao, and M. R. Hill, "A route to drastic increase of CO₂ uptake in zirconium metal organic framework UiO-66," *Chem. Commun.*, vol. 49, no. 35, pp. 3634–3636, 2013.

- [260] J. Tu, X. Zeng, F. Xu, X. Wu, Y. Tian, X. Hou, and Z. Long, "Microwave-induced fast incorporation of titanium into UiO-66 metal-organic frameworks for enhanced photocatalytic properties," *Chem. Commun.*, vol. 53, no. 23, pp. 3361–3364, 2017.
- [261] Handbook on the Physics and Chemistry of Rare Earths), author=Görrler-Walrand, C. and Binnemans, K., title=Rationalization of crystal-field parametrization, in Handbook on the Physics and Chemistry of Rare Earths. Elsevier, 1996.
- [262] E.G. Rogers and P. Dorenbos, "Vacuum energy referred $\text{Ti}^{3+/4+}$ donor/acceptor states in insulating and semiconducting inorganic compounds," *J. Lumin.*, vol. 153, pp. 40–45, 2014.
- [263] J. R. Levin, W. L. Dornfner, A. X. Dai, P. J. Carroll, and E. J. Schelter, "Density functional theory as a predictive tool for cerium redox properties in nonaqueous solvents," *Inorg. Chem.*, vol. 55, no. 24, pp. 12651–12659, 2016.
- [264] C. Loschen, A. Migani, S. T. Bromley, F. Illas, and K. M. Neyman, "Density functional studies of model cerium oxide nanoparticles," *Phys. Chem. Chem. Phys.*, vol. 10, no. 37, pp. 5730–5738, 2008.
- [265] P. Vinet, J. Ferrante, J.H. Rose, and J.R. Smith, "Compressibility of solids," *J. Geophys. Res. Solid Earth*, vol. 92, no. B9, pp. 9319, 1987.
- [266] C. Freysoldt, B. Grabowski, T. Hickel, J. Neugebauer, G. Kresse, A. Janotti, and C. G de Walle, "First-principles calculations for point defects in solids," *Rev Mod Phys*, vol. 86, no. 1, pp. 253–305, 2014.
- [267] M.A.L. Marques, *Time-Dependent Density Functional Theory*, Springer, 2006.
- [268] R. J. Marshall and R. S. Forgan, "Postsynthetic modification of zirconium Metal-Organic frameworks," *Eur. J. Inorg. Chem.*, vol. 2016, no. 27, pp. 4310–4331, 2016.
- [269] J. Zhao, L. Mi, J. Hu, H. Hou, and Y. Fan, "Cation exchange induced tunable properties of a nanoporous octanuclear Cu(II) wheel with Double-Helical structure," *J. Am. Chem. Soc.*, vol. 130, no. 46, pp. 15222–15223, 2008.
- [270] D. Son, S. M. Hughes, Y. Yin, and P. A. Alivisatos, "Cation exchange reactions in ionic nanocrystals," *Science*, vol. 306, no. 5698, pp. 1009–1012, 2004.

- [271] H. Fei, C. H. Pham, and S. R.J. Oliver, "Anion exchange of the cationic layered material $[\text{Pb}_2\text{F}_2]^{2+}$," *J. Am. Chem. Soc.*, vol. 134, no. 26, pp. 10729–10732, 2012.
- [272] J. Santaclara, A. Suarez, A. Nelson, D. Osadchii, M. A. Nasalevich, M. A. van der Veen, F. Kapteijn, A. M. Sheveleva, S. L. Veber, M. V. Fedin, A. Murray, C. H. Hendon, A. Walsh, and J. Gascon, "Revisiting the incorporation of Ti(IV) in UiO-type metal-organic frameworks: metal exchange versus grafting and their implications on photocatalysis," *Chem. Mater.*, 2017.
- [273] M. Janulevicius, P. Marmokas, M. Misevicius, J. Grigorjevaite, L. Mikoliunaite, S. Sakirzanovas, and A. Katelnikovas, "Luminescence and luminescence quenching of highly efficient $\text{Y}_2\text{Mo}_4\text{O}_{15}:\text{Eu}^{3+}$ phosphors and ceramics," *Sci. Rep.*, vol. 6, no. 1, pp. 26098, 2016.
- [274] Y.-Y. Liu, R. Decadt, T. Bogaerts, K. Hemelsoet, A. M. Kaczmarek, D. Poelman, M. Waroquier, V. Speybroeck, R. Deun, and P. Van Der Voort, "Bipyridine-Based nanosized Metal-Organic framework with tunable luminescence by a postmodification with Eu(III): an experimental and theoretical study," *J. Phys. Chem. C*, vol. 117, no. 21, pp. 11302–11310, 2013.
- [275] P. Dorenbos, "Ce $^{3+}$ 5d-centroid shift and vacuum referred 4f-electron binding energies of all lanthanide impurities in 150 different compounds," *J. Lumin.*, vol. 135, pp. 93–104, 2013.
- [276] H.E. Hoefdraad, "Charge-transfer spectra of tetravalent lanthanide ions in oxides," *J. Inorg. Nucl. Chem.*, vol. 37, no. 9, pp. 1917 – 1921, 1975.
- [277] Luis Seijo and Zoila Barandiarán, "Intervalence charge transfer luminescence: The anomalous luminescence of cerium-doped $\text{Cs}_2\text{LiLuCl}_6$ elpasolite," *J. Chem. Phys.*, vol. 141, no. 21, pp. 214706, 2014.
- [278] D. S. Sholl and R. P. Lively, "Defects in Metal-Organic frameworks: Challenge or opportunity?," *J. Phys. Chem. Lett.*, vol. 6, no. 17, pp. 3437–3444, 2015.
- [279] Z. Fang, B. Bueken, D. E. De Vos, and R. A. Fischer, "Defect-Engineered Metal-Organic frameworks," *Angew. Chem. Int. Ed. Engl.*, vol. 54, no. 25, pp. 7234–54, 2015.
- [280] G. C. Shearer, S. Chavan, J. Ethiraj, J. G. Vitillo, S. Svelle, U. Olsbye, C. Lamberti, S. Bordiga, and K. Lillerud, "Tuned to perfection: Ironing

- out the defects in Metal-Organic framework UiO-66,” *Chem. Mater.*, vol. 26, no. 14, pp. 4068–4071, 2014.
- [281] G. C. Shearer, S. Chavan, S. Bordiga, S. Svelle, U. Olsbye, and K. Lillerud, “Defect engineering: Tuning the porosity and composition of the Metal-Organic framework UiO-66 via modulated synthesis,” *Chem. Mater.*, vol. 28, no. 11, pp. 3749–3761, 2016.
- [282] O. V Gutov, M. Hevia, E. C. Escudero-Adán, and A. Shafir, “Metal-Organic framework (MOF) defects under control: Insights into the missing linker sites and their implication in the reactivity of Zirconium-Based frameworks,” *Inorg. Chem.*, vol. 54, no. 17, pp. 8396–8400, 2015.
- [283] S. Rogge, J. Wieme, L. Vanduyfhuys, S. Vandenbrande, G. Maurin, T. Verstraelen, M. Waroquier, and V. Speybroeck, “Thermodynamic insight in the High-Pressure behavior of UiO-66: effect of linker defects and linker expansion,” *Chem. Mater.*, vol. 28, no. 16, pp. 5721–5732, 2016.
- [284] F. Vermoortele, B. Bueken, Gaëlle Bars, B. de Voorde, M. Vandichel, K. Houthoofd, A. Vimont, M. Daturi, M. Waroquier, V. Speybroeck, C. Kirschhock, and D. E Vos, “Synthesis modulation as a tool to increase the catalytic activity of Metal-Organic frameworks: The unique case of UiO-66(Zr),” *J. Am. Chem. Soc.*, vol. 135, no. 31, pp. 130726133410000, 2013.
- [285] J. Canivet, M. Vandichel, and D. Farrusseng, “Origin of highly active metal-organic framework catalysts: defects? defects!,” *Dalton Trans.*, vol. 45, no. 10, pp. 4090–9, 2016.
- [286] D. Yang, S. OO Odoh, J. Borycz, T. C. Wang, O. K. Farha, J. T. Hupp, C. J. Cramer, L. Gagliardi, and Bruce C. Gates, “Tuning Zr₆Metal-Organic framework (MOF) nodes as catalyst supports: Site densities and Electron-Donor properties influence molecular iridium complexes as ethylene conversion catalysts,” *Acs Catal.*, vol. 6, no. 1, pp. 235–247, 2016.
- [287] H. Wu, Y. Chua, V. Krungleviciute, M. Tyagi, P. Chen, T. Yildirim, and W. Zhou, “Unusual and highly tunable Missing-Linker defects in zirconium Metal-Organic framework UiO-66 and their important effects on gas adsorption,” *J. Am. Chem. Soc.*, vol. 135, no. 28, pp. 10525–10532, 2013.

- [288] A.W. Thornton, R. Babarao, A. Jain, F. Trouselet, and F-X. Coudert, "Defects in metal-organic frameworks: a compromise between adsorption and stability?," *Dalton Trans.*, vol. 45, no. 10, pp. 4352–9, 2016.
- [289] J. K. Bristow, K. L. Svane, D. Tiana, J. M. Skelton, J. D. Gale, and A. Walsh, "Free energy of ligand removal in the Metal-Organic framework UiO-66," *J. Phys. Chem. C*, vol. 120, no. 17, pp. 9276–9281, 2016.
- [290] S. Ling and B. Slater, "Dynamic acidity in defective UiO-66," *Chem. Sci.*, vol. 7, no. 7, pp. 4706–4712, 2016.
- [291] M. Vandichel, J. Hajek, A. Ghysels, A. De Vos, M. Waroquier, and V. Van Speybroeck, "Water coordination and dehydration processes in defective UiO-66 type metal-organic frameworks," *Crystengcomm*, vol. 18, no. 37, pp. 7056–7069, 2016.
- [292] D. Yang, S. O. Odoh, T. C. Wang, O. K. Farha, J. T. Hupp, C. J. Cramer, L. Gagliardi, and B. C. Gates, "Metal-Organic framework nodes as nearly ideal supports for molecular catalysts: NU-1000- and UiO-66-Supported iridium complexes," *J. Am. Chem. Soc.*, vol. 137, no. 23, pp. 7391–7396, 2015.
- [293] A. Walsh, K. T. Butler, and C. H. Hendon, "Chemical principles for electroactive metal-organic frameworks," *MRS Bulletin*, vol. 41, no. 11, pp. 870–876, 2016.
- [294] M. Usman, S. Mendiratta, and K-L. Lu, "Semiconductor Metal-Organic frameworks: Future Low-Bandgap materials," *Adv. Mater.*, vol. 29, no. 6, 2017.



Funding was received from the European Research Council under the European Community's Seventh Framework Programme [FP7(2007-2013) ERC grant agreement number 240483], the Research Board of Ghent University (BOF) and BELSPO in the frame of IAP/6/27



Computational resources (Stevin Supercomputer Infrastructure) and services were provided by Ghent University.

